# NUMERICAL MODELING OF PROGRESSIVE FRACTURE IN THE COMPRESSIONAL LOADING OF CYLINDRICAL CAVITIES

BY

EDWARD JOHN DZIK

A Thesis
Submitted to the Faculty of Graduate Studies
in Partial Fulfillment of the Requirements
for the Degree of

DOCTOR OF PHILOSOPHY

Department of Civil and Geological Engineering
University of Manitoba
Winnipeg, Manitoba

ISBN   0-612-16127-7

Canada

TITLE: NUMERICAL MODELING OF PROGRESSIVE FRACTURE IN THE COMPRESSIONAL LOADING OF CYLINDRICAL CAVITIES

Name EDWARD DZIK

*Dissertation Abstracts International* and *Masters Abstracts International* are arranged by broad, general subject categories. Please select the one subject which most nearly describes the content of your dissertation or thesis. Enter the corresponding four-digit code in the spaces provided.

MINING ENGINEERING

SUBJECT TERM

0 5 5 1

SUBJECT CODE

**UMI**

## Subject Categories

# THE HUMANITIES AND SOCIAL SCIENCES

**COMMUNICATIONS AND THE ARTS**
Architecture ............................... 0729
Art History .................................. 0377
Cinema ...................................... 0900
Dance ........................................ 0378
Fine Arts .................................... 0357
Information Science .................... 0723
Journalism ................................. 0391
Library Science ........................... 0399
Mass Communications ............... 0708
Music ........................................ 0413
Speech Communication ............. 0459
Theater ...................................... 0465

**EDUCATION**
General ...................................... 0515
Administration ............................ 0514
Adult and Continuing ................. 0516
Agricultural ................................ 0517
Art ............................................. 0273
Bilingual and Multicultural ......... 0282
Business ..................................... 0688
Community College ..................... 0275
Curriculum and Instruction ......... 0727
Early Childhood ......................... 0518
Elementary ................................. 0524
Finance ...................................... 0277
Guidance and Counseling ......... 0519
Health ........................................ 0680
Higher ....................................... 0745
History of ................................... 0520
Home Economics ....................... 0278
Industrial ................................... 0521
Language and Literature ............ 0279
Mathematics ............................... 0280
Music ......................................... 0522
Philosophy of ............................. 0998
Physical ..................................... 0523

Psychology ................................ 0525
Reading ..................................... 0535
Religious .................................... 0527
Sciences .................................... 0714
Secondary .................................. 0533
Social Sciences .......................... 0534
Sociology of ............................... 0340
Special ....................................... 0529
Teacher Training ........................ 0530
Technology ................................. 0710
Tests and Measurements ............ 0288
Vocational .................................. 0747

**LANGUAGE, LITERATURE AND LINGUISTICS**
Language
    General .................................. 0679
    Ancient .................................. 0289
    Linguistics .............................. 0290
    Modern .................................. 0291
Literature
    General .................................. 0401
    Classical ................................ 0294
    Comparative ........................... 0295
    Medieval ................................ 0297
    Modern .................................. 0298
    African ................................... 0316
    American ................................ 0591
    Asian ..................................... 0305
    Canadian (English) ................ 0352
    Canadian (French) ................. 0355
    English ................................... 0593
    Germanic ................................ 0311
    Latin American ....................... 0312
    Middle Eastern ....................... 0315
    Romance ................................ 0313
    Slavic and East European ..... 0314

**PHILOSOPHY, RELIGION AND THEOLOGY**
Philosophy ................................. 0422
Religion
    General .................................. 0318
    Biblical Studies ...................... 0321
    Clergy .................................... 0319
    History of ............................... 0320
    Philosophy of ......................... 0322
Theology .................................... 0469

**SOCIAL SCIENCES**
American Studies ....................... 0323
Anthropology
    Archaeology ........................... 0324
    Cultural ................................. 0326
    Physical ................................. 0327
Business Administration
    General .................................. 0310
    Accounting ............................. 0272
    Banking .................................. 0770
    Management ........................... 0454
    Marketing ............................... 0338
Canadian Studies ...................... 0385
Economics
    General .................................. 0501
    Agricultural ............................ 0503
    Commerce-Business ............... 0505
    Finance .................................. 0508
    History ................................... 0509
    Labor ..................................... 0510
    Theory ................................... 0511
Folklore ...................................... 0358
Geography ................................. 0366
Gerontology ............................... 0351
History
    General .................................. 0578

Ancient ...................................... 0579
Medieval .................................... 0581
Modern ...................................... 0582
Black ......................................... 0328
African ....................................... 0331
Asia, Australia and Oceania 0332
Canadian ................................... 0334
European ................................... 0335
Latin American ........................... 0336
Middle Eastern .......................... 0333
United States ............................. 0337
History of Science ...................... 0585
Law ............................................ 0398
Political Science
    General .................................. 0615
    International Law and
        Relations ........................... 0616
    Public Administration ............. 0617
Recreation ................................. 0814
Social Work ............................... 0452
Sociology
    General .................................. 0626
    Criminology and Penology ... 0627
    Demography ........................... 0938
    Ethnic and Racial Studies ..... 0631
    Individual and Family
        Studies .............................. 0628
    Industrial and Labor
        Relations ........................... 0629
    Public and Social Welfare .... 0630
    Social Structure and
        Development ...................... 0700
    Theory and Methods ............. 0344
Transportation ........................... 0709
Urban and Regional Planning .... 0999
Women's Studies ....................... 0453

# THE SCIENCES AND ENGINEERING

**BIOLOGICAL SCIENCES**
Agriculture
    General .................................. 0473
    Agronomy .............................. 0285
    Animal Culture and
        Nutrition ............................ 0475
    Animal Pathology .................. 0476
    Food Science and
        Technology ....................... 0359
    Forestry and Wildlife ............. 0478
    Plant Culture .......................... 0479
    Plant Pathology ...................... 0480
    Plant Physiology ..................... 0817
    Range Management ............... 0777
    Wood Technology .................. 0746
Biology
    General .................................. 0306
    Anatomy ................................. 0287
    Biostatistics ............................ 0308
    Botany ................................... 0309
    Cell ........................................ 0379
    Ecology .................................. 0329
    Entomology ............................ 0353
    Genetics ................................. 0369
    Limnology ............................... 0793
    Microbiology .......................... 0410
    Molecular ............................... 0307
    Neuroscience .......................... 0317
    Oceanography ........................ 0416
    Physiology .............................. 0433
    Radiation ................................ 0821
    Veterinary Science .................. 0778
    Zoology .................................. 0472
Biophysics
    General .................................. 0786
    Medical .................................. 0760

**EARTH SCIENCES**
Biogeochemistry ........................ 0425
Geochemistry ............................ 0996

Geodesy .................................... 0370
Geology ..................................... 0372
Geophysics ................................ 0373
Hydrology .................................. 0388
Mineralogy ................................ 0411
Paleobotany .............................. 0345
Paleoecology ............................. 0426
Paleontology ............................. 0418
Paleozoology ............................. 0985
Palynology ................................ 0427
Physical Geography ................... 0368
Physical Oceanography ............. 0415

**HEALTH AND ENVIRONMENTAL SCIENCES**
Environmental Sciences ............. 0768
Health Sciences
    General .................................. 0566
    Audiology ............................... 0300
    Chemotherapy ........................ 0992
    Dentistry ................................ 0567
    Education ................................ 0350
    Hospital Management ............. 0769
    Human Development .............. 0758
    Immunology ............................ 0982
    Medicine and Surgery ........... 0564
    Mental Health ......................... 0347
    Nursing .................................. 0569
    Nutrition ................................. 0570
    Obstetrics and Gynecology .. 0380
    Occupational Health and
        Therapy ............................. 0354
    Ophthalmology ....................... 0381
    Pathology ............................... 0571
    Pharmacology ........................ 0419
    Pharmacy ............................... 0572
    Physical Therapy .................... 0382
    Public Health .......................... 0573
    Radiology ............................... 0574
    Recreation .............................. 0575

Speech Pathology ...................... 0460
Toxicology ................................. 0383
Home Economics ....................... 0386

**PHYSICAL SCIENCES**

Pure Sciences
Chemistry
    General .................................. 0485
    Agricultural ............................ 0749
    Analytical ............................... 0486
    Biochemistry ........................... 0487
    Inorganic ................................ 0488
    Nuclear .................................. 0738
    Organic .................................. 0490
    Pharmaceutical ...................... 0491
    Physical ................................. 0494
    Polymer .................................. 0495
    Radiation ................................ 0754
Mathematics ............................... 0405
Physics
    General .................................. 0605
    Acoustics ................................ 0986
    Astronomy and
        Astrophysics ...................... 0606
    Atmospheric Science .............. 0608
    Atomic ................................... 0748
    Electronics and Electricity ...... 0607
    Elementary Particles and
        High Energy ...................... 0798
    Fluid and Plasma ................... 0759
    Molecular ............................... 0609
    Nuclear .................................. 0610
    Optics .................................... 0752
    Radiation ................................ 0756
    Solid State .............................. 0611
Statistics .................................... 0463

Applied Sciences
Applied Mechanics .................... 0346
Computer Science ...................... 0984

Engineering
    General .................................. 0537
    Aerospace .............................. 0538
    Agricultural ............................ 0539
    Automotive ............................. 0540
    Biomedical ............................. 0541
    Chemical ................................ 0542
    Civil ....................................... 0543
    Electronics and Electrical ...... 0544
    Heat and Thermodynamics ... 0348
    Hydraulic ............................... 0545
    Industrial ............................... 0546
    Marine ................................... 0547
    Materials Science ................... 0794
    Mechanical ............................. 0548
    Metallurgy .............................. 0743
    Mining .................................... 0551
    Nuclear .................................. 0552
    Packaging .............................. 0549
    Petroleum ............................... 0765
    Sanitary and Municipal .......... 0554
    System Science ....................... 0790
Geotechnology .......................... 0428
Operations Research .................. 0796
Plastics Technology ................... 0795
Textile Technology ..................... 0994

**PSYCHOLOGY**
General ...................................... 0621
Behavioral ................................. 0384
Clinical ...................................... 0622
Developmental ........................... 0620
Experimental .............................. 0623
Industrial ................................... 0624
Personality ................................. 0625
Physiological ............................. 0989
Psychobiology ........................... 0349
Psychometrics ............................ 0632
Social ........................................ 0451

THE UNIVERSITY OF MANITOBA

FACULTY OF GRADUATE STUDIES

COPYRIGHT PERMISSION

NUMERICAL MODELING OF PROGRESSIVE FRACTURE IN THE

COMPRESSIONAL LOADING OF CYLINDRICAL CAVITIES

BY

EDWARD JOHN DZIK

A Thesis/Practicum submitted to the Faculty of Graduate Studies of the University of Manitoba in partial fulfillment of the requirements for the degree of

DOCTOR OF PHILOSOPHY

Edward John Dzik      © 1996

# Abstract

AECL has constructed the Underground Research Laboratory (URL) as part of its assessment of the feasibility and safety of deep geological disposal of nuclear fuel waste. One of the operating phase experiments conducted at the URL involved the excavation of a mine-by tunnel with a circular cross section lying in the plane of the far-field maximum and minimum principal stresses. This configuration was chosen to maximize the damage occurring in the compressive stress concentrations of the tunnel. An extensive research program was undertaken in an attempt to understand the mechanisms involved in creating this damage zone.

To supplement the field studies, a laboratory testing program was carried out at the University of Manitoba to investigate the course of fracture around a circular opening in granite specimens. A suite of specimens were tested, each containing a circular hole of radius varying between 2.5 and 50 mm. To minimize boundary effects, the blocks were cut to a size where the radius to block width ratio was kept at around ten. Although some biaxial tests were conducted as well, the modeling in this thesis uses data from uniaxial compression tests. The block faces and occasionally the insides of the cavity were instrumented with strain gauges. These were used to detect fracture initiation at the three usual action areas: the primary fracture regions which occur at the tensile stress concentrations at the hole perimeter, the remote or secondary fracture regions which occur in quadrant positions a short distance from the perimeter of the hole, and the spalling fracture regions which occur in the compression zones near the hole perimeter. Fracture propagation along both the

primary and the remote fracture directions were also tracked with the aid of strain gauges. Because all three fracture types are thought to be governed by identical initiation and propagation mechanisms, a fracture model successful at representing the behavior of one of the fracture types could potentially be used to model the other two types (including fractures found around the URL mine-by tunnel). With this in mind, the fracture with the simplest geometry would be the logical choice to calibrate a fracture model against. The primary fracture fits this description and modeling its behavior is the focus of this thesis.

To interpret the results, two computer programs were constructed. One, InSight$^{2D}$, is based on the finite element technique, the other, EJDBEM, on the boundary element method. What distinguishes these programs from others in the education or commercial spheres is that both represent a new approach to fracture through the implementation of a finite-width crack model. In these programs a crack is represented by a slot that, in contrast to classical fracture mechanics, has finite width. Fracturing events are detected through the use of a stress-based criterion that relies on contributions from both in-plane principal stresses. This allows fracturing to be controlled not only by the lateral tensile principal stress, as is commonly done in fracture mechanics, but also by the axial compressive stress. A stress averaging technique is used in conjunction with this stress-based fracture criterion to address the size effect commonly observed in laboratory testing.

The results from the physical model testing showed a pronounced size effect for the initiation and propagation histories of all three fracture types. In addition to the size effect it was found that the finite dimensions of the laboratory specimens significantly controlled fracturing events. The most intriguing result was that, through structural size changes, fracture propagation appeared to go from a very stable fracture propagation mode at small radius cavities to an (almost) unstable mode for the larger cavity sizes. Most of the existing analytical models ignore boundary effects (infinite medium assumed) and fail to explain the size effect on primary fracture propagation. Exceptions to this are Bažant's and Carpinteri's treatment of size-effect. The two numerical models of this thesis were successful in modeling

the test results.

Using the finite-width fracture model in combination with the stress averaging technique (size effect model), axial fracture propagation under compressive loading can be reproduced, including the formation of the frequently observed axial tensile fracture arrays (e.g., *en echelon* fractures). While engineering fracture mechanics is limited to the extension of a single crack through fracture at the crack tip proper, the stress averaging technique allows fracture to occur anywhere in the material domain. In fact, the fracture site often shifts away from the crack tip to produce a "step-out" condition. The conditions for producing "step-outs" and hence crack arrays can be simulated with the finite-width fracture model provided rock strength is treated as a point-to-point variable (heterogeneous material).

# Acknowledgements

I express my sincere gratitude to my advisor, Emery Lajtai, for his guidance and support throughout this study. The task of completing this thesis with him was indeed a pleasure.

I am grateful to Wojciech Grajewski and Wayne Pitura for preparing the laboratory samples and conducting the laboratory experiments. Their technical skill made this project a success.

I thank AECL and specifically Gary Simmons, Mitch Ohta, and Neil Chandler who have allowed me the time and support over the years required to complete this endeavor. I would also like to extend my heartfelt thanks to Derek Martin who started all this. His seemingly boundless energy and incredible store of new ideas constantly renews my interest in science.

Finally, with love I thank my wife Catherine Shields and sons Evan and Eli. Thank you for your patience, understanding, and faith throughout these busy times.

# Contents

# List of Figures

xiii

# List of Tables

# Symbols and Notation

| | |
|---|---|
| $E$ | Young's modulus |
| $\nu$ | Poisson's ratio |
| $\sigma_1$ | Maximum principal stress |
| $\sigma_3$ | Minimum principal stress |
| $C_0$ | Uniaxial compressive strength |
| $T_0$ | Uniaxial tensile strength |
| $R$ | Cavity radius |
| $Ra^2$ | Degree of freedom adjusted coefficient of determination |
| $c$ | Crack half length |
| $L$ | Total crack length $= 2c$ |
| $K_I$ | Mode I stress intensity factor |
| $K_{Ic}$ | Mode I critical stress intensity factor (fracture toughness) |
| $G$ | Strain energy release rate |
| $\gamma_s$ | Specific surface energy |
| $\gamma_p$ | Work done in plastic deformation |
| USR | Unconfined Strength Ratio (factor of safety) |
| $d$ | Averaging distance |
| $\Delta y$ | Averaging offset |
| fw | Fracture width |

# Chapter 1

# Introduction

## 1.1 Scope of Study

The process of fracturing has always been of great interest in any field relying on the strength of materials for structural stability. Areas of research include such diverse fields as civil engineering, mining, aeronautics, and dentistry. The process of fracturing is usually studied from a structural stability viewpoint. In the mining industry, for example, fractures can lead to the ultimate collapse of underground excavations. With the push for larger extraction ratios and deeper excavations, conditions underground become increasingly hazardous. A fundamental understanding of the driving mechanisms behind fracturing would undoubtedly allow the ground control engineer greater flexibility in the design of a safe mine.

Recently, considerable interest in fractures has been generated from an engineered barrier standpoint. The concept of permanent underground disposal of high level nuclear fuel waste has gained popularity in Canada, the United States, and in Europe [68]. A fracture system intersecting a waste canister would obviously provide a convenient path for transporting waste, thus compromising the effectiveness of the repository.

In both of the above examples fracturing occurs in an environment dominated by compressive loads. To date, the majority of fracture studies has focused on fractures propagating under tensile loading conditions with very little attention paid to fracture under compressive conditions.

1

Griffith [34] laid the foundation for modern day fracture mechanics, propounding crack initiation theories for both types of loading conditions (tensile and compressive). In his theories a material is assumed to contain numerous microscopic flaws which act as stress concentrators when the material is subjected to a load. These "Griffith fractures" will propagate if tensile stresses develop, at a flaw boundary, that are sufficient to break material bonds. Griffith assumed the microscopic flaws were elliptical in shape. A mathematical simplification can be introduced by collapsing the elliptical flaw to a negligible width (a zero-width fracture). Under tensile loading conditions a fracture will propagate in its own plane (perpendicular to the applied tensile load). Because of this simple geometry, Griffith was able to formulate an energy balance expression for fracturing under tensile loading conditions. Under compressive loading conditions it is well known that fractures will propagate in the direction of the applied load (or more correctly, perpendicular to the minimum principal stress trajectory). A zero-width fracture, oriented parallel to the compressive loading direction, will not propagate. Griffith realized this shortcoming and for this reason introduced a second fracture criterion for compressive loading conditions. By inclining the zero-width fracture to the loading direction it is possible to initiate fractures near the fracture tips. These fractures eventually curve out from the inclined fracture and align themselves with the loading direction; these are known as "wing cracks". Due to the complicated geometry of this problem (fractures no longer travel in their own plane), Griffith resorted to a stress-based fracture criterion for compressive loading conditions. A shortcoming of "wing cracks", is that they will only propagate a short distance and then stall, even under increased loads.

The literature points to the absence of "wing cracks" in brittle materials. The physical absence and undesirable behavior of the zero-width elliptical flaw under compressive loading conditions is one of the motivating forces for the work presented in this thesis. By "opening up" the zero-width fracture it is possible to cause it to propagate parallel to the applied load. Due to the complicated geometry of the finite-width fracture, this problem has received very

little attention to date. With powerful computers now commonplace, and the development of advanced numerical methods, this problem is now solvable. Modeling the propagation of a finite-width fracture under compressive loads is the first contribution of this thesis.

In addition to the crack propagation problem stated above, compressive fracture in brittle materials also shows a pronounced size effect. A small sample will appear to have a higher compressive strength than a large sample. Although numerous theories exist, size effect is not well understood. These theories can be roughly categorized into stress-gradient- and energy-based approaches. A gradient-based approach, that was originally proven for fracture initiation problems, is applied to a fracture propagation problem in this thesis. Addressing the size effect problem of fracture propagation is the second contribution of this thesis.

A numerical tool has been developed to model discrete fractures in brittle materials under compressive loading conditions. This thesis describes the development of this fracture model and the calibration of this model to laboratory data. The model is applied specifically to primary tensile fractures emanating from circular cavities in granite under uniaxial compressive loading conditions.

## 1.2 Thesis Outline

This thesis is subdivided into the following chapters.

- Chapter 1 introduces the problem being investigated and outlines the organization of the thesis.

- Chapter 2 gives a brief overview of the general characteristics and behavior of rock. This is followed by a section describing the laboratory testing that was done in support of this thesis. It is hoped that these results will provide the reader with "fuel for thought" when weighing the various theories described in the literature review.

- Chapter 3 provides a literature survey. The major topics covered include fracture mechanics with a focus on fracture under compressive loading conditions and the size effect problem. The literature review will demonstrate that fracture propagation under compressive loads and size effect is still poorly understood and that many questions remain unanswered.

- Chapter 4 describes the implementation of a finite-width fracture model in two numerical computer programs developed specifically for this research topic. These models have the potential to correctly model the initiation and propagation of all fracture types observed in the compressional loading of a brittle material. In this chapter the models are calibrated to fracture propagation data, from primary tensile fractures, obtained from the uniaxial compressive testing of granite blocks.

- Chapter 5 concludes with a summary of the major contributions and results of this research. Suggestions are also made for future studies in fracture propagation.

# Chapter 2

# Experimental Work

This chapter provides a brief description of the general characteristics and behavior of rock. This material is intended to introduce the reader to a few important phenomena that occur in the laboratory testing of granite samples. The laboratory testing is described in detail in the second part of this chapter. It is hoped that knowing the results of the experimental work it will be more meaningful for the reader to follow through the extensive literature review, provided in the next chapter, and readily see the areas where gaps exist in the current state of knowledge.

## 2.1 General Characteristics and Behavior of Rock

A large body of theoretical and experimental work exists in the field of fracturing of polycrystalline materials especially in the area of failure of brittle rocks (for example see Jaeger and Cook [47]). The mechanism of brittle fracture of rock under compressive loads has been detailed by Bieniawski [6] and is summarized here. When a sample of rock is subjected to monotonically increasing compressive loads, several crack related phenomenon can be identified from the stress-strain response curves (Figure 2.1).

At the start of loading the initial response of the rock is nonlinear (region A-B in Figure 2.1) and is considered to be a result of the closing of preexisting cracks. This is followed by a linear response in all three curves (region B-C). Crack initiation occurs at
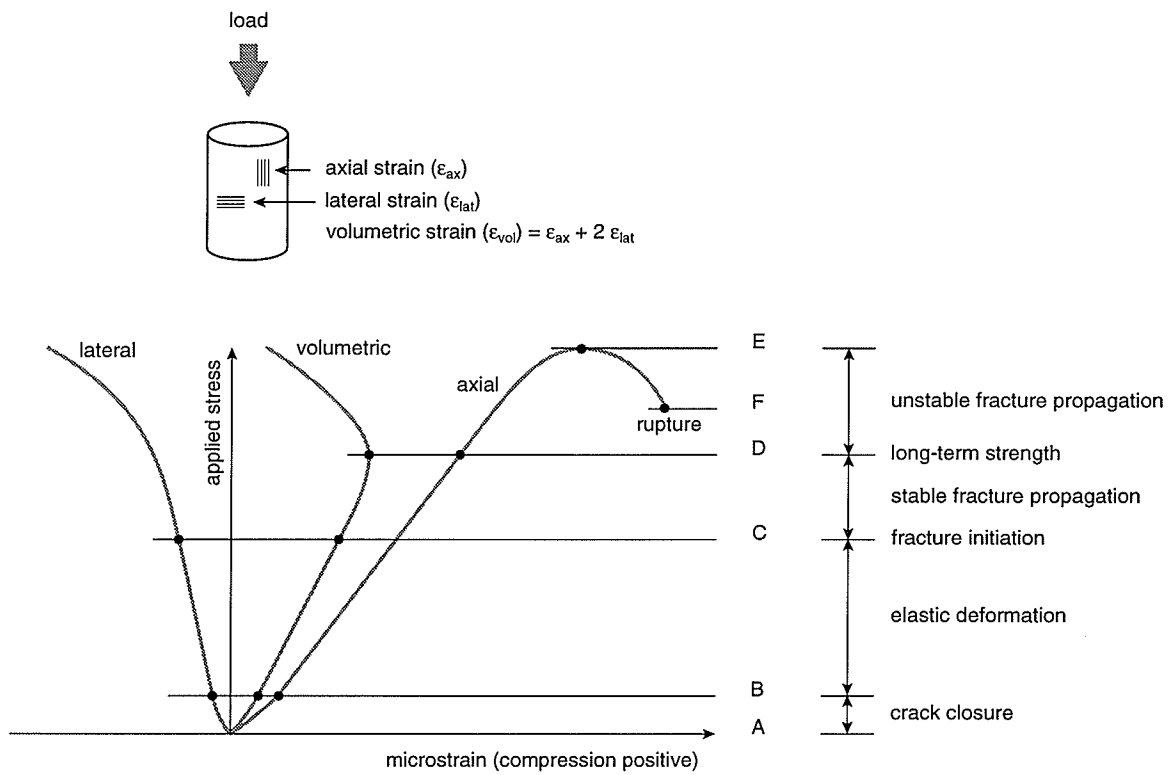
Figure 2.1: Mechanism of brittle fracture of rock in multiaxial compression (from Bieni-awski [6]).

the stress level where the lateral strain departs from the linear trend (stress level C). The axial strain remains linear until the long-term strength stress level is reached (stress level D). This level is also marked by a reversal in the trend of the volumetric strain curve (onset of dilation). According to Brace et al. [13] the dilation is caused by the opening of axial cracks. Up to this point the rock behaves in an elastic manner and crack propagation is stable (crack growth can be controlled by the load). An applied stress greater than level D causes irreversible damage in the rock and marks the level of stress at which unstable crack propagation occurs. Fracture propagation is termed *unstable* when a unique relation between crack length and applied load ceases to exist. Below stress level D (stable crack growth) crack growth can be stopped by stopping load increases. Above level D (unstable crack growth) fractures propagate uncontrollably even though the applied load may be held constant. Maintaining a stress level above the long-term strength will eventually lead to the ultimate failure of the sample. In a uniaxial test the peak load sustained by the sample occurs at level E and corresponds to the uniaxial compressive strength of the sample. The post-peak behavior of the rock (level F) is more difficult to capture. A stiff testing machine with a servo-controlled loading mechanism with a feedback loop is required.

The long-term strength (level D in Figure 2.1) is sometimes referred to as the crack damage stress [17]. This threshold is marked by a reversal in the volumetric strain curve and a departure from linearity of the axial curve. Martin [69] demonstrated that the crack damage threshold is a function of the amount of damage present in the sample. This is largely load path dependent. By performing a series of cyclic loading tests on granite samples Martin was able to incrementally increase the damage sustained in a sample. Under uniaxial compressive loading conditions he found that the crack initiation point remained relatively constant. However, the crack damage level dropped and reached a plateau at the same level as crack initiation. The Cold Spring granite used in this thesis can be classified as undamaged. The samples do not contain a pervasive system of microcracks as is found in damaged samples.

The features described above are examples of the average response of a rock mass to compressional loading. The departure of the lateral curve from a linear trend is attributed to the dilation of axial cracks. For the most part, axial cracks do not influence the axial stiffness of the rock hence the linear axial stress-strain curve.

Interpretation of the strength parameters from the stress-strain diagram is still open to argument. Lajtai and Dzik [62] have suggested that for a heterogeneous material there may be many crack initiation and crack damage thresholds reflecting the variable properties of the different materials comprising the sample. Pinpointing macroscopic damage thresholds thus becomes a problem. However, for the work of this thesis, which assumes linear, isotropic, and homogeneous behavior for the modeling of Cold Spring granite it suffices that the interpretation of material properties from laboratory testing is done in a consistent manner. That is if the measured compressive strength of Cold Spring granite was 228 MPa and it is later found that it is actually 100 MPa the results of modeling can be scaled appropriately because of the linearity assumption.

Even though fracture and failure of a brittle material in an overall compressive stress field is still poorly understood it is generally agreed that under compressive loads the mechanism of failure in a brittle rock is due to the growth and coalescence of microcracks [54, 40, 25]. These microcracks follow the maximum principal stress ($\sigma_1$) trajectory [7, 86, 21, 75, 57, 85, 54, 25]. When a brittle elastic material containing a circular void is subjected to a uniaxial compressive load the $\sigma_1$ trajectories and the resulting fractures flow around the void (Figure 2.2). These fractures can be classified into three groups: primary, remote, and slabbing (sidewall) fractures (Figure 2.2).

Primary fractures form at the tensile stress concentrations and propagate in a straight line path toward the loading direction. A remote fracture commonly initiates in each quadrant around the circular void in a region removed from the void. These fractures are initiated by a critical combination of tensile and compressive stresses. The slabbing fractures form at the compressive stress concentrations of the circular void. All three fracture types are
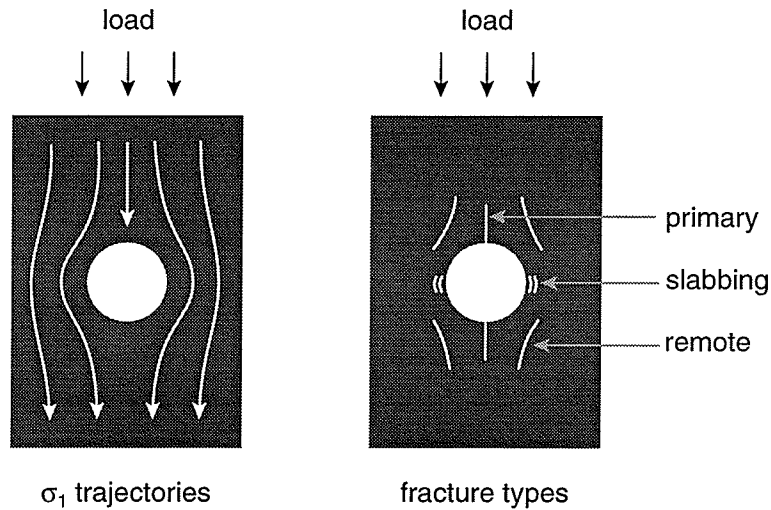
Figure 2.2: Three fracture types associated with circular voids loaded in compression.

genetically similar; all are tensile fractures and all propagate parallel to the $\sigma_1$ stress trajectory as is illustrated in Figure 2.2. Figures 2.3–2.5 are photos of the three fracture types in granite. This thesis focuses on modeling the behavior of the primary fractures emanating from circular voids.

## 2.2 Laboratory Testing

### 2.2.1 Experimental Procedure

Granite blocks were obtained from Cold Spring Quarry located within the Lac du Bonnet granite batholith located in southeastern Manitoba (Figure 2.6). The geological setting has been described in detail by Brown et al. [15] and Everitt et al. [28]. In summary, the batholith is considered to be representative of many granitic intrusions of the Precambrian Canadian Shield and is dated as Late Kenoran age (2680 ± 81 Ma). The batholith consists of relatively undifferentiated pink and grey massive porphyritic granite-granodiorite. The pink color is due to alteration by groundwater flow. The Cold Spring pink granite, which was used for the laboratory testing, is medium- to coarse-grained (0.5–20 mm) has a relatively uniform texture and composition and consists of 28% quartz, 31% microcline, 36% oligoclase, and
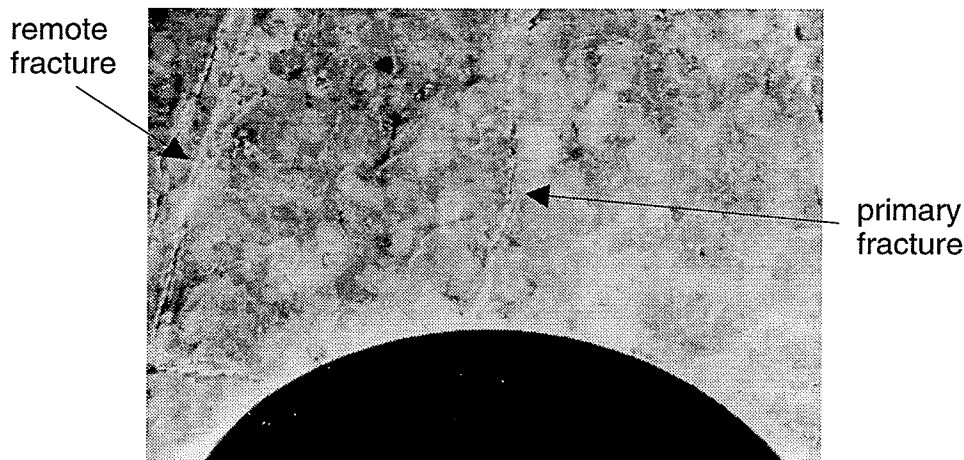
Figure 2.3: Photograph of primary and remote fractures around a circular void in Cold Spring granite loaded in uniaxial compression.

5% biotite [59]. The mechanical properties of the granite are: Poisson's ratio, $\nu = 0.25$; Young's modulus, $E = 71000$ MPa; uniaxial tensile strength, $T_0 = -13.5$ MPa; uniaxial compressive strength, $C_0 = 228$ MPa; mode I fracture toughness, $K_{Ic} = 2.57$ MPa$\sqrt{m}$ [69].

The samples were cut and polished into blocks of various sizes. Each block had a circular hole drilled through the narrowest dimension with hole size ranging from $R = 2.5$ mm to $R = 50$ mm. The block dimensions are summarized in Table 2.1. The last column in Table 2.1 assigns an easily remembered name to each data set; the data set name corresponding to the approximate hole radius of the block being tested.

Samples were loaded in uniaxial compression at a constant loading rate. Loading was paused periodically to visually examine fracture formation. A test took anywhere from 1–4 hours to complete. All samples were tested with steel platens on the top and bottom of the sample with the following exceptions. J4S1 and J4S4 had an additional granite platen placed between the top of the sample and the top steel platen. J15S1 had a teflon insert placed between the top of the sample and the top steel platen. J15S3 had a granite platen glued to the top of the sample and a steel platen placed on top of this. Data sets R20A and R20B are from the top and bottom primary fractures, respectively, of sample J149.
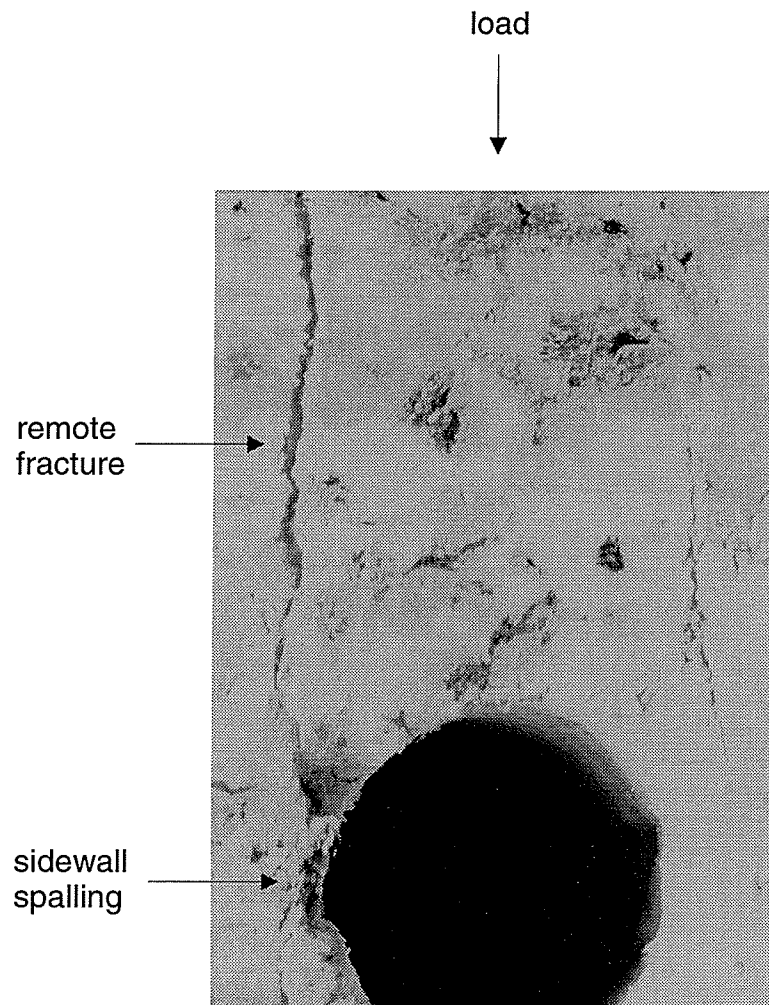
Figure 2.4: Photograph of spalling type fracture in the compressive stress concentration and remote fractures around a circular void in Cold Spring granite.
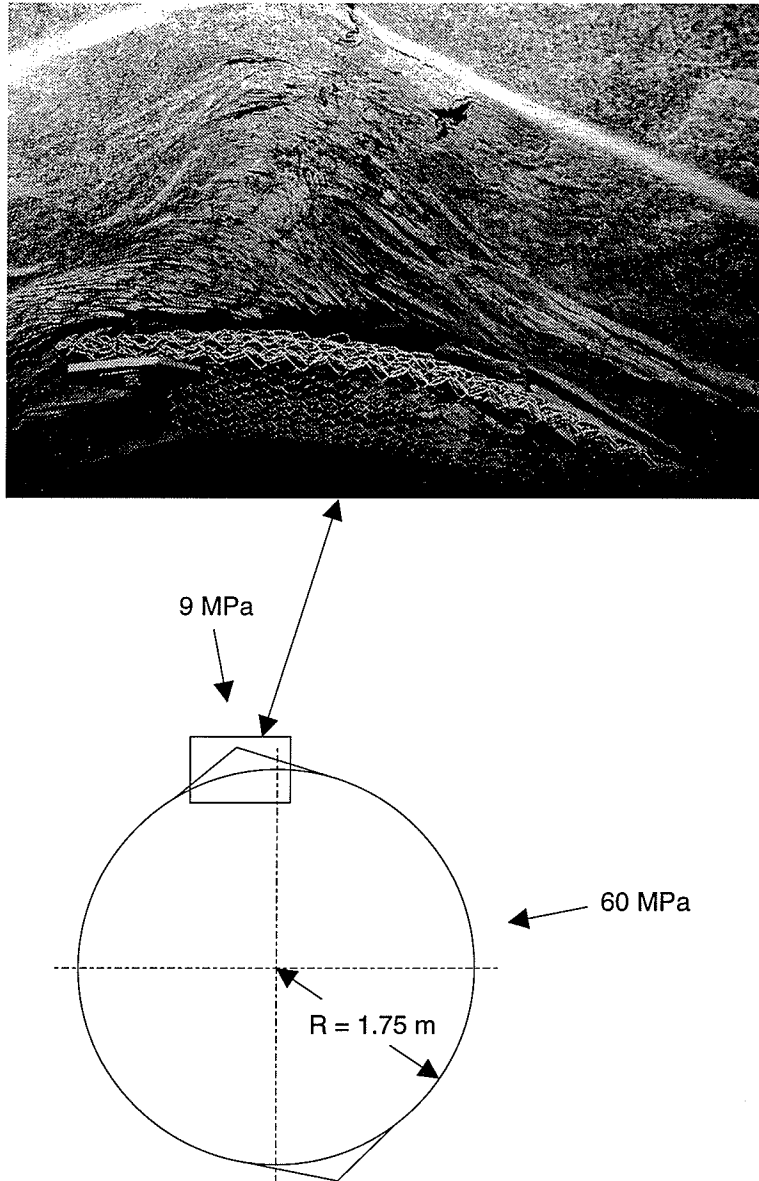
Figure 2.5: Photograph of spalling type fracture in the compressive stress concentration of AECL's URL Mine-by tunnel [76] excavated in Lac du Bonnet granite.
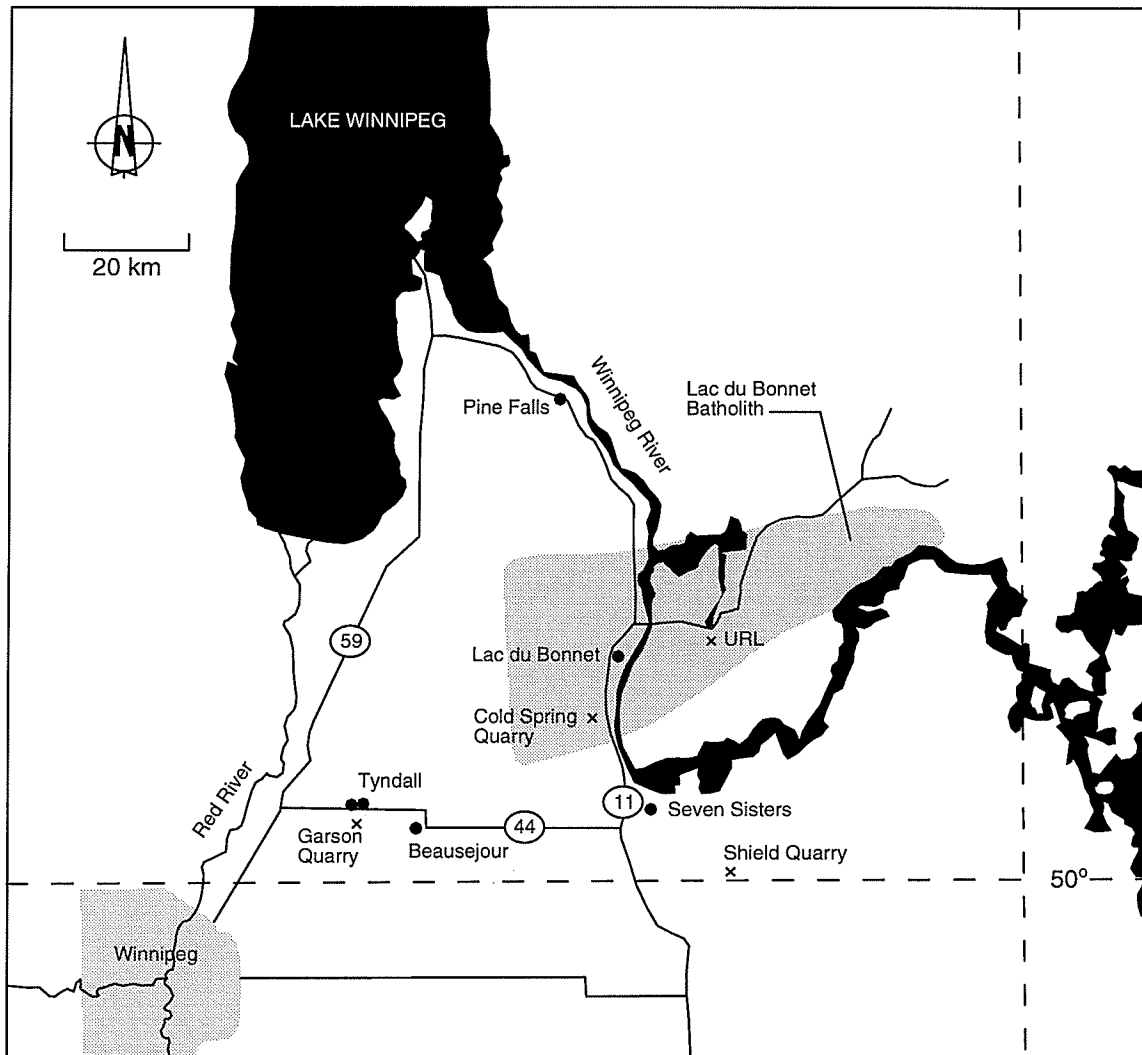
Figure 2.6: Location map of the Lac du Bonnet batholith and Cold Spring Quarry.

| Sample Name | Nominal Block Dimensions $H \times W \times D$ (mm) | Hole Radius $R$ (mm) | Data Set Name |
|---|---|---|---|
| J5MM | $376 \times 108 \times 70$ | 2.5 | R2.5 |
| J10MM | $380 \times 108 \times 61$ | 5.0 | R5 |
| J4S1 | $152 \times 110 \times 102$ | 10.0 | R10 |
| J4S2 | $152 \times 110 \times 102$ | 10.0 | |
| J4S3 | $152 \times 110 \times 102$ | 10.0 | |
| J4S4 | $152 \times 110 \times 102$ | 10.0 | |
| J149 | $348 \times 204 \times 63$ | 19.1 | R20A, R20B |
| PGHOLE1 | $356 \times 356 \times 108$ | 30.4 | R30A, R30B |
| J15S1 | $587 \times 382 \times 105$ | 38.1 | R40 |
| J15S2 | $587 \times 382 \times 105$ | 38.1 | |
| J15S3 | $587 \times 382 \times 105$ | 38.1 | |
| J20S1 | $740 \times 508 \times 105$ | 50.8 | R50A |
| J20S2 | $740 \times 508 \times 105$ | 50.8 | R50B |

Table 2.1: Summary of laboratory sample dimensions.

Data sets R30A and R30B are from the top and bottom primary fractures, respectively, of sample PGHOLE1.

Each block was instrumented with electrical resistance strain gauges. The gauges were strategically placed to pick up fracturing events in the three potential fracture locations (primary, remote, slabbing) (Figure 2.7). Each block was loaded in uniaxial compression and the gauges were continuously monitored using a PC-based data acquisition system called *EZDAQ*[1] (Figure 2.8). A typical stress strain plot is shown in Figure 2.9. The response of the granite to loading is, for the most part, linear elastic until a fracturing event passes through or near a strain gauge. Once this occurs the stress strain curve abruptly departs from its linear trend. All three types of fracturing events can be tracked precisely using a combination of the logged data and visual inspection of the sample during loading.

### 2.2.2 Results

The initiation and propagation histories of all three fracture types (primary, remote, slabbing) were recorded for the samples tested. From Figure 2.10 it can be seen that a pronounced size effect exists for the initiation of all the fracture types. The general trend is as the hole size increases, crack initiation stress decreases. A similar size effect can be seen for the propagation histories of the primary fractures (Figure 2.11).

For the smallest hole (J5MM, $R = 2.5$ mm) primary cracks did not form, only remote fractures were found. For the next larger size (J10MM, $R = 5$ mm) primaries initiated and propagated a very short distance. Remote fractures dominated again. In the remaining samples all three fracture types were detected. The $R = 10$ mm data was compiled from samples J4S1–4. Data for both primary fractures (top and bottom) were tracked from sample PGHOLE1 (shown as R30A and R30B, respectively, in Figure 2.11). Primary fractures were not tracked directly in samples J15S2 and J15S3 and are not included in this data set.

---

[1]Developed by E. Z. Lajtai.
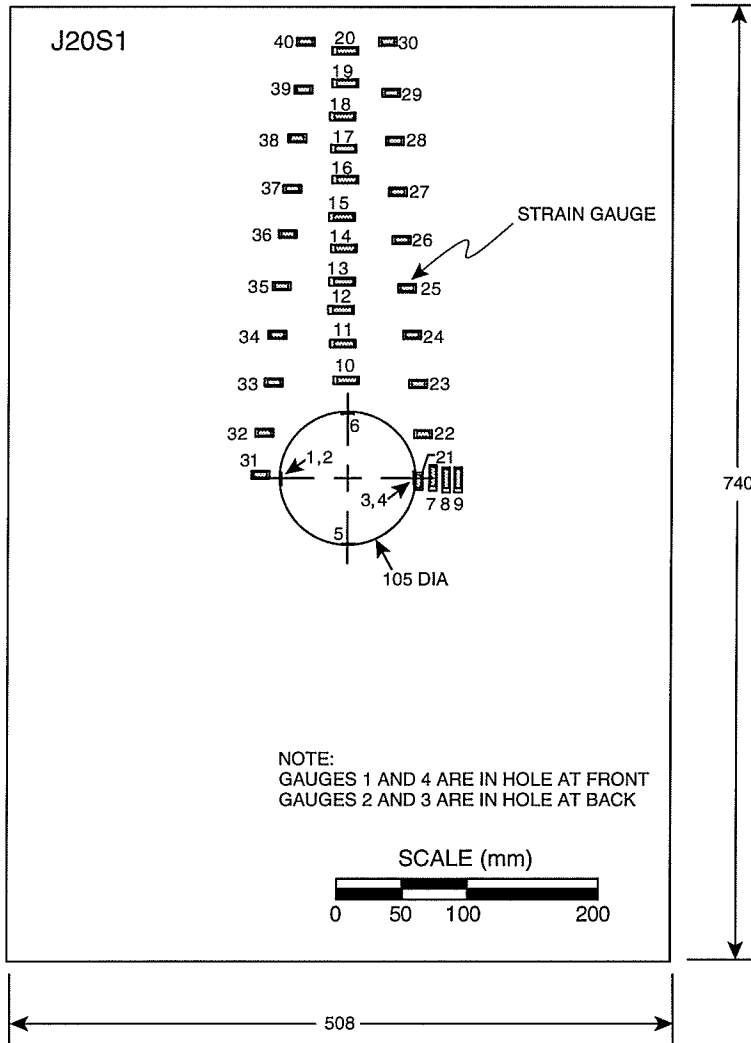
Figure 2.7: Strain gauge placement on block J20S1.

Figure 2.8: Compression testing of a granite block.

When remote fractures form, the strain energy from the loading platens is essentially diverted from driving the primary fractures to driving the remote fractures. Because of this "shielding" effect created by the remote fractures a primary fracture tends to "stall" once a remote fracture initiates. As a result primary fractures require drastically increased loads to continue propagating. This phenomenon can be seen in the primary fracture propagation history of the $R = 20$ mm sample in Figure 2.11 where remote fractures initiated at $\approx 67$ MPa. A dramatic increase in loading is required at this point to further propagate the primary fracture. This hardening trend is not seen in the $R = 10$ mm data set where remotes initiated at 86–108 MPa. The only other data set that shows this abrupt hardening trend is the R50B data. In this sample, remote fractures initiated at 58 MPa. However, the R50A sample also had remote fracture initiation occurring at an almost identical value (59 MPa) without the dramatic hardening trend shown by the R50B primary fracture. This may indicate that in the R50B sample remote fractures actually initiated at a lower value than 58 MPa and were not detected.
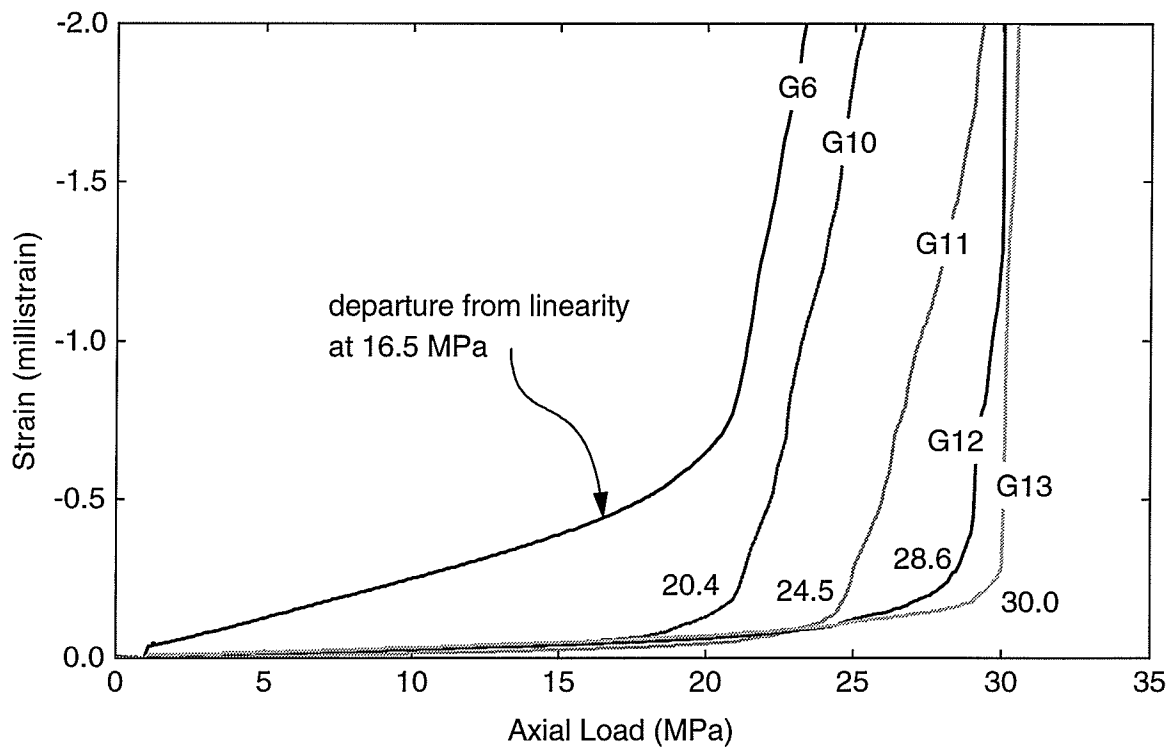
Figure 2.9: Strain gauge response from uniaxial loading of sample J20S1. G6,10–13 are strain gauges shown on Figure 2.7.
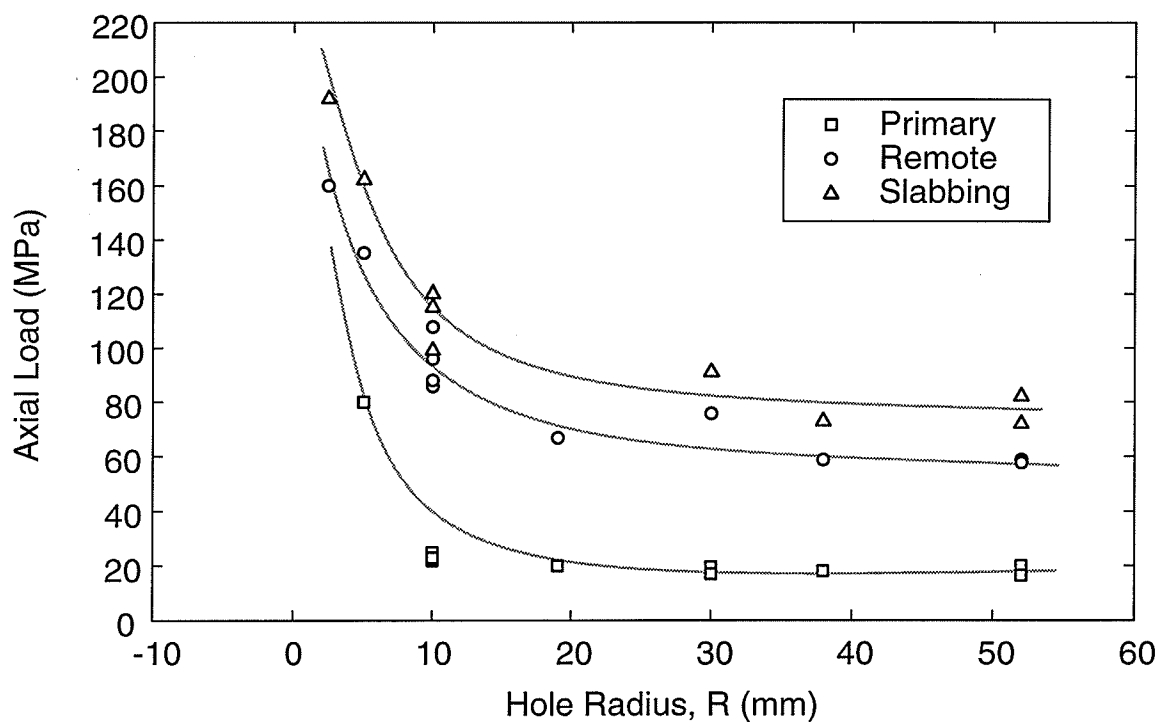
Figure 2.10: Crack initiation stress for primary, remote, and slabbing fractures versus hole radius. The solid grey lines indicate the general trend of the data.
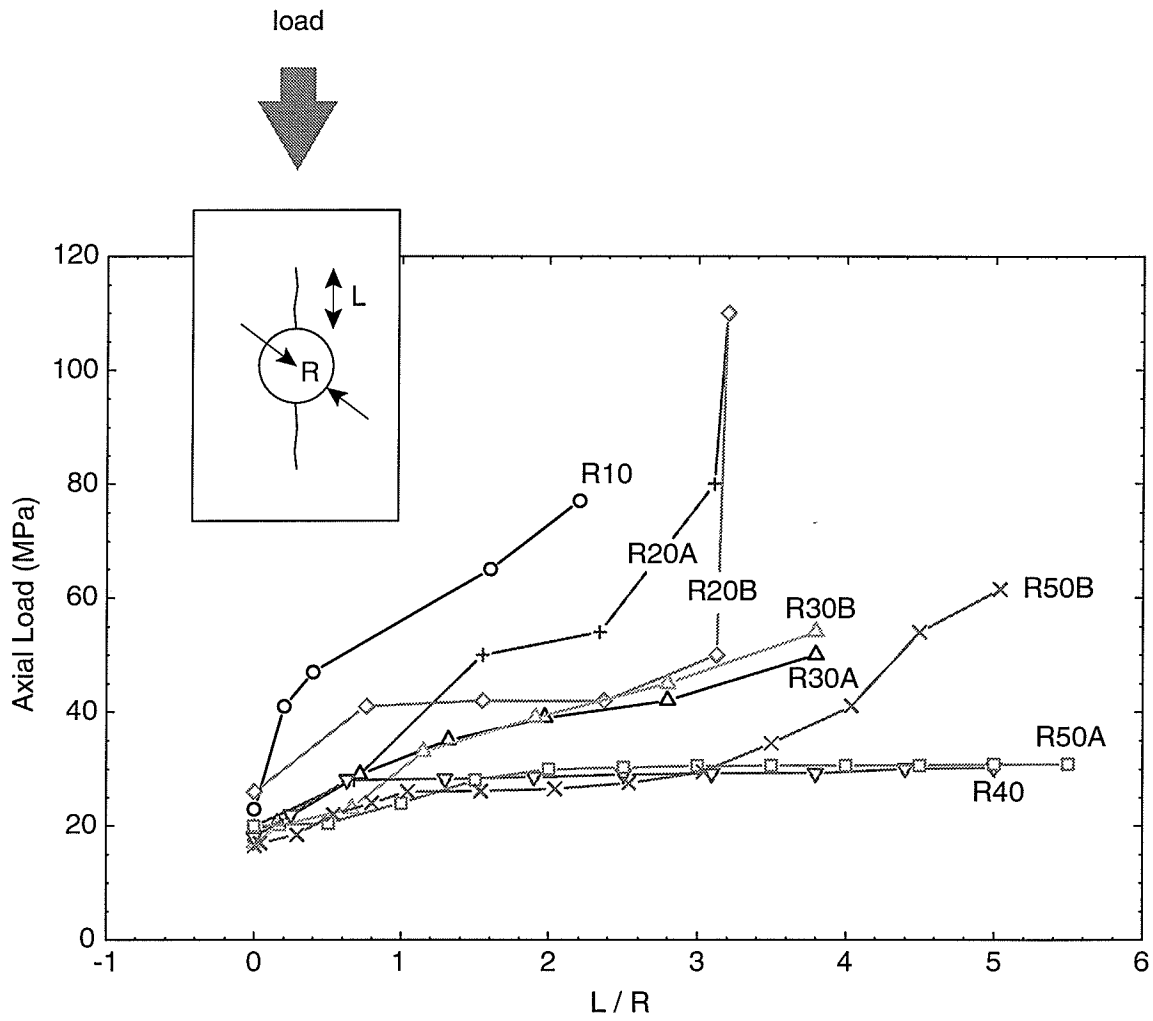
Figure 2.11: Crack propagation stress for primary fractures versus normalized crack length.

Figure 2.11 illustrates that primary fracture propagation is very stable for small hole sizes as indicated by the very high loads required to propagate the primaries from the $R = 10$ mm hole. In contrast, the largest holes tested ($R = 40$ and $50$ mm) show an almost unstable trend. The primary fracture propagated through the sample at an almost constant load of approximately 32 MPa. The two 50 mm samples show two different trends for the propagating primary fracture. The primary in sample J20S1 (50A in Figure 2.11) almost "shoots" through the sample at a load of approximately 32 MPa while the primary in sample J20S2 (50B in Figure 2.11) requires increasingly higher loads to propagate the fracture. The fracture in J20S1 was in fact stable since slight increases in load were required to propagate the fracture. The reason for the much greater stability of the primary in J20S2 compared to J20S1 is unknown at present. Both samples had identical boundary conditions. Sample J15S1 (R40) shows the same level of instability as J20S1 (R50A). This could be attributed to reduced friction at the platens from the use of teflon at the rock platen interface.

It is worthwhile, at this point, to summarize the observations obtained from the set of crack propagation tests performed on two additional samples (J15S2, J15S3) that had the same dimensions as J15S1 (the R40 sample). As was stated previously, J15S1 had a teflon insert placed between the steel platen and the sample. This sample was instrumented to track the propagation of a primary crack. The second case (J15S2) was tested with a steel platen only and the third case (J15S3) had a granite platen glued directly to the sample with a steel platen placed on top. These last two samples were instrumented to follow the propagation of a remote fracture only, however, the primary fractures could still be tracked visually and by the response of the remote gauges as the primary fracture propagated past. At a steel-granite interface a substantial amount of friction usually develops resulting in greater stability of the sample. This was not the case here. In all three tests the primary fractures propagated through the samples at similar stress levels in almost unstable fashion. It could be argued then that some slippage did occur at the platen boundaries. As a result of these findings one of the boundary conditions assumed in the numerical modeling is

allowing the platen boundaries to slip.

At any rate a pronounced size effect is noted with the propagation of the primary fractures. A more or less continuous trend from very stable crack propagation at the small holes to almost unstable crack propagation at the large holes is seen.

The general behavior of rocks under compressive loads has been summarized in this chapter. The important points are restated here. All cracks propagate parallel to the $\sigma_1$ stress trajectory in a rock subjected to a compressive load. A pronounced size effect is seen in the compression testing of rocks in both the crack initiation and crack propagation results.

The next chapter provides an extensive literature review of fracture under compressive loads in an attempt to explain the mechanism behind propagation of axial cracks and the associated size effect.

# Chapter 3

# Literature Survey

## 3.1  Introduction

This chapter provides a review of the literature pertaining to the process of fracture under compressive loading conditions in a brittle material. This work extends Carter's work [18] on crack initiation under compressive stress states to include fracture propagation. It will be shown that several existing models are able to represent the size effect phenomenon demonstrated by propagating primary fractures.

## 3.2  Physical Model Testing in the Literature

Published results on physical model testing of materials with circular voids in compression is sparse. Usually a small number of small scale samples are tested resulting in very limited data sets. These are usually inadequate to reveal a size effect. The model testing results in the literature, however, are consistent with the small scale tests (R10 data set) performed for this thesis. The crack propagation data collected for this thesis is probably the most extensive and complete set of information available for crack propagation and size effect in rocks. This abundance of reliable data provides ample evidence for proving out the models presented in the open literature that relied primarily on small scale testing.

Hoek [36, 37] tested a fine-grained chert-dyke material. The geometry of the sample was the same as the laboratory samples described in Chapter 2 (circular hole in a block).

The dimensions of his sample were $127 \times 127 \times 3.2$ mm with a hole radius $R = 9.5$ mm. The sample was loaded in biaxial compression with a monotonically increasing proportional load. Fractures were tracked photoelastically using high speed photography. Hoek found that the primary fractures were first to initiate. They propagated in a stable manner for a short distance, and then "stalled" at a normalized crack length of $L/R = 0.5$–$0.6$. At increased loads remote fractures formed and led to the eventual collapse of the sample. Because of the biaxial loading conditions and differing rock type Hoek's results cannot be directly compared with the thesis samples. Also, because results were only published for a single test the possibility of investigating size effect is eliminated.

Lajtai et al. [55, 63] and Nestova and Lajtai [71] tested Plaster-of-Paris blocks containing circular cavities under various compressive loading conditions. They related the observed size effect in the crack initiation stress to the stress gradient around the circular opening.

Gay [30, 31] investigated fracture growth around circular and rectangular holes in quartzite and sandstone under uniaxial and biaxial loading conditions. However, these were model studies for large scale excavations and did not focus on primary fracture propagation.

A problem with similar geometry to the one being investigated is that of a well-bore in production wells in the oil industry. Even though the geometry is similar to the problem being investigated in this thesis the loading conditions differ. To create a hydraulically induced fracture in a well-bore, the well-bore is internally pressurized and primary fractures are created at weak points around the boundary. Fracture mechanics adequately models this scenario since the fractures are mode I and propagate strictly from tensile loads.

Sammis and Ashby [80] tested small glass and PMMA samples ($170 \times 50$–$100 \times 10$ mm) with a circular hole ($R = 2.5, 5, 10$ mm) drilled through the center. The hole was notched with a starter crack. They found that crack propagation was stable in uniaxial compression. Once again a small number of similar samples of limited size were tested. A small size effect was noted but as usual a greater number of large scale samples is required.

Carter [17, 20, 18] tested potash, limestone, and granite models with circular voids. His

work focused on modeling crack initiation and the formation of remote fractures.

In summary, the testing documented in the literature was limited to small samples with a very limited size range. In the literature we see only crack hardening behavior from the physical testing because of the small scale of the samples tested. The data set obtained from the suite of tests done for this thesis is unique. The propagation trends show a continuous behavior from stable to almost unstable propagation modes as the hole radius increases.

## 3.3 Fracture and Failure Theories

Failure generally refers to a global process in which a material suffers permanent damage affecting a structure's ability to sustain a load. Although fracture and failure are sometimes used synonymously the two processes are not interchangeable. Failure is generally viewed from a macroscopic perspective while fracture, occurring at a smaller scale, is usually described from a mechanistic viewpoint. The process of fracture growth and coalescence in rock materials commonly results in failure.

Keeping this distinction in mind, failure theories can be classified into two groups: phenomenological and mechanistic theories. Phenomenological theories are based on the global failure process and commonly provide a functional relation describing a material's ability to support a load. Mechanistic theories have a theoretical foundation and consider the actual mechanism of failure (growth and coalescence of microcracks for example). Both viewpoints are examined more closely in the following sections.

### 3.3.1 Phenomenological Theories

Numerous phenomenological theories exist. The most familiar of these are: maximum stress, Coulomb, and Hoek-Brown theories. The maximum stress theory assumes a material fails when the maximum tensile stress reaches the tensile strength of the material. No accounting is made for the affect of the maximum compressive stress. The Coulomb and Hoek-Brown theories predict linear and parabolic relations, respectively, between the maximum principal

stress ($\sigma_1$) at failure and the confining pressure ($\sigma_3$).

A relatively new empirical strength relation is given by the Rocker function [19],

$$\sigma_{1f} = C_0 \left(1 - \frac{\sigma_3}{T_0}\right)^R \tag{3.1}$$

where $\sigma_{1f}$ = maximum principal stress at failure

$\sigma_3$ = minimum principal stress at failure

$R$ = curve fitting exponent ($0 <= R <= 1$)

$T_0$ = uniaxial tensile strength

$C_0$ = uniaxial compressive strength

This is a specific case of Johnston's [48] strength relation. This function anchors the strength curve at the unconfined compressive strength ($C_0$) and the unconfined tensile strength ($T_0$). This is similar to the Hoek-Brown strength formulation, however, the Rocker function provides a better fit to laboratory data when confinement is low or the test is in tension (i.e., $\sigma_3$ is small or negative).

A material's ability to sustain a load is commonly expressed through the use of a safety factor (SF). The traditional safety factor in rock mechanics is usually given as a ratio between available material strength and the actual state of stress at that point (i.e., SF = strength/stress). A safety factor greater than one indicates "safe" conditions and a safety factor less than or equal to one, "unsafe" conditions. A problem with the traditional SF approach is that it is limited to the $\sigma_3 > T_0$ space. A tension cutoff is usually used when a material point falls outside this space and SF is arbitrarily assigned a constant value less than one. This tension cutoff has the unwanted side effect of creating discontinuous SF contours.

An alternate approach to safety factor as a failure criterion has been proposed by Lajtai et al. [61]. This safety factor, known as *Unconfined Strength Ratio* or USR, is similar in principal to the traditional safety factor but is not limited to the $\sigma_3 > T_0$ strength space. USR is defined for any point in the $\sigma_1$–$\sigma_3$ space of the stability diagram and varies in
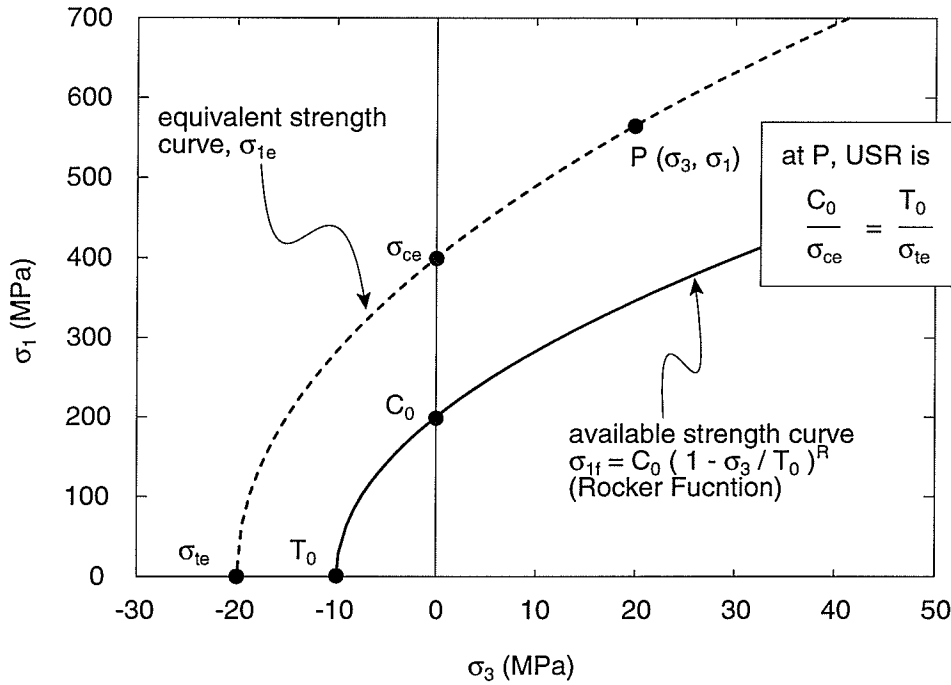
Figure 3.1: Rocker function and USR.

a smooth continuous manner unlike the traditional SF which becomes discontinuous at $\sigma_3 = T_0$. USR may be based on the Rocker function and is defined as the ratio of the unconfined strength $(C_0)$ to the equivalent unconfined strength $(\sigma_{ce})$, (USR $= C_0/\sigma_{ce}$). The tensile strength ratio can also be used to calculate USR (USR $= T_0/\sigma_{te}$). USR is calculated by first determining an equivalent strength curve $(\sigma_{1e})$ that includes the stress coordinates $P(\sigma_1, \sigma_3)$ of the point in question (Figure 3.1). The equivalent strength curve has the additional requirement that the ratios of tensile strength to compressive strength are kept the same for both the available strength curve $(\sigma_{1f})$ and the equivalent strength curve $(\sigma_{1e})$. The equivalent strength curve is calculated by varying $\sigma_{ce}$ and $\sigma_{te}$ in the Rocker function, while preserving the $\sigma_{ce}/\sigma_{te} = C_0/T_0$ ratio, until the curve passes through $P(\sigma_1, \sigma_3)$. The USR definition of safety factor is consistent with the conventional safety factor in that failure occurs when USR $\leq 1$.

| Mode I | Mode II | Mode III |
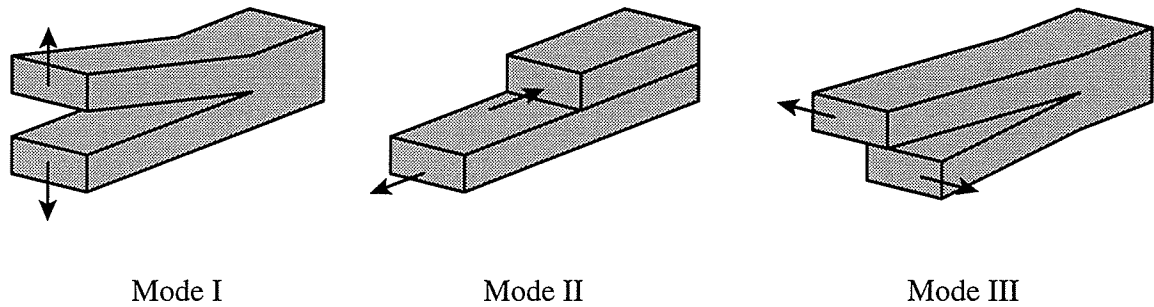
Figure 3.2: The three basic modes of crack loading and corresponding deformation.

## 3.3.2 Mechanistic Theories

Mechanistic theories are based on the actual mechanism of failure and form the basis of many fracture mechanics, numerical, and analytical models. Because fracture behavior is the focus of this thesis a brief history of fracture mechanics is provided. This is followed by a more detailed exposition on fracture mechanics as it applies to rock (fracture under compressive loading conditions).

**A Brief History of Fracture Mechanics**

The stress field near a fracture tip can be divided into three basic types, each associated with a local mode of deformation (Figure 3.2). Mode I represents an opening mode. Mode II a shearing mode and mode III an out of plane tearing mode. The short history provided below is from a mode I perspective.

In an attempt to explain the apparent differences in strength of varying sizes of glass rods Griffith [33] developed an energy balance approach to predict crack initiation stress. Using the theorem of minimum energy and Inglis' [42] formulation for stresses around an elliptical crack in a plate (Figure 3.3), Griffith derived the following formula which relates fracture size to fracture strength.

$$\sigma\sqrt{\pi c} = \sqrt{2E\gamma_s} \tag{3.2}$$

$$\text{where} \quad c = \quad \text{crack half length}$$
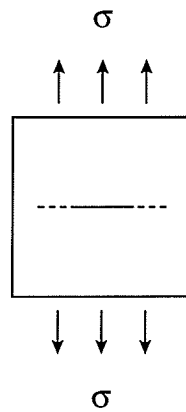
Figure 3.3: A "zero-width" elliptical crack in an infinite plate subjected to uniform tension at infinity. The dashed lines indicate crack propagation direction.

$$\sigma \;=\; \text{applied stress}$$

$$E \;=\; \text{Young's modulus}$$

$$\gamma_s \;=\; \text{specific surface energy}$$

To simplify the mathematics, Griffith assumed the crack to have negligible width. In the configuration shown in Figure 3.3 the crack will extend in its own plane. The crack will grow when the applied stress multiplied by $\sqrt{\pi c}$ exceeds the right hand side of equation 3.2. Griffith noted that this threshold value is constant for a given material.

Westergaard [89] developed an analytical solution for stresses around a crack tip for a crack that is centrally located in an infinite biaxially loaded plate (equation 3.3 and Figure 3.4). Using Westergaard's approach Irwin [46] noted that the stresses near the crack tip are only dependent on the crack length ($c$) and the applied stress ($\sigma$). He called the term $\sigma\sqrt{c}$ stress intensity factor and denoted it by $k_I$. The $\pi$ was later included in $\sigma\sqrt{c}$ to give us what we commonly know today as the stress intensity factor, $K_I = \sigma\sqrt{\pi c}$. The stress field in the vicinity of a crack tip is considered to be characterized by $K_I$. It can be readily seen that the left hand side of Griffith's equation (equation 3.2) is equal to Irwin's $K_I$ and the fracture criterion can now be stated as $K_I = \sqrt{2E\gamma_s}$. This material constant is
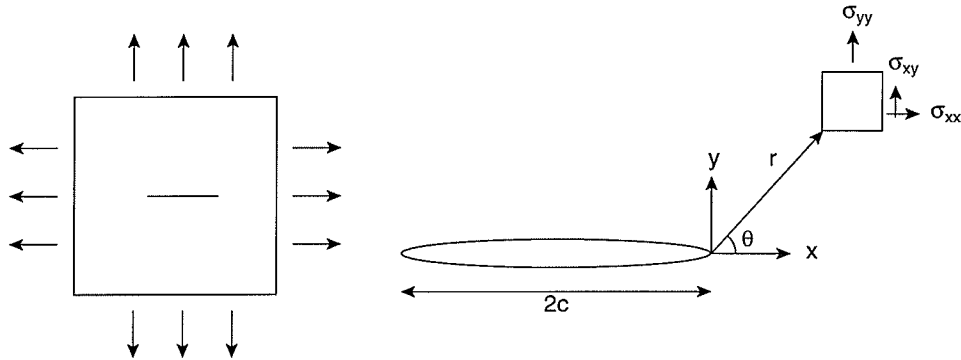
Figure 3.4: Geometry of crack tip for Westergaard solution.

known as the critical stress intensity factor ($K_{Ic}$) or fracture toughness.

$$\sigma_{xx} = \frac{\sigma\sqrt{\pi c}}{\sqrt{2\pi r}}\cos\frac{\theta}{2}\left(1 - \sin\frac{\theta}{2}\sin\frac{3\theta}{2}\right) = \frac{K_I}{\sqrt{2\pi r}}\cos\frac{\theta}{2}(\ldots) \qquad (3.3)$$

$$\sigma_{yy} = \frac{\sigma\sqrt{\pi c}}{\sqrt{2\pi r}}\cos\frac{\theta}{2}\left(1 + \sin\frac{\theta}{2}\sin\frac{3\theta}{2}\right)$$

$$\sigma_{xy} = \frac{\sigma\sqrt{\pi c}}{\sqrt{2\pi r}}\cos\frac{\theta}{2}\left(\sin\frac{\theta}{2}\sin\frac{3\theta}{2}\right)$$

$$u_x = \frac{\sigma\sqrt{\pi c}}{4\mu}\sqrt{\frac{r}{2\pi}}\left((2k-1)\cos\frac{\theta}{2} - \cos\frac{3\theta}{2}\right)$$

$$u_y = \frac{\sigma\sqrt{\pi c}}{4\mu}\sqrt{\frac{r}{2\pi}}\left((2k+1)\sin\frac{\theta}{2} - \sin\frac{3\theta}{2}\right)$$

$$\text{where} \quad \sigma\sqrt{\pi c} = K_I$$

$$k = (3-4\nu)/(1+\nu) \quad \text{for plane stress}$$

$$\mu = \text{shear modulus}$$

Griffith's hypothesis is based on the assumption that the material behaves in a brittle elastic manner which was reasonable for the glass rods he was testing. Metals, concrete, and rock display nonelastic behavior ahead of the fracture tip. In metals the zone immediately ahead of the fracture tip undergoes large plastic deformation. On the other hand, a fracture in concrete or rock is characterized by a zone of microfracturing immediately ahead of the fracture tip. This microfracturing zone is known as the "process zone" and its behavior can be roughly approximated by a plastic model. Irwin [46] and Orowan [72] independently

modified Griffith's equation to include a plastic deformation term $\gamma_p$ to give:

$$\sigma\sqrt{\pi c} = \sqrt{2E(\gamma_s + \gamma_p)} \tag{3.4}$$

$\gamma_s$ and $\gamma_p$ are sometimes combined into an apparent specific surface energy term $\gamma_{eff}$. $\gamma_p$ is used when a material displays the plastic behavior described previously. If equation 3.2 is rearranged as shown below

$$\frac{\sigma^2 \pi c}{E} = 2\gamma_s = G \tag{3.5}$$

the left hand side represents the elastic energy per unit crack surface (the energy available for crack extension). This term, $G$ (in honor of Griffith), is called the strain energy release rate or crack driving force. $G$ can also be equated to $2(\gamma_s + \gamma_p)$ if the material displays the nonlinear behavior ahead of the fracture tip.

Similar derivations of modes II and III stress intensity factors ($K_{II}$, $K_{III}$) can be made. The point to be made here is that all three stress intensity factors are used in a similar manner. That is, a stress intensity factor can be calculated (for each deformation mode) for a given fracture. If $K_I > K_{Ic}$ or $K_{II} > K_{IIc}$ or $K_{III} > K_{IIIc}$ then the crack will extend according to the specific mode of deformation. All three critical stress intensity factors are material constants. Modes I and II describe the complete deformation characteristics of a fracture in a plane. The primary fractures seen in the laboratory testing of Chapter 2 are purely mode I fractures. Shearing (mode II) or out of plane deformation (mode III) are not considered in this thesis.

It is well known that the zero-width mathematical crack model is unresponsive to normal stresses that are parallel with the crack axis [92] (Figure 3.5(a)). If the fracture is inclined to the load the fracture will undergo mode II deformation (Figure 3.5(b)) and the fracture will propagate out of the plane of the fracture and follow the maximum compressive stress trajectory ($\sigma_1$), (Figure 3.5(b)). Because of the complex geometry of this out of plane propagation, Griffith was unable to derive an energy balance relation for crack initiation for fractures subjected to compressive loads. For this reason he developed a stress-based

(a) Crack will not propagate.

(b) Crack propagates out of the plane of the original crack.
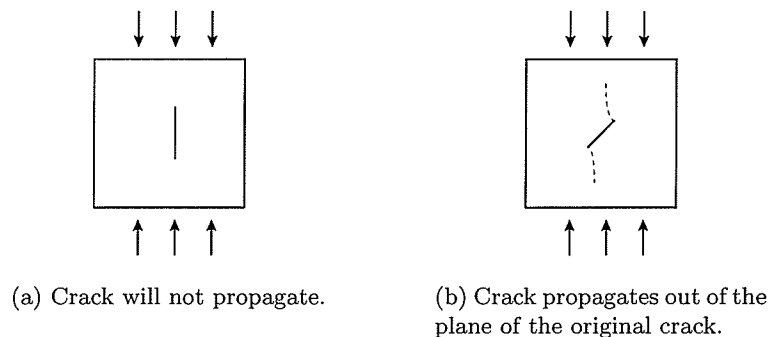
Figure 3.5: "Zero-width" elliptical crack subjected to compressive loading conditions. The dashed lines indicate crack propagation direction.

approach for fractures under compressive loads.

In Griffith's [34] stress-based criterion a crack is proposed to extend when tensile stresses induced at or near the crack tip exceed the molecular cohesive strength (tensile strength) of the material. Using Inglis's formulation, Griffith derived a functional relation for crack initiation from a single inclined zero-width crack under compressive loading conditions.

$$(\sigma_1 - \sigma_3)^2 + 8T_0(\sigma_1 + \sigma_3) = 0 \qquad (3.6)$$

$$\text{where} \quad T_0 = \text{uniaxial tensile strength}$$

In this formulation the applied stresses $\sigma_1$ and $\sigma_3$ are at infinity. When $\sigma_3$ is zero (uniaxial compression), crack initiation from this zero-width flaw is most critical when it is inclined at an angle $\theta = 30°$ to the maximum principal stress $\sigma_1$ (Figure 3.6).

The Griffith hypothesis assumes that a material contains numerous critical flaws (Griffith cracks). These flaws are spaced far enough apart so as not to influence each other allowing Equation 3.6 to be valid for a material with multiple flaws.

**Fracture Under Compressive Loads**

When placed in a compressive stress field, the inclined Griffith crack "closes" and friction develops along the crack faces. McClintock and Walsh [70] added this modification to the
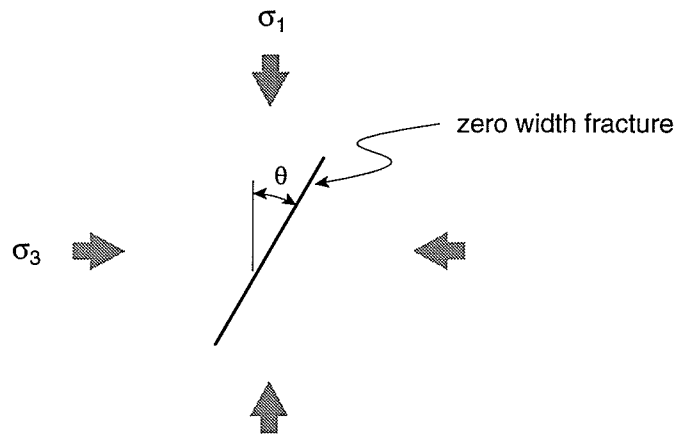
Figure 3.6: Inclined zero-width fracture for Griffith's stress-based fracture criterion.

Griffith criterion. Several authors later introduced sliding crack models that included shear stresses that developed along the crack walls over and above that due to friction [22, 41, 49, 50]. There were numerous attempts to use the Griffith and modified Griffith criteria as failure criteria or to explain fault growth (shear fracture) but with limited success [11, 8, 9, 38, 12, 44, 41, 35].

The out of plane crack propagation problem has been addressed extensively through mixed mode (modes I and II) and global energy balance fracture theories (for example see [27, 73, 83, 84]). Despite the abundance of the wing-crack initiation and propagation theories the literature points to an absence of natural Griffith cracks in real brittle materials. It is generally agreed that fracturing in the direction of the major applied load is the true failure mode of rock in compression [7, 75, 57, 85, 40, 25]. Even though the wings of the wing-cracks do propagate parallel to the $\sigma_1$ trajectory the wing cracks are short lived. After propagating a short distance the wing cracks stall even under increased loads (see Brace and Bombolakis [11], and Bombolakis [8]). In reality axial fractures continue propagating under increasing loads. Nevertheless, wing cracks are still commonly used for modeling purposes (see for example [77, 24]). The zero-width fracture restriction is easy to implement. But, at what cost? The actual fracture behavior is not reproduced.
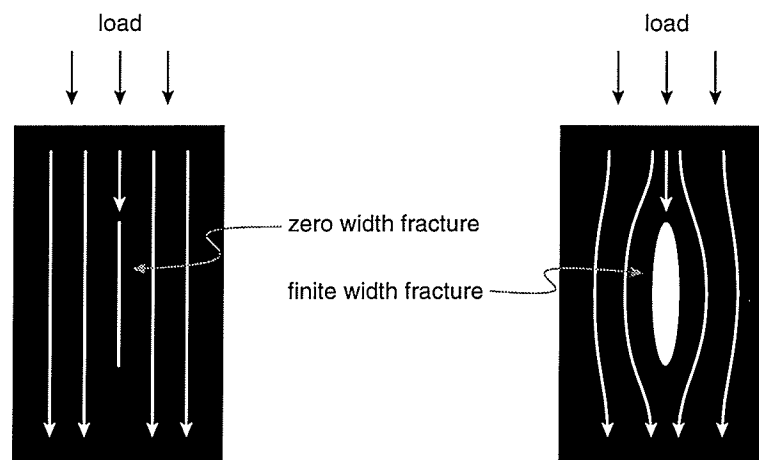
Figure 3.7: Stress field surrounding a zero-width and a finite-width axial crack.

One alternative to the inclined Griffith crack would be a finite-width crack. Unlike the zero-width axial fracture the finite-width axial fracture will perturb the stress field and create stress concentrations at the fracture tips (Figure 3.7). Under sufficient loads the axial finite-width crack will propagate in its own plane (in the axial direction).

## 3.4 Analytical Fracture Nucleation and Propagation Models

The extensive fracture initiation and fracture propagation data of this thesis marks it as an important proving ground for models in the literature. In this section several analytical fracture nucleation and propagation models are evaluated. The "goodness of fit" of a model is judged by using a "degree of freedom adjusted coefficient of determination", $Ra^2$. The $Ra^2$ statistic is an $R^2$ statistic (coefficient of determination) that is adjusted for the number of parameters in the model and the number of data observations. In many cases it is difficult to directly compare the fit produced by two different models, even when the same data set is used. One model may be constrained to work in a partial range of the data while another may operate on the entire range (i.e., how do you quantitatively compare the goodness of fit from a model valid for all primary crack lengths, $L$, to one that is valid for $L \geq R$?). For this reason the analytical models that are evaluated in this thesis are done so from a
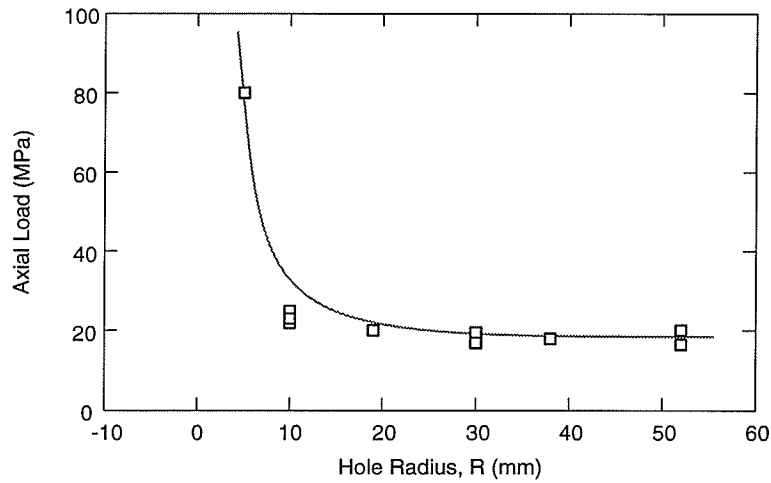
Figure 3.8: Crack initiation stress for primary fractures versus hole radius. The gray line indicates the general trend of the data.

somewhat qualitative point of view.

Primary fracture initiation is thoroughly covered by Carter [17, 18], but it is still important to address it here. Fitting analytical models to crack initiation data will produce values for material constants $(T_0, C_0, K_{Ic})$ and other fitting parameters which could be important in the subsequent modeling of crack propagation. The crack initiation and propagation data described in Chapter 2 and to be fit by the analytical models is repeated here for convenience in Figures 3.8 and 3.9.

Before looking at any fracture models in the literature the analytical solution for the stresses around the circumference of a circular hole in an infinite plate loaded in uniaxial compression should be examined. These are supplied by the Kirsch equations [53]. Under an applied uniaxial load $P$ the stresses at the crown and invert of the hole will be $(\sigma_1, \sigma_3) = (0, -P)$ as shown in Figure 3.10.

Now, looking at the size effect demonstrated by the Cold Spring granite primary crack initiation data in Figure 3.8 we see that with increasing hole size the crack initiation stress appears to decrease asymptotically reaching a constant level at large $R$. Noticing that at large scales the size effect is mostly eliminated, we would expect the asymptote of this curve
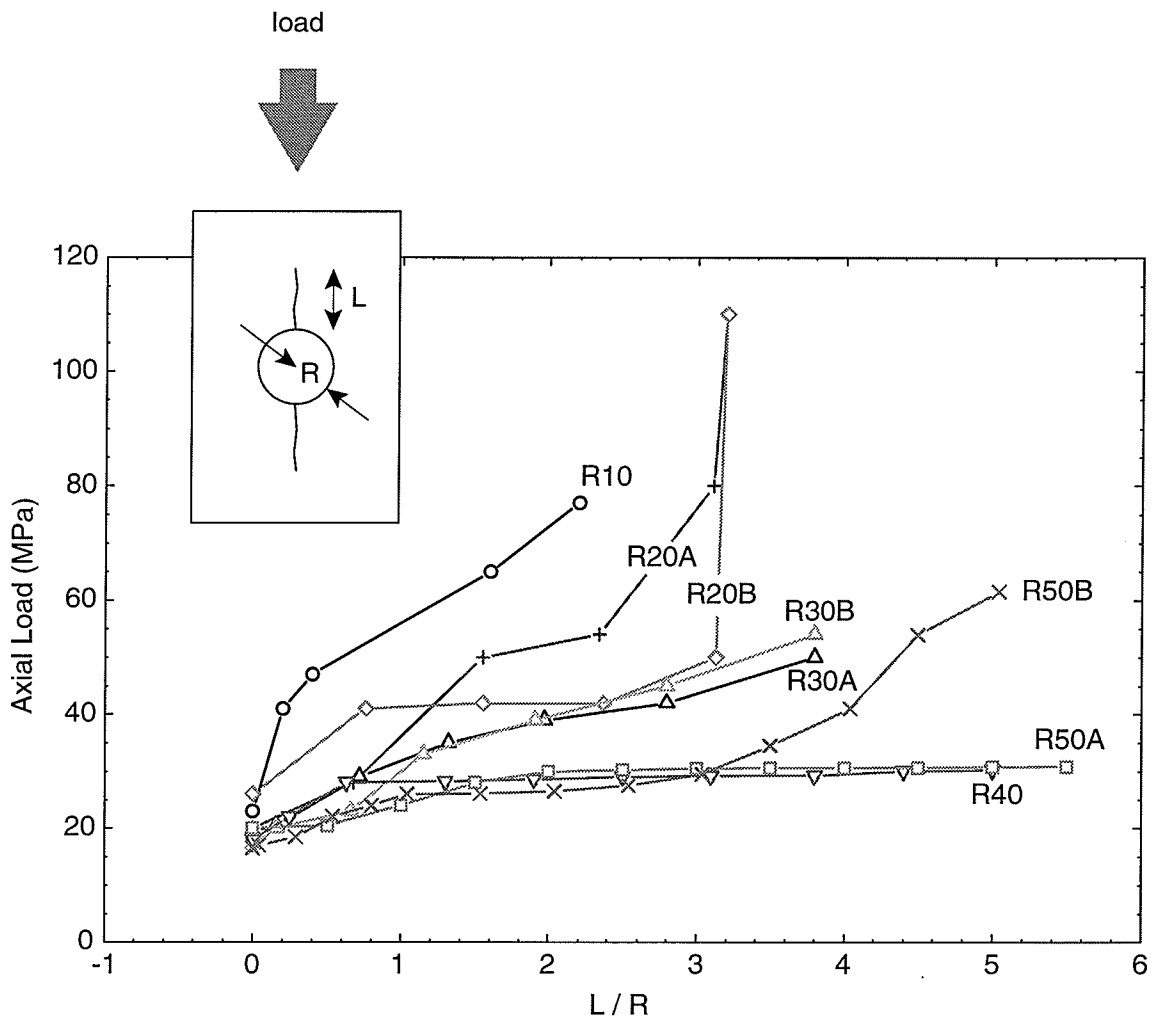
Figure 3.9: Crack propagation load for primary fractures versus normalized crack length.
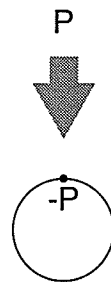


Figure 3.10: Stress at the apex of a hole in an infinite plate loaded in compression.
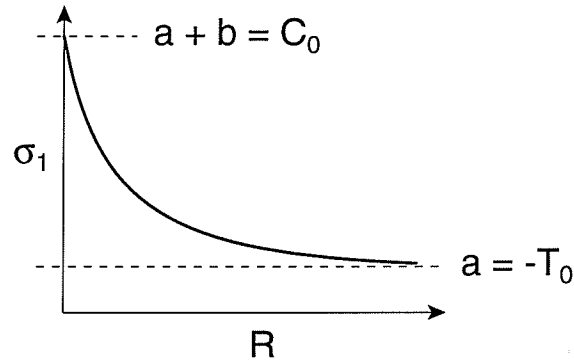
Figure 3.11: Three parameter exponential model.

to approach the analytical value predicted by the Kirsch solution. In other words, at large scales, primary crack initiation should be expected to occur at an applied load of $P = -T_0$ (the uniaxial tensile strength of the granite). At the other end of the crack initiation curve shown in Figure 3.8 it would be logical to assume that a sample with hole size $R = 0$ would break at its uniaxial compressive strength, $C_0$. To be more precise, the applied stress at which axial tensile fractures propagate across a sample block containing no artificial cavity would be close to $C_0$. Therefore we can come to the conclusion that primary crack initiation (and propagation) loads are bounded by $\sigma_1 = -T_0$ and $\sigma_1 = C_0$.

Looking at things from a strictly empirical sense, a function with desirable characteristics to fit the crack initiation data appears to be the exponential curve shown below and in Figure 3.11.

$$\sigma_1 = a + \frac{b}{e^{R/c}} \tag{3.7}$$

This curve can be set to intersect the $\sigma_1$-axis at $C_0$ and made to approach a horizontal asymptote of $\sigma_1 = -T_0$. This simple equation provides an excellent fit to the Cold Spring granite lab data as is illustrated in Figure 3.12.

Numerous models dealing with primary fracture propagation from a circular void loaded in compression have been put forth in recent years. These models can be divided into two types: fracture-mechanics- and stress-based. Fracture mechanics largely deals with

Figure 3.12: Exponential curve fit to Cold Spring granite primary crack initiation data. $Ra^2$ = degree of freedom adjusted coefficient of determination.

the fracture propagation problem with less attention paid to the crack initiation problem. Generally speaking, fracture mechanics models use the stress intensity factor (SIF) or $K_I$ approach to model fracture propagation. This type of formulation takes into account the crack geometry and boundary conditions. The models are usually derived for simple crack geometries. The critical SIF ($K_{Ic}$) is assumed to be a material property and fracture is assumed to occur when $K_I >= K_{Ic}$ at the crack tip. Of the fracture mechanics models to be presented (Griffith, Gonano, Rooke and Cartwright, Sammis and Ashby, Rummel, Kemeny and Cook) the first two models are for crack initiation only. The remaining fracture mechanics models predict crack propagation. In order to use these latter models to simulate crack initiation it is necessary to use an initial crack length (starter crack) for the fitting process.

Two stress-based models for crack initiation (Lajtai, Carter) are also evaluated. In these models the actual stresses around a given geometry are calculated and used in a failure criterion. If the measured strength is greater than the available strength the material is assumed to fail or fracture (safety factor approach).

Figure 3.13: Griffith equation fit to Cold Spring granite primary crack initiation data. $Ra^2$ = degree of freedom adjusted coefficient of determination.

## 3.4.1 Griffith

If, for the moment, we assume that Griffith's [34] original energy-based fracture criterion is applicable to any flaw geometry, a reasonable match to the laboratory data can be obtained with a simplified version of his model given below:

$$\sigma = \frac{\sqrt{2E\gamma_s}}{\sqrt{\pi c}} = \frac{m}{\sqrt{R}} \tag{3.8}$$

An optimal value for parameter $m$ to fit the crack initiation data can be easily determined. The results are shown in Figure 3.13. Even though the Griffith model produces an adequate fit to the data it has undesirable asymptotes (as $R \to 0$, $\sigma_1 \to \infty$ and as $R \to \infty$, $\sigma_1 \to 0$). If this model produced a better fit it would be extremely attractive because of its simplicity and the fact that parameter $m$ is a material property.

## 3.4.2 Gonano

Gonano [32] presents a model for crack initiation using the critical strain energy release rate approach. The model is described by:
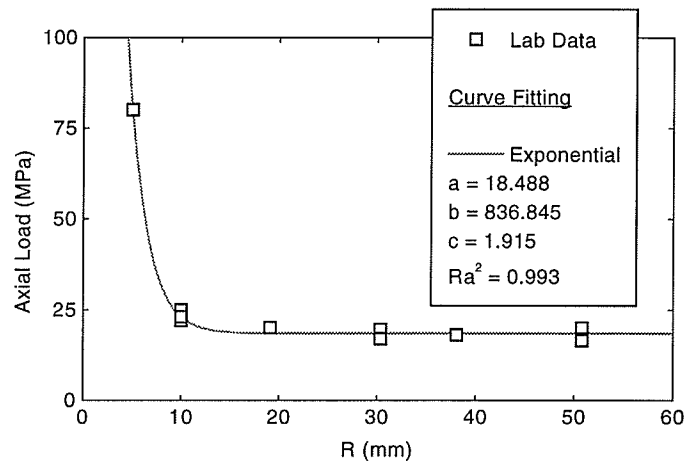
$$\sigma_1 = bR^m \tag{3.9}$$

Figure 3.14: Gonano equation fit to Cold Spring granite primary crack initiation data. $Ra^2$ = degree of freedom adjusted coefficient of determination.

which is a refined version of Griffith's model. Since fracture toughness is directly related to strain energy release rate the model is closely related to the LEFM (linear elastic fracture mechanics) approaches. The model is based on the premise that crack initiation occurs when the strain energy release rate in the sample volume reaches a critical value. Gonano concluded that for fractures in model tests, size dependence is primarily controlled by strain gradient, critical volume, and critical surface area. Gonano postulated that a plot of primary fracture initiation stress against the hole radius should produce a straight line relation when using log-log axes. The fit produced by this model (Figure 3.14) is slightly better than the Griffith model. Gonano's curve approaches $\sigma_1 = \infty$ as $R \to 0$ and approaches $\sigma_1 = 0$ as $R \to \infty$.

It is interesting to note that the Weibull [88] distribution takes the same form as equation 3.9. The Weibull distribution implies that the most probable strength is proportional to $R^{-1/\beta}$ where $\beta$ is a material constant. This distribution uses an empirical statistical approach to explain the "size effect".
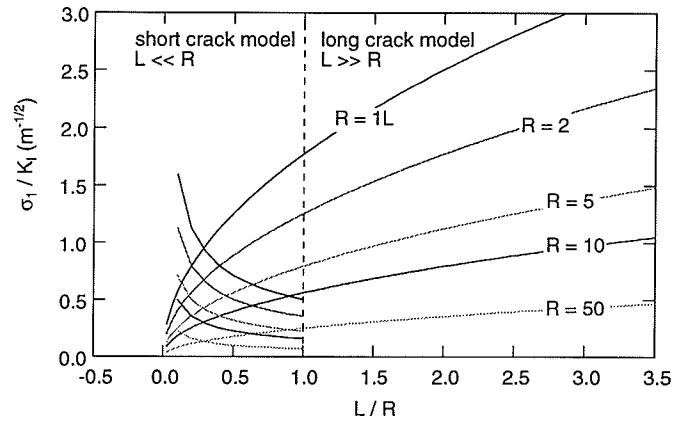
Figure 3.15: Predicted crack propagation trends using Rooke and Cartwright short and long crack models ($C = 1$).

## 3.4.3 Rooke and Cartwright

Rooke and Cartwright [78] proposed the following two models for crack propagation from a circular void:

$$\sigma_1 = \frac{K_I}{1.12\sqrt{\pi L}} \tag{3.10}$$

$$\sigma_1 = \frac{K_I\sqrt{\pi L}}{CR} \tag{3.11}$$

Equation 3.10 is valid for small crack lengths ($L << R$) and equation 3.11 for large crack lengths ($L >> R$). Together these curves predict initially unstable crack growth followed by a stable, hardening trend as shown in Figure 3.15. The short crack model approximates the circular void-primary crack geometry by an edge crack. The long crack model assumes the same geometry is approximated by a straight crack, oriented parallel to $\sigma_1$, with a set of point forces at the center of the crack.

As can be seen, equation 3.10 is independent of $R$ which implies a constant crack initiation stress for our case. On the other hand when $K_I$, $L$, and $C$ are used as fitting parameters in equation 3.11 the curve shown in Figure 3.16 is obtained. This long crack model provides a reasonable fit to the crack initiation data. However, the starter crack length is unusually

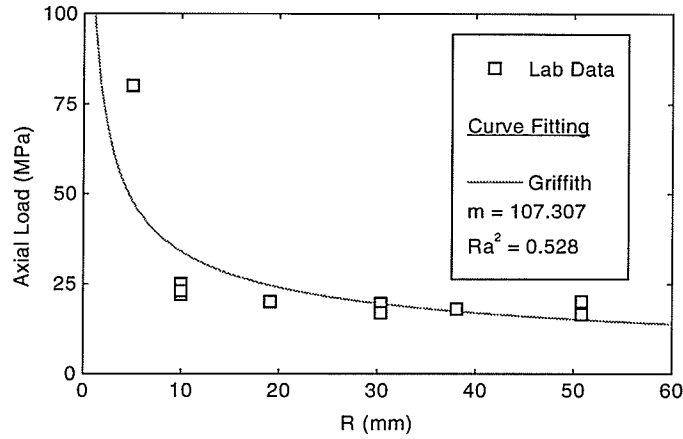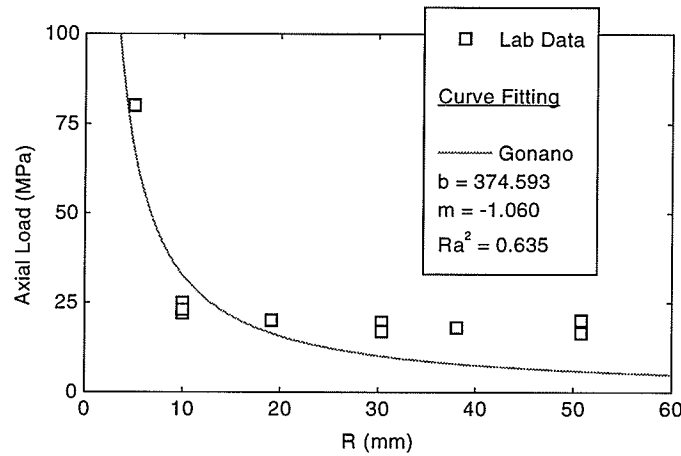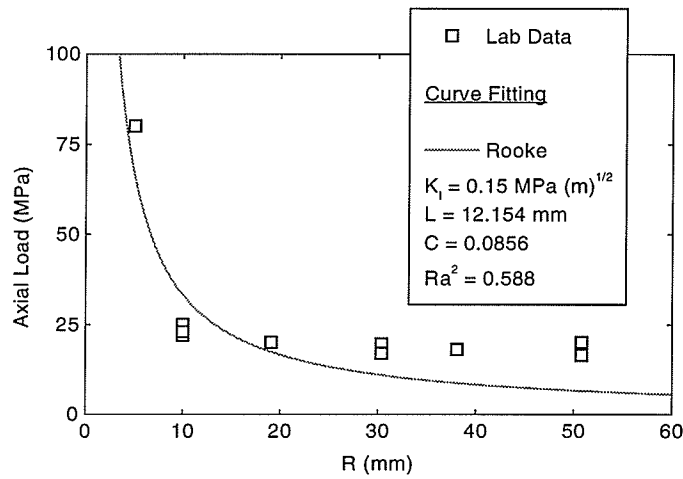Figure 3.16: Rooke and Cartwright long crack model fit to Cold Spring granite primary crack initiation data. $Ra^2$ = degree of freedom adjusted coefficient of determination.

large ($L = 12$ mm). Equation 3.11 has the following asymptotes: as $R \to 0$, $\sigma_1 \to \infty$ and as $R \to \infty$, $\sigma_1 \to 0$.

If we look at equation 3.10 it has already been noted that there is no size dependence built into the small crack model (equation 3.10). But if we assume that the starter crack length $L$ is proportional to the hole radius $R$ we end up with the Griffith equation described previously in equation 3.8 and shown below:

$$\sigma = \frac{K_I}{1.12\sqrt{\pi L}} = \frac{m}{\sqrt{R}} \tag{3.12}$$

This size dependent starter crack model is what is plotted as the short crack model in Figure 3.15.

In a general sense the long crack model shows the correct size effect behavior that is indicated by the laboratory data. That is, primary cracks become easier to propagate as $R$ increases. The laboratory data does not include the initial unstable propagation predicted by Rooke and Cartwright's short crack model, but this is due to the way the data was produced. A stiff testing machine with a strain controlled feedback loop to control the applied load would allow this instability to be recorded. An interesting point to note is

that the Rooke and Cartwright long crack model produces a concave down curve. The laboratory data (Figure 3.9) appears to show both types of curvature (concave up and concave down). The results of fitting the crack propagation data to the long crack model are shown in Figure 3.17. The curves roughly follow the data for the fractures displaying highly stable fracture propagation trends (R10, R20A, R30A, R30B, R50B). The almost unstable propagation shown by R40 and R50A could not be fit adequately.

### 3.4.4  Sammis and Ashby

Sammis and Ashby's [80] model for fracture propagation from a circular void is

$$\sigma_1 = \frac{K_I \left(1 + L/R\right)^{3.3}}{1.1\sqrt{\pi L}} \tag{3.13}$$

It is valid for $L > 0$. The curve is derived from fitting an equation to an exact solution (by superposition), tabulated by Sih [82], for the circular void primary crack propagation problem in an infinite plate loaded in compression. Sammis and Ashby's approximation to Sih's exact solution is compared in Figure 3.18.

The Sammis and Ashby model shows the similar initial instability followed by stable crack growth as in Rooke and Cartwright's model except that the concavity of the stable portions of two models have an opposite sense (compare Figures 3.19 and 3.15)

Using $K_I$ and $L$ as fitting parameters a good fit is obtained to the crack initiation data with this model (Figure 3.20). This curve also approaches $\infty$ as $R \to 0$. However, when $R \to \infty$, $\sigma_1 \to K_I/(1.1\sqrt{\pi L})$; not the typical $\sigma_1 = 0$ asymptote displayed by the previous fracture mechanics models. Using the best fit parameters in Figure 3.20 the horizontal asymptote is $\sigma_1 = 8.8$ MPa (a reasonable approximation for $T_0$ for the Cold Spring granite).

The Sammis and Ashby model predicts the correct softening trend shown by the lab data with increasing $R$. Using $K_I$ as a fitting parameter the model can be fit to the crack propagation data (Figure 3.21). The model is valid for all $L > 0$ resulting in the exclusion of the initial crack nucleation point from each data set in the curve fitting. Of all the data sets only the R20A data set produced a reasonable fit.
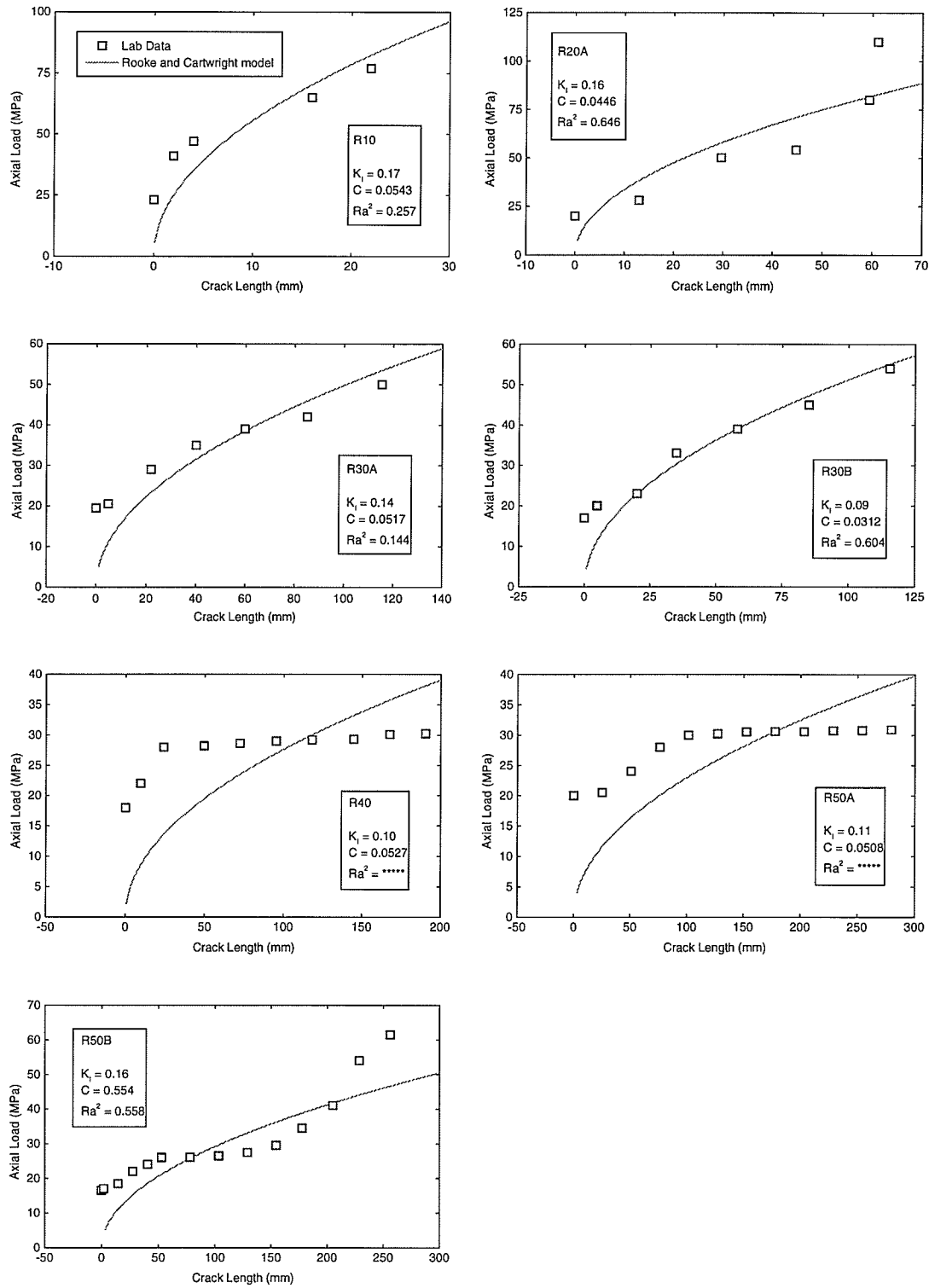
Figure 3.17: Rooke and Cartwright long crack model fit to Cold Spring granite primary fracture propagation data ($K_I$ in MPa$\sqrt{\mathrm{m}}$). $Ra^2 =$ degree of freedom adjusted coefficient of determination. ***** indicates negative $Ra^2$.
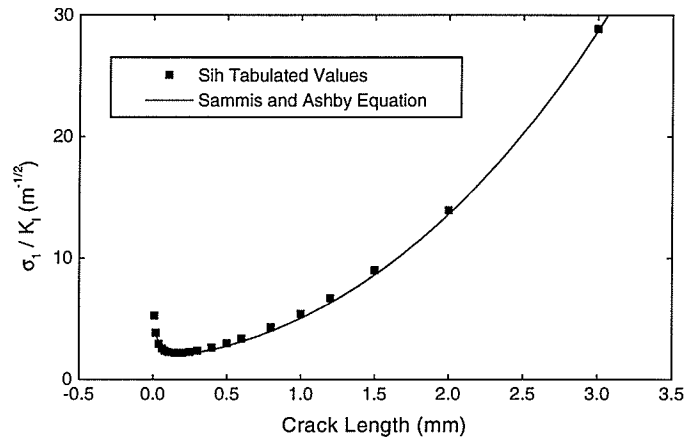
Figure 3.18: Comparison of Sammis and Ashby model with Sih tabulated results ($R = 1$ mm).
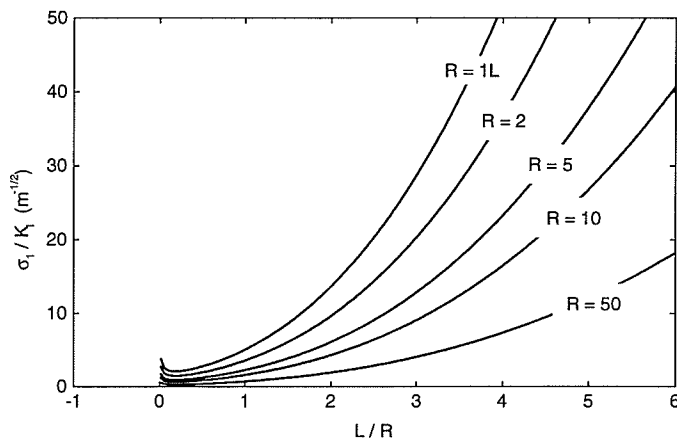


Figure 3.19: Predicted crack propagation trends for varying $R$ using Sammis and Ashby model.
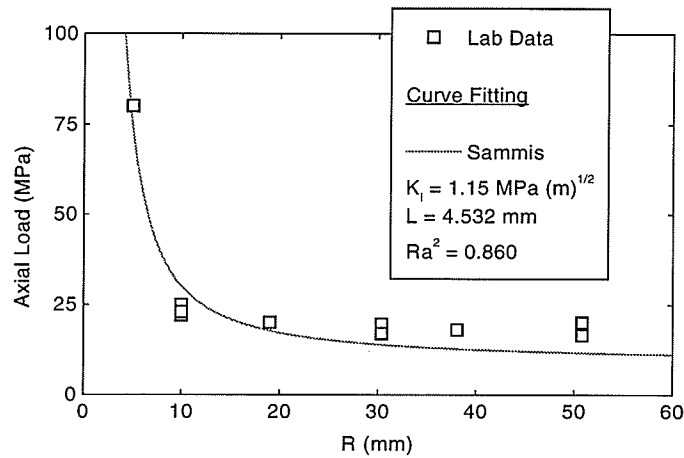
Figure 3.20: Sammis and Ashby model fit to Cold Spring granite primary crack initiation data. $Ra^2$ = degree of freedom adjusted coefficient of determination.

### 3.4.5 Rummel

Rummel [79] derived an analytical approximation for a crack emanating from a circular void under a compressive load. This model is based upon Paris and Sih's [74] general formulation for the stress intensity factor for a tension crack, of half length $a$, in an infinite plate. Paris and Sih's formulation is:

$$K_I = \frac{1}{\sqrt{\pi a}} \int_{-a}^{a} \sigma_y(x, 0) \sqrt{\frac{a+x}{a-x}} dx \qquad (3.14)$$

In this equation $\sigma_y$ is the stress normal to the crack axis along the line $y = 0$ (Figure 3.22). By substituting the Kirsch [53] solution (stress field around a circular hole loaded in compression) for $\sigma_y(x, 0)$ in equation 3.14 the circular void primary crack geometry can be mimicked. Rummel makes the simplification of ignoring the circular hole in the integration limits of equation 3.14 limiting the integration to the intervals $-(R + a), -R$ and $R + a, R$ (Figure 3.22.) Rummel's equation reduces to

$$\sigma_1 = \frac{K_I}{2} \sqrt{\frac{\pi \left(\frac{R+L}{R}\right)^7}{R\left(\left(\frac{R+L}{R}\right)^2 - 1\right)}} \qquad (3.15)$$
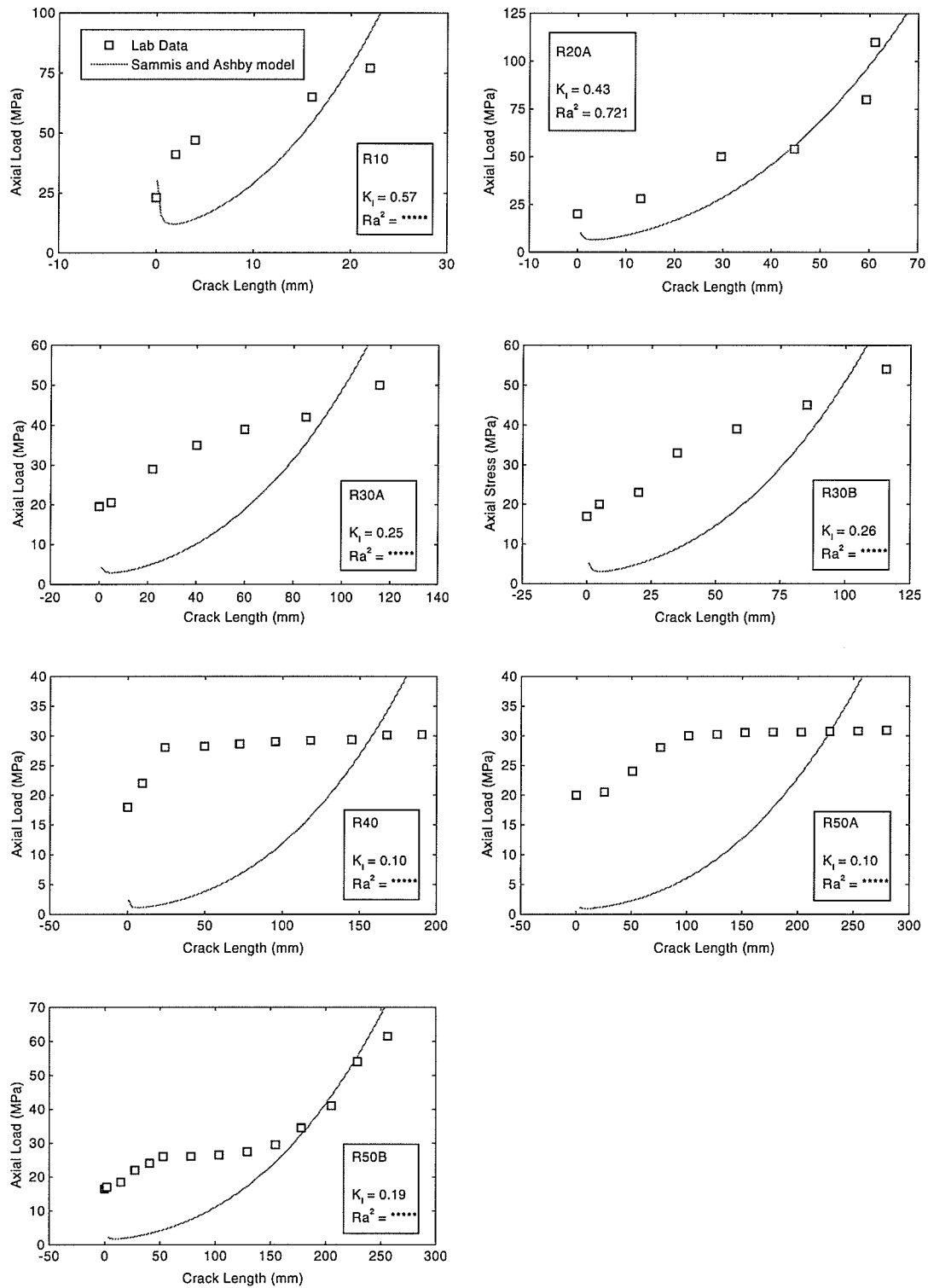
Figure 3.21: Sammis and Ashby model fit to Cold Spring granite primary fracture propagation data ($K_I$ in MPa$\sqrt{\text{m}}$). $Ra^2$ = degree of freedom adjusted coefficient of determination. ***** indicates negative $Ra^2$.
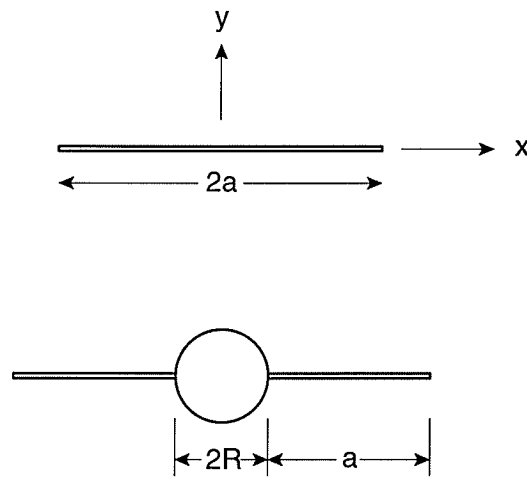
Figure 3.22: Geometry for Paris and Sih model (top) and Rummel model (bottom).

Rummel demonstrated that this model agreed reasonably well with the classic solution derived by Bowie [10]. Using a complex variable method and applying Griffith's energy approach for brittle failure, Bowie solved the class of plane stress/strain problems in elasticity corresponding to a distribution of radial cracks originating at a circular hole in an infinite plate.

Figure 3.23 compares Rummel's solution to Sih's [82] exact solution, for the circular void primary crack problem. Figure 3.24 shows the propagation trends predicted by Rummel's model with varying hole radius. Both of these figures are almost identical to those produced with Sammis and Ashby's model (Figures 3.18 and 3.19). For practical purposes both models behave the same and in fact both models have the same asymptotes and result in similar parameter values when fit to the crack initiation and crack propagation data (compare Figure 3.25 with 3.20 and Figure 3.26 with 3.21).

### 3.4.6   Kemeny and Cook

Kemeny and Cook [50] introduced two "generic" crack models (equations 3.16 and 3.17) that take into account all of the phenomenon observed in a crack in a rock subjected to
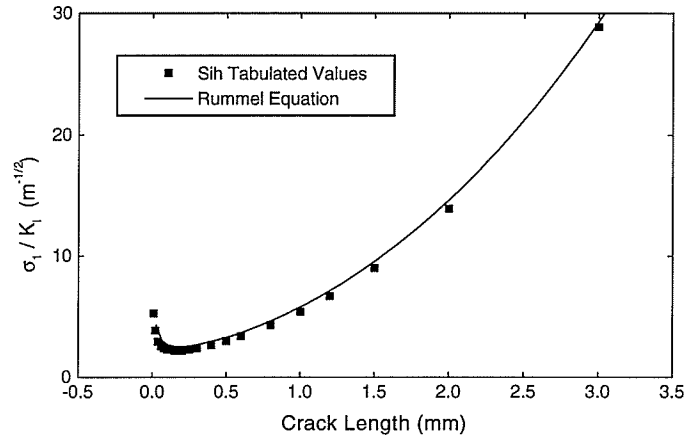
Figure 3.23: Comparison of Rummel model with Sih tabulated results ($R = 1$ mm).
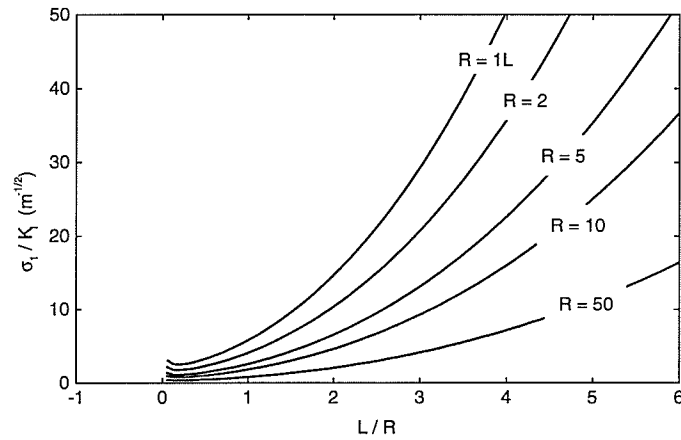


Figure 3.24: Predicted crack propagation trends for varying $R$ using Rummel model.

Figure 3.25: Rummel equation fit to Cold Spring granite primary crack initiation data. $Ra^2 = $ degree of freedom adjusted coefficient of determination.

compressive stresses.

$$\sigma_1 = \frac{K_I\sqrt{\pi}}{2C\sqrt{L}\arcsin(a/L)} \tag{3.16}$$

$$\sigma_1 = \frac{K_I\sqrt{\pi}}{2C\sqrt{L}((2-L/a)\arcsin(a/L)+\sqrt{1-(a/L)^2})} \tag{3.17}$$

These models consist of a crack of length $2L$ oriented in the direction of $\sigma_1$ and subjected to a tensile stress over a region of length $2a$ as shown in Figure 3.27. The first model assumes that the tensile stress is uniformly distributed over $2a$ while the second model assumes the tensile stress decreases linearly from the crack center. To mimic the circular hole geometry with the Kemeny and Cook models we assume the stress field applied over $2a$ in Figure 3.27 is equivalent to that created by a circular void. In other words we set $a = R$.

Both of these models basically mimic the stable behavior exhibited by Rooke and Cartwright's long crack model (compare Figures 3.28 and 3.29 to Figure 3.15). Kemeny and Cook suggested using the same small crack model as Rooke and Cartwright (equation 3.10) to describe the initial unstable crack growth. These are also shown on Figures 3.28 and 3.29 where $L < a$.

Using $K_I, L,$ and $C$ as fitting parameters reasonable fits are produced for the crack initiation data (Figures 3.30 and 3.31). Both models have the typical fracture mechanics

Figure 3.26: Rummel model fit to Cold Spring granite primary fracture propagation data ($K_I$ in MPa$\sqrt{\mathrm{m}}$). $Ra^2$ = degree of freedom adjusted coefficient of determination. ***** indicates negative $Ra^2$.

Figure 3.27: Geometry of Kemeny and Cook's generic crack model. a) constant tensile stress over distance $2a$ at the crack center. b) linearly decreasing stress.
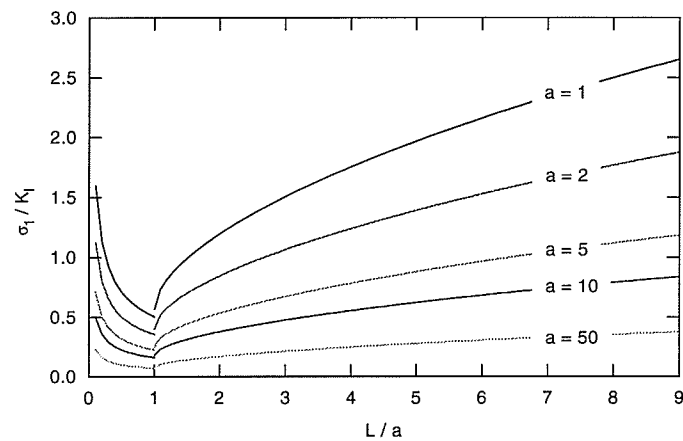


Figure 3.28: Predicted crack propagation trends for varying $a$ using Kemeny and Cook's first model (equation 3.16).
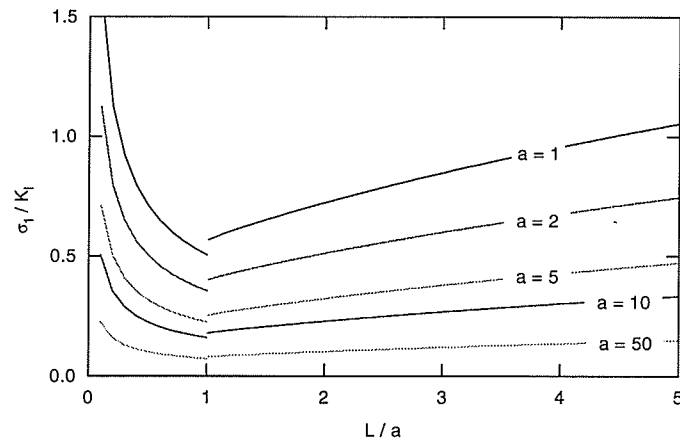
Figure 3.29: Predicted crack propagation trends for varying $a$ using Kemeny and Cook's second model (equation 3.17).
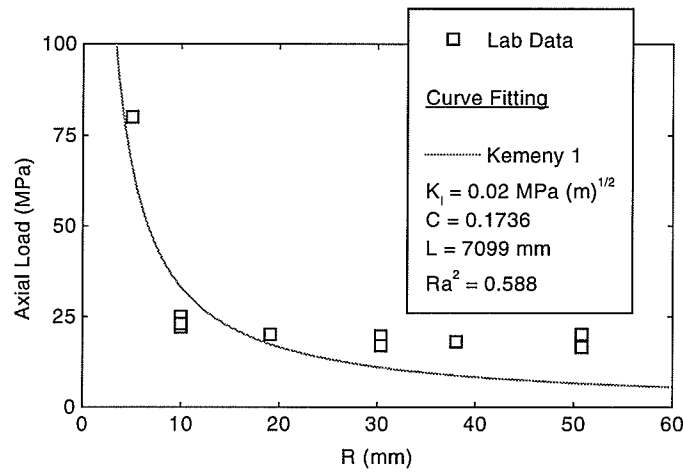


Figure 3.30: Kemeny and Cook model 1 (equation 3.16) fit to Cold Spring granite primary crack initiation data. $Ra^2$ = degree of freedom adjusted coefficient of determination.

asymptotes of: $\sigma_1 \to \infty$ as $a \to 0$ and $\sigma_1 \to 0$ as $a \to \infty$. In order to fit the crack initiation data, the starter crack length $L$ had to be constrained to the domain $L \geq R$ to prevent the equations from becoming singular. In this case this restriction forces the starter crack length to have a value greater than 50.8 mm which is unrealistic. Nonetheless, a reasonable fit is produced even though the models are intended for crack propagation problems.

When fitting the long crack models to the crack propagation data sets the propagation

Figure 3.31: Kemeny and Cooke model 2 (equation 3.17) fit to Cold Spring granite primary crack initiation data. $Ra^2$ = degree of freedom adjusted coefficient of determination.

data had to be restricted to crack lengths greater than or equal to $R$. This meant excluding a substantial number of points in the curve fitting, especially for the small sized holes. The results of the curve fitting are shown in Figure 3.32. In these figures Kemeny 1 corresponds to equation 3.16 and Figure 3.27(a) and Kemeny 2 corresponds to equation 3.17 and Figure 3.27(b). As with the Rooke and Cartwright models a reasonable fit was obtained to the propagation data that showed a strong preference for hardening (data sets R10, R20A, R30A, R30B, R50B) and an inadequate fit resulted for the remaining data sets (R40, R50A).

### 3.4.7 Lajtai

Lajtai [56] proposed a stress averaging model to account for the size effect seen in the crack initiation data. His hypothesis was that under high stress gradients even brittle materials behave in a plastic manner and distribute stresses into regions of lower stress. This inelastic behavior can be simulated by replacing the point stresses in a material with the stresses averaged over a constant distance $d$. This averaging distance is considered to be a material property. Lajtai's model (equation 3.18) uses the stress gradient at a point to approximate
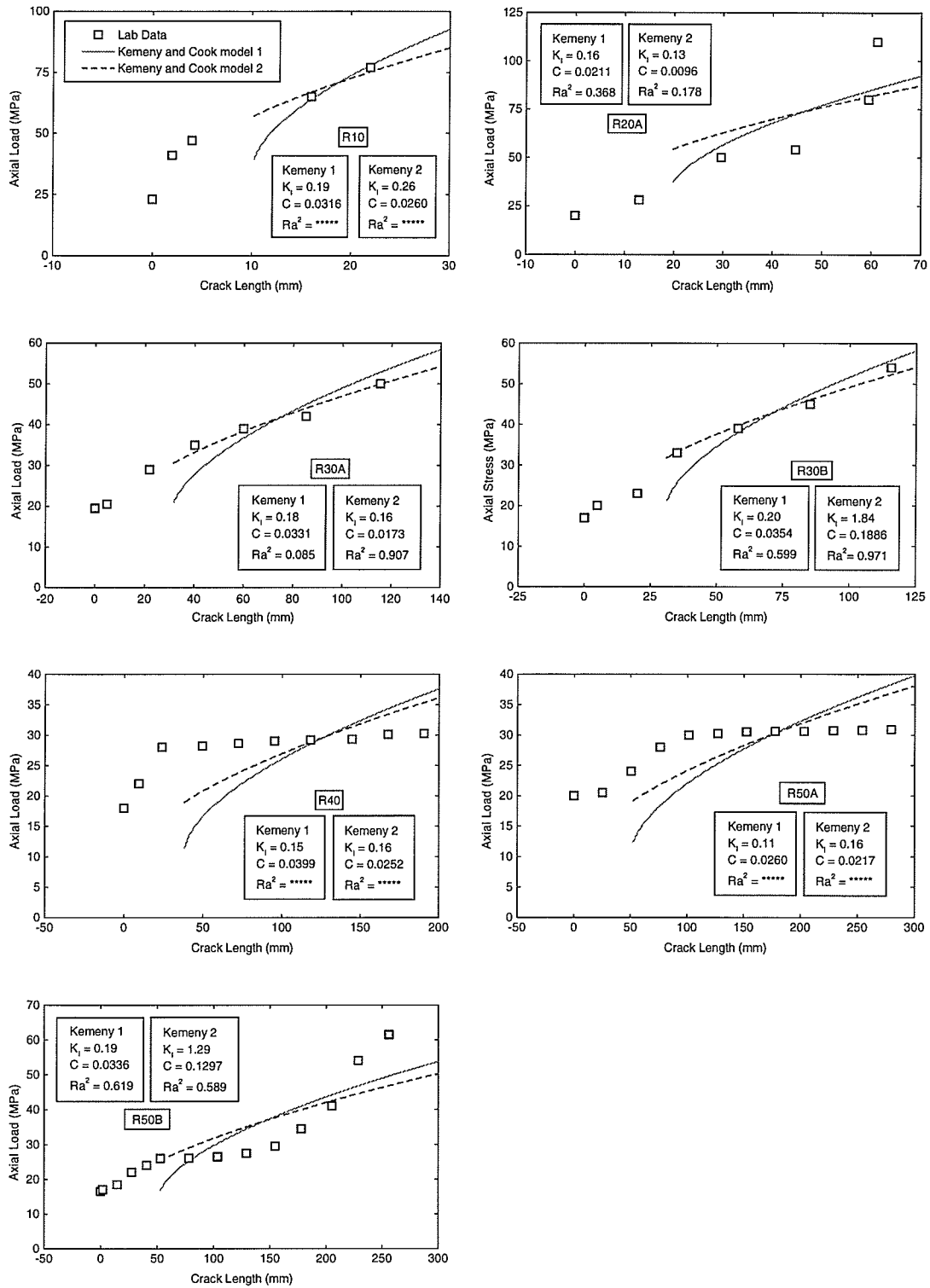
Figure 3.32: Kemeny and Cook models fit to Cold Spring granite primary fracture propagation data ($K_I$ in MPa$\sqrt{\text{m}}$). $Ra^2$ = degree of freedom adjusted coefficient of determination. ***** indicates negative $Ra^2$.
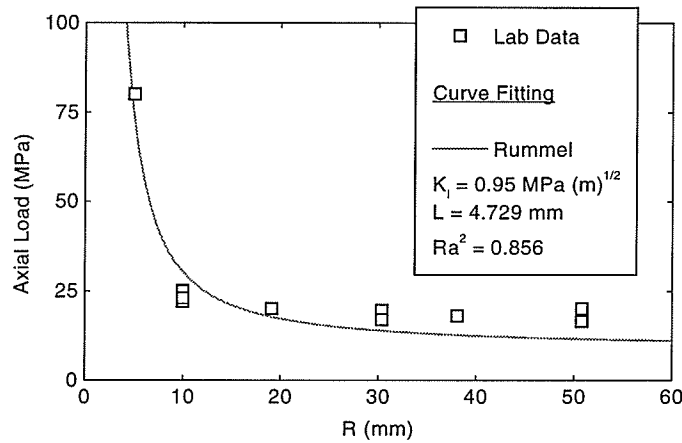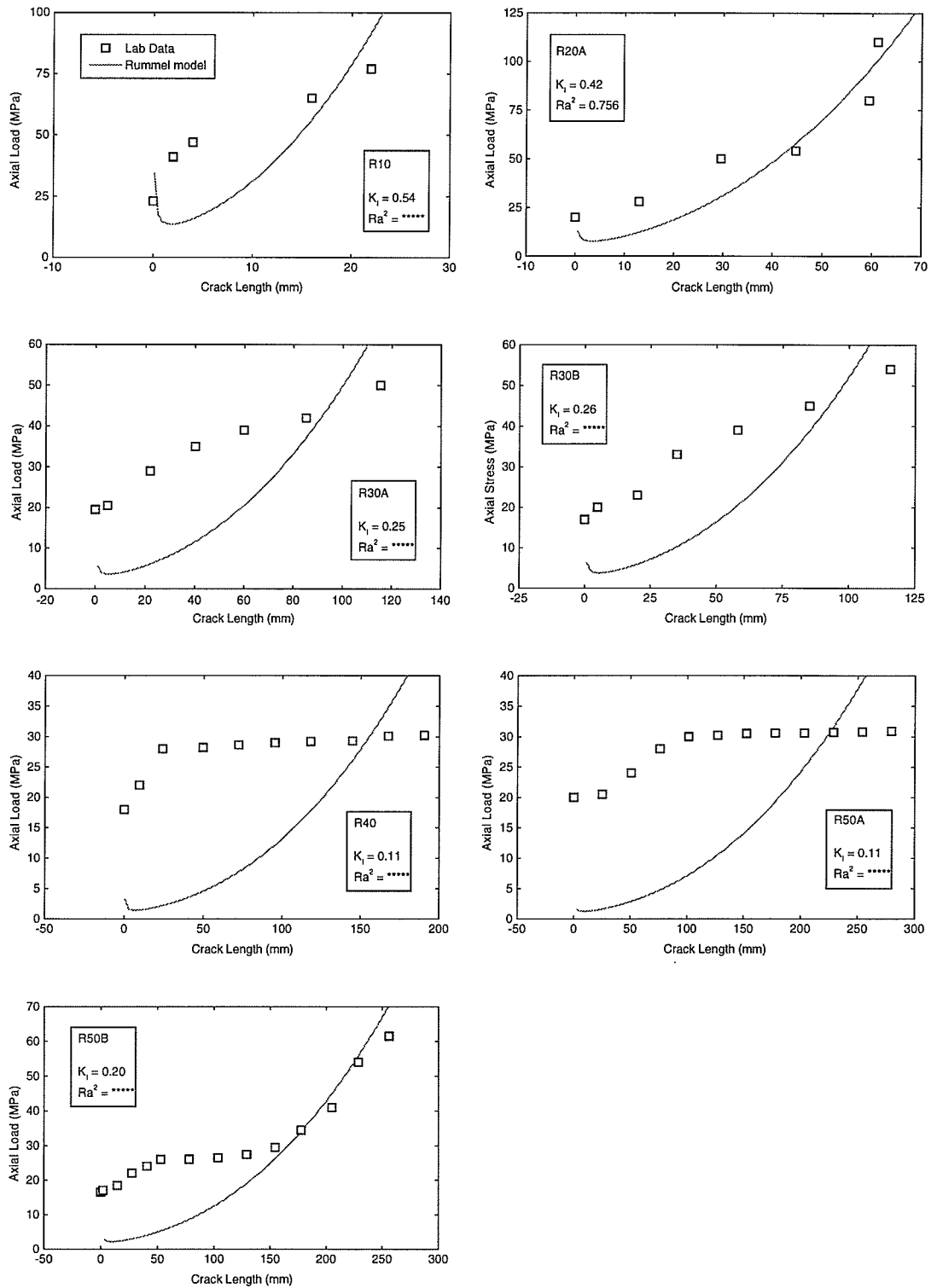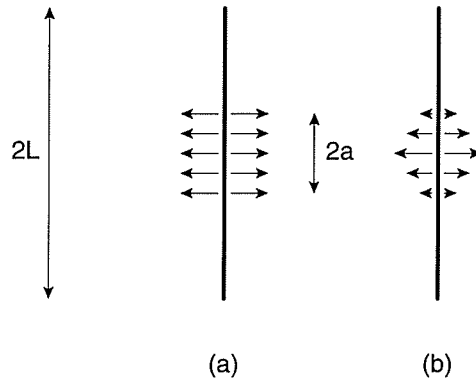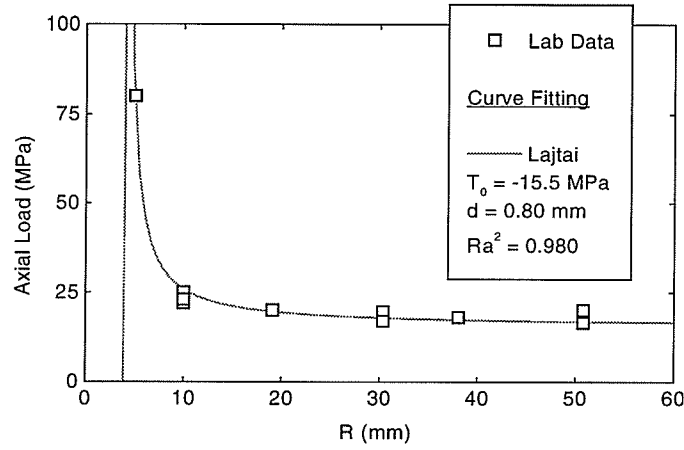
Figure 3.33: Lajtai's crack initiation model fit to Cold Spring granite primary crack initiation data. $Ra^2$ = degree of freedom adjusted coefficient of determination.

the stress ($\sigma_1$) at a distance $d$ from that point.

$$\sigma_1 = -\frac{T_0}{5\frac{d}{R} - 1} \tag{3.18}$$

The stress gradient along this path is assumed to be linear and failure is based on the maximum stress theory (failure occurs when $\sigma_3 \leq T_0$).

Lajtai's function provides an excellent fit to the crack initiation data (Figure 3.33). However, his function has a singularity at $R = 5d$ ($\sigma_1 \to -\infty$). Also at $R = 0$, $\sigma_1 = 0$ indicating 0 compressive strength for a sample without a hole. The function does have the desirable asymptote of $\sigma_1 = -T_0$ at large $R$ giving an estimate of $T_0 = -15.5$ MPa for the Cold Spring granite.

### 3.4.8 Carter

Rather than assuming a linear gradient Carter [20] modified Lajtai's averaging scheme by determining the actual average stress over the critical distance $d$. His model is given by:

$$\sigma_1 = \frac{2dT_0}{R^2}\left(\frac{(R+d)^3}{R^2 - (R+d)^2}\right) \tag{3.19}$$

This function also provides a good fit to the lab data (Figure 3.34). This function has the following asymptotes: as $R \to 0$, $\sigma_1 \to \infty$ and as $R \to \infty$, $\sigma_1 \to -T_0$. This gives an
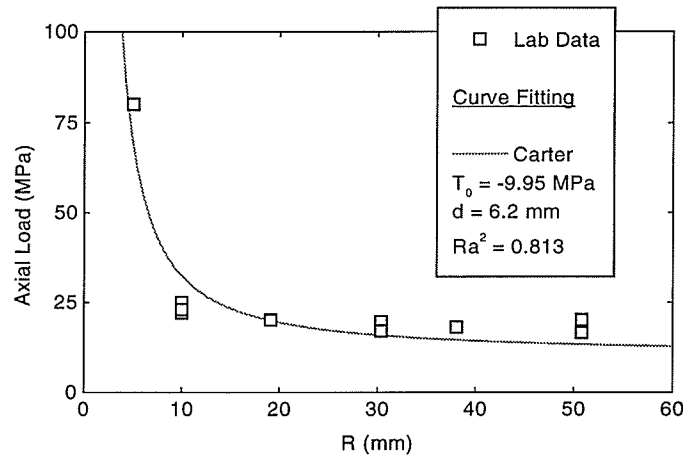
Figure 3.34: Carter's crack initiation model (equation 3.19) fit to Cold Spring granite primary crack initiation data. $Ra^2$ = degree of freedom adjusted coefficient of determination.

estimate for uniaxial tensile strength of -9.95 MPa.

Carter also provides a model (equation 3.20) similar to above except that it uses USR instead of the maximum stress criterion as a fracture criterion.

$$\sigma_1 = \frac{T_0}{\frac{A}{2} - \sqrt{\frac{A^2}{4} + (\frac{BT_0}{C_0})^2}} \tag{3.20}$$

$$\text{where} \quad A = \frac{R^2}{2d}\left(\frac{R^2}{(R+d)^3} - \frac{1}{(R+d)}\right)$$

$$B = \frac{1}{d}\left(d - 2R + \frac{5R^2}{2(R+d)} - \frac{R^4}{2(R+d)^3}\right)$$

The fitting results are shown in Figure 3.35. The asymptotes for this equation are: as $R \to 0$, $\sigma_1 \to C_0$ and as $R \to \infty$, $\sigma_1 \to -T_0$. This equation is relatively insensitive to the value of $C_0$. Therefore $C_0$ was set at the actual compressive strength of the Cold Spring granite (226 MPa) for the curve fitting. The estimate for $T_0$ produced by this model is -15.1 MPa. This model produces a good fit and has desirable limits.

### 3.4.9   Summary of Crack Initiation Results

The parameters from the crack initiation curve fitting are summarized in Table 3.1. The fitting parameter $K_I$ in the analytical models actually results in the critical stress intensity
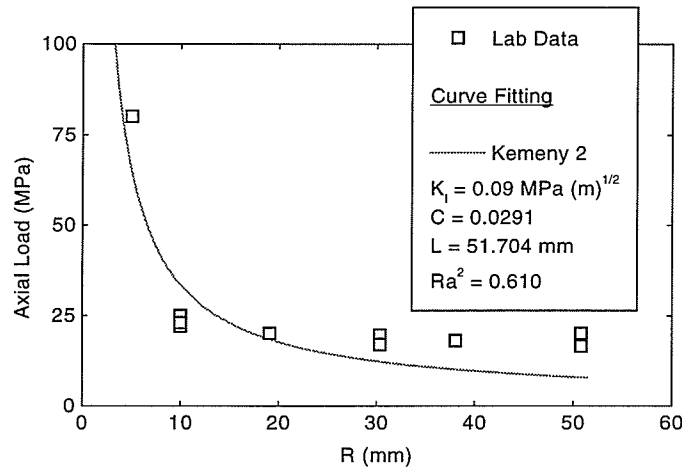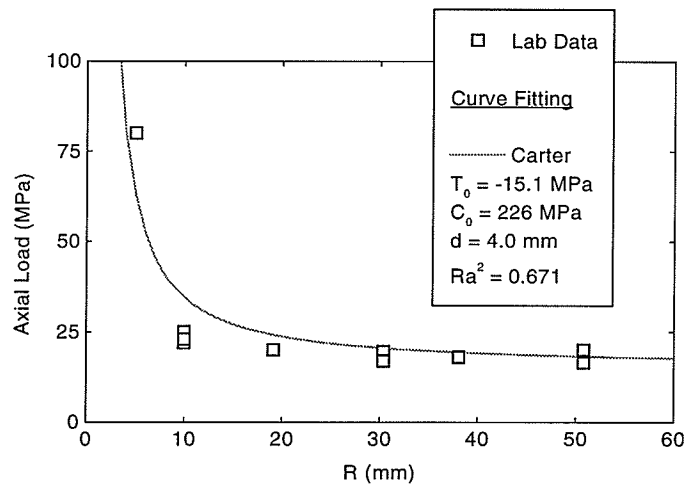
Figure 3.35: Carter's USR-based crack initiation model (equation 3.20) fit to Cold Spring granite primary crack initiation data. $Ra^2$ = degree of freedom adjusted coefficient of determination.

factor $(K_{Ic})$ when fit to the crack initiation lab data. As can be seen, there is a large variation in the parameter values $(L, d, K_{Ic})$. However, the values for $T_0$ remained relatively consistent $(-18.5, -15.5, -9.95, -15.1)$. $K_{Ic}$, a material property, should have remained relatively consistent for each model as well. The averaging distance, $d$, varied because Lajtai's and Carter's models used two different formulations for their average stresses. The starter crack lengths are unreasonably large for the Rooke and Cartwright and the Kemeny and Cook models. However, these models were not intended to model crack initiation, but were tried with the limiting case of $L = 0$ to see how they would perform.

Whittaker et al. [90] compiled a table of 100 reported values of $K_{Ic}$ for granite. The published values varied from 0.385–3.02 MPa$\sqrt{m}$. Only the Sammis and Ashby and Rummel models produced SIFs in this range. The other fracture mechanics solutions produced SIFs below this range. Carter et al. [20] gives the fracture toughness of Lac du Bonnet (Cold Spring) granite as 2.45 MPa$\sqrt{m}$ using results from a double torsion test. Wilkins' [91] value for $K_{Ic}$ for Lac du Bonnet granite is 1.53 MPa$\sqrt{m}$ as determined from three-point bending tests.

| Function | Parameter Values | | | $Ra^2$ |
|---|---|---|---|---|
| Exponential eq. 3.7 | $a = 18.488$ | $b = 836.845$ | $c = 1.915$ | 0.993 |
| Lajtai eq. 3.18 | $d = 0.80$ | $T_0 = -15.5$ | | 0.980 |
| Sammis eq. 3.13 | $L = 4.532$ | $K_I = 1.15$ | | 0.860 |
| Rummel eq. 3.15 | $L = 4.729$ | $K_I = 0.95$ | | 0.856 |
| Carter eq. 3.19 | $d = 6.2$ | $T_0 = -9.95$ | | 0.813 |
| Carter eq. 3.20 | $d = 4.0$ | $T_0 = -15.1$ | $C_0 = 226$ | 0.671 |
| Kemeny eq. 3.17 | $L = 51.704$ | $K_I = 0.09$ | $C = 0.0291$ | 0.610 |
| Gonano eq. 3.9 | $m = -1.060$ | $b = 374.593$ | | 0.635 |
| Kemeny eq. 3.16 | $L = 7099$ | $K_I = 0.02$ | $C = 0.174$ | 0.588 |
| Rooke eq. 3.11 | $L = 12.154$ | $K_I = 0.15$ | $C = 0.0856$ | 0.588 |
| Griffith eq. 3.8 | $m = 107.307$ | | | 0.528 |

Table 3.1: Parameter values used to fit Cold Spring granite primary crack initiation data to various models arranged according to goodness of fit. $Ra^2$ = degree of freedom adjusted coefficient of determination. Units: $L$ and $d$ in mm, $K_I$ in MPa$\sqrt{\mathrm{m}}$, $T_0$ and $C_0$ in MPa.

Of all the models the exponential model gave the best fit. Generally speaking the stress-based functions performed better than the fracture-mechanics-based models and the simpler models produced better results than the more complicated models.

The stress-based functions would only require one parameter ($d$) to be determined if the tensile strength of the material was known beforehand. This makes them very attractive for curve fitting. Similarly, the curve fitting for the fracture mechanics models could be simplified if $K_{Ic}$ were given. However, judging from the large variation in $K_{Ic}$ used in the fitting process a very good fit would not be obtained with a fixed value for $K_{Ic}$. The stress-based models seem to be more robust in this respect.

### 3.4.10   Summary of Crack Propagation Results

The parameters from the crack propagation curve fitting are summarized in Tables 3.2–3.6. Generally speaking the curve fitting exercise was largely unsuccessful. None of the models that were investigated produced adequate fits to the propagation data for the entire range of hole sizes. The Sammis and Ashby (Table 3.3) and Rummel (Table 3.4) models show a

| Data Set | $K_{Ic}$ (MPa$\sqrt{\mathrm{m}}$) | $C$ | $Ra^2$ |
|---|---|---|---|
| R10 | 0.17 | 0.0543 | 0.257 |
| R20A | 0.16 | 0.0446 | 0.646 |
| R30A | 0.14 | 0.0517 | 0.144 |
| R30B | 0.09 | 0.0312 | 0.604 |
| R40 | 0.10 | 0.0527 | ***** |
| R50A | 0.11 | 0.0508 | ***** |
| R50B | 0.16 | 0.0554 | 0.558 |

Table 3.2: Rooke and Cartwright parameter values used to fit Cold Spring granite primary crack propagation data. $Ra^2$ = degree of freedom adjusted coefficient of determination. ***** indicates negative $Ra^2$.

| Data Set | $K_{Ic}$ (MPa$\sqrt{\mathrm{m}}$) | $Ra^2$ |
|---|---|---|
| R10 | 0.57 | ***** |
| R20A | 0.43 | 0.721 |
| R30A | 0.25 | ***** |
| R30B | 0.26 | ***** |
| R40 | 0.10 | ***** |
| R50A | 0.10 | ***** |
| R50B | 0.19 | ***** |

Table 3.3: Sammis and Ashby parameter values used to fit Cold Spring granite primary crack propagation data. $Ra^2$ = degree of freedom adjusted coefficient of determination. ***** indicates negative $Ra^2$.

decreasing trend for $K_{Ic}$ as hole size increases. This was expected since these are only one parameter models when used for crack propagation modeling. $K_{Ic}$ is the only parameter allowed to change to compensate for the observed size effect. On the other hand, Rooke and Cartwright's (Table 3.2) and Kemeny and Cook's (Table 3.5) first model produce more consistent values for $K_{Ic}$ as hole size increases. In these models the second curve fitting parameter $C$ compensates for the size effect. Kemeny and Cook's second model (Table 3.6) produces erratic values for $K_{Ic}$ as hole size varies.

| Data Set | $K_{Ic}$ (MPa$\sqrt{\text{m}}$) | $Ra^2$ |
|---|---|---|
| R10 | 0.54 | ***** |
| R20A | 0.42 | 0.756 |
| R30A | 0.25 | ***** |
| R30B | 0.26 | ***** |
| R40 | 0.11 | ***** |
| R50A | 0.11 | ***** |
| R50B | 0.20 | ***** |

Table 3.4: Rummel parameter values used to fit Cold Spring granite primary crack propagation data. $Ra^2$ = degree of freedom adjusted coefficient of determination. ***** indicates negative $Ra^2$.

| Data Set | $K_{Ic}$ (MPa$\sqrt{\text{m}}$) | $C$ | $Ra^2$ |
|---|---|---|---|
| R10 | 0.19 | 0.0316 | ***** |
| R20A | 0.16 | 0.0211 | 0.368 |
| R30A | 0.18 | 0.0331 | 0.085 |
| R30B | 0.20 | 0.0354 | 0.599 |
| R40 | 0.15 | 0.0399 | ***** |
| R50A | 0.11 | 0.0260 | ***** |
| R50B | 0.19 | 0.0336 | 0.619 |

Table 3.5: Kemeny and Cook (model 1, equation 3.16) parameter values used to fit Cold Spring granite primary crack propagation data. $Ra^2$ = degree of freedom adjusted coefficient of determination. ***** indicates negative $Ra^2$.

| Data Set | $K_{Ic}$ (MPa$\sqrt{m}$) | $C$ | $Ra^2$ |
|----------|--------------------------|--------|--------|
| R10  | 0.26 | 0.0260 | ***** |
| R20A | 0.13 | 0.0096 | 0.178 |
| R30A | 0.16 | 0.0173 | 0.907 |
| R30B | 1.84 | 0.1886 | 0.971 |
| R40  | 0.16 | 0.0252 | ***** |
| R50A | 0.16 | 0.0217 | ***** |
| R50B | 1.29 | 0.1297 | 0.589 |

Table 3.6: Kemeny and Cook (model 2, equation 3.17) parameter values used to fit Cold Spring granite primary crack propagation data. $Ra^2$ = degree of freedom adjusted coefficient of determination. ***** indicates negative $Ra^2$.

The hardening trend of the Sammis and Ashby and Rummel functions is much too severe. These models predict much more stable fracture growth than the lab data shows. As was previously mentioned, the initial instability shown by the Sammis and Ashby and Rummel functions is not represented in the lab data. This factor also contributes to the poor fit obtained with these models.

The Rooke and Cartwright long crack model is valid for $L \gg R$, but was fit to all the available propagation data including data where $L \leq R$ since it was available and followed the general trend of the function. Even though the model is not valid for short cracks it has the annoying property of being anchored at the origin which severely restricts the flexibility of the curve fitting.

The Kemeny and Cook models produced reasonably good fits to the propagation data from the small holes ($R \leq 30$ mm) but could not account for the almost unstable propagation shown in the larger holes.

The propagation trends demonstrated by the lab data are quite complex. Concave up (strain hardening at an increasing rate) and down (strain hardening at a decreasing rate) trends are seen along with trends showing more than one inflection point. One single analytical model does not seem to be able to explain all these observed phenomenon even

though an individual model may explain the trend observed in a single data set. The different boundary conditions for the analytical models (infinite boundaries) and the laboratory samples (finite boundaries) is a likely candidate responsible for the poor performance of the analytical models in representing the trends of the laboratory data. Overall, the analytical models in the literature do not seem very well suited to modeling this size dependent data.

## 3.5 Size Effect

Size effect theories can be split into two broad categories: (i) statistical size effect and (ii) energy approaches. In the statistical theories a material is considered to be inhomogeneous, containing localized zones of weakness. In the energy approaches a larger structure is assumed to consume a greater amount of strain energy to generate the fracture. This is similar to the gradient-based or stress averaging approaches presented earlier (e.g., Lajtai's model [56]) where stresses are assumed to become redistributed in a fixed-size fracture process zone.

Two important size effect models are discussed in this section: Bažant's energy-based size effect law and Carpinteri's multifractal scaling law. Following this the author develops several new empirical, analytical models to represent the behavior shown by the primary fracture propagation laboratory data. The section on size effect is concluded with a general discussion on statistical size effect.

### 3.5.1 Bažant Model

Bažant's [3] size effect model is considered to be one of the most important contributions to fracture mechanics. In concrete and rocks, it is known that fracture is preceded by a zone of microcracking ahead of the tip of a continuous crack. In this zone, known as the process zone, high stresses are redistributed resulting in nonlinear behavior immediately ahead of the crack tip. Bažant states that this type of fracture may be modeled as the propagation of a band of uniformly and continuously distributed (smeared) cracks with a fixed width

at the fracture front. Based on energy considerations at the propagating crack band front, Bažant derived the following relation

$$\sigma_N = \frac{B f_t}{\sqrt{1 + \lambda/\lambda_0}} \tag{3.21}$$

which can be linearized to get

$$\left(\frac{f_t}{\sigma_N}\right)^2 = \frac{1}{B^2} + \frac{1}{B^2 \lambda_0}\lambda \tag{3.22}$$
$$Y = a + b\lambda$$

In these equations $\sigma_N$ is the nominal stress at failure characterizing the stress state at a certain critical point of the structure (i.e., the crack initiation stress). $f_t$ is the direct tensile strength of the sample. $\lambda$ is a parameter describing the "relative structure size". In this case $\lambda = $ cavity size divided by the grain size. $B$ and $\lambda_0$ are fitting parameters.

Bažant states that to separate size effect from other influences, one must consider structures of different sizes but geometrically similar shapes. For his derivations he considers two geometrically similar structures with a fracture originating at a weak spot in the side (Figure 3.36). Both structures are geometrically similar because they have the same $a_0/d$ ratios. The crack band width, $h$, is considered to be a material property and is therefore constant and independent of the structure size. In his model Bažant postulates that the formation of the crack band relieves stress and releases strain energy into the fracture front (shown as the light grey strip in Figure 3.36). If the fracture increases in length by $\Delta a$ in both structures this zone of strain energy release is larger for the larger structure. Assuming that the energy dissipated by the fractures is constant it can be easily seen that the fracture in the larger structure will propagate more readily than the fracture in the smaller structure.

After separating the Cold Spring granite propagation data into geometrically similar groups, that is each group has a constant $L/R$ ratio as shown in Figure 3.37, Bažant's linear equation 3.22 can be applied. The results are shown in Figure 3.38. In general, the
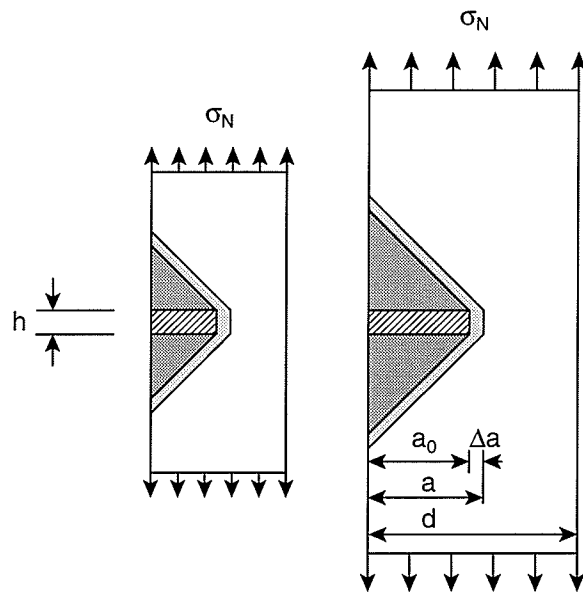
propagating crack band

zone where strain energy has already been released

zone from which strain energy is released into
the fracture front when fracture grows by $\Delta a$

Figure 3.36: Geometry for Bažant's size effect model.
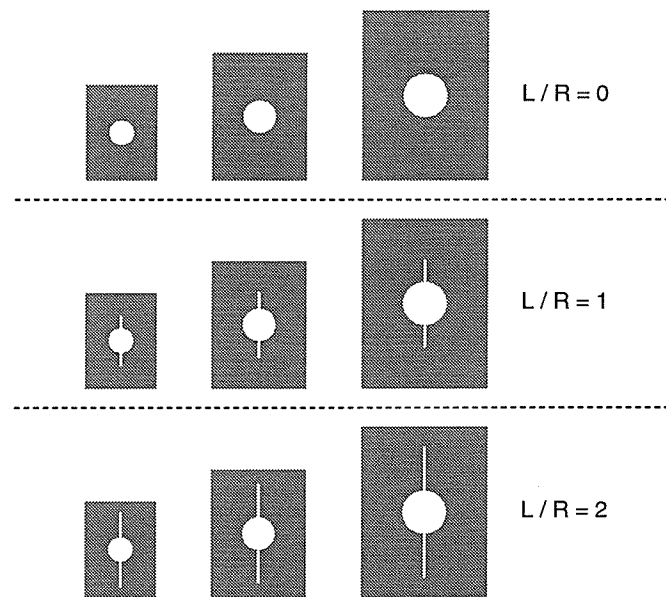
Figure 3.37: Laboratory tests grouped into geometrically similar structures.

least squares fit becomes progressively better as the fracture grows until it reaches the point where $L/R = 1.25$. From this point on the fit becomes worse.

Because Bažant's model is a crack propagation model, the poor fit obtained when the cracks are initiating is not unexpected. Also, as the primary cracks grow, the tendency for remote fractures to form increases. In the small samples the remote fractures initiated at a normalized primary fracture length of approximately $L/R = 2$. Once the remote fractures initiate the structures are no longer geometrically similar (some have only primary fractures and some have both primary and remote fractures). Thus after the remotes appear there is no longer a basis for comparison of the samples. Nonetheless, using the parameters from the curve fitting we can create an axial load versus normalized crack length plot (Figure 3.39) and see that a very good match is obtained.

### 3.5.2 Carpinteri Model

Carpinteri et al. [16] noted that in concrete structures, when considering scale variations over several orders of magnitude, there is evidence that the tensile strength appears to approach a

Figure 3.38: Bažant's size effect model fit to Cold Spring granite primary crack initiation and propagation data. $Ra^2$ = degree of freedom adjusted coefficient of determination.

Figure 3.39: Predicted primary crack propagation trends for Cold Spring granite using Bažant's model.

constant finite value (non-zero) at large scales. It was previously noted, that at large scales, Bažant's size effect law is governed by LEFM and predicts zero tensile strength for structures approaching an infinite size. Carpinteri states that Bažant's underlying hypothesis for his size effect law is responsible for the anomalous strength behavior demonstrated in his size effect law.

In his formulation Bažant assumed notched specimens were loaded in tension. The notch, which is responsible for the stress singularity, is scaled proportionally to the structure size. Carpinteri disagrees on this point and states that when applying Bažant's size effect law to unnotched specimens the size of the characteristic flaw, which is responsible for crack propagation, should be independent of specimen size. To take into account the variable influence of the characteristic flaw size Kim et al. [52] replaced $\lambda_0$ in Bažant's model (equation 3.21) with a monotonically decreasing function of ratio $a/d$ where $a$ is the characteristic flaw size and $d$ is the structure size. This leads to larger values for $\lambda_0$ as the specimen size increases resulting in a less severe reduction in strength as the structure size increases. Because of the difficulty in deriving the function for $\lambda_0$, Kim and Eo [51] and Bažant et al. [5] proposed an empirical "modified size effect law" which included a term, $\sigma_0$, to produce a more realistic nonzero asymptote at large scales. The modified law is,

$$\sigma_N = \frac{Bf_t}{\sqrt{1 + \lambda/\lambda_0}} + \sigma_0 \tag{3.23}$$

This equation became too cumbersome to fit as a three-parameter model and it was decided to set $\sigma_0$ equal to the tensile strength of Cold Spring granite as a lower bound. The results of curve fitting to the grouped data and predicted propagation trends are shown in Figures 3.40 and 3.41 respectively. Judging from the $Ra^2$ statistic in Figures 3.38 and 3.40 the fit is slightly worse than Bažant's original model.

Carpinteri approaches the size effect problem by assuming the material strength behaves according to a multifractal scaling law. At small scales the material is assumed to contain a self-similar distribution of Griffith cracks. At larger scales this disorder is no longer visible
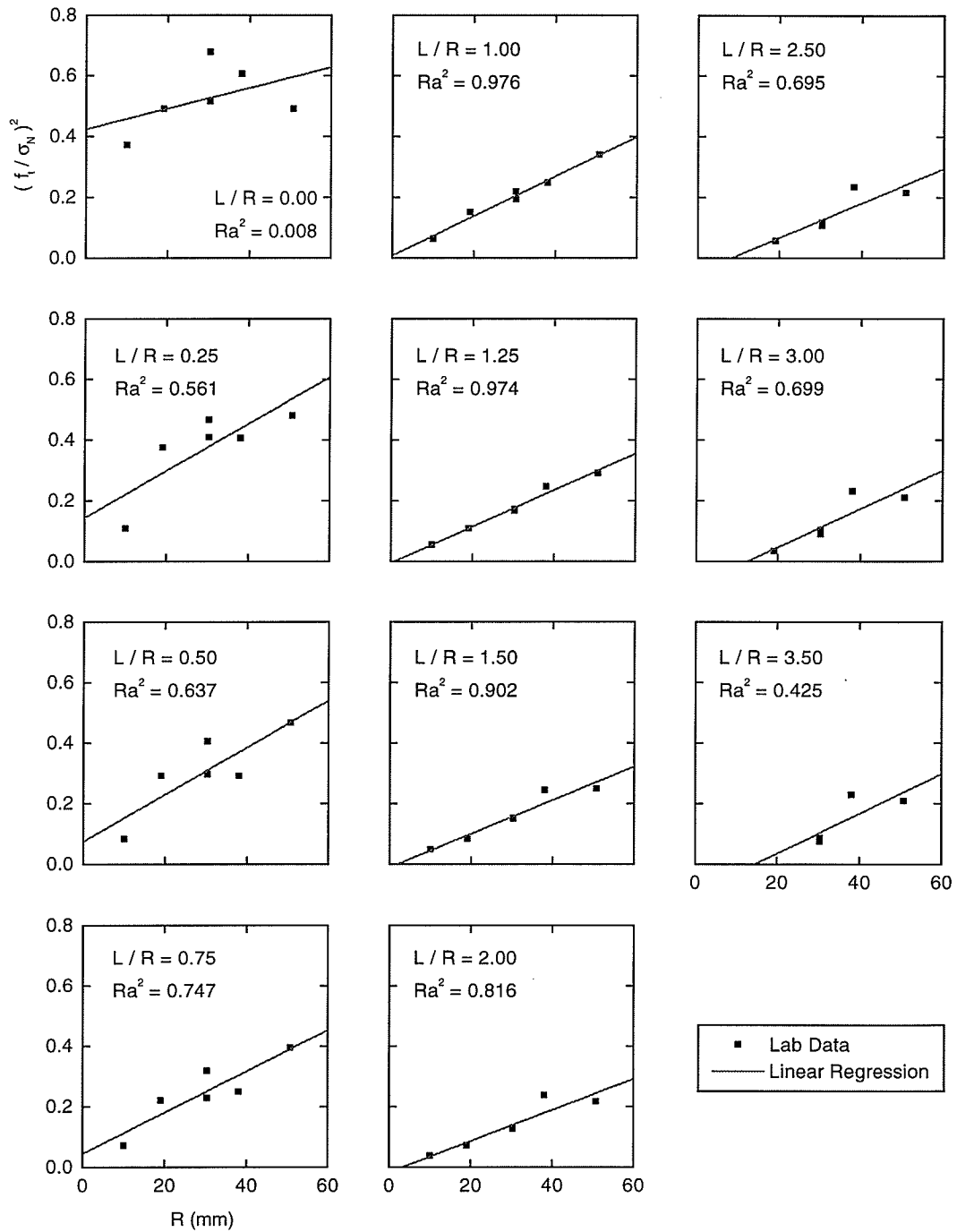
Figure 3.40: Bažant's modified size effect model fit to Cold Spring granite primary crack initiation and propagation data. $Ra^2$ = degree of freedom adjusted coefficient of determination.
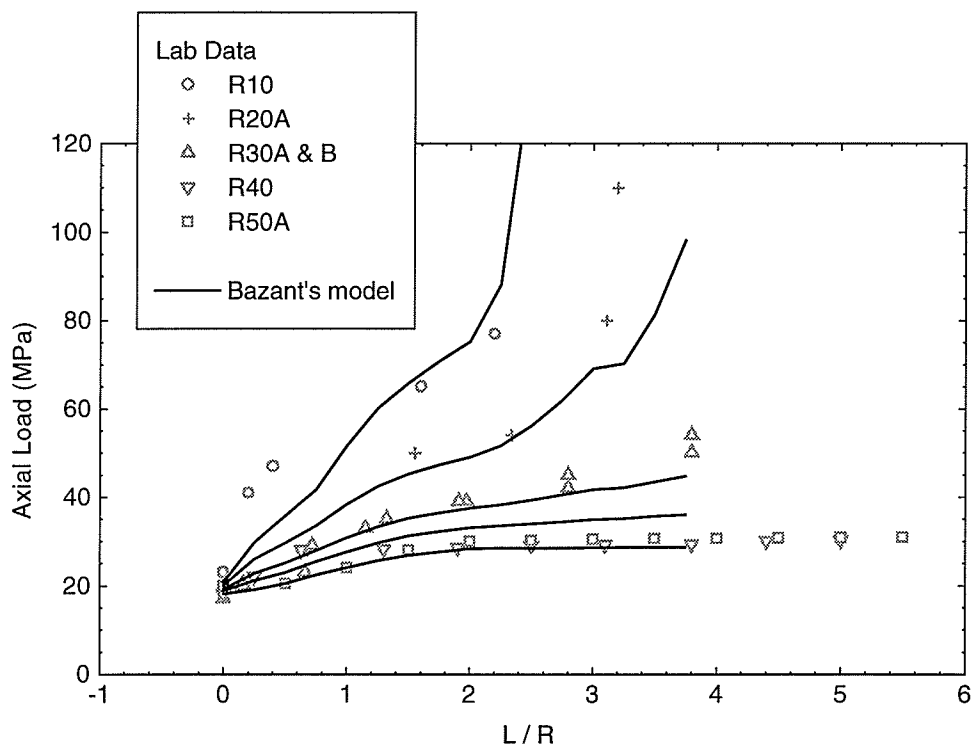
Figure 3.41: Predicted primary crack propagation trends for Cold Spring granite using Bažant's modified size effect model.

because of the limited size of the defects and heterogeneities in the material. This is the homogeneous regime. Carpinteri states that there may be a dimensional transition from disorder to order and bases the following model on these concepts.

$$\sigma_N = \sqrt{A + \frac{B}{d}} \qquad (3.24)$$

$\sigma_N$ is the nominal tensile strength, $d$ is the characteristic structure size, A is a constant with units of $(MPa)^2$, and $B$ is a constant with units of $(MPa\sqrt{m})^2$. The general shape of equation 3.24 is shown in Figure 3.42. Unlike Bažant's model this model approaches a horizontal asymptote of $\sqrt{A}$ at large structure sizes and predicts infinite tensile strength for structure sizes approaching zero.

Taking the logarithm of equation 3.24 produces,

$$\log \sigma_N = \frac{1}{2} \log \left( A + \frac{B}{10^X} \right) \qquad (3.25)$$

In this equation $X = \log d$. Figure 3.42 also shows the general form of this equation plotted on log-log scale. This curve has two asymptotes; one corresponding to the fractal or disordered regime and the other corresponding to the ordered or homogeneous regime. An interesting feature of this model is that the slope of the fractal regime asymptote is $-1/2$ which implies that LEFM governs the material strength at small scales. Carpinteri maintains that this is consistent with Griffith's pioneering work. The Griffith mode of failure, which is governed by a $1/\sqrt{c}$ stress singularity (slope $= -1/2$ on a logarithmic scale), becomes the governing failure mechanism when the structure size approaches zero (i.e., no crack interaction problems). The high strengths predicted with Carpinteri's model at small scales is also consistent with Griffith's tests on the strength of glass fibers (tensile strength was found to increase dramatically as the diameter of the glass fiber was reduced).

Fitting equation 3.24 to the "grouped" Cold Spring granite crack propagation data produces a very good fit up to about an $L/R$ ratio of 2.5 (Figure 3.43). After this point the fit degrades. The goodness of fit follows the same general trend shown by fitting Bažant's
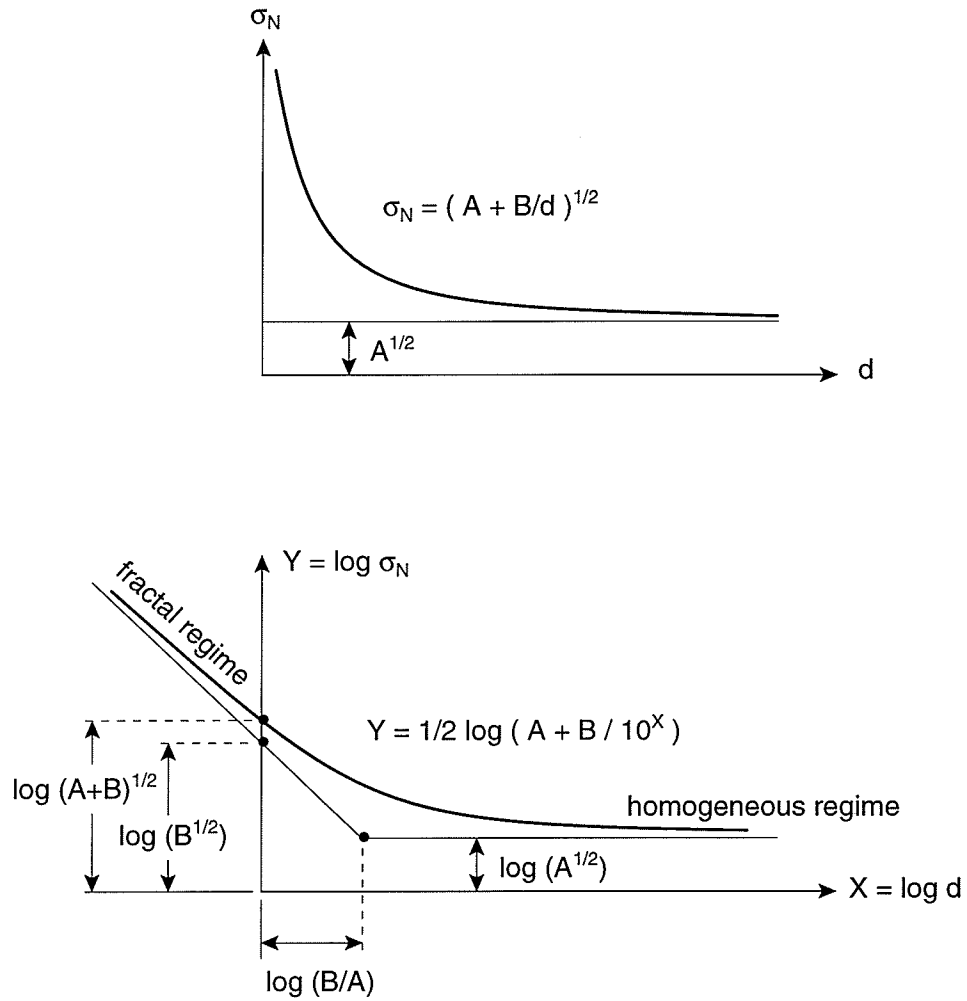
Figure 3.42: Carpinteri's multifractal scaling law linear axes (top) and log-log axes (bottom) (modified from [16]).

models; the fit becomes progressively better as the crack grows and then degrades. The predicted primary crack propagation trends from this model are shown in Figure 3.44.

A problem becomes apparent after looking at the curve fitting results. Parameter $A$ (the controlling value for the horizontal asymptote) takes on negative values once the normalized crack length exceeds $L/R = 0.25$. It is therefore impossible to determine where the transition occurs from a fractal to homogeneous regime using this model. Judging from the curves in Figure 3.43 it appears that Cold Spring granite is largely governed by the randomness of the fractal regime since a horizontal asymptote is not even approached by the curve fitting.

In the models investigated so far a multitude of fitting parameters had to be determined to fit the entire range of crack lengths. In the case of the Cold Spring granite data, the data was split into 21 geometrically similar groups ($L/R$ increments of 0.25 were used). For the Carpinteri model this curve fitting exercise required the determination of 42 parameters (21 $A$'s and $B$'s). Obviously it would be beneficial to find a functional relation between a model's parameters and normalized crack length ($L/R$). This curve finding exercise was attempted here and it was found that a simple relation did indeed exist between Carpinteri model parameters ($A$ and $B$) and normalized crack length ($L/R$). These are shown in Figure 3.45. Figure 3.46 shows the predicted crack propagation trends using these functional relations for model parameters $A$ and $B$; a very good fit once again. The author was unsuccessful at finding a functional relation between model parameters and normalized crack length for Bažant's models.

Up to this point it had been found that analytical crack initiation models were able to represent the behavior of the laboratory data. On the other hand, analytical crack propagation models were, for the most part, inadequate. Size effect models produced the best results, so far, in representing primary fracture behavior. However, the size effect models were cumbersome to use because of the large number of parameter values to determine and the lack of extrapolation and interpolation potential of the models. Due to the deficiencies
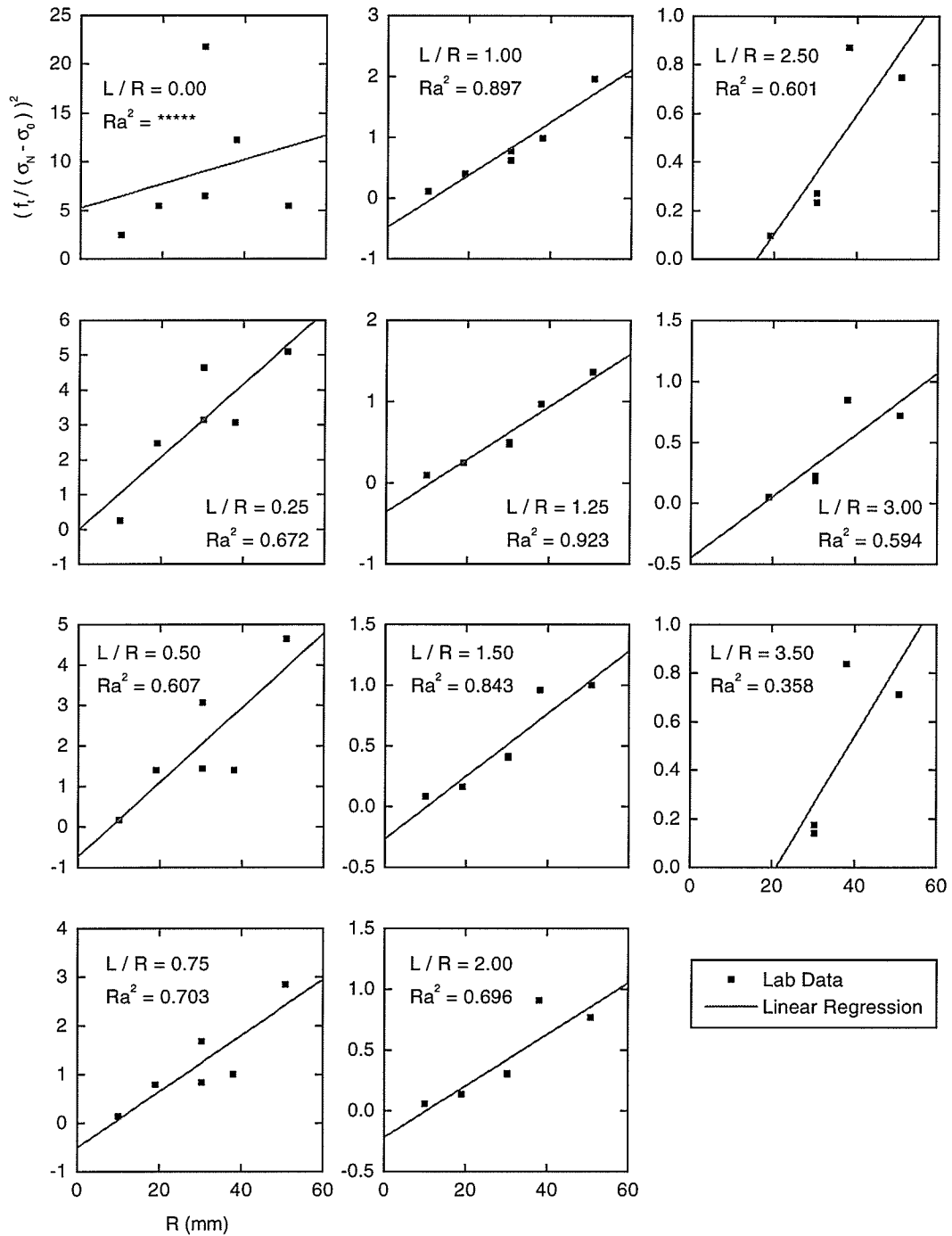
Figure 3.43: Carpinteri's size effect model fit to Cold Spring granite primary crack initiation and propagation data. $Ra^2$ = degree of freedom adjusted coefficient of determination.
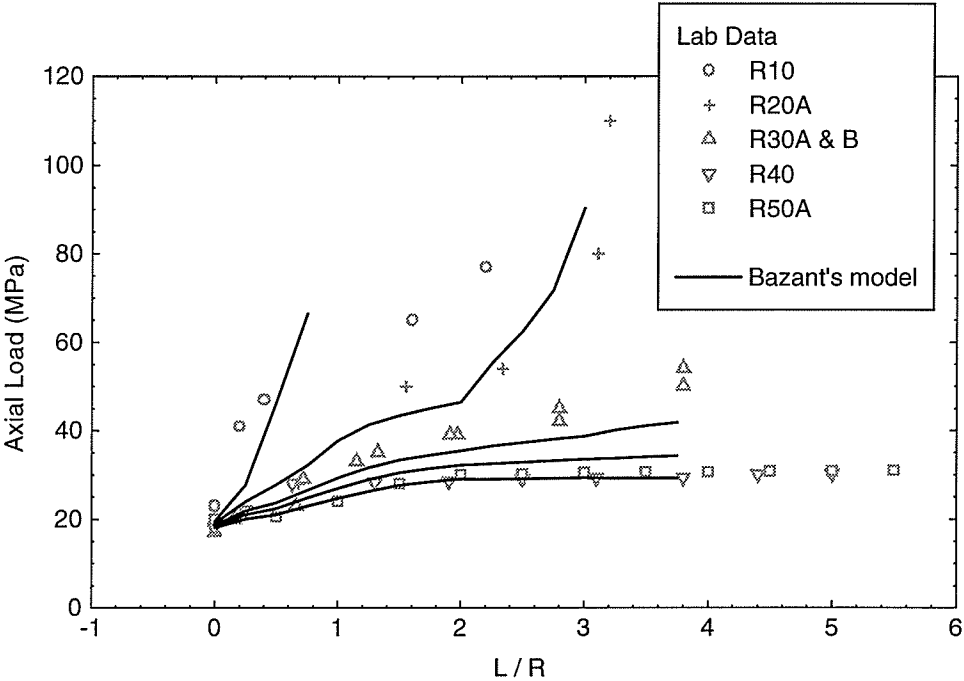
Figure 3.44: Predicted primary crack propagation trends for Cold Spring granite using Carpinteri's model.
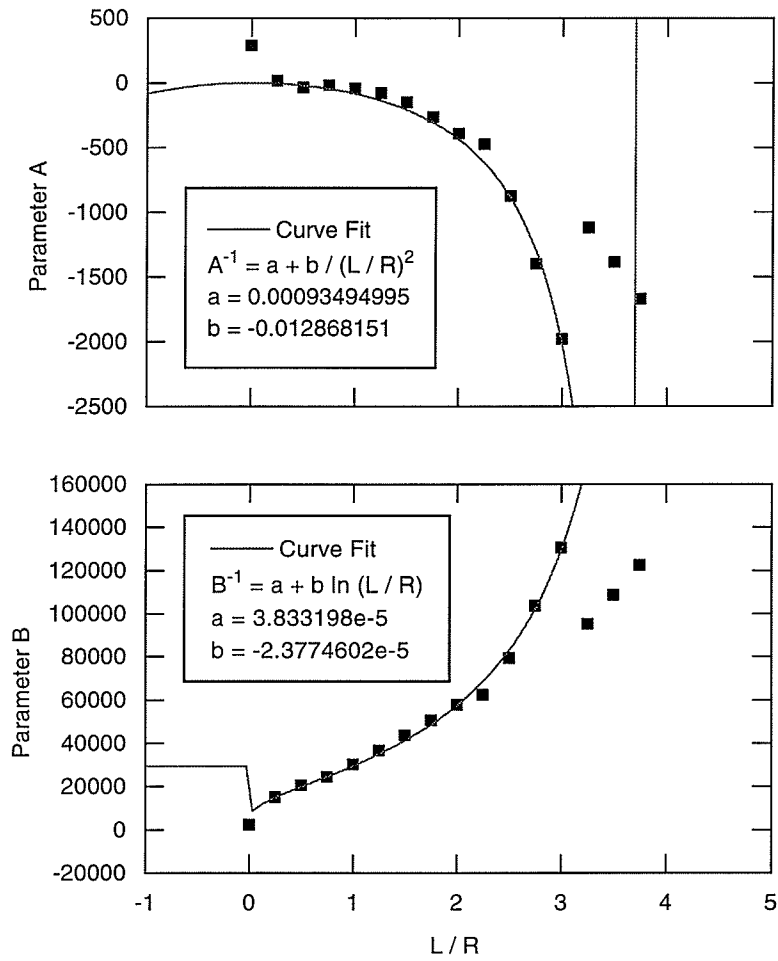
Figure 3.45: Carpinteri model parameters $A$ and $B$ and regression results versus normalized crack length for Cold Spring granite crack propagation data.

Figure 3.46: Predicted primary crack propagation trends for Cold Spring granite using Carpinteri's model with parameters $A$ and $B$ determined by functions of $L/R$.

and inconvenience of the primary fracture propagation and size effect models it was the author's goal to find a simple analytical relation to represent primary fracture behavior. Two empirical primary fracture propagation models are introduced in the following two sections.

### 3.5.3 Griffith Model Revisited

If crack propagation is assumed to be a series of crack initiation events (which it is) then the geometrically similar groupings of Figure 3.37 could represent crack initiation events from different structures. Choosing any single structure geometry (e.g., $L/R = 2$) it can be readily noticed that the crack initiation from this structure shows a marked size effect. The size effect from each structure typically shows the same type of trend demonstrated by the crack initiation (from a circular hole, $L/R = 0$) data that was studied at the start of this section (see Figure 3.12, page 38); a negative exponential type of behavior. One of the simplest models that worked with the crack initiation data was Griffith's original energy balance equation. If the simplified version of the Griffith equation, given below,

$$\sigma = \frac{\sqrt{2E\gamma_s}}{\sqrt{\pi c}} = \frac{m}{\sqrt{R}} \tag{3.26}$$

is fit to the grouped crack propagation data a reasonable fit is produced (Figure 3.47). The predicted crack propagation trends from this model are shown in Figure 3.48.

Taking things a step further it is possible to find a simple functional relation between parameter $m$ and $L/R$ as is illustrated in Figure 3.49. The primary crack propagation trends for Cold Spring granite are easily determined when the simple formula for parameter $m$ (given in Figure 3.49) is substituted into equation 3.26. The results are shown in Figure 3.50.

### 3.5.4 Exponential Model Revisited

A similar curve fitting exercise as was done in the last section is repeated here with the same exponential model that was used in the crack initiation curve fitting (see page 37).
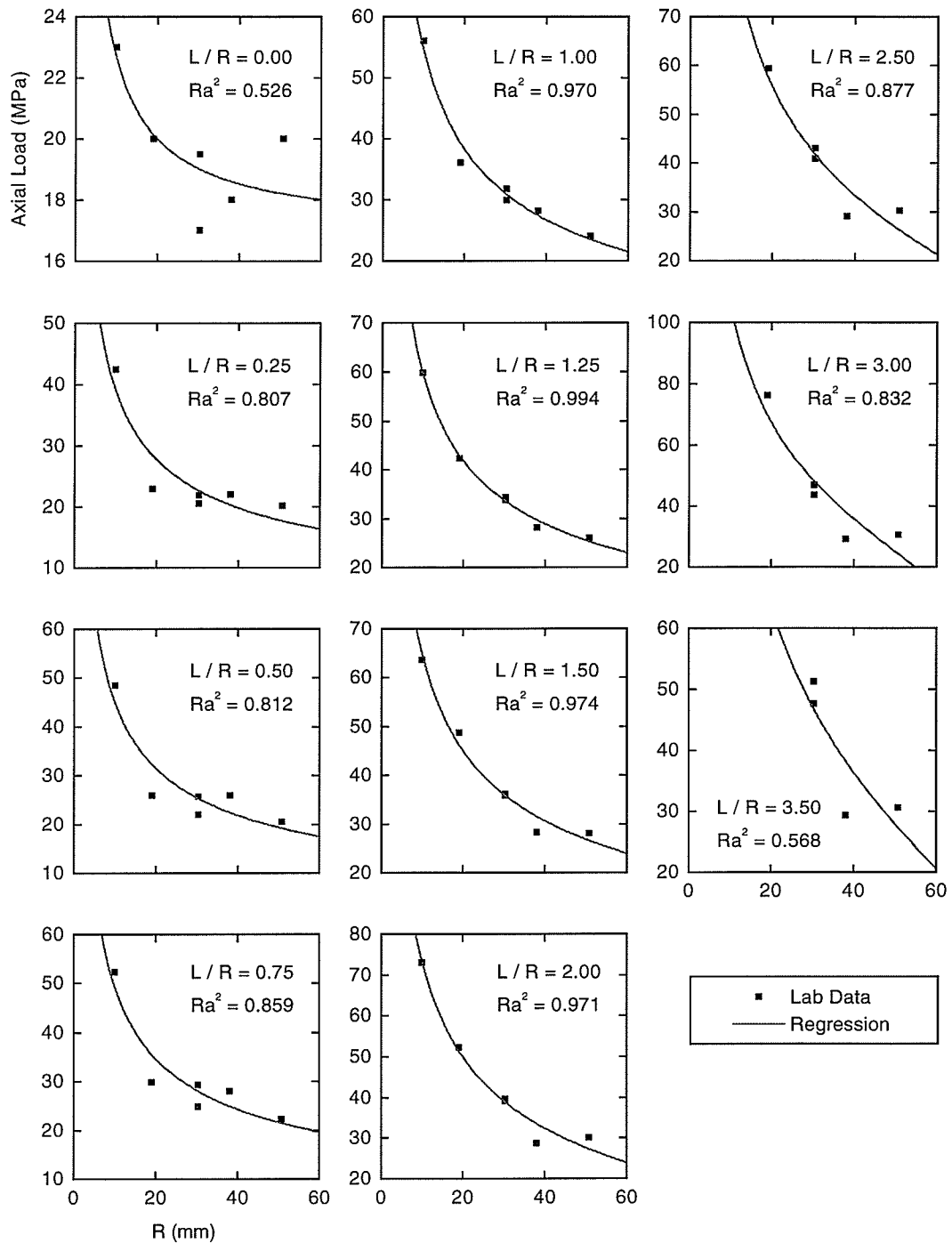
Figure 3.47: Griffith model fit to Cold Spring granite primary crack initiation and propagation data. $Ra^2$ = degree of freedom adjusted coefficient of determination. ***** indicates negative $Ra^2$.
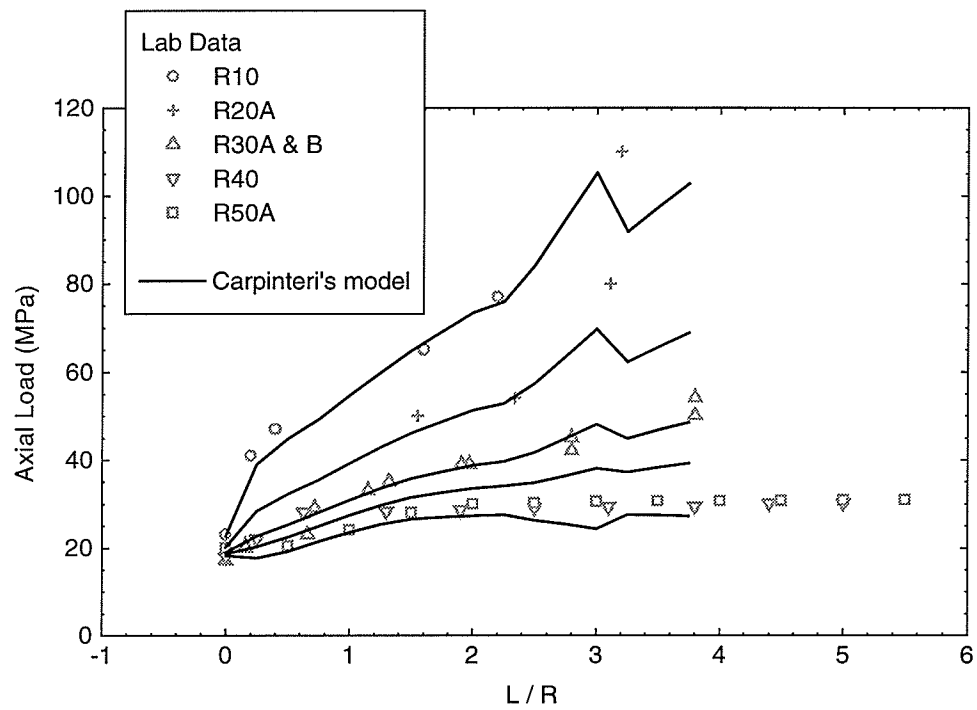
Figure 3.48:  Predicted primary crack propagation trends for Cold Spring granite using Griffith model.
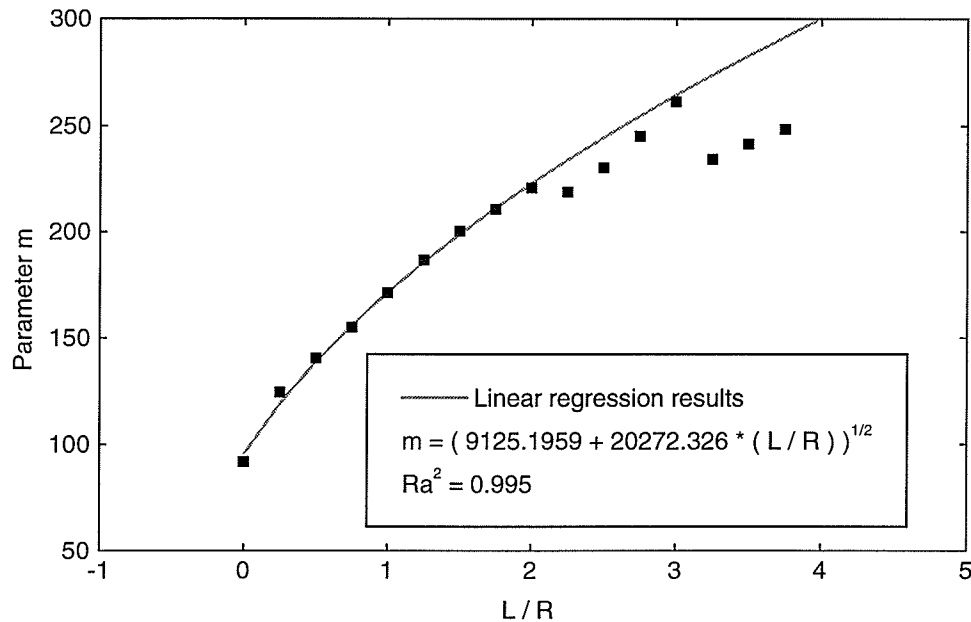
Figure 3.49: Griffith parameter $m$ versus normalized crack length for Cold Spring granite crack propagation data. $Ra^2$ = degree of freedom adjusted coefficient of determination. Curve fit with $L/R \leq 2$ data only.

The exponential model is given as

$$\sigma = a + \frac{b}{e^{R/c}} \tag{3.27}$$

Unlike Bažant's or Carpinteri's models the exponential equation is bounded by finite values at both ends of the size spectrum. The model fit the grouped data extremely well (Figure 3.51) and resulted in an excellent fit to the propagation data (Figure 3.52). However, 48 parameters were required (16 $a$'s, $b$'s, and $c$'s were determined). No obvious relation could be found between $L/R$ and parameters $a, b, c$.

It was noticed that parameters $a$ and $b$ varied the least (probably because they are constrained by the uniaxial tensile and compressive strengths of the granite). By fixing these parameters at their mean values ($a = 23$ and $b = 140$ MPa) a linear relation between $R$ and parameter $c$ is obtained and is shown in Figure 3.53. Using this model the resulting predicted crack propagation trends are not too far off for crack lengths of $L/R \leq 3$ (Figure 3.54). An interesting feature of this one parameter model is that it has the ability to produce both
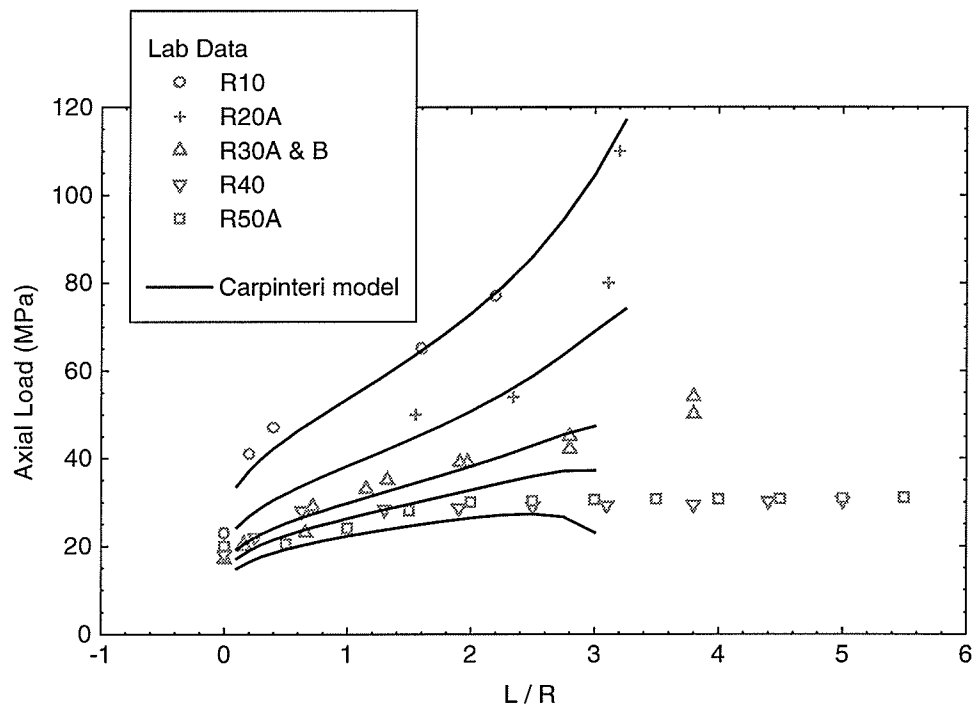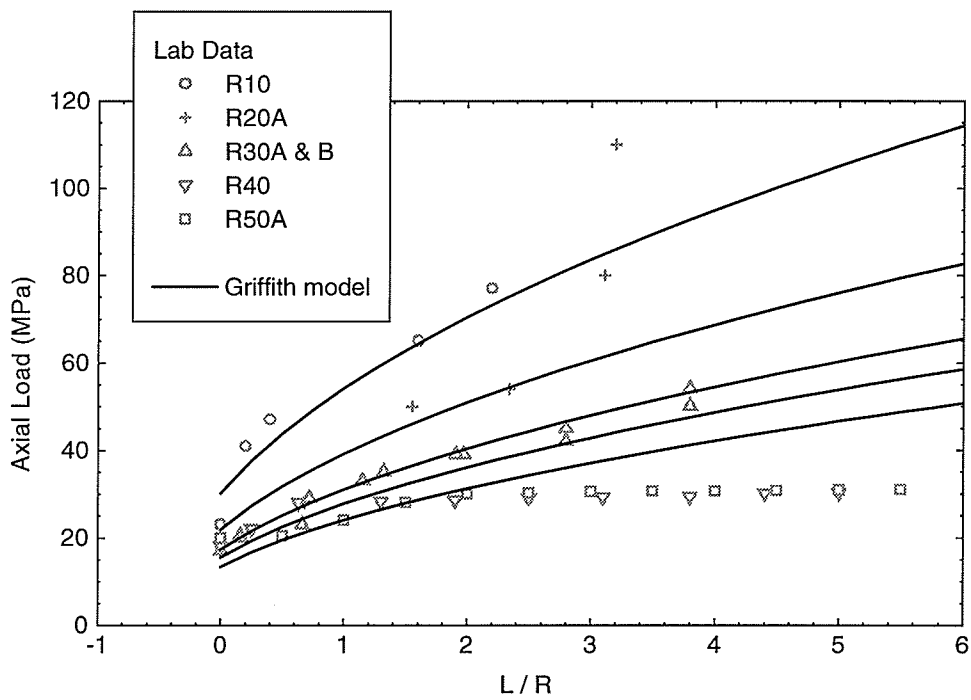
Figure 3.50: Predicted primary crack propagation trends for Cold Spring granite using Griffith model with parameter $m$ a function of $L/R$.
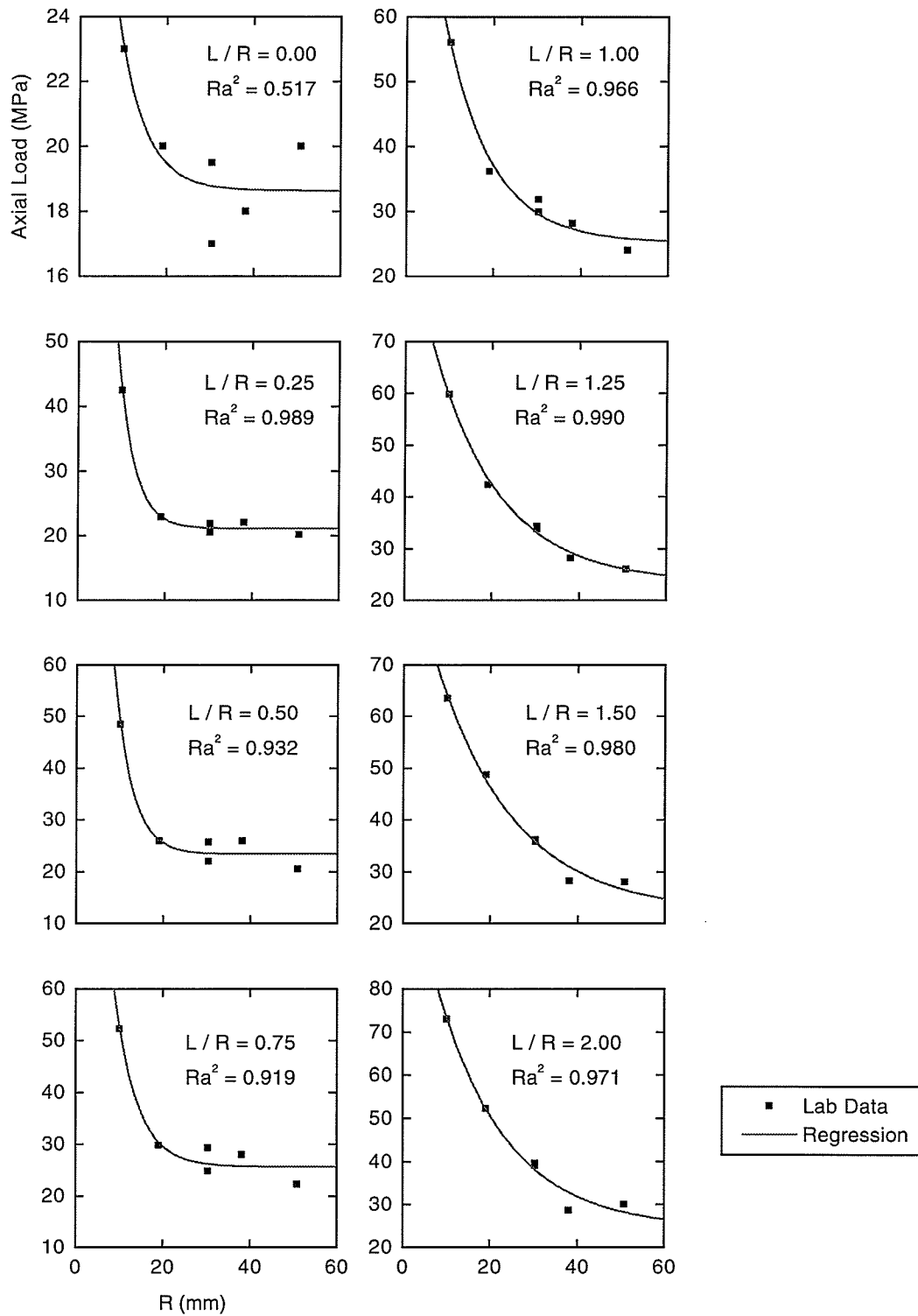
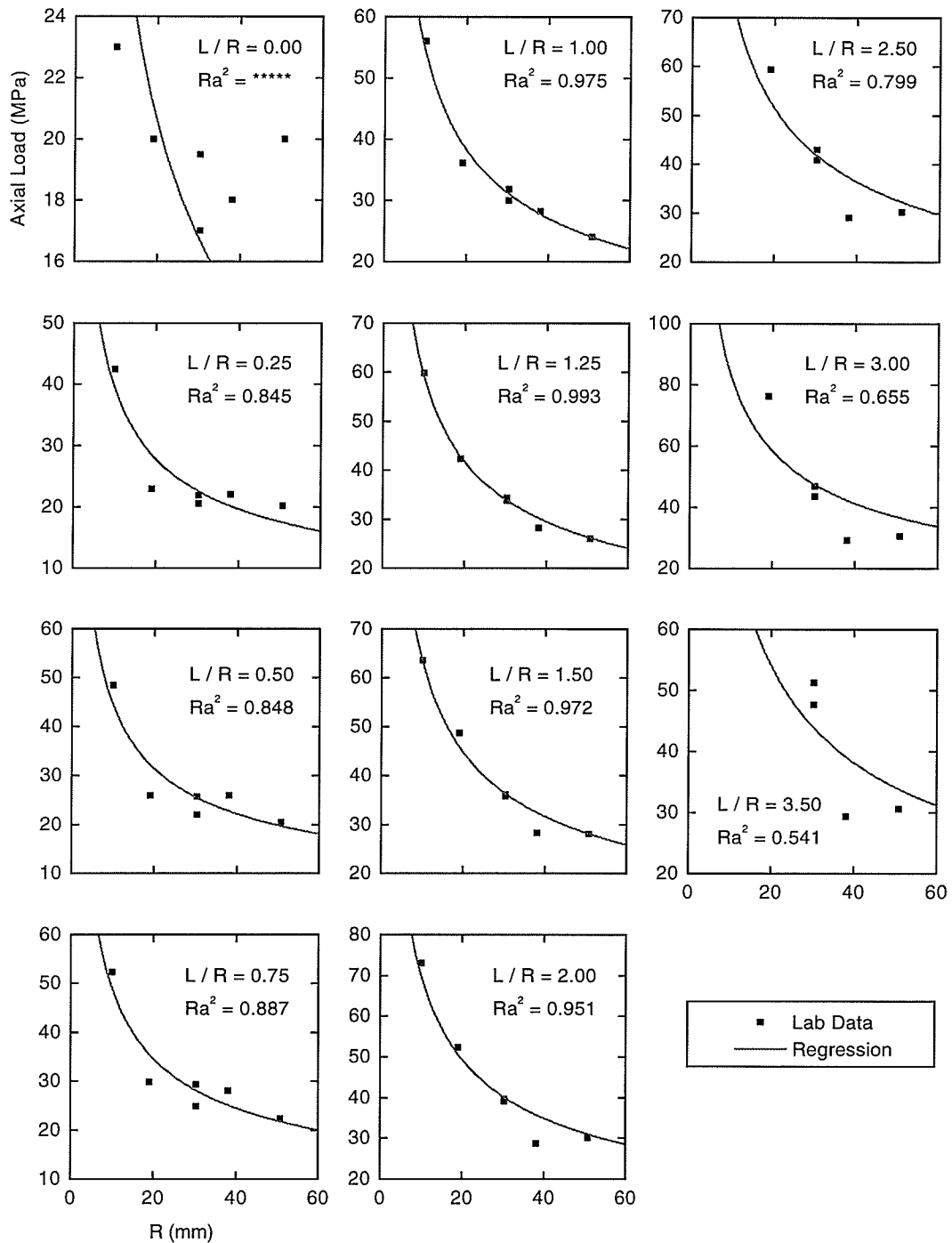Figure 3.51: Three-parameter exponential model fit to Cold Spring granite primary crack initiation and propagation data. $Ra^2$ = degree of freedom adjusted coefficient of determination. ***** indicates negative $Ra^2$.
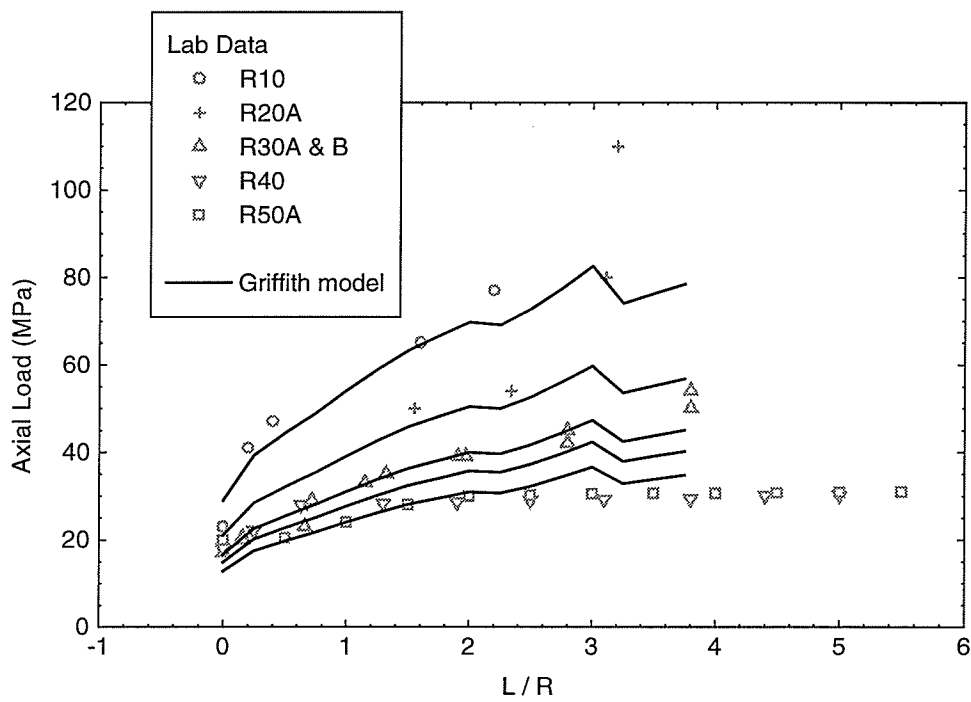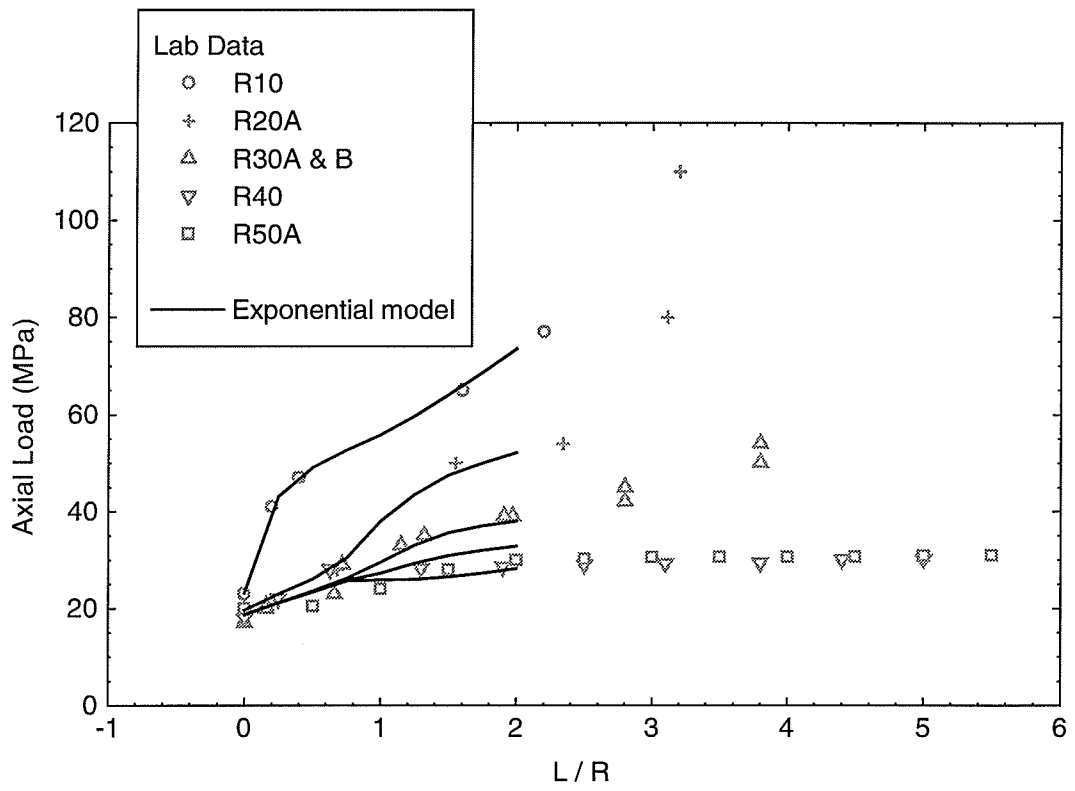
Figure 3.52: Predicted primary crack propagation trends for Cold Spring granite using 3-parameter exponential model.
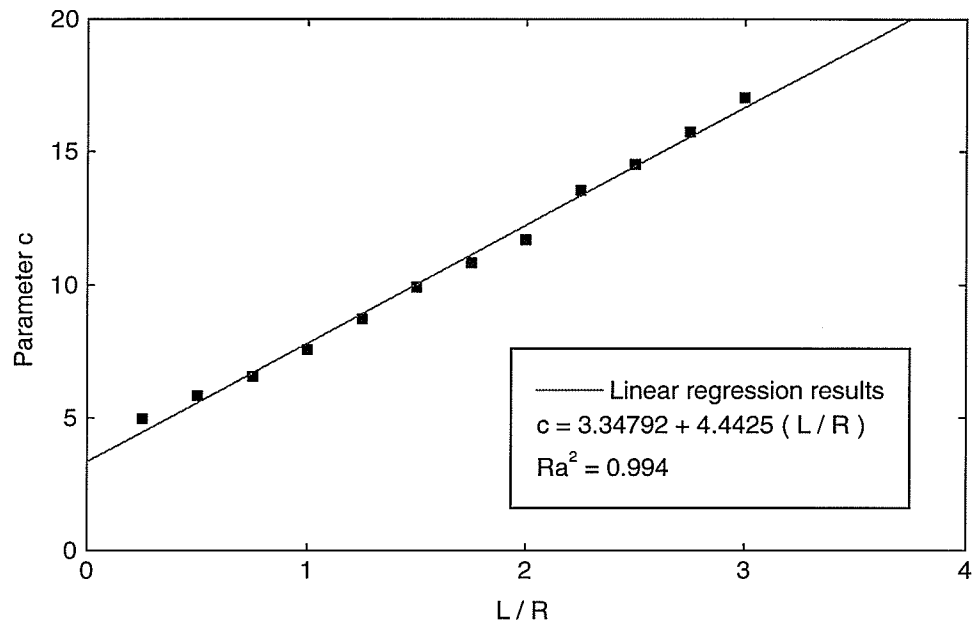
Figure 3.53: Exponential function parameter $c$ versus normalized crack length for Cold Spring granite crack propagation data. $Ra^2$ = degree of freedom adjusted coefficient of determination.

concave up and concave down curves.

### 3.5.5 Statistical Size Effect

This section touches on a few aspects of statistical size effect theories that have not yet been discussed. Bažant [3] actually compares fracture mechanics approaches with a statistical approach. A summary of his discussion is given here.

Since rock is a heterogeneous material composed of mineral grains of varying strength its strength varies randomly throughout the structure. This strength variation is assumed to be independent of structure size. However, stress gradients usually vary inversely with structure size. In Figure 3.55, for example, the region of high stress is larger in the larger structure. Therefore the chance of encountering a region of low strength is greater in the larger structure. Because of this, the larger structure is apt to fail prior to the smaller structure if both are subjected to identical loads. Therefore there is an apparent reduction
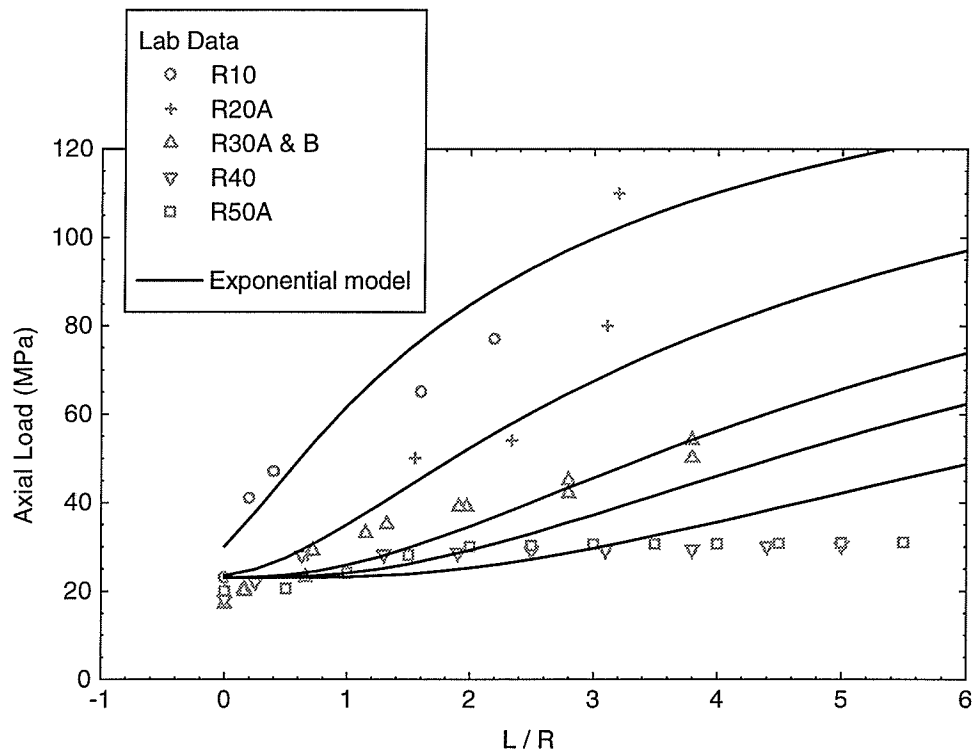
Figure 3.54: Predicted primary crack propagation trends for Cold Spring granite using 3-parameter exponential curve model with parameters $a$ and $b$ fixed at $a = 23$ and $b = 140$ and parameter $c$ a function of $L/R$.
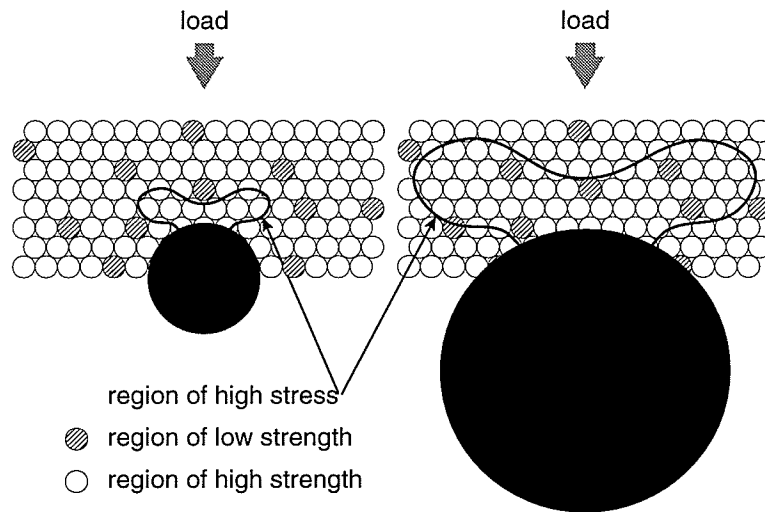
Figure 3.55: Stress gradients around geometrically similar structures subjected to identical loads.

in strength with increasing structure size. When the region of high stress becomes much larger than the regions of low strength, as is the case for very large structures, the decline in strength stops and reaches a plateau. Therefore, in a statistical size effect model we would expect the strength to approach a horizontal asymptote as structure size increased (Figure 3.56).

In the classical fracture mechanics models $\sigma \propto 1/\sqrt{R}$. On a log-log scale this type of function would produce a straight line with slope $= -1/2$ as is shown in Figure 3.56. Nonlinear fracture mechanics models, such as Bažant's [3] model has an upper limiting value for tensile strength at small scales and approaches the classical fracture mechanics solution at large scales (Figure 3.56).

It is difficult to determine which size effect law governs a specific material due to the lack of data at large scales. However, if the Cold Spring granite crack initiation data is plotted on a log-log scale (Figure 3.57) a statistical size effect seems to be the driving mechanism. On the other hand, the opposite argument could be made for the Cold Spring granite propagation data shown in Figure 3.58. Additional large scale data is once again
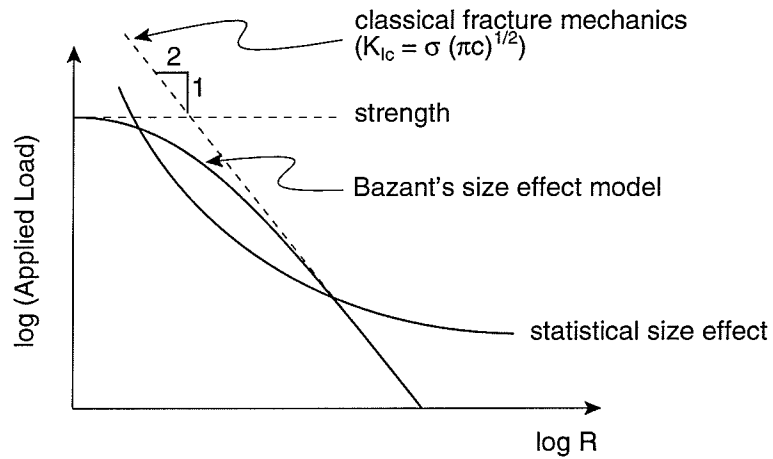
Figure 3.56: Statistical versus fracture mechanics size effect models.
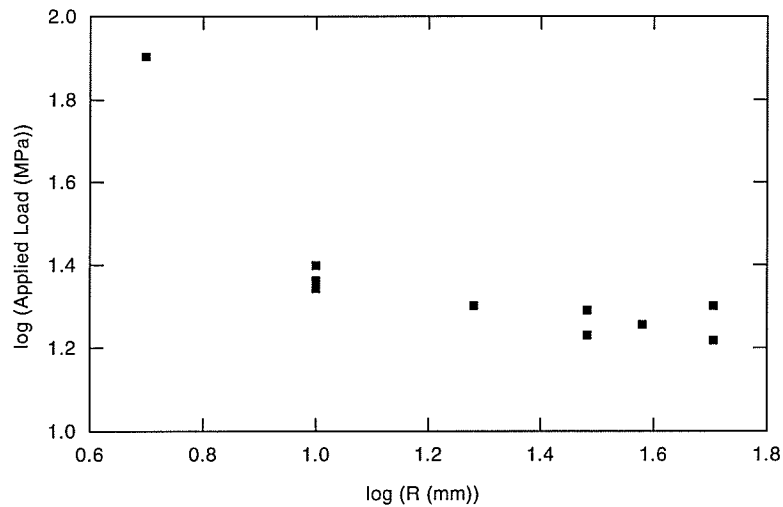


Figure 3.57: Log-log plot of Cold Spring granite crack initiation data.

required to see if the structures approach an asymptotic value for strength or not.

In the classical Weibull [88] strength theory, the strength size relation is as follows:

$$\left(\frac{P_1}{P_2}\right)^m = \left(\frac{V_2}{V_1}\right) \tag{3.28}$$

In this theory, also known as the weakest link theory, there is an inverse relation between the strength of a sample $(P)$ and its volume $(V)$. An enormous volume of work exists on this
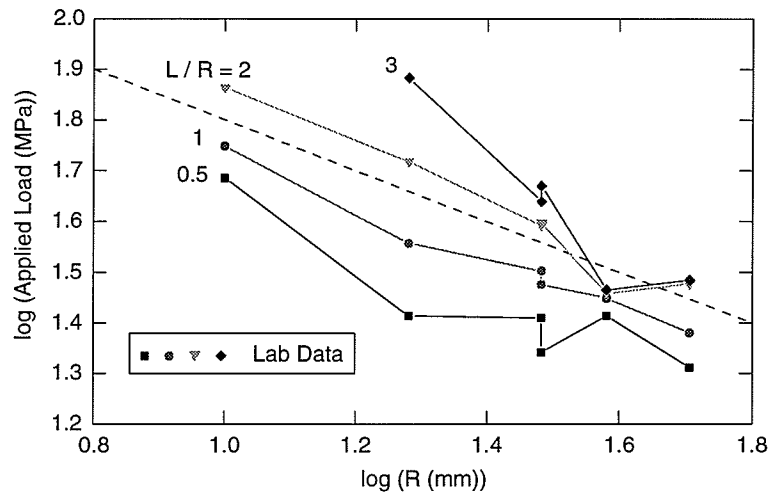
Figure 3.58: Log-log plot of Cold Spring granite crack propagation data. The dashed line has a slope of $-1/2$ showing the general trend of a material governed by a classical fracture mechanics law.

theory and its application. In applications to granite, Lundborg [66] tested granite samples in compression and Brazilian loading configurations and found that the strength values obtained coincided with the Weibull theory. Lajtai [58, 64, 65, 60] has also successfully applied this theory to the time-dependent behavior exhibited by rock subjected to sustained loads. The basic premise behind this statistical theory is the same as was described by Bažant at the start of this section. That is, there is a greater chance of finding "weak links" in a large volume of material than in a small volume. Gonano's model, at the start of this chapter, takes the same form as the Weibull model and produced a reasonably good match to the lab data. Applying this empirical relation to the fracture propagation results (as was done for Bažant's, Carpinteri's, and the other empirical models) would undoubtedly produce another reasonable fit to the propagation data. However, this curve fitting exercise is left as future work.

## 3.6 Numerical Fracture Models

Looking back at Irwin's and Westergaard's derivations for stresses near a crack tip (equation 3.3 and Figure 3.4) we see that as $r \rightarrow 0$ the stress at the fracture tip approaches infinity. This singularity can be mimicked in numerical models with quarter-point singularity crack tip elements [2]. Also, we see from equation 3.3 that two of the expressions relate the displacements $(u_x, u_y)$ near the crack tip to $K_I$. Hence, knowing the displacements near a crack tip (routinely calculated in displacement-based numerical models) we can calculate $K_I$ at the crack tip. These features are incorporated into two finite element codes, Wawrzynek and Ingraffea's FRANC2D [87] and Ayari's SIMEX [1], built specifically to model crack propagation problems.

A FRANC2D model was created of the primary crack circular hole geometry (Figure 3.59). The model consisted of a non-cohesive edge crack with a singularity crack tip element emanating from a circular hole. The mesh was composed of quadratic, triangular, isoparametric, elements with a rosette of eight quarter-point elements surrounding the crack tip. The crack actually has a finite width (Figure 3.60) which makes it sensitive to the compression parallel stress and causes $K_I$ at the propagating crack tip to eventually reach a constant, nonzero, value at some distance away from the circular void. Edge loading (applied force formulation) was applied at the platen boundaries. Half symmetry was used and the sample was allowed to slip laterally both at the platen and the $y = 0$ line of symmetry. The boundary conditions used are shown in Figure 3.61. Friction or non-slip platen boundaries were not considered in this modeling exercise because of the similar primary crack propagation trends shown by identically sized samples with different platen boundary conditions (samples J15S1, J15S2, and J15S3, used teflon, steel, and granite at the platens respectively with similar almost unstable primary crack propagation trends). Simulations were done using a linear elastic analysis and plane stress conditions. All modeling in this thesis is based on similar assumptions and loading conditions.
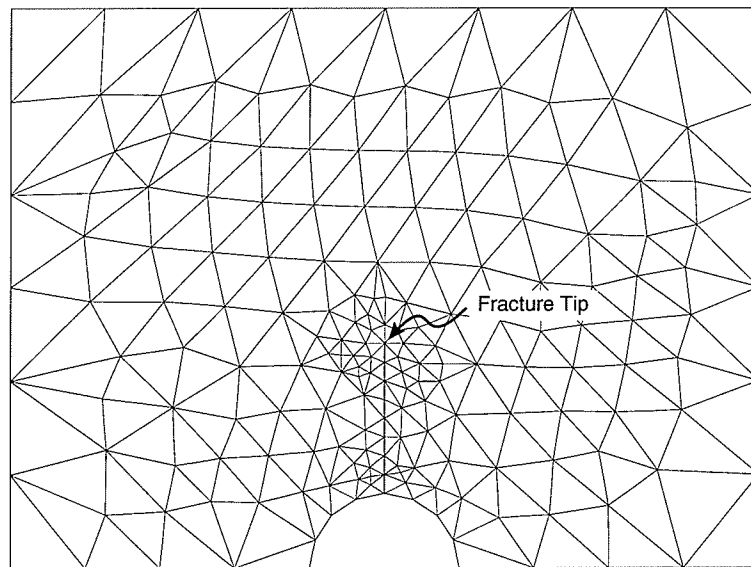
Figure 3.59: Example mesh generated by FRANC2D ($L/R = 2$).

In the case of modeling the rectangular block with circular opening geometry the application of a uniform force along the specimen loading surface will result in a non-uniform distribution of displacement along the loading surface. This is because the hole in the specimen reduces the effective stiffness in the central portion of the specimen resulting in more displacements along the center of the loading surfaces. However, this effect is unlikely to occur in the laboratory tests presented in this thesis where the Young's modulus of the steel loading platens is one to two orders of magnitude greater than that of the granite. In the numerical modeling the effect of these non-uniform displacements on primary fracture propagation can be reduced by increasing the specimen height. In hindsight an applied displacement formulation would probably represent the laboratory loading conditions much more realistically. However, as a first run at the problem an applied force formulation was used and the applied displacement simulations left for future work.

Before any calibration to the laboratory data was attempted, the FRANC2D model was used to evaluate potential boundary effects on the propagating crack. For this purpose the block dimensions in the FRANC2D model were incrementally increased until the solution
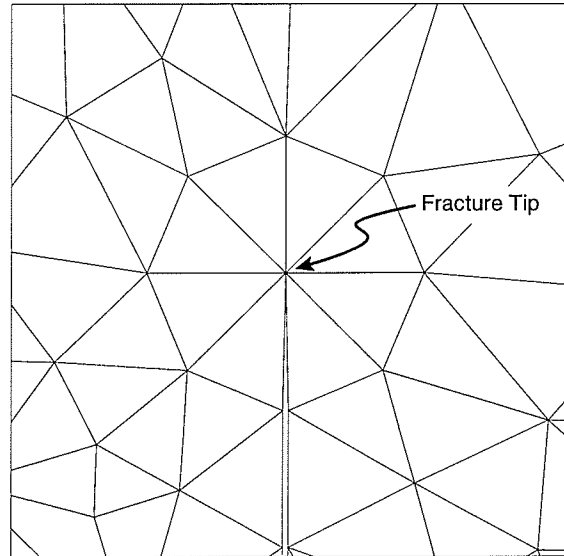
Figure 3.60: FRANC2D mesh showing crack tip detail.
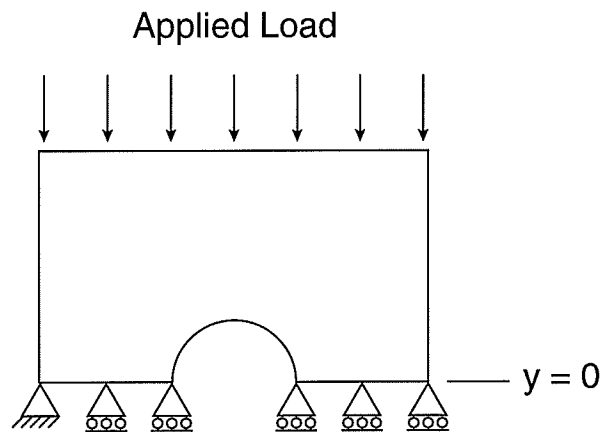


Figure 3.61: Boundary and loading conditions used in FRANC2D and SIMEX modeling.
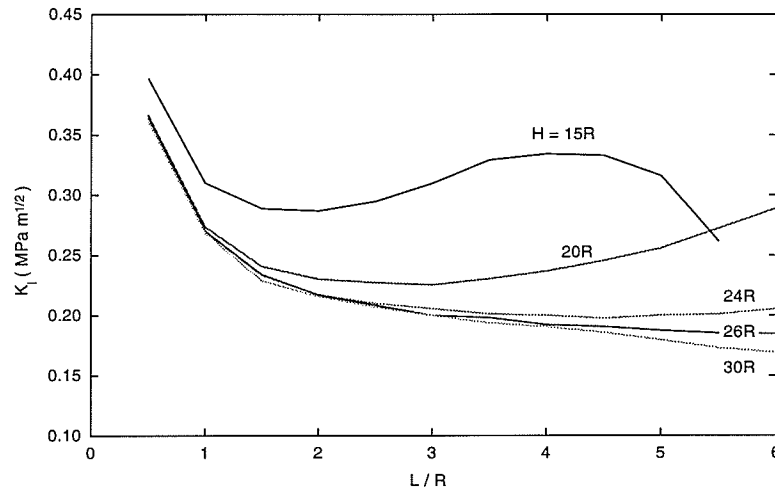
Figure 3.62: Variation of $K_I$ at crack tip for a block of variable height and constant width (FRANC2D model, $W = 10R$).

at the crack tip converged. The block dimensions for the R50A lab test were used as a starting point. This block had a primary crack which was tracked for the longest distance ($L/R = 5$). Block dimensions for this sample (height $H$ and width $W$) normalized to hole radius $R$ are $H = 15R$ and $W = 10R$. The first set of results are shown in Figure 3.62. In this figure the block width was kept constant at $W = 10R$ and the block height varied from $15R$ to $30R$. A large boundary influence can be seen with the shorter blocks ($H < 24R$). What appears to be happening is as the primary fracture approaches a platen boundary it becomes increasingly difficult to propagate. A reason for this is as the primary fracture propagates through the sample, two slender columns are created; one on each side of the sample (Figure 3.63). When edge loading conditions are used each column tends to buckle outward from the sample center and at the same time a folding inwards occurs at the platen boundary. This buckling phenomenon increases the compressive stresses normal to the crack axis at the tip thereby reducing its tendency to propagate.

It is easier to see how the solution converges if $K_I$ at the $L/R = 5$ fracture tip is plotted against varying block height (Figure 3.64). The solution converges to a reasonably stable value at approximately $H = 30R$.
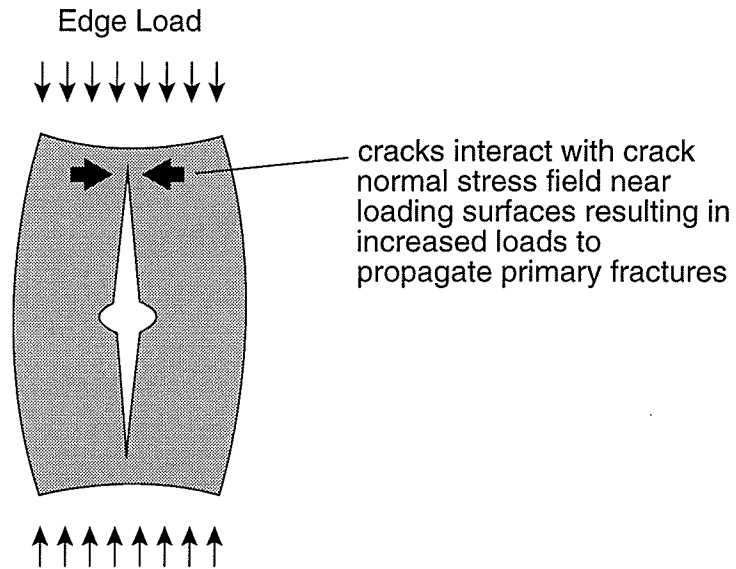
Figure 3.63: Buckling phenomenon observed in modeling primary fracture propagation with edge loading conditions.
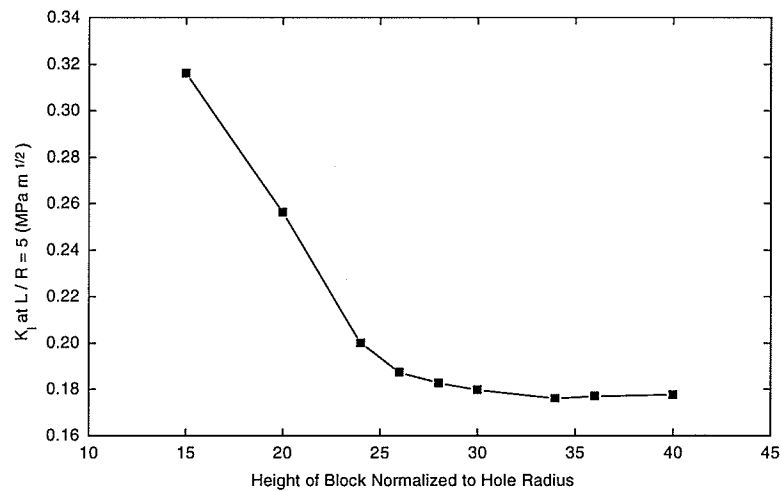


Figure 3.64: Variation of $K_I$ at $L/R = 5$ crack tip for a block of variable height and constant width (FRANC2D model, $W = 10R$).
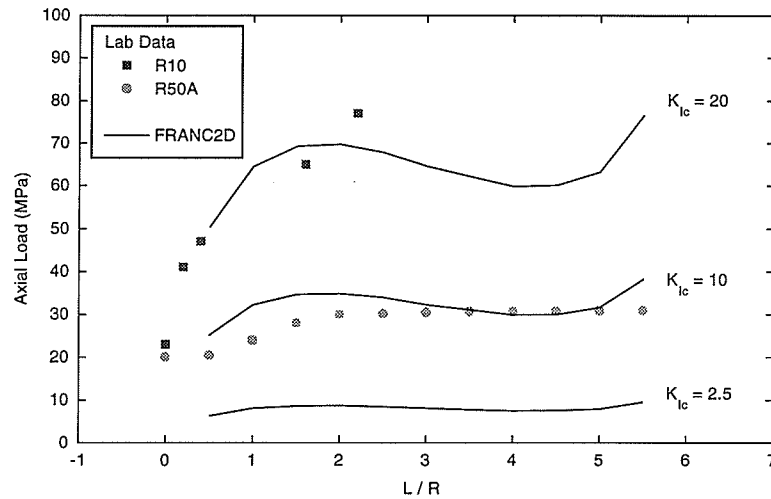
Figure 3.65: Primary crack propagation trends predicted by FRANC2D ($K_{Ic}$ in MPa$\sqrt{m}$). Block dimensions are $H = 15R$ and $W = 10R$.

These modeling results can also be viewed in terms of propagation loads and directly compared to the laboratory results (Figures 3.65 and 3.66). This naive approach of varying the fracture toughness illustrates the large range in toughness required to match the laboratory propagation data at the limits of the the data set. $K_{Ic}$ for the laboratory specimens is approximately 2.5 MPa$\sqrt{m}$ (shown as the lowest curve in Figure 3.65). The taller block ($H = 30R$) of Figure 3.66 appears to produce a better fit to the laboratory data than the shorter block results of Figure 3.65.

The latter two figures assume that $K_{Ic}$ is size dependent. It is not, of course. Some arguments have been made that fracture toughness may depend on fracture length (Ingraffea and Schmidt [45], Schmidt and Lutz [81]) but it is generally thought of as being a material property. There are several theories available to incorporate size effect into fracture mechanics models.

Ingraffea [43] modeled primary and remote fractures around a circular opening using a finite element approach. Crack propagation was governed by Erdogen and Sih's [27] $\sigma(\theta)_{max}$ theory of mixed-mode fracture mechanics. The model consisted of linear strain, triangular, isoparametric elements with quarter-point singularity crack tip elements [2]. His
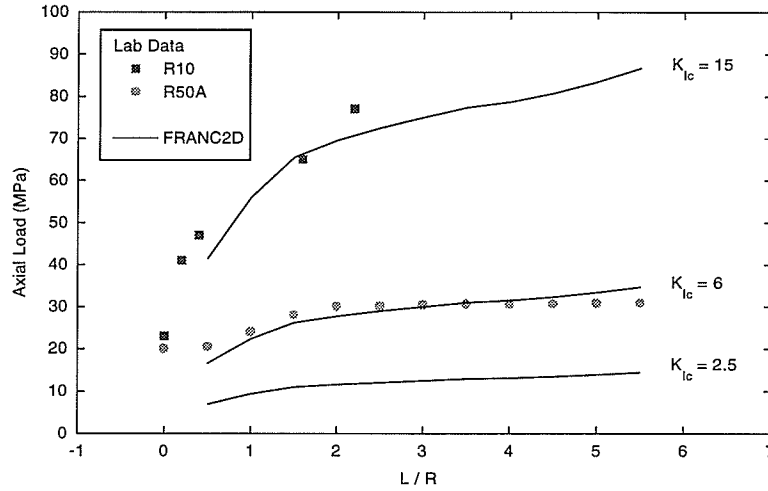
Figure 3.66: Primary crack propagation trends predicted by FRANC2D ($K_{Ic}$ in MPa$\sqrt{\text{m}}$). Block dimensions are $H = 30R$ and $W = 10R$.

results compared quite favorably with the laboratory results from Hoek [36, 37] who tested a small chert sample, containing a circular hole, under biaxial loading conditions. However, Ingraffea did run into difficulties initiating the remote (secondary) fracture. He states that although the maximum computed tensile stress in the remote region was significantly lower than $T_0$, a secondary tensile crack was assumed to form at the appropriate place when the stress level reached the remote crack initiation stress level determined by Hoek. It is shown later (Chapter 4) that remote fractures depend on a critical combination of both $\sigma_1$ and $\sigma_3$ to initiate.

In the $\sigma(\theta)_{\text{max}}$ theory crack initiation is assumed to occur at the crack tip in a direction in which $\sigma_\theta$ (the circumferential stress) is a maximum (Figure 3.67). Crack initiation takes place when this maximum tangential stress ($\sigma(\theta)_{\text{max}}$) reaches the tensile strength of the material. The stress state near the crack tip is calculated at a characteristic distance, $r$, from the tip and is given by,

$$\sigma_\theta = \frac{1}{\sqrt{2\pi r}} \cos\frac{\theta}{2} \left[ K_I \cos^2\frac{\theta}{2} - \frac{3}{2} K_{II} \sin\theta \right] + \dots \qquad (3.29)$$
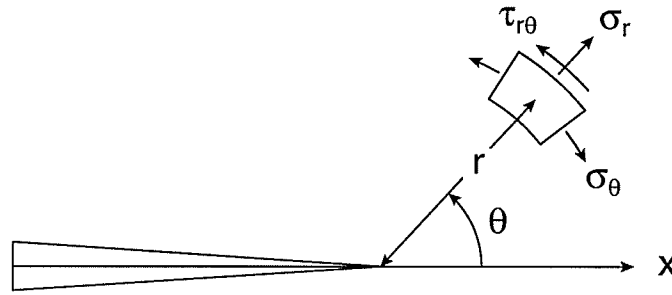
$$\sigma_r = f(r, \theta, K_I, K_{II})$$

Figure 3.67: Notation for stresses at crack tip for $\sigma(\theta)_{\text{max}}$ theory.

$$\tau_{r\theta} = f(r, \theta, K_I, K_{II})$$

The characteristic distance $r$ is assumed to be a material property.

Knowing a priori that the primary fractures propagate in a purely mode I fashion ($K_{II} = 0$) in a direction parallel to the load ($\theta = 0°$) $\sigma_\theta$ in equation 3.29 will reduce to,

$$\sigma_\theta = \frac{K_I}{\sqrt{2\pi r}} \tag{3.30}$$

and crack propagation will occur when $\sigma_\theta = T_0$, assuming tensile strength at a point is the same as the macroscopic tensile strength.

This characteristic distance incorporates a size effect into the model since it remains fixed. By incorporating the $\sqrt{r}$ scale factor into the FRANC2D results of Figure 3.66 a reasonable match is obtained to the laboratory data without varying the fracture toughness (Figure 3.68). Using the same approach with the smaller block of Figure 3.65 a less favorable match is obtained (Figure 3.69).

A similar type of argument as was presented for the $\sigma(\theta)_{\text{max}}$ theory can be presented for Sih's [84] minimum strain energy density criterion ($S(\theta)_{\text{min}}$ theory). In this theory fracture initiates at a point on the flaw with the maximum tensile stress and travels in a direction, $\theta$, determined by the minimum value of strain energy at a characteristic distance $r$ from the initiation point (the potential energy is maximum along this direction). Fracture occurs when the strain energy density ($\partial U/\partial V$), along this minimum direction, reaches a
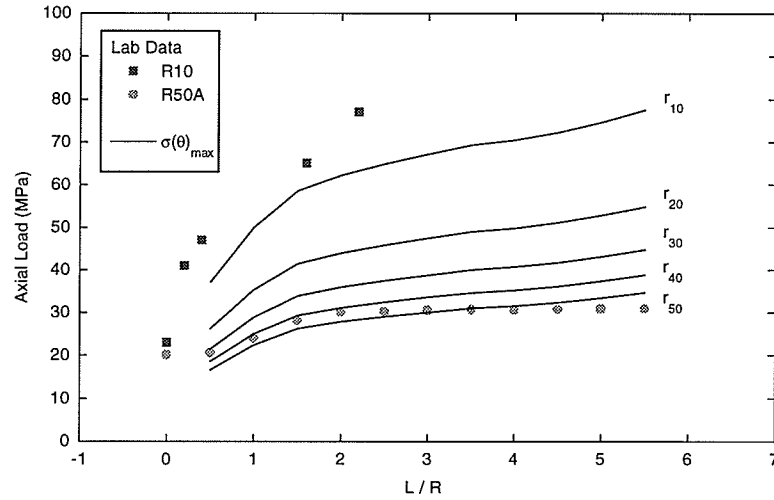
Figure 3.68: Primary crack propagation trends predicted by FRANC2D using $\sigma(\theta)_{max}$ theory. Block dimensions are $H = 30R$ and $W = 10R$.
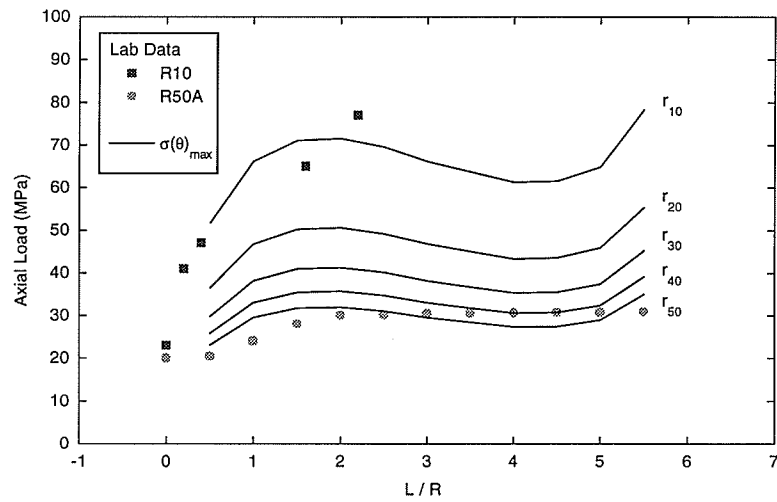


Figure 3.69: Primary crack propagation trends predicted by FRANC2D using $\sigma(\theta)_{max}$ theory. Block dimensions are $H = 15R$ and $W = 10R$.

critical material value, $(\partial U/\partial V)_c$. The strain energy density intensity is determined from the following equations:

$$\frac{\partial U}{\partial V} = \frac{S}{r} \qquad (3.31)$$

where,

$$S = a_{11}K_I^2 + 2a_{12}K_I K_{II} + a_{22}K_{II}^2$$

$$a_{11}, a_{12}, a_{22} = f(r, \theta, E, \nu)$$

Once again for the primary fracture propagation case $K_{II} = 0$ resulting in fracture occurring when

$$\left(\frac{\partial U}{\partial V}\right)_c = \frac{a_{11}K_I^2}{r} \qquad (3.32)$$

If we take the square root of both sides of equation 3.32 we end up with,

$$C_1 = \frac{K_I}{\sqrt{rC_2}} \qquad (3.33)$$

where,

$$C_1, C_2 = \text{material constants}$$

which resembles equation 3.30. Therefore both the $\sigma(\theta)_{\max}$ and $S(\theta)_{\min}$ theories can be calibrated to produce identical predictions for the primary crack propagation data.

The prior modeling exercise removed much of the boundary influences imposed by the top and bottom block edges by extending the block to a height of $30R$. All blocks had a constant width of $10R$ (all tested blocks had a width dimension approximately $10R$). This simplified the modeling because a single model was only required and results were appropriately scaled to hole dimension $R$. The same modeling exercise was repeated with SIMEX and the influence of sample width was also assessed.

In SIMEX, cracks have a zero width. For the modeling the mesh was composed of eight noded isoparametric serendipity elements with quarter-point singularity crack tip elements. The zero-width crack is insensitive to the compression parallel load but in this case the
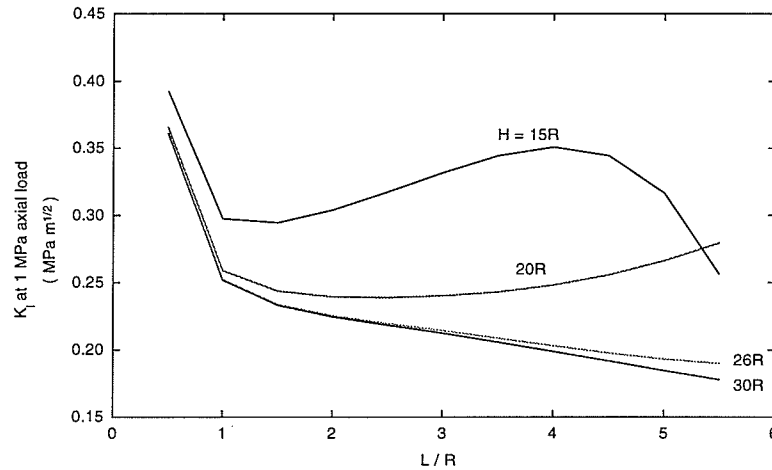
Figure 3.70: Variation of $K_I$ at crack tip for a block of variable height and constant width (SIMEX model, $W = 10R$).

crack will propagate because of the tension zone created around the circular void. A similar type of boundary influence exercise was tried with SIMEX as was done with FRANC2D. The results are similar (compare Figures 3.70 and 3.71 with Figures 3.62 and 3.64). Figures 3.72 and 3.73 make a direct comparison between the two numerical models for two different block sizes. It appears that the FRANC2D finite-width crack model does not have much of an influence on the mode I propagation of the primary crack.

An additional modeling exercise was tried with SIMEX. The influence of block width on crack propagation was studied (Figures 3.74 and 3.75). Block width has a tremendous influence on primary fracture propagation. Primary cracks are much more difficult to propagate in wide samples. Since the primary fractures propagate in a mode I fashion they are highly sensitive to the lateral stiffness of the structure. The propagating crack essentially splits the sample into two columns. If the sample is narrow the columns can deform much more easily in a lateral direction than if the sample is wide. SIMEX does converge to a solution at block dimensions of $W = 50R$ (Figure 3.75).

Figure 3.76 compares modeling results from a block of dimensions $H = 30R$ and $W = 50R$ (the dimensions of a block at which boundary influences are negligible) to the laboratory
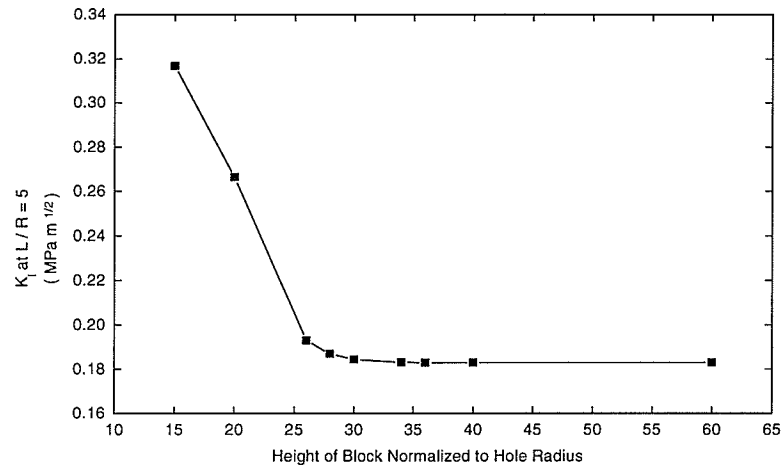
Figure 3.71: Variation of $K_I$ at $L/R = 5$ crack tip for a block of variable height and constant width (SIMEX model, $W = 10R$).
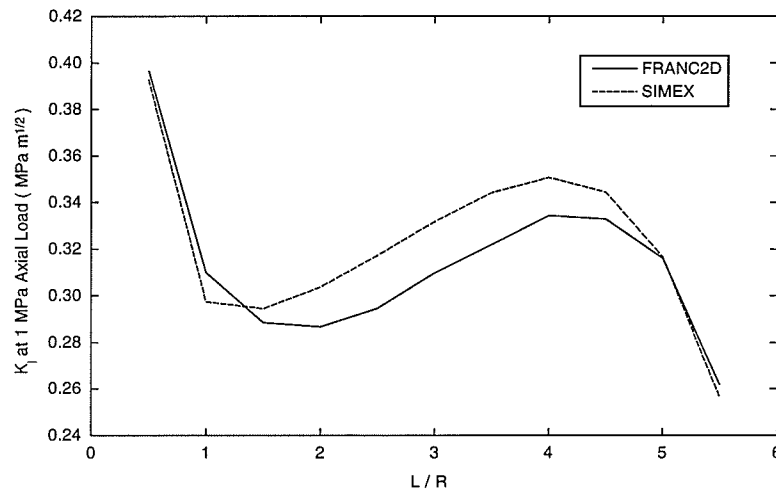


Figure 3.72: Comparison of results from FRANC2D and SIMEX. Variation of $K_I$ at crack tip for a block of dimensions $H = 15R$ and $W = 10R$.
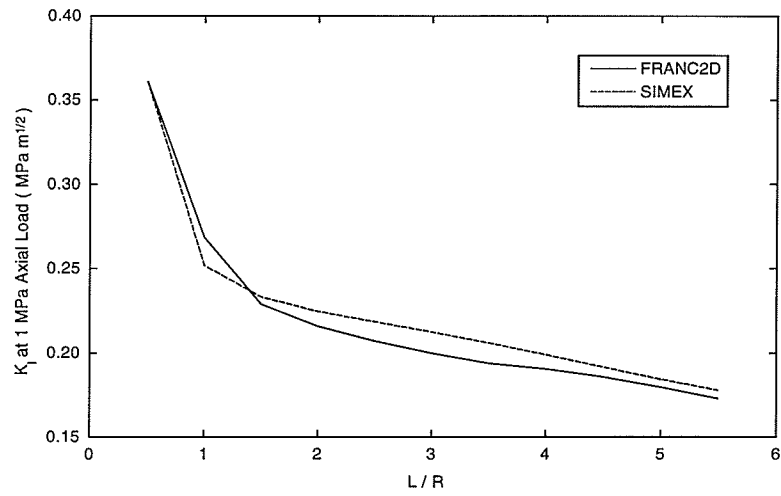
Figure 3.73: Comparison of results from FRANC2D and SIMEX. Variation of $K_I$ at crack tip for a block of dimensions $H = 30R$ and $W = 10R$.
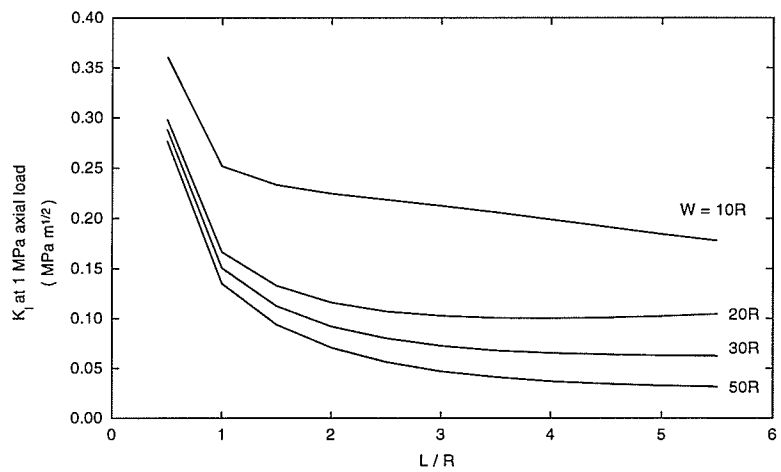


Figure 3.74: Variation of $K_I$ at crack tip for a block of variable width and constant height (SIMEX model, $H = 30R$).
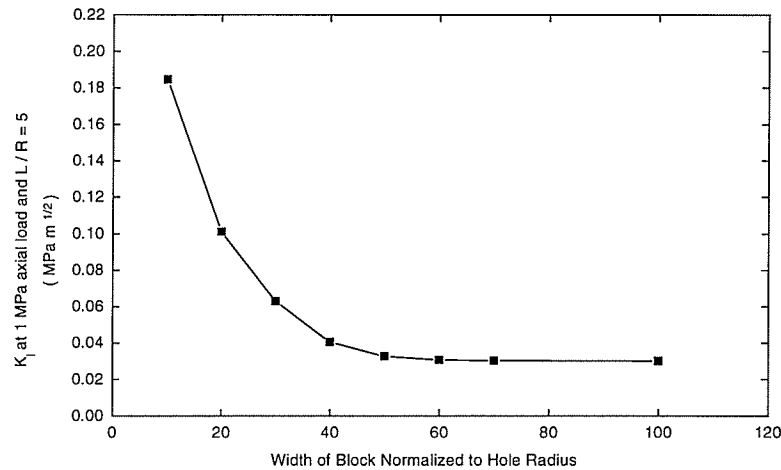
Figure 3.75: Variation of $K_I$ at $L/R = 5$ crack tip for a block of variable width and constant height (SIMEX model, $H = 30R$).

propagation data using the $\sigma(\theta)_{\max}$ theory. These results appear to give a poorer match to the laboratory data than the results from a narrow block model (Figure 3.68). The initial hardening trend of crack propagation curve in Figure 3.66 roughly follows the trend set by the $R10$ data while the flattened portion of the curve follows the easily propagating R50A data. The wide model (Figure 3.76) results in a fracture that is much too difficult to propagate.

If the actual sample dimensions are used in a SIMEX model the best match to the lab data is obtained (Figures 3.77–3.80). The sample boundaries obviously have a large influence on primary fracture propagation. The $R = 30$ mm sample was the shortest of all samples tested with a height of approximately $12R$. This model produced the best match to the laboratory data (Figure 3.79). The $R = 20$ mm laboratory data show a dramatic hardening trend (Figure 3.78). This is not a boundary affect, but is due to the initiation of remote fractures at either side of the primary fracture at about 67 MPa. Once a remote fracture initiates stresses are relieved at the primary fracture and concentrated in the remote locations. Once this stress relief occurs the primary fracture becomes increasingly difficult to propagate. The SIMEX models did not consider the formation of remote fractures.
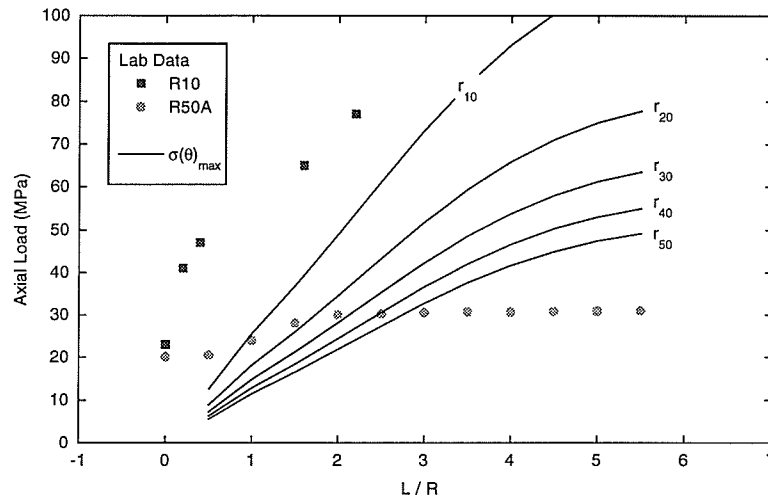
Figure 3.76: Primary crack propagation trends predicted by SIMEX using $\sigma(\theta)_{\max}$ theory. Block dimensions are $H = 30R$ and $W = 50R$.
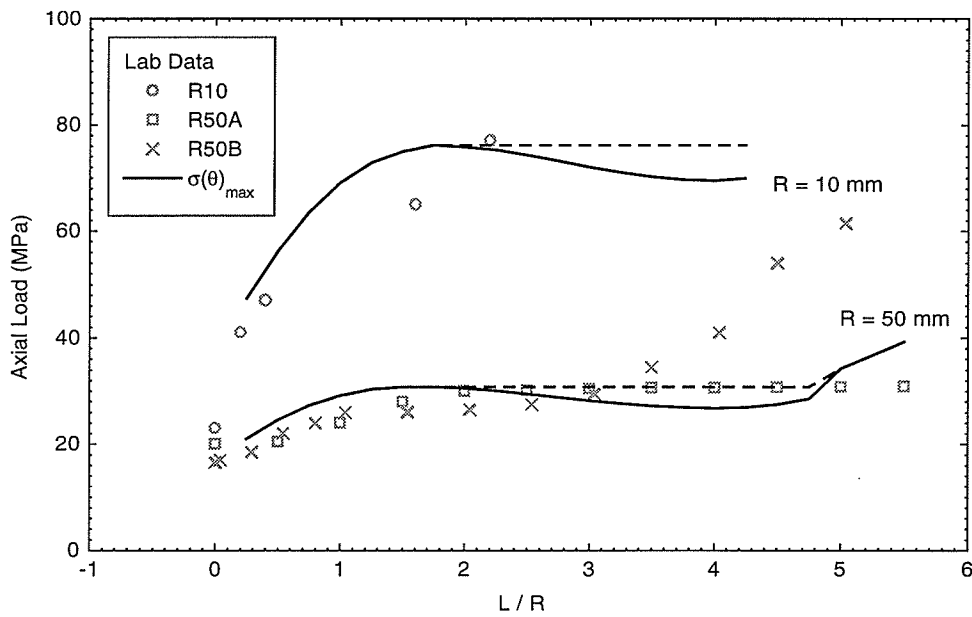


Figure 3.77: Primary crack propagation trends predicted by SIMEX using $\sigma(\theta)_{\max}$ theory and actual block dimensions ($R = 10$ and $50$ mm). The dashed line indicates the propagation trend that would be observed in the laboratory. The unstable mode would not be detected.
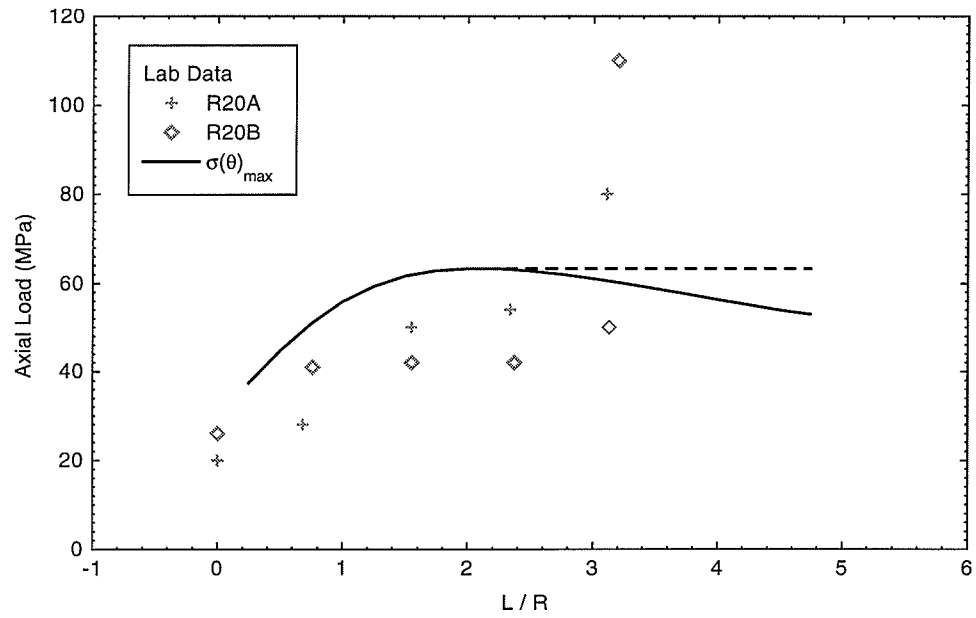
Figure 3.78: Primary crack propagation trends predicted by SIMEX using $\sigma(\theta)_{\max}$ theory and actual block dimensions ($R = 20$ mm). The dashed line indicates the propagation trend that would be observed in the laboratory. The unstable mode would not be detected.
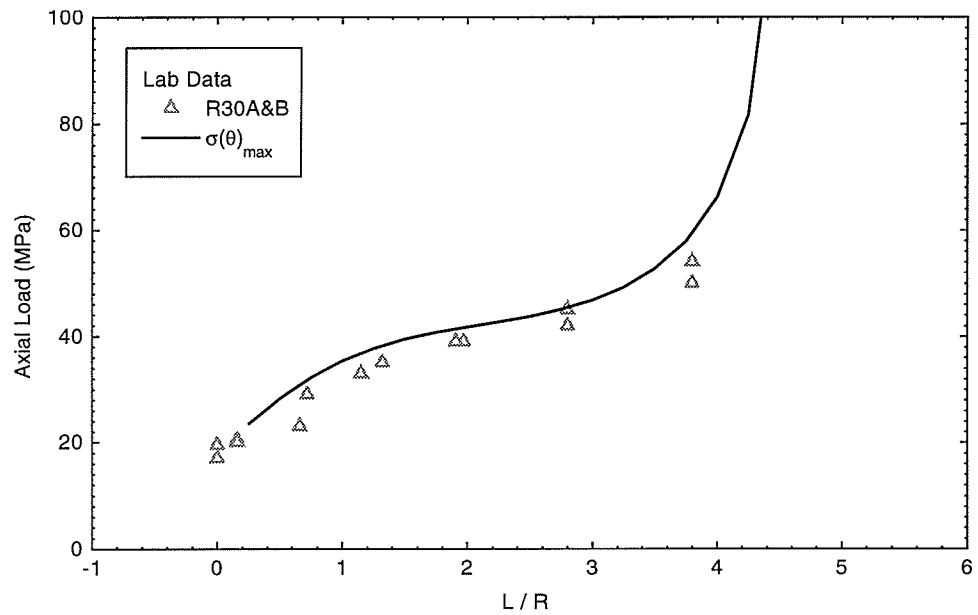


Figure 3.79: Primary crack propagation trends predicted by SIMEX using $\sigma(\theta)_{\max}$ theory and actual block dimensions ($R = 30$ mm).
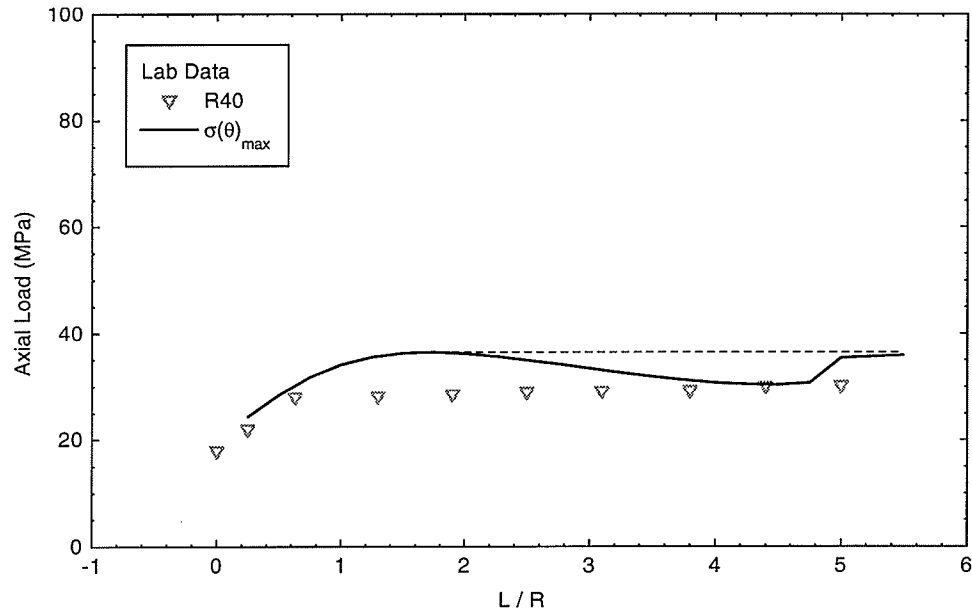
Figure 3.80: Primary crack propagation trends predicted by SIMEX using $\sigma(\theta)_{\max}$ theory and actual block dimensions ($R = 40$ mm). The dashed line indicates the propagation trend that would be observed in the laboratory. The unstable mode would not be detected.

Carter [17] propagated a finite-width primary fracture to see the effect it would have on remote fracture formation. He maintained a constant element size ahead of the propagating fracture tip to account for the size effect. Maintaining a constant element size accounts for the affect of the stress gradient by averaging the stresses over a constant area.

Yuan et al. [92] "opened up" the zero-width elliptical crack of fracture mechanics to account for the effect of the axial compressive stress. His derivations include a redefinition of stress intensity factor to that shown below,

$$K_I = - \left( b\sqrt{\frac{\pi}{a}} \right)^3 P \tag{3.34}$$

In this equation $a$ and $b$ are the semi-major and semi-minor axes of the elliptical crack. However this $K_I$ is not the same as the $K_I$ of fracture mechanics; it has units of $\mathrm{MPa}\sqrt{\mathrm{m}}^3$. We can see that Yuan's model behaves similar to the classical fracture mechanics models. That is as $b \to 0$ the axial load $P$ required to propagate the crack approaches infinity. A similar result is shown by Madenci [67] through the use of a slightly open, penny-shaped
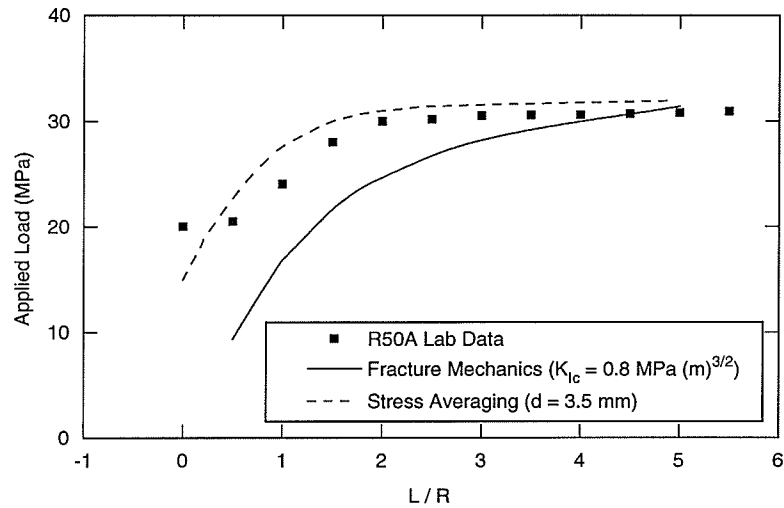
Figure 3.81: Yuan's model fit to R50A crack propagation data set (modified from Yuan et al. [92]).

crack.

Yuan incorporated his model into Ayari's [1] finite element modeling code SIMEX and calibrated it to the R50A data set (Figure 3.81). A good match was obtained. However, the fracture width used to obtain the match is unknown and the smaller holes, which showed more stable behavior, were not modeled.

Yuan also modeled the primary crack propagation problem through the use of a stress averaging technique. This technique is similar to Lajtai's [56] model for crack initiation modeling discussed previously. In this model stress at a point is replaced with stresses that are averaged over a constant distance $d$. The averaged stresses are then used in a fracture criterion (Yuan used USR). A good match to the R50A propagation data is obtained again (Figure 3.81), but without any indication of the fracture width used.

## 3.7  Summary

Several analytical and numerical models were tested in an attempt to fit the primary crack initiation and propagation data of this thesis. In a general sense the curve fitting was

successful for the analytical fracture initiation models, but largely unsuccessful for the analytical fracture propagation models. This shortcoming is most likely due to boundary effects. The analytical models are based on infinite boundaries while laboratory specimens have finite dimensions. It is noteworthy that there are two distinct behaviors shown by the analytical models for crack propagation (Figure 3.82). One school of thought suggests that the propagation curves should be concave upward (strain hardening at an increasing rate) while the other suggests the opposite, convave downward (strain hardening at a decreasing rate). The concave upward trend is supported by Sih [82] and his followers (Sammis and Ashby [80] and Rummel [79]). The concave downward trend is supported by two analytical models (Rooke and Cartwright [78] and Kemeny and Cook [50]). The numerical fracture models (FRANC2D [87] and SIMEX [1]) demonstrate a concave downward propagation trend if platen boundary influences are minimized. Conversely, the confining influence of the platen boundaries force the propagation curves to reverse their trend from concave down to concave up. The numerical models (FRANC2D and SIMEX) produce the best fit to the data when fracture propagation is governed by Erdogen and Sih's [27] $\sigma(\theta)_{max}$ theory and the modeled specimen sizes correspond to actual specimen dimensions. When platen boundary influences are minimized by increasing the height of the modeled blocks a reasonably good match to the laboratory data is also obtained. Judging from numerical modeling results the concave down propagation trend appears to be the "true" mode of fracture propagation from a circular void loaded in compression when boundary influences are minimized.

Good results were also obtained with Bažant's [3] classical energy-based size effect law as well as with Carpinteri et al. [16] multifractal law. These models rely on having an extensive data set available and do not seem to be easily applicable to extrapolating propagation trends.

Three new empirical fracture propagation models are introduced. One is based on simplifying Carpinteri's size effect model by finding a functional relation between Carpinteri
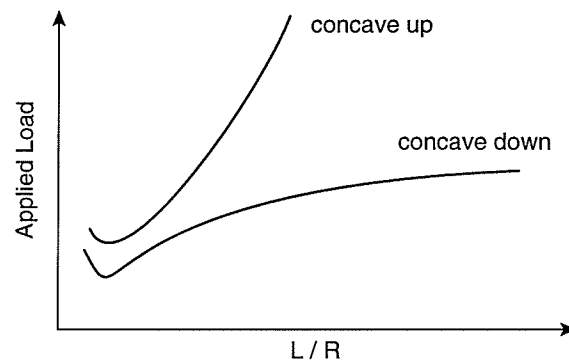
Figure 3.82: Fracture propagation trends predicted by numerical and analytical models.

model parameters and normalized crack length. The remaining two models are based on fitting Griffith's energy balance equation and an exponential equation to "grouped" fracture propagation data. These three models each provide a simple expression to represent the primary fracture behavior demonstrated by the laboratory data.

# Chapter 4

# Model Development and Calibration

From the previous chapter it was seen that basic linear elastic fracture mechanics provided a good model to simulate primary fracture propagation from a circular void. However, fracture mechanics has the weakness that it does not provide a size dependent crack initiation theory (i.e., the initiation stress cannot be correctly predicted in locations where cracks do not exist). For example the crack initiation of the the primary crack ($L/R = 0$) can not be predicted unless a small starter crack is used. The same holds true for the remote and sidewall spalling types of fractures found around the circular void. This is the reason Ingraffea [43] inserted a starter crack, in his numerical model, in the remote location, at the stress level dictated by the lab results. The finite element model he was using did not have the ability to correctly predict the initiation level of the remote fracture. In lieu of these shortcomings and because of Carter's [17, 18] success at modeling fracture initiation and propagation with Lajtai's [56] stress averaging approach it was decided to further Lajtai's and Carter's work by attempting to model the size dependent propagation data presented in this thesis. Lajtai's stress averaging model provides a unified approach to modeling all the fracture phenomenon (crack initiation and propagation at any position in a structure) observed in brittle materials under compressive loads. In addition to crack initiation and propagation Lajtai's model has the ability to correctly represent the "step-out" phenomenon

and potential to model *en echelon* crack formation commonly observed in rocks subjected to compressive loads. The finite-width crack model also has the ability to "stand on its own." That is, an isolated finite-width crack can be propagated under an axial compressive load. The zero-width fracture commonly used in fracture mechanics does not have this ability unless, of course, it is inclined to the loading direction.

Two two-dimensional linear elastic numerical models were written, in support of this thesis, to model fracture propagation under compressive loads. The first model is a finite element program called InSight$^{2D}$. The second is a boundary element program called EJDBEM. Both programs are DOS based, written in "C", will run on 386-type (or above) machines equipped with EGA graphics (or better), and will use extended or expanded memory if available. The programs will take advantage of Pentium type processors and high resolution graphics (SVGA) which is the recommended configuration for modeling crack propagation problems. The programs use a dynamic hierarchical linked list data structure to store model geometries and meshes. This type of data structure allows unmatched flexibility and efficiency in accessing and editing data types (e.g., meshes, polylines, nodes). Memory is allocated as required and any unused items are immediately returned to the computer's free memory stack. In addition to these features both codes use a virtual memory model allowing huge problems (meshes) to be created and solved with limited RAM. For example, InSight$^{2D}$ has the ability to handle a finite element mesh (2D, linear triangles) with over 1,000,000 elements with only 8 MB of RAM. Problems with 3000 elements were routinely solved with only this amount of memory.

The program development focused on ease of use and code stability. Both programs have intuitive, mouse-driven, CAD-like graphical user interfaces. Each program is divided into three functional components: (i) a preprocessor, (ii) a computation engine, and (iii) a postprocessor. The preprocessor is used to set up the model geometry, create the FE or BE mesh, and set up loading conditions, etc. DXF file (a common CAD file format) import and export capabilities are supported to facilitate model building and graphics output.

Once a model has been set up in the preprocessor it is saved in a file and the computation engine solves for the unknown displacements and stresses in the mesh. The computation engine is available on mainframe systems as well as for PCs.

After the computation step is complete the model can be easily interpreted using the numerous postprocessing features. The postprocessor has the same user interface as the preprocessor and allows the user to produce contour plots of stress, strain, displacements, and safety factor. Output can be saved in HPGL or DXF type files for easy importing into documents.

InSight$^{2D}$ contains a powerful 2D mesh generator which was tailored to automatically generating finite element meshes containing discrete finite-width fractures. Multiple material types are supported. EJDBEM also uses linear elements and also contains a convenient automatic mesh generator supporting the discrete fracture model. Both models have stress averaging capabilities.

## 4.1 Finite Element Model InSight$^{2D}$

This section describes model development and calibration using InSight$^{2D}$. The InSight$^{2D}$ models were based on similar assumptions (linear elastic, plane strain conditions) and used similar loading and boundary conditions as the FRANC2D and SIMEX models. Symmetry was not used. The boundary conditions used are shown in Figure 4.1.

### 4.1.1 The Finite Width Crack Model

InSight$^{2D}$'s crack propagation model is based on Lajtai's [56] stress averaging technique combined with a finite-width crack model. A discrete fracture in InSight$^{2D}$ is represented by a constant-finite-width opening with a specialized fracture tip (Figure 4.2). The fracture tip contains a group of elements used specifically for stress averaging. The geometry of these tip elements remains unchanged as a fracture propagates. Fracture extension at the crack tip is proposed to occur when the average stress in front of the crack tip satisfies the
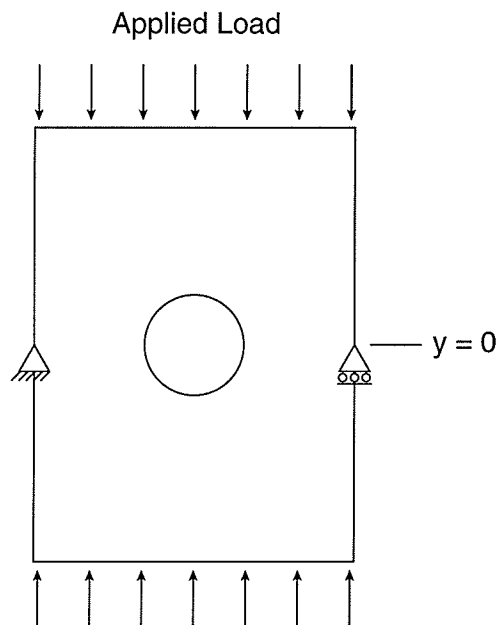
Figure 4.1: Boundary and loading conditions used in InSight$^{2D}$ modeling.

fracture criterion, USR in this case (see section 3.3.1 and Figure 4.3).

The average stress is calculated by averaging the stresses at the Gauss points of the shaded elements at the tip in Figure 4.2. For a given averaging distance, the shaded fracture tip elements remain a constant size and shape, forcing averaging over a constant area. The basis behind InSight$^{2D}$'s stress averaging capabilities is keeping the "averaging" elements at the fracture tips consistent throughout the propagation history of a fracture [20]. This avoids the size effect problems commonly encountered with simple stress-based safety factor analysis [39].

The sequence of events used to nucleate and propagate fractures using InSight$^{2D}$ starts by generating an "unfractured" finite-element mesh. The applied loads are initially set to zero, and are progressively increased to *in situ* values. The sequence for each loading step is as follows:

1. Compute stresses at Gauss points, contour the safety factor (USR) and check for regions where USR < 1 (Figure 4.3).
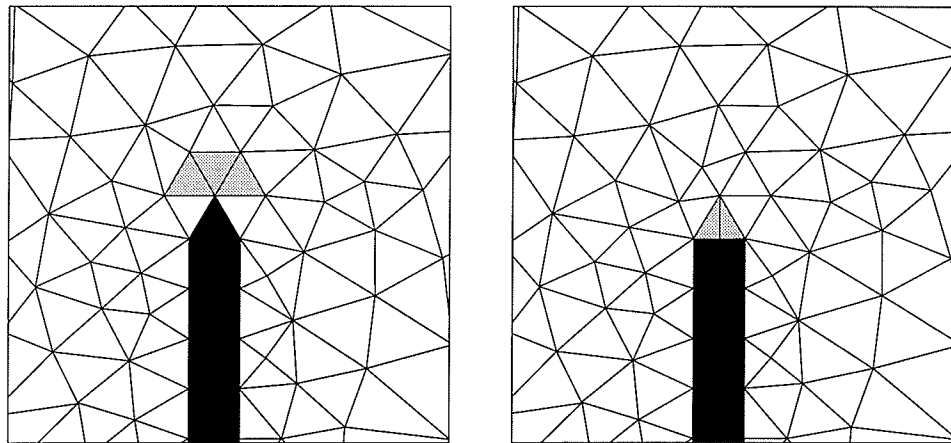
Figure 4.2: Crack tip geometries used in InSight$^{2D}$. Sharp-tip fracture, three-point averaging (left), flat-tip fracture, two-point averaging (right). Shaded elements are used to compute the average stress at the fracture tip.

2. If failure does not occur, increase the load and go to step (1).

3. If failure occurs, draw in a new fracture "backbone" (the fracture centerline) in the failed region or extend existing fractures into the failed region. The fracture is assumed to propagate parallel to the maximum principal stress trajectory, $\sigma_1$. Regenerate the mesh and go to step (1).

InSight$^{2D}$ models were influenced by boundaries to a similar extent as the FRANC2D and SIMEX models. Boundary influences at the $L/R = 5$ crack tip became small at block dimensions of $H = 30R$ and $W = 50R$ as shown in Figures 4.4 and 4.5.

### 4.1.2  Calibration of InSight$^{2D}$

Fractures in InSight$^{2D}$ are controlled by two parameters: fracture width $fw$ and averaging distance ($d$). Since there is no way, at present, to measure these parameters they are chosen arbitrarily. The affect of each parameter can be seen in Figure 4.6. Increasing fracture width facilitates fracture propagation while increasing averaging distance makes fracture propagation more difficult. As can be seen a wide range of fracture behavior can be modeled by varying these parameters.
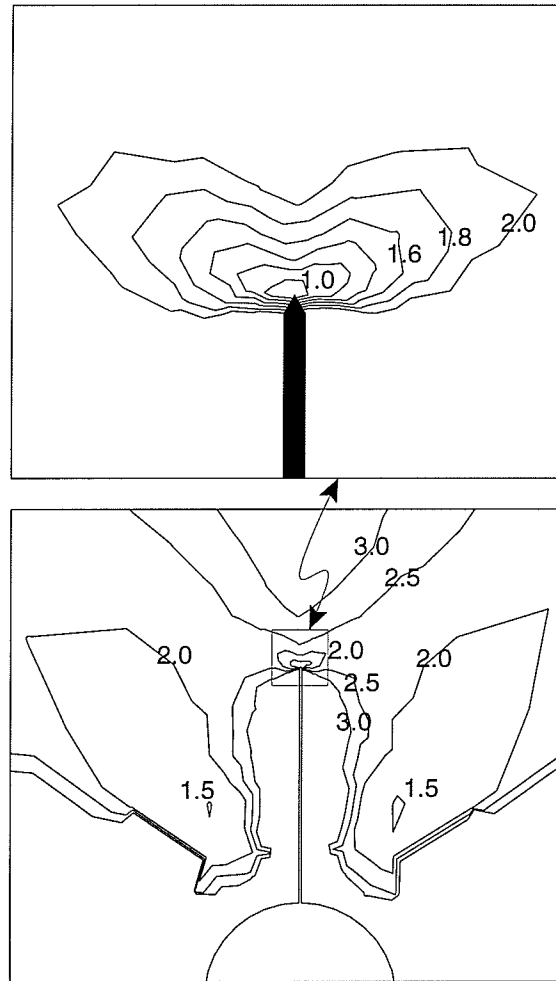
Figure 4.3: USR contours around circular opening with primary fracture and close up of fracture tip ($R = 20$ mm, fracture width $= 0.5$ mm, $d = 0.5$ mm, $L/R = 3.5$, axial load $= 65$ MPa). Note the indication of remote fracture formation on either side of the primary fracture at USR $= 1.5$.
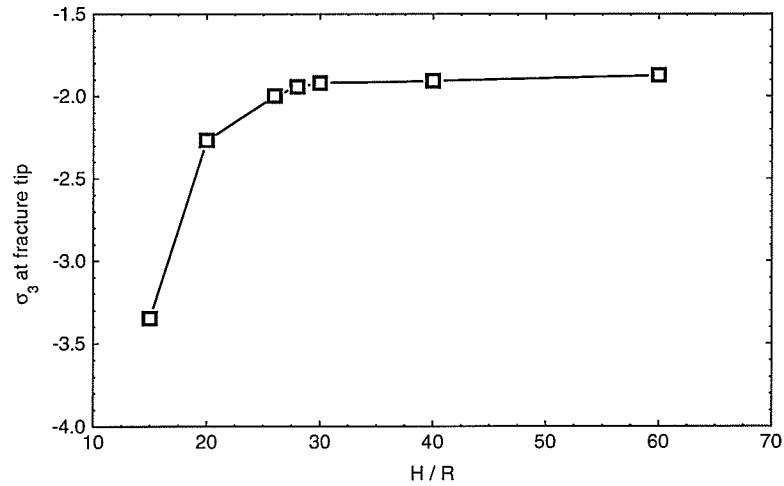
Figure 4.4: Variation of $\sigma_3$ at field point ahead of $L/R = 5$ crack tip for a block of variable height and constant width (InSight$^{2D}$ model, $W = 10R$, flat tip fracture two-point averaging, fracture width $= 0.01R$, $d = 0.01R$).
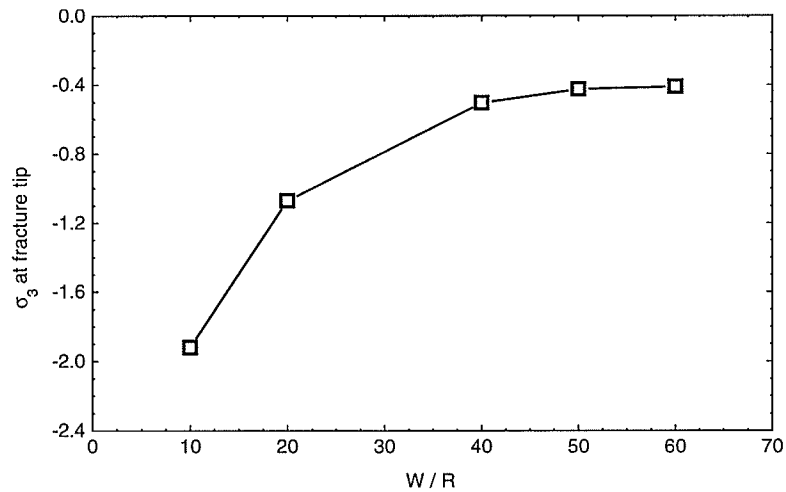


Figure 4.5: Variation of $\sigma_3$ at field point ahead $L/R = 5$ crack tip for a block of variable width and constant height (InSight$^{2D}$ model, $H = 30R$, flat tip fracture two-point averaging, fracture width $= 0.01R$, $d = 0.01R$ ).
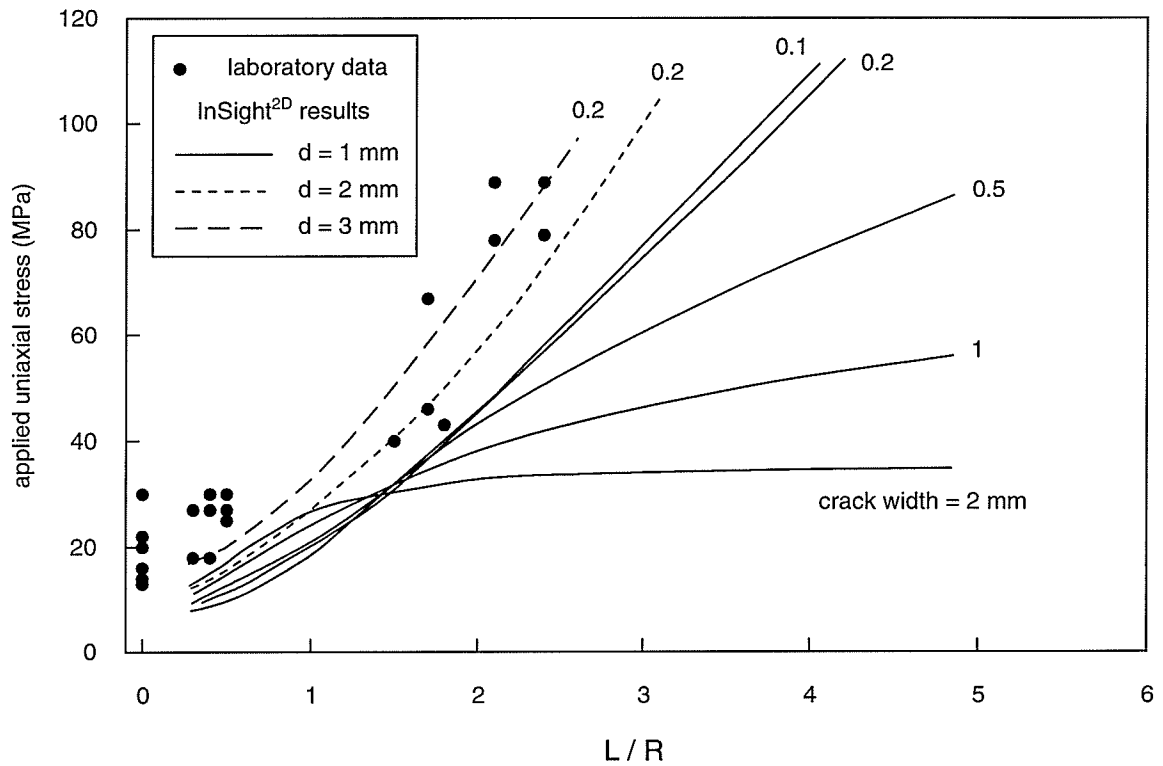
Figure 4.6: Effect of fracture width and averaging distance on fracture propagation from an $R = 10$ mm cavity. Crack initiation and propagation results from additional tests are included. (InSight$^{2D}$ model, flat-tip fracture, two-point averaging)
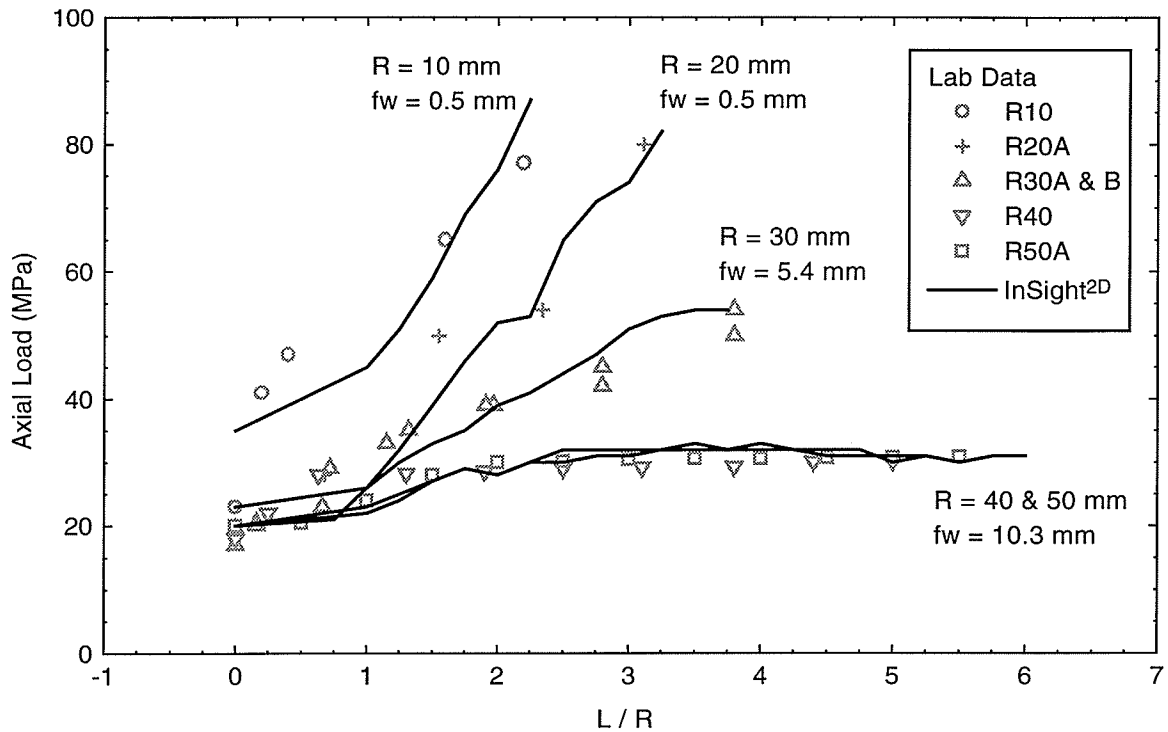
Figure 4.7: InSight$^{2D}$ calibration results (sharp-tip fracture, three-point averaging, $d =$ 0.5 mm).

It is interesting to note that reducing fracture width has little affect on propagation once the fracture reaches a width of 0.2 mm. However, changing the averaging distance at this narrow width still has an influence.

To calibrate InSight$^{2D}$ to the complete data set it was found that fracture width had to be varied while maintaining a constant $d$ (Figure 4.7). These parameter values were determined by trial and error. A fracture width and averaging distance of 0.5 mm were arbitrarily chosen as a starting point. This was the first attempt at calibrating the finite-width fracture model to the propagation data.

A further attempt was made to model the fracture propagation using InSight$^{2D}$ with a slightly different averaging scheme. The sharp angles at the corners of the rectangular fracture tip create extremely high gradients which cause the solution to be inaccurate near the crack tip. The averaging scheme was modified by moving the "averaging elements" a
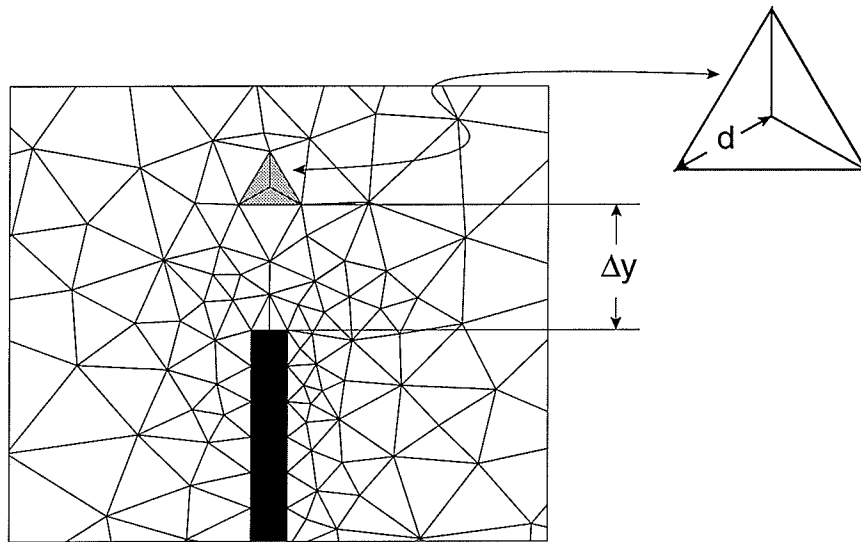
Figure 4.8: Modified crack tip geometry used in InSight$^{2D}$(flat-tip fracture, three-point averaging). Shaded elements are used to compute the average stress at the fracture tip.

short distance ahead of the fracture tip as shown in Figure 4.8. These elements are not directly connected to the fracture corners resulting in a solution that is not as prone to the fluctuations (due to mesh sensitivity) encountered with the original averaging method. An almost perfect match is obtained with this modified model without varying the fracture width or averaging distance for the entire range of hole sizes (Figure 4.9). However, the averaging distance in this model is controlled by two parameters: (i) the size of the elements to be averaged ($d$) and (ii) the offset of these elements from the fracture tip $\Delta y$. If parameter $d$ is kept small, as it is in this case, it becomes more of a control of the accuracy of the solution (i.e., solution convergence generally achieved with smaller elements). Parameter $d$ can be dropped altogether if a one-point averaging scheme is adopted. That is, assume the state of stress at the fracture tip is replaced by the state of stress occurring at a single point at a distance $\Delta y$ ahead of the fracture tip. This is explored further in the boundary element modeling section.

A problem that was encountered with InSight$^{2D}$ was generating valid finite element meshes for the problem geometry when a very thin fracture was required inside one of the
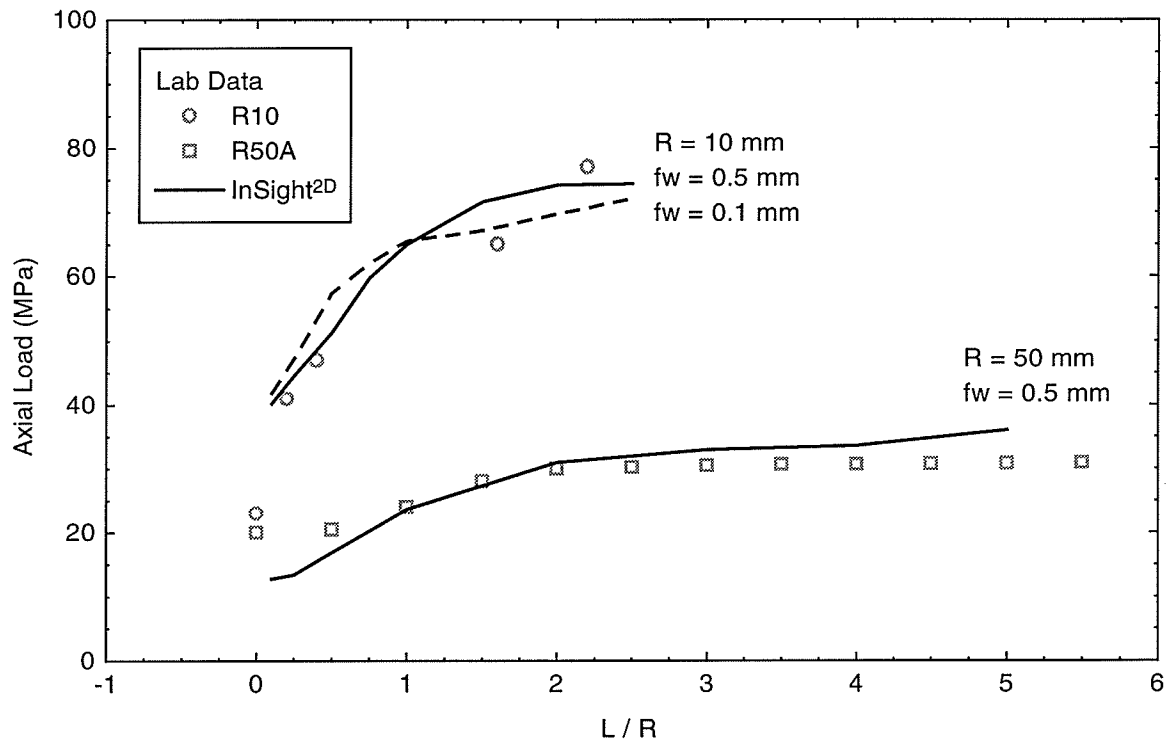
Figure 4.9: InSight$^{2D}$ calibration results using revised averaging technique. ($W = 10R$, $H = 30R$, flat-tip fracture, three-point averaging, fracture width = 0.5 mm, $d = 0.5$ mm, $\Delta y = 2$ mm.

larger blocks ($R = 50$ mm). A very thin finite-width fracture in a large structure requires an extreme range of element sizes. A fracture width to structure size of approximately 1:100,000 could be reliably created in InSight$^{2D}$using single precision mathematics. An example mesh generated by InSight$^{2D}$is given in Figure 4.10. This figure shows the wide range of element sizes required to model a finite-width fracture. The use of an artificial singularity, as is done in fracture mechanics, eliminates this problem. An element of any size can be made to have a singularity by forcing the midside nodes to the quarter point position. Small elements are not necessarily required at the fracture tip in this case, but finer discretization generally improves the accuracy of the solution. InSight$^{2D}$ approached its resolution limits for the large radius holes ($R = 50$ mm) and further discretization of the region near the fracture tip was not possible. It would be desirable to show how InSight$^{2D}$'s solution converged as the number of elements surrounding the fracture tip increased, but this is not easily achievable.

A unique feature frequently observed during the propagation of a fracture in a rock subjected to a compressive load is the "step-out" condition (Figure 4.11). Under increasing loads a propagating fracture often stops propagating and a new fracture initiates near the stalled fracture tip. This new fracture continues to propagate in a direction perpendicular to the minimum principal stress trajectory. One of the products of this "step-out" phenomenon is the formation of "en echelon" crack bands which are often attributed to shear failure in compression tests (Figure 4.12).

By pure chance, while modeling a propagating fracture in InSight$^{2D}$, the fracture "stepped out" (Figure 4.13). This specific step-out condition was found to be a result of a very slight irregularities in the mesh. InSight$^{2D}$'s meshes are not symmetric therefore slight differences in the calculated stresses exist on each side of the fracture tip. It was found that very minor variations in material strength around the fracture tip are required to cause step-outs to occur. The step-out phenomenon is investigated further in the latter part of this chapter.
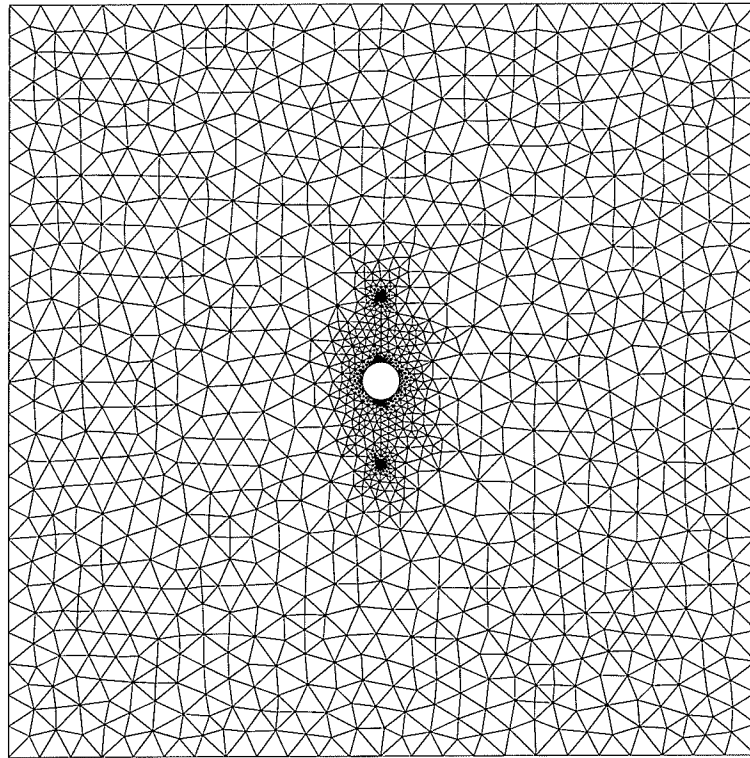
(a) Entire mesh
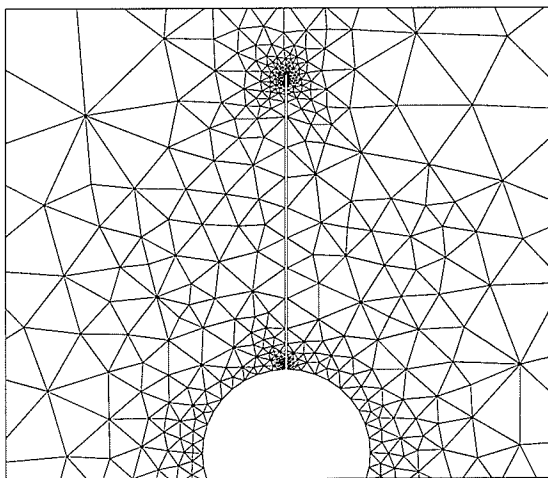


(b) Detail surrounding fracture.
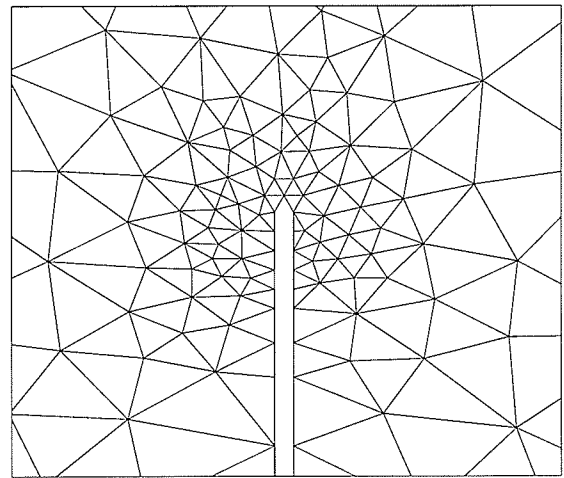


(c) Detail surrounding fracture tip.

Figure 4.10: Example mesh produced by InSight$^{\text{2D}}$ ($R = 20$ mm, $d = 0.25$ mm, fracture width $= 0.5$ mm, $L/R = 3.5$, 1689 vertices, 3130 elements).

Figure 4.11: Photo of step-out fractures in Cold Spring granite.

### 4.1.3 Tracking the State of Stress at the Tip of a Propagating Fracture

It is a useful exercise to track the state of stress at various points in the numerical model to get a better understanding of how stresses are distributed and which components contribute to the fracture process. Figure 4.14 tracks $\sigma_1$ and $\sigma_3$ at an averaging point ahead of a propagating fracture in an $R = 50$ mm hole. It can be seen that after an initial unstable mode (up to approximately $L/R = 1$) that the compressional stresses at the tip increase while the tensile stresses decrease. This, of course, is a direct result of using the USR fracture criterion which bases failure on contributions from both principal stresses. If a purely tensile-based fracture criterion were used (maximum tensile stress theory for example) the crack tip tension line would remain at a constant value of $T_0$ and the crack tip compression line would still show a small increase as the crack propagates. In this example the contribution of the compressional stresses at the crack tip are minor which explains why the numerical fracture
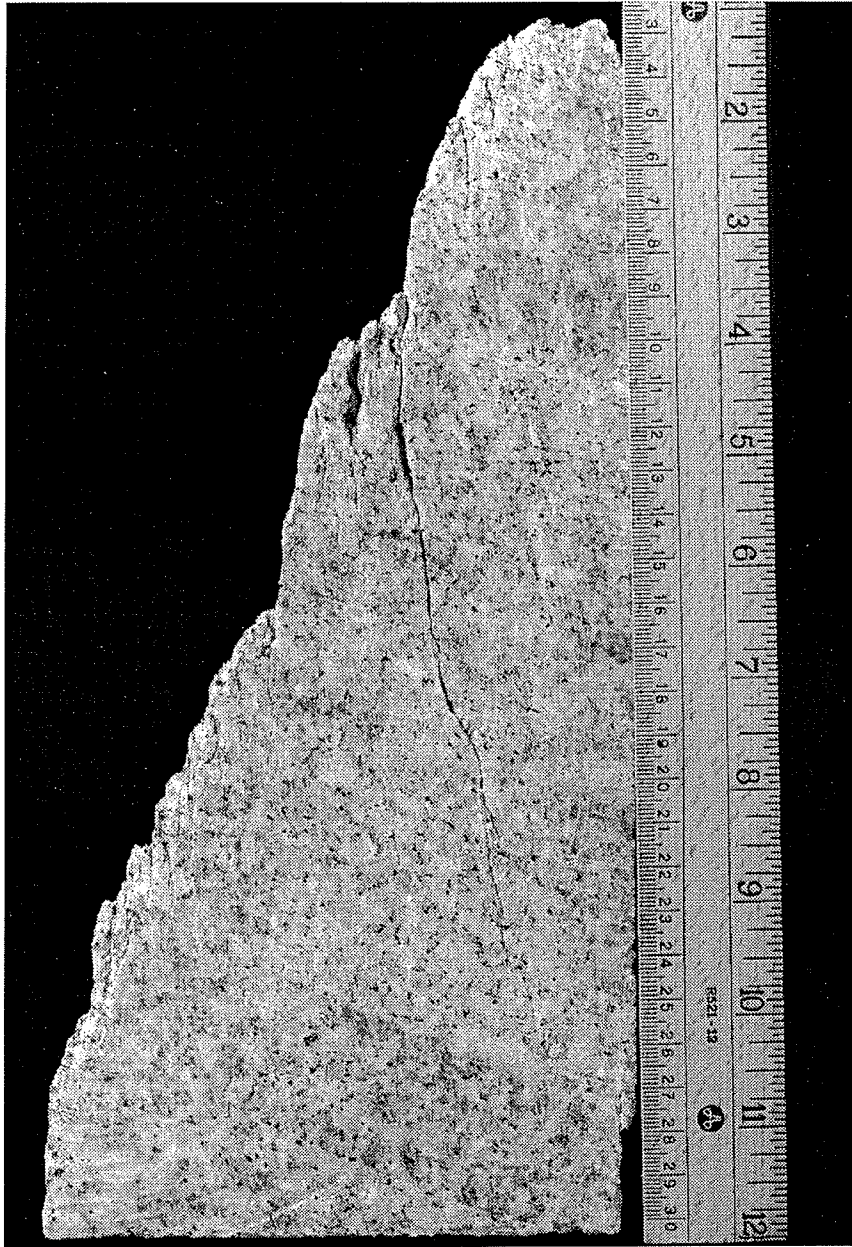
Figure 4.12: Photo of "shear band" formation in granite sample (from AECL's Underground Research Laboratory) tested in uniaxial compression.
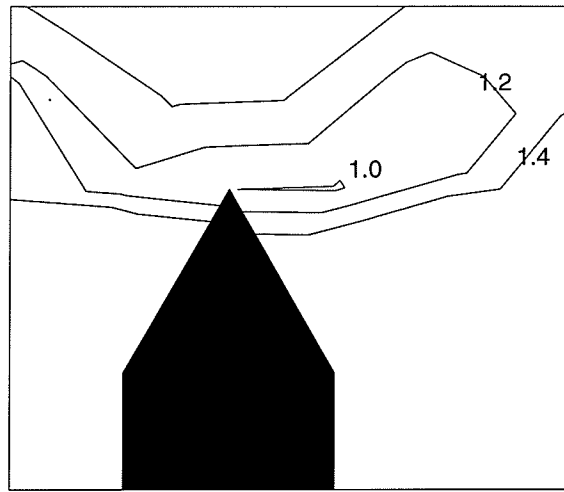
Figure 4.13: USR contours near fracture tip showing development of a "step-out" fracture at USR = 1.

mechanics models of the previous chapter produced a reasonable match to the propagation data (the Mode I theories presented rely on $\sigma_3$ alone).

However, a different story arises when the crack tip stresses are compared to stresses in the region where a remote fracture will eventually nucleate. Figure 4.15 simultaneously tracks the tensile stresses at a propagating primary fracture and the remote fracture nucleation point. In this figure, USR fracture criterion was used, resulting in the crack tip tension dropping as the crack propagates (similar to what is shown in Figure 4.14). While this is occurring the tensile stresses in the remote region increase. The remote region reaches a critical USR value at about $L/R = 3.5$. At this point the tension in the remote region still falls short of what would be required to initiate a fracture using the $\sigma_3 <= T_0$ theory. This is the precise problem Ingraffea [43] encountered in his fracture propagation studies. He could not generate enough tension in the remote region to initiate a fracture using the $\sigma_3 <= T_0$ theory. Figure 4.15 implies that a critical combination of both in plane principal stresses is vital to initiating remote fractures which the USR criterion seems to handle. However, in the laboratory, remote fractures for the $R = 10$ mm samples initiated between 86 and 108 MPa at $L/R \approx 2.5$. The InSight[2D] model obviously needs more calibrating, but
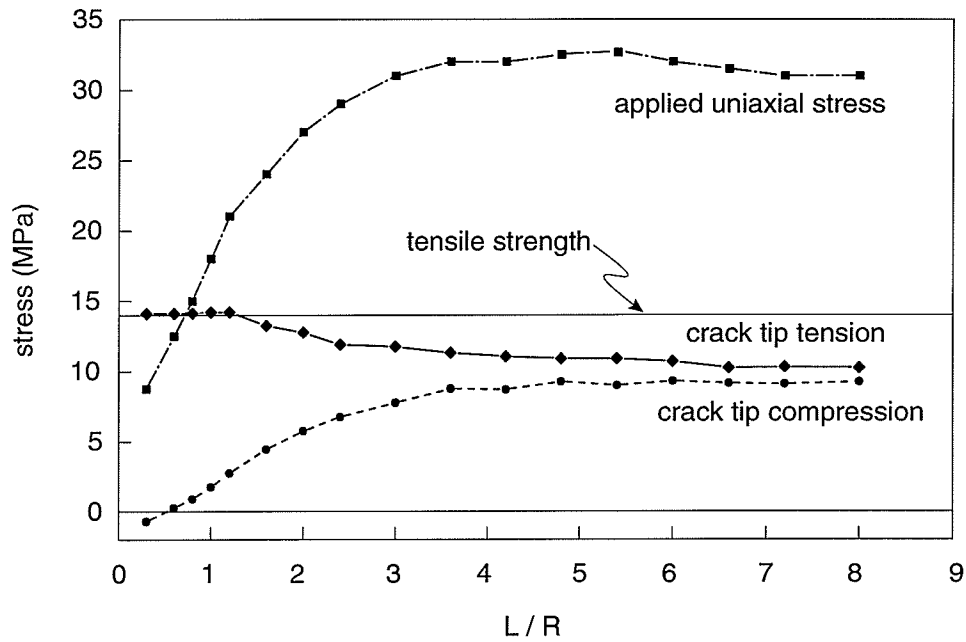
Figure 4.14: Modeled crack tip stresses from a propagating crack from an $R = 50$ mm cavity (InSight$^{2D}$ model, flat-tip fracture, two-point averaging).

the general trend of the stress redistribution is still valid.

The task of creating InSight$^{2D}$ and using it as a modeling tool provided the author with valuable knowledge in numerical fracture mechanics and modeling. However, the inconvenience of remeshing and the resolution problems of InSight$^{2D}$ led to another implementation of the finite-width crack model in a boundary element code. The boundary element approach is much more applicable to the finite-width fracture modeling problem than the finite element approach. Because of this, a more thorough investigation of fracture propagation is presented in the following section

## 4.2   Boundary Element Model EJDBEM

The use of a 2D boundary element method eliminated the need for complicated remeshing of the domain as is required with finite element models. The boundary element method is also conducive to the stress averaging technique used. Stress averaging can be done at any
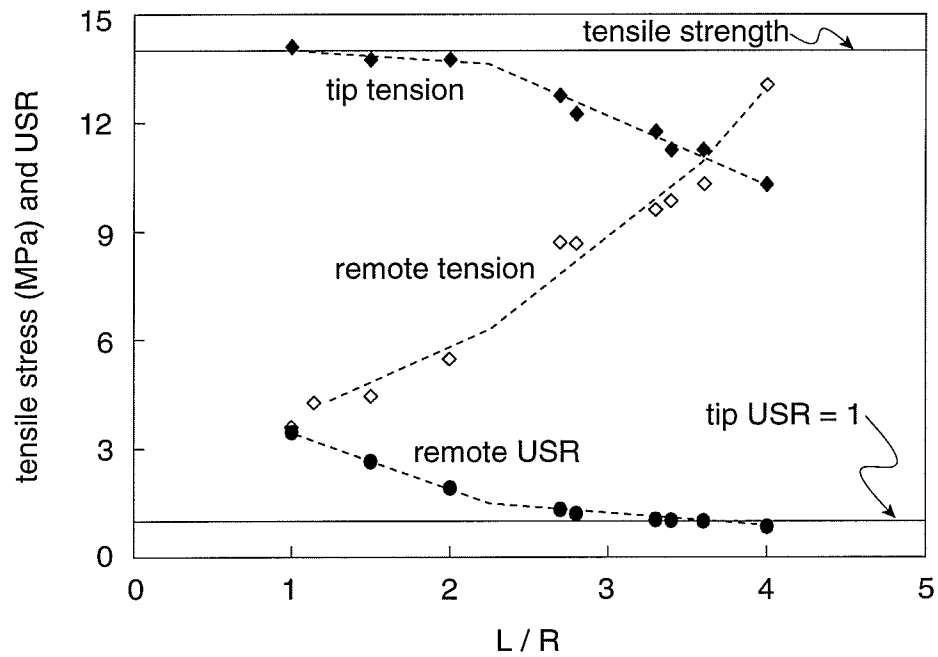
Figure 4.15: Modeled crack tip stresses from a propagating crack from an $R = 10$ mm cavity (InSight$^{2D}$ model, flat-tip fracture, two-point averaging).

arbitrary point in the material domain because there is no need to set up a mesh specific to an averaging task. The boundary element solution used for EJDBEM is Crouch and Starfield's [23] fictitious stress method.

The underlying assumptions for the EJDBEM models were similar to all the previous numerical models (linear elastic, plane strain conditions). One quarter symmetry conditions were used eliminating the need to prescribe boundary conditions (the model is automatically forced to be held stationary about its center and free to displace laterally and vertically).

### 4.2.1 The Finite Width Crack Model

Propagation of fractures in EJDBEM was modeled in a similar manner as fracture propagation in InSight$^{2D}$. That is, the load on a model was progressively increased until the specified fracture criterion was met. At this point the fracture was extended (or initiated) in the $\sigma_1$ trajectory direction.

Several arbitrarily chosen fracture shapes were used with EJDBEM (Figure 4.16). The fracture shapes can be divided into two categories: fixed-width fractures and variable-width (elliptical) fractures. Fixed-width fractures have parallel sides, separated by a finite distance, with a cap placed on the end for the fracture tip. The transition between the fracture side and fracture tip is $C^1$ continuous with the tip shape described by the following equations:

$$
\begin{aligned}
x &= P\cos\beta + r\cos 3\beta \\
y &= Q\sin\beta - r\sin 3\beta
\end{aligned}
\tag{4.1}
$$

In these equations $P$, $Q$, and $r$ are parameters and $\beta$ is an angle. When $r = 0$ the equations describe an ellipse with semi-axis lengths $P$ and $Q$. When $r \neq 0$ the equation describes and ovaloid (a square with rounded corners). Parameter $r$ controls the "squareness" of the ovaloid. This tip avoided the high stress concentrations created by the sharp corners of the flat fracture tip, providing a solution that smoothly converged to an asymptotic value.
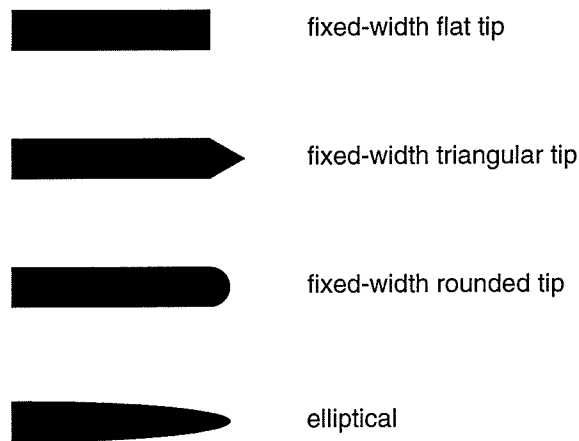
Figure 4.16: Fracture tips used in EJDBEM.

The variable-width fracture was represented by an ellipse. The difference between the two fracture types (fixed-width and variable-width) is that as a fracture grows the aspect ratio of the variable-width fracture becomes progressively larger whereas the fixed-width fracture is "self similar" during its propagation history.

Several stress averaging schemes were also tried in EJDBEM and are shown in Figure 4.17.

In order to propagate the discrete fractures correctly a reasonably accurate solution was required at points very close to the fracture tip. It is well known that a boundary element (and finite element) model usually converges to a solution as the number of elements is increased. An exercise was done to shed some light on the discretization required to obtain a good solution for the discrete fracture problem. For this exercise a single fracture (200 mm long, 2 mm wide) was loaded in uniaxial compression with 100 MPa (Figure 4.18). A field point was placed 0.1 mm in front of the circular fracture tip. Both a fixed-width and an elliptical fracture were tested. To see how the solution behaved the $\sigma_1$ component of the stress tensor at the field point was plotted as a function of the number of elements used. There is an analytical solution for the stresses at the field point for an elliptical fracture [14] giving a good basis for comparison but one could not be found for the fixed-width fracture
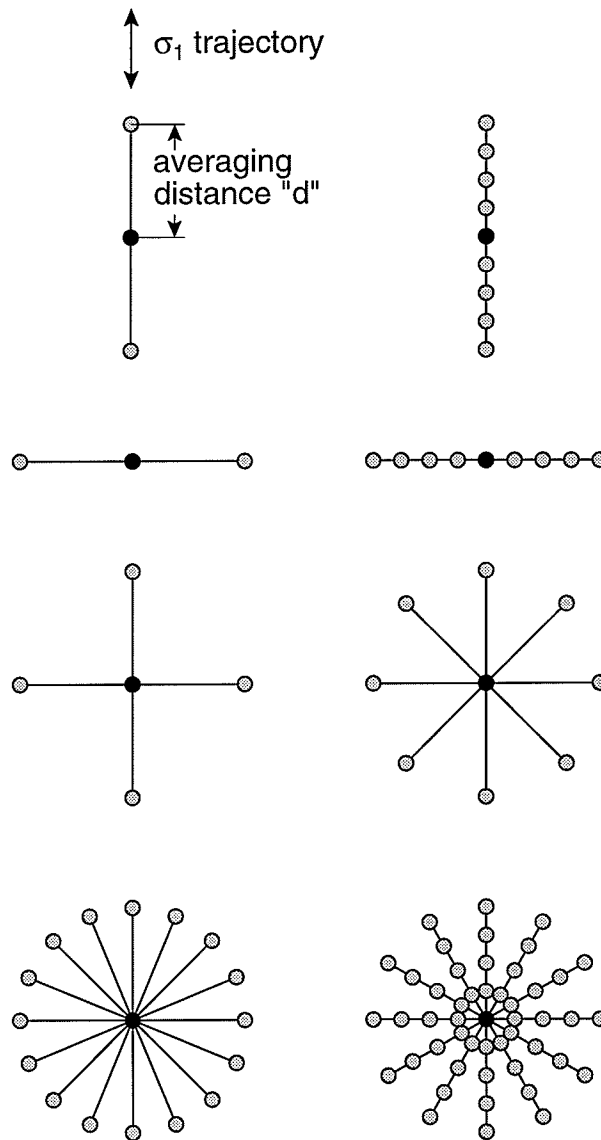
Figure 4.17: Some averaging schemes tried with EJDBEM. Stress at the center point is assumed to be the average of the stresses found at the surrounding (shaded) points.
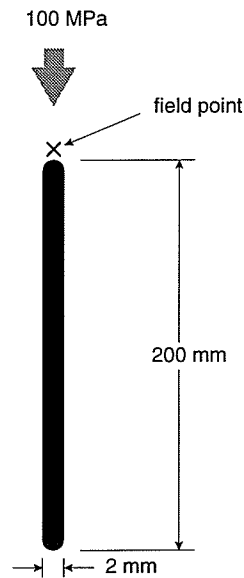
Figure 4.18: Fracture geometry used to test convergence of boundary element solution.

with circular tips.

Figure 4.19(a) shows $\sigma_1$ at the field point ahead of the fixed-width fracture with a circular tip as the number of elements at the tip is varied. It appears that the solution is converging. It is interesting to see that if $\sigma_1$ at the field point is plotted as an inverse function of the number of elements at the fracture tip an almost linear trend is observed (Figure 4.19(b)). A straight line was fit to this latter plot (Figure 4.19(b)) and then the function was inverted and plotted as the regression line in Figure 4.19(a). The inverse function in Figure 4.19(a) does have an asymptote at $\sigma_1 = -3.98$ MPa. Using this asymptote as an estimate of the exact solution the convergence of the problem can be plotted as a percent difference from this asymptote (Figure 4.20). At 190 tip elements there is approximately a 4% difference from the asymptotic solution. At 378 elements this drops to about 2%. The level of discretization at 4% of the asymptotic solution was judged to be adequate for the fracture propagation modeling to be done.

It is important to point out that with the complete range of fracture tip discretizations used in Figure 4.19 the value of $\sigma_1$ at the field point varies by less then 1% of the applied
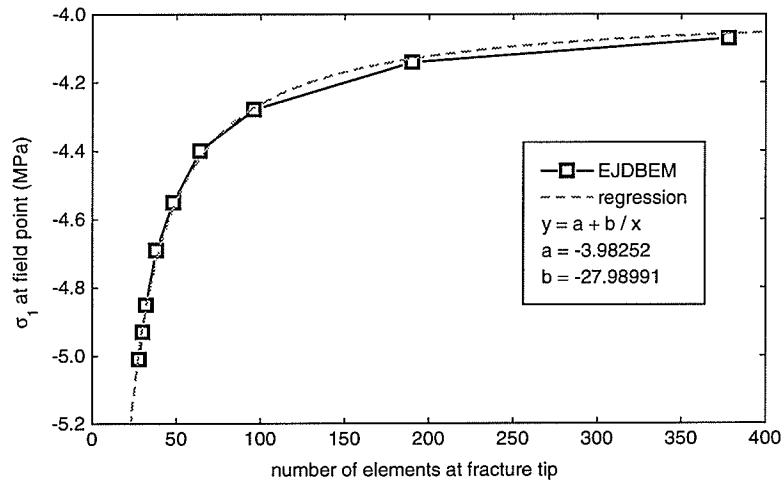
(a) $\sigma_1$ at field point versus number of elements at fracture tip.
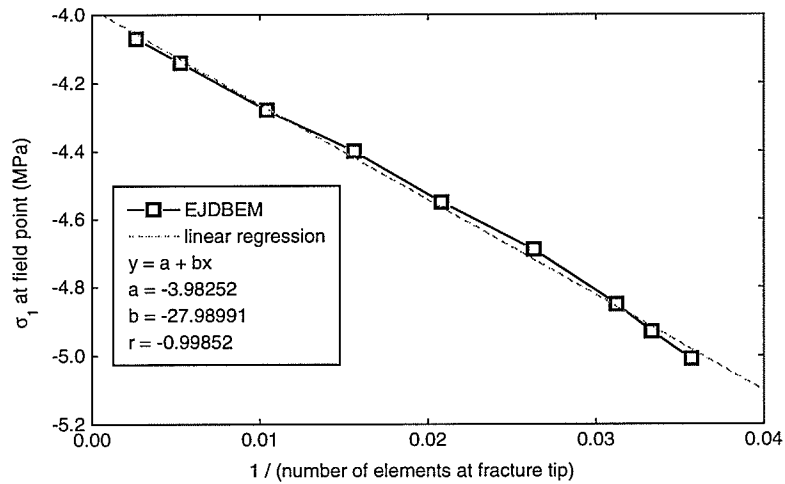


(b) $\sigma_1$ at field point versus 1/ (number of elements at fracture tip).

Figure 4.19: Convergence of boundary element solution at a point near the tip of a fixed-width fracture with a circular fracture tip.
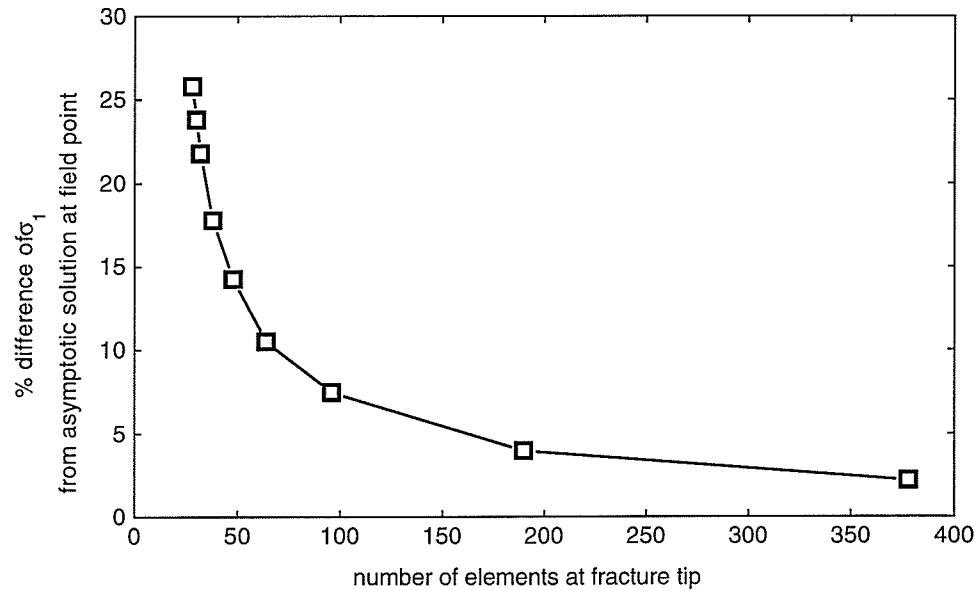
Figure 4.20: Convergence of boundary element solution at a point near the tip of a fixed-width fracture with a circular fracture tip.

load. This small difference is indicative of a stable solution.

Figure 4.21 shows the BEM solution convergence results for an elliptical fracture. This is compared directly with the analytical solution. The discretization of an elliptical fracture was controlled by the fracture aperture. A boundary element was not allowed to be longer than the fracture aperture at a specific position along the fracture. For example at the widest portion of the fracture, elements were no larger than $2\times$ the minor axis dimension. As the tip is approached the elements become progressively smaller. At the extreme fracture tip it was always ensured that the element size was less than half the distance of the closest field point. This was determined from a user specified averaging distance $d$. For the propagation exercises an elliptical fracture was typically discretized at the same level which produced about a 2% difference from the analytical solution for the single fracture.

Another interesting point from the convergence check exercise that was not shown is that $\sigma_1$ is in tension at the field point ahead of the fixed-width fracture ($\sigma_1 = -4$ MPa). It is under considerable compression at the similar point ahead of the elliptical fracture
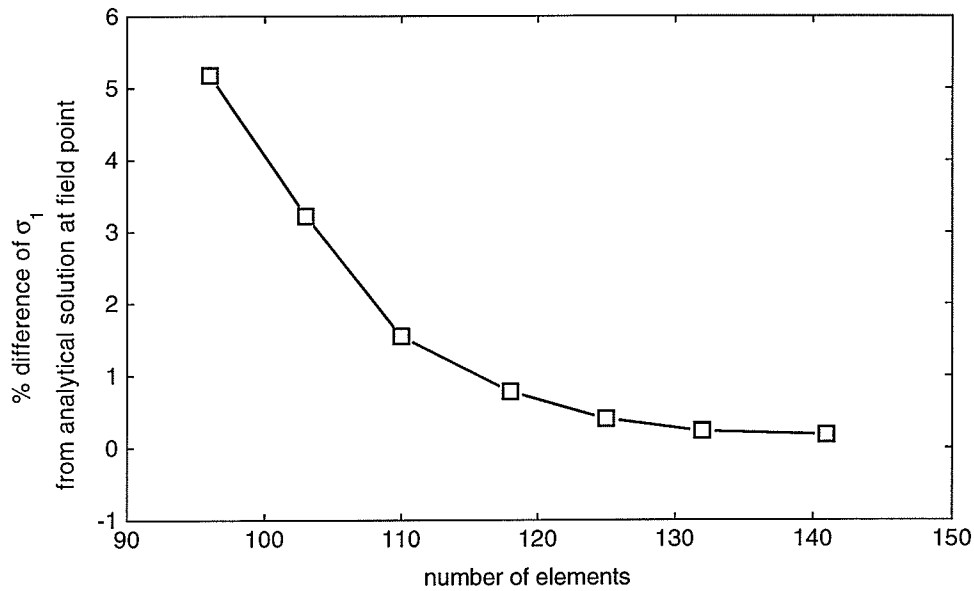
Figure 4.21: Convergence of boundary element solution at a point near the tip of an elliptical fracture.

($\sigma_1$ = 59 MPa). The fixed-width fracture obviously wants to propagate faster than the elliptical fracture.

Figures 4.22 and 4.23 show the differences in behavior demonstrated by elliptical and fixed-width fractures propagated in an infinite material loaded in compression. The elliptical fracture (Figure 4.22) shows the expected hardening behavior while the fixed-width fracture (Figure 4.23) reaches a length after which the load required to propagate the fracture remains constant. This is expected. Unlike the elliptical fracture, the fixed-width fracture has a fracture tip that maintains a constant radius of curvature. Once the head of the fracture is beyond the influence of the tail it reaches an equilibrium propagation state. Based on these findings, the fixed-width fracture should be easier to propagate than an elliptical fracture.

EJDBEM models were influenced by boundaries to a similar extent as FRANC2D, SIMEX, and InSight[2D] models. Boundary influences at the $L/R = 5$ crack tip became small at block dimensions of $H = 30R$ and at $W = 50R$ (Figures 4.24 and 4.25).
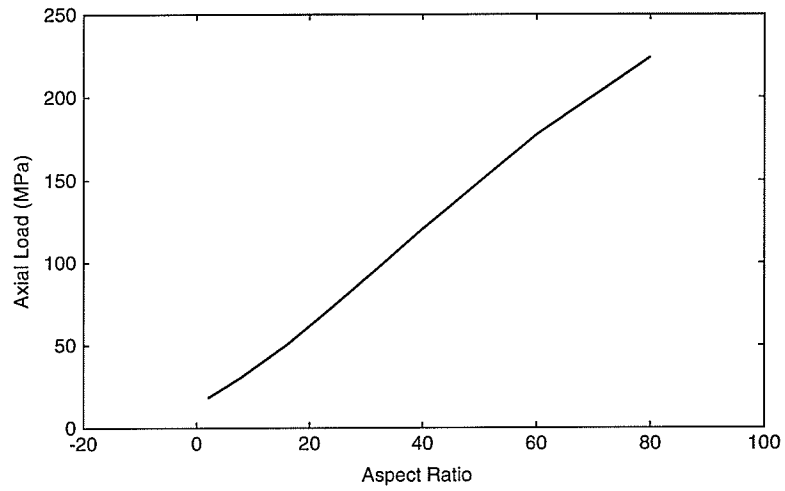
Figure 4.22: Propagation of an isolated elliptical fracture under an axial load.
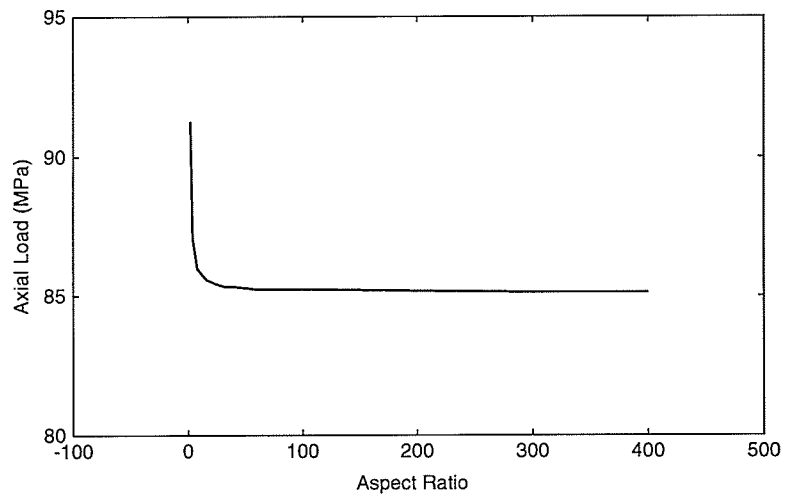


Figure 4.23: Propagation of an isolated constant-width fracture under an axial load.
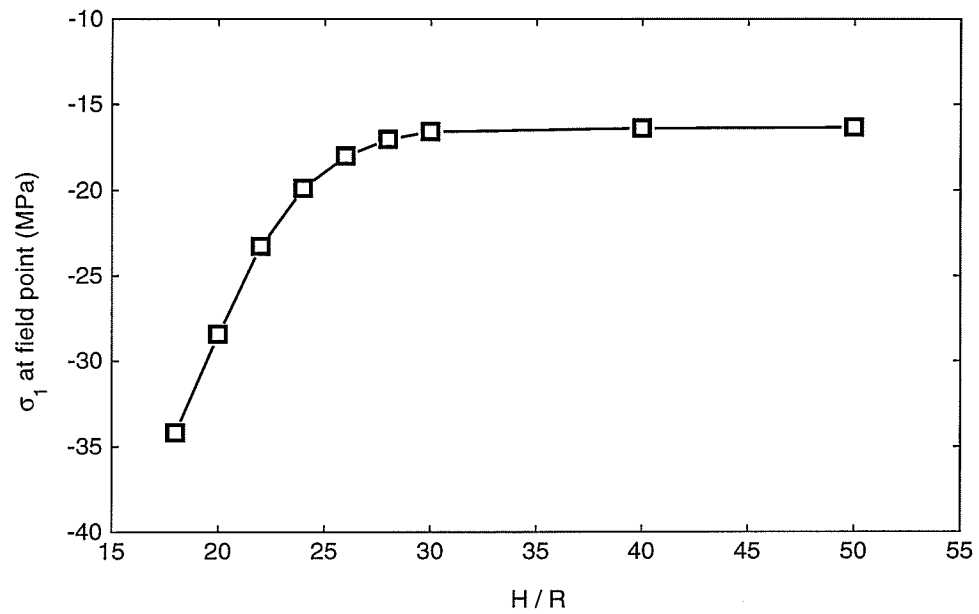
Figure 4.24: Variation of $\sigma_1$ field point ahead of $L/R = 5$ rounded crack tip for a block of variable height and constant width (EJDBEM model, $W = 10R$).
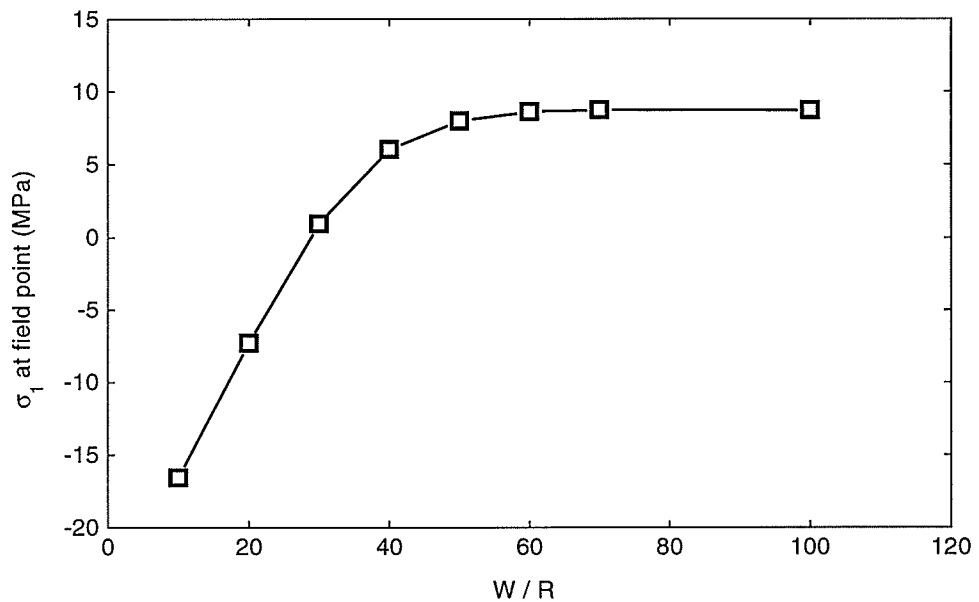


Figure 4.25: Variation of $\sigma_1$ field point ahead of $L/R = 5$ rounded crack tip for a block of variable width and constant height ($H = 30R$, EJDBEM model).
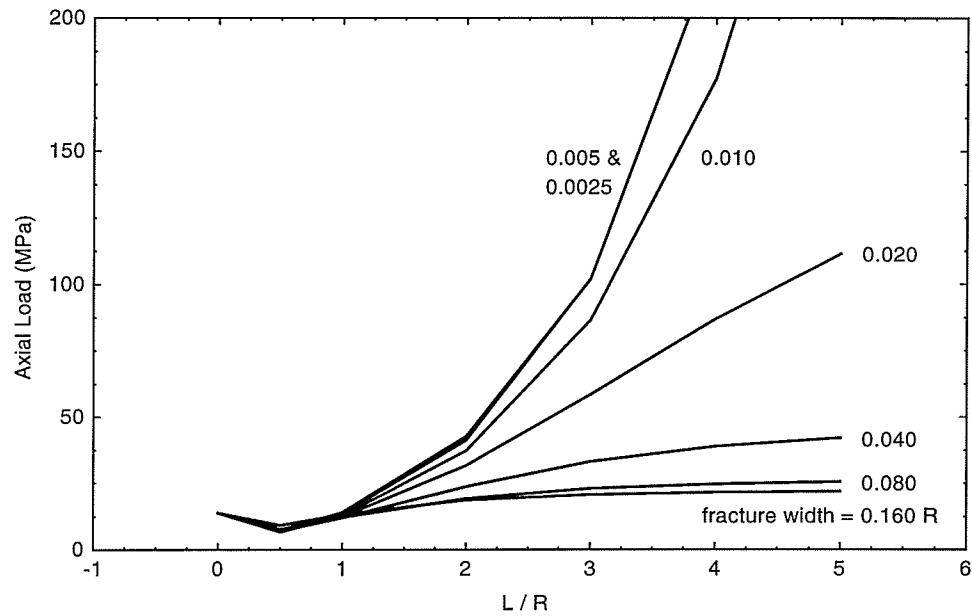
Figure 4.26: Influence of crack width on primary fracture propagation from a circular void (EJDBEM model, fixed-width fracture, circular crack tip, infinite boundaries, $d = 0.005R$).

## 4.2.2  Calibration of EJDBEM

Figure 4.26 shows the influence of crack width on primary fracture propagation of a fixed-width fracture with a circular tip. These results are similar to what was shown in Figure 4.6; wider cracks facilitate fracture propagation. Another interesting point can be gleaned from this figure. That is, the fracture propagation curves tend to cluster at opposite ends of the fracture width spectrum. The propagation curves for the two thinnest fractures (fracture widths $0.0025R$ and $0.005R$) are almost identical. The same holds true for the two widest fractures (fracture widths $0.080R$ and $0.160R$). This finding indicates that if fracture width is a parameter that is allowed to be varied, there exists a limited range of fracture widths that can be chosen for a given averaging distance to produce a proper fit to the laboratory data.

**Fixed Width Fractures**

The results from modeling a fixed-width primary fracture propagating from a circular void were similar regardless of the fracture tip that was used (semi-circle, ellipse, ovaloid). To simplify matters only the circular tip results are shown. Similar results were also obtained from modeling a fixed-width fracture with a flat tip. However, the flat tip produced erratic results the cause of which is likely the high gradients at the sharp angles of the fracture corners.

As a first step fracture propagation from all hole sizes was modeled with a single model of block dimensions $W = 10R$ and $H = 30R$. This model had the approximate width of the actual samples that were tested and had a height which minimized the platen boundary influences on fracture propagation. Figure 4.27 shows the results from modeling the two extreme hole sizes ($R = 10$ mm and $R = 50$ mm). Two cases were modeled: constant fracture width and fracture width proportional to hole radius $R$. As can be seen a good match can be obtained at one end of the spectrum while a poorer match occurs at the other.

The next step was modeling fracture propagation using the actual block dimensions. Two cases were modeled again: constant fracture width and fracture width proportional to $R$. The results are shown in Figures 4.28–4.31. Obviously, the finite boundaries do influence primary fracture propagation. It is interesting to point out that a good fit to the R50A laboratory data is obtained when a fracture width varies in direct proportion to hole size and a good fit to the R50B laboratory data is obtained when fracture width remains constant for all hole sizes (Figure 4.28). The upward curving (hardening) of the modeled $R = 50$ mm curves in Figure 4.28 are a result of the finite boundary influence. As was pointed out earlier the hardening of the laboratory data could be due to either the formation of remote fractures or a boundary influence. Remote fractures were not detected in the R50A and R50B samples until 59 and 58 MPa respectively which leaves boundary influences as a possible explanation of the hardening seen in the R50B data. The R50A data

Figure 4.27: EJDBEM calibration results (fixed-width fracture, circular tip, finite block boundaries $W = 10R$, $H = 30R$, $\Delta y = 1.75$ mm).

does not appear to be influenced by the upper block boundary. The same holds true for the R40 data in Figure 4.31. Figure 4.29 shows a reasonably good match to the $R = 20$ mm data taking into account that the "hardening" of the R20A and R20B data sets is known to be due to the formation of remote fractures and not a boundary influence. If remote fractures were modeled, the $R = 20$ mm EJDBEM propagation curves would show a hardening trend. The $R = 30$ mm results (Figure 4.30) are probably the best results. The hardening in this case is due to the boundary influence and not remote fracture formation.

When comparing the results of Figures 4.28–4.31 (pages 141–142) to the fracture mechanics results of Figures 3.77–3.80 (pages 105–107) it seems that classical fracture mechanics provides better results than the finite-width fracture model. An interesting feature to point out about the fracture mechanics results is that the fracture propagation load reaches a high peak after which an unstable mode prevails until the boundary influence forces the propagation curve to harden again (see the $R = 50$ mm curve in Figure 3.77

Figure 4.28: EJDBEM calibration results, $R = 10$ and $50$ mm (fixed-width fracture, circular tip, finite boundaries with actual sample dimensions, one point averaging, $\Delta y = 2.5$ mm).



Figure 4.29: EJDBEM calibration results, $R = 20$ mm (fixed-width fracture, circular tip, finite boundaries with actual sample dimensions, one point averaging, $\Delta y = 2.5$ mm).

Figure 4.30: EJDBEM calibration results, $R = 30$ mm (fixed-width fracture, circular tip, finite boundaries with actual sample dimensions, one point averaging, $\Delta y = 2.5$ mm).



Figure 4.31: EJDBEM calibration results, $R = 40$ mm (fixed-width fracture, circular tip, finite boundaries with actual sample dimensions, one point averaging, $\Delta y = 2.5$ mm).

and the $R = 40$ mm curve in Figure 3.80). It is interesting to point out that this stable-unstable-stable behavior is seen in the modified ring test used for determining Mode I fracture toughness [29]. The ring test has similar geometry and loading conditions as the granite blocks that were tested except that the block sides are rounded instead of flat. The EJDBEM model with the fixed-width fracture did not show this behavior.

If all boundary influences are removed (infinite boundaries) EJDBEM produces the results seen in Figures 4.32 and 4.33. Figure 4.32 compares results for a propagating fracture whose width is assumed to either remain constant (independent of hole size) or be scaled proportionally to hole radius. When fracture width is independent of hole size it is seen that the $R = 10$ mm and $R = 50$ mm curves fall within a very narrow range. However, when fracture width is assumed to vary with hole size the complete range of behavior of the $R = 10$–50 mm data is covered. Modeling results for all five hole sizes are shown in Figure 4.33 assuming fracture width varies proportionally with hole radius. This is a surprisingly good match considering there are no external boundary influences. A convincing argument could be made that boundary influences were minimal from this figure.

**Elliptical Fracture**

The same modeling exercise that was presented in the last section is duplicated in this section with the exception that an elliptical fracture is used in place of the fixed-width fracture. The elliptical fracture proved to be more difficult to model than the fixed-width fracture. In boundary element modeling it is generally assumed that closely spaced elements (as those on opposite sides of a fracture) should have a length of at least the distance separating them in order to produce a reasonably accurate solution. Because of this, the elliptical fracture required much finer discretization closer to the fracture tip than the fixed-width fracture due to its tapering geometry. Also, as an elliptical fracture grew the required discretization became increasingly finer due to the increasing aspect ratio (and thinness) of the fracture. This resulted in accuracy and precision problems once a fracture
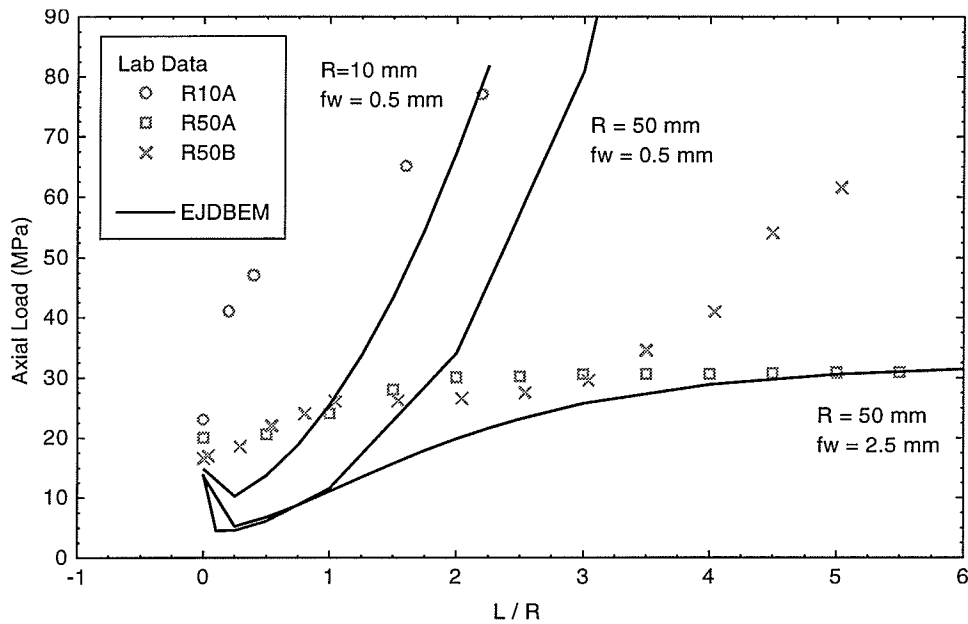
Figure 4.32: EJDBEM calibration results for $R = 10$ mm and $R = 50$ mm hole sizes (fixed-width fracture, circular tip, infinite boundaries).
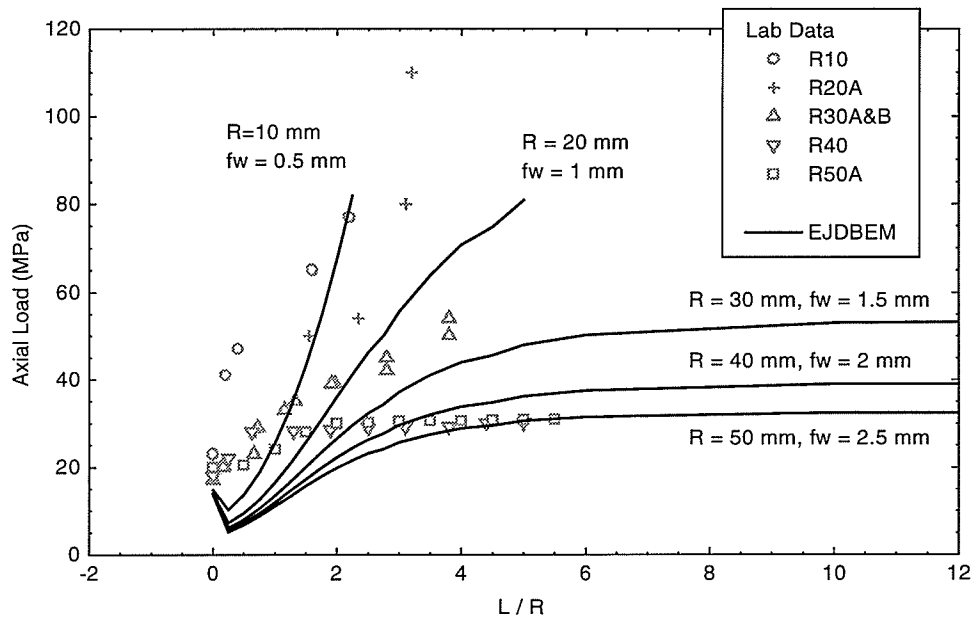


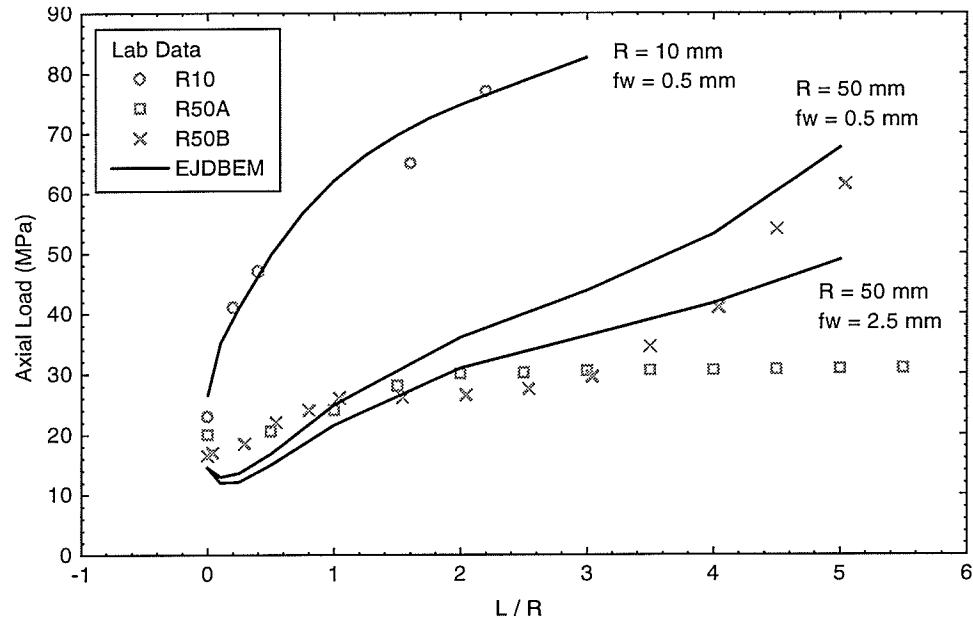Figure 4.33: EJDBEM calibration results for all hole sizes (fixed-width fracture, circular tip, infinite boundaries).
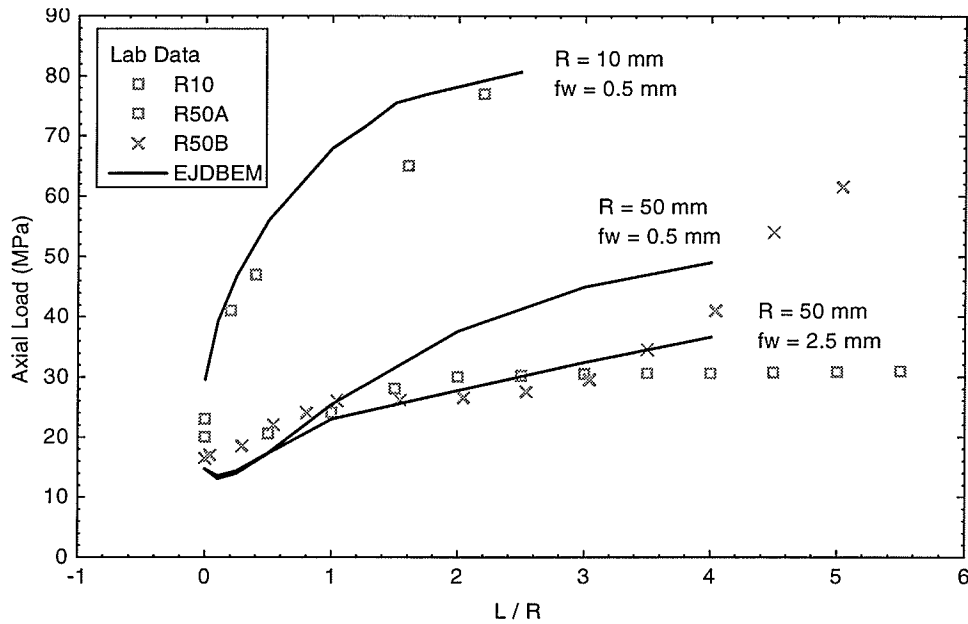
Figure 4.34: EJDBEM calibration results (elliptical fracture, finite block boundaries $W = 10R$, $H = 30R$, $\Delta y = 2$ mm).

reached a certain length. It is interesting to point out that almost identical behavior is demonstrated by the elliptical fracture as its fixed-width counterpart when modeled block boundaries are finite (compare Figure 4.27 with Figure 4.34, also compare Figures 4.28–4.31 with Figures 4.35–4.38).

When infinite boundaries are considered the elliptical fracture behaves differently than the fixed-width fracture (compare Figures 4.32 with Figure 4.39). Even when the elliptical fracture's width is scaled in proportion to hole size it hardens much too rapidly to get a proper match to the $R = 50$ mm laboratory data in Figure 4.39. As the elliptical crack grows the radius of curvature at the crack tip progressively gets reduced making the fracture more difficult to propagate. At high aspect ratios the elliptical fracture would be expected to behave similar to the zero-width mathematical fracture. And indeed it does. The EJDBEM elliptical fracture emanating from a circular void model is consistent with the analytical fracture models in infinite plates presented in Chapter 3 (e.g., Sammis and Ashby, Rummel,
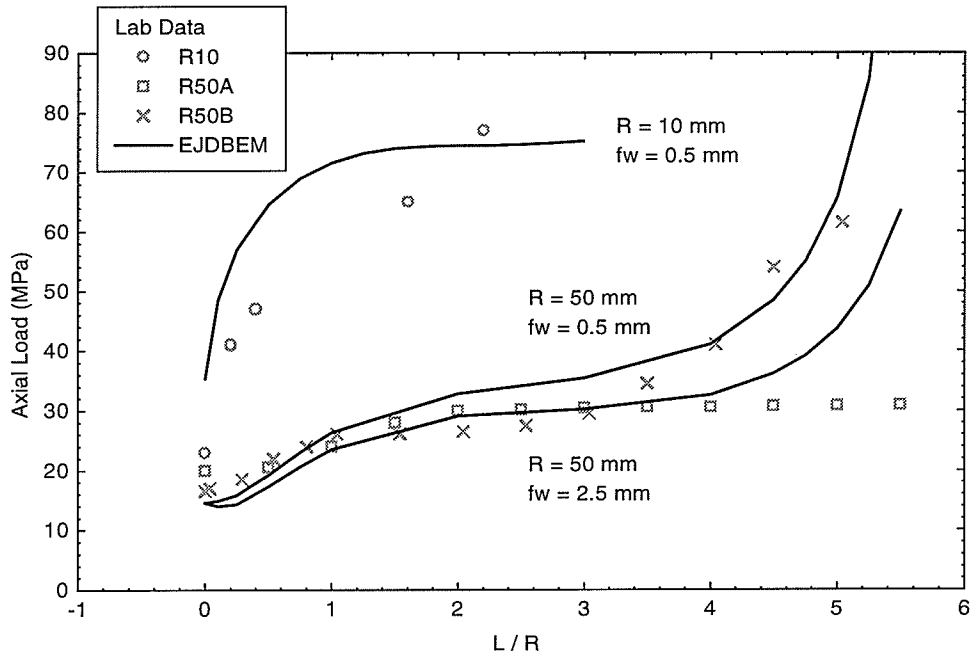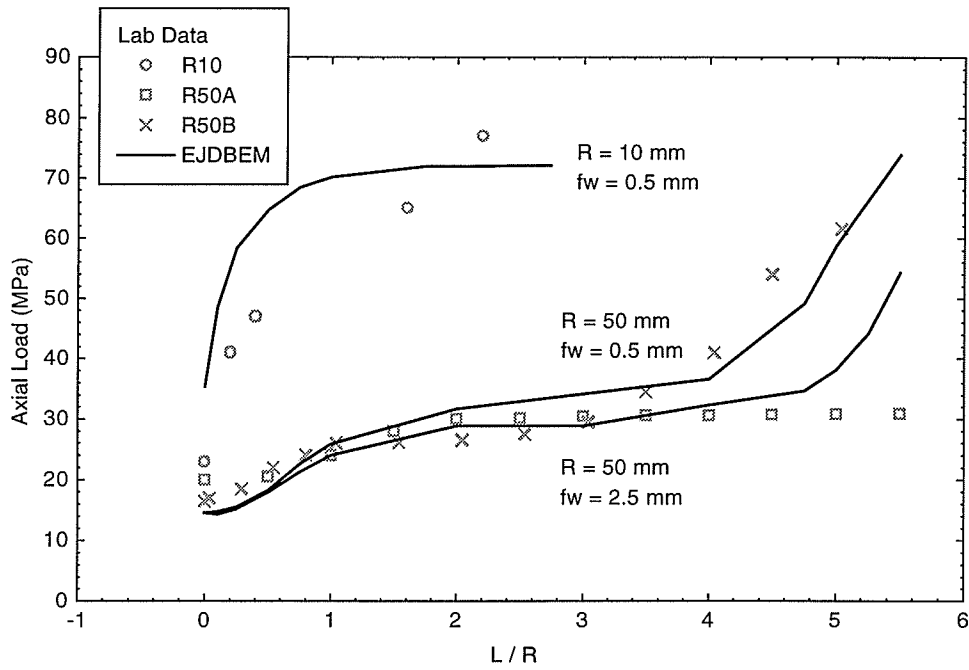
Figure 4.35: EJDBEM calibration results, $R = 10$ and 50 mm (elliptical fracture, finite boundaries with actual sample dimensions, one point averaging, $\Delta y = 2.5$ mm).
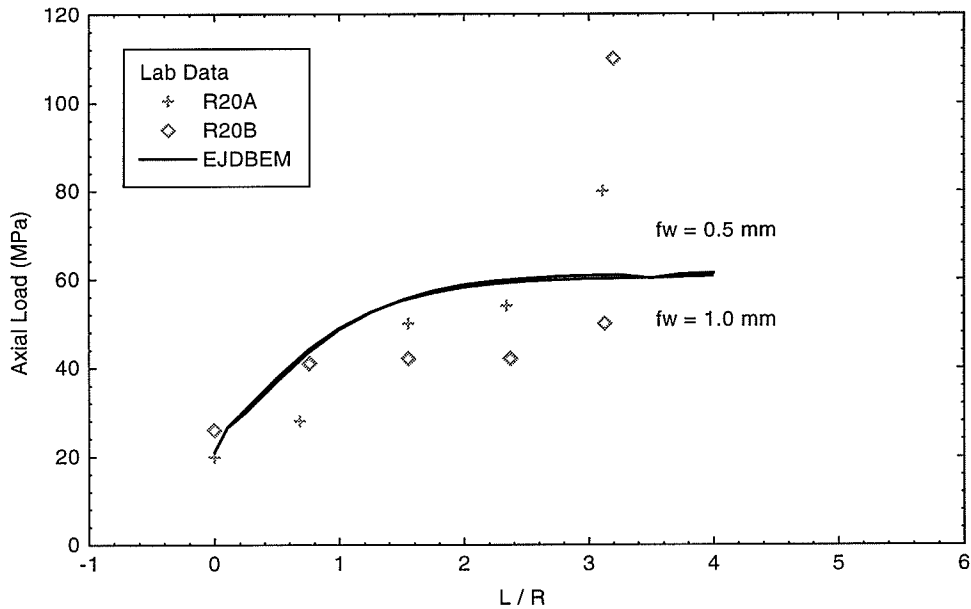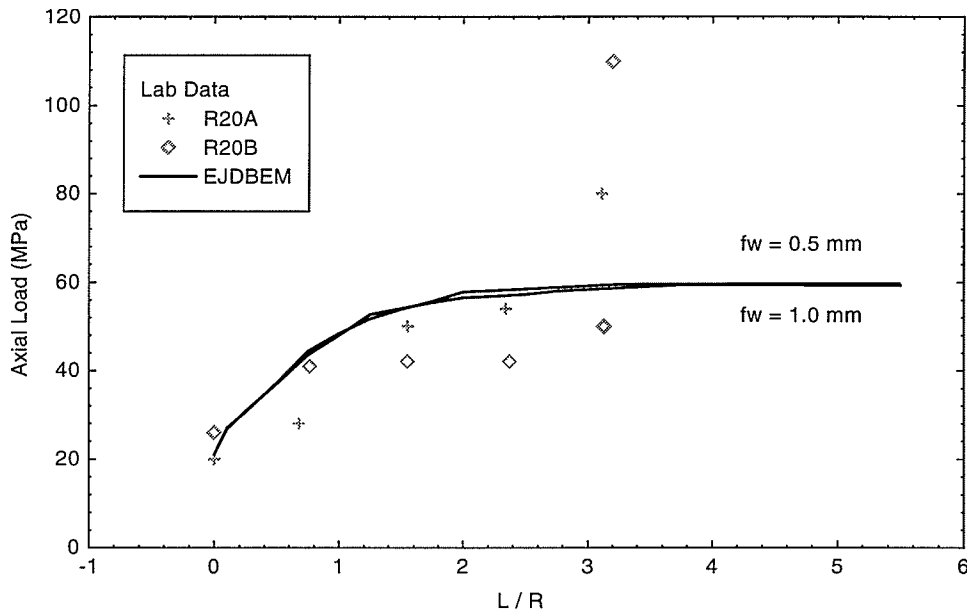


Figure 4.36: EJDBEM calibration results, $R = 20$ mm (elliptical fracture, finite boundaries with actual sample dimensions, one point averaging, $\Delta y = 2.5$ mm).
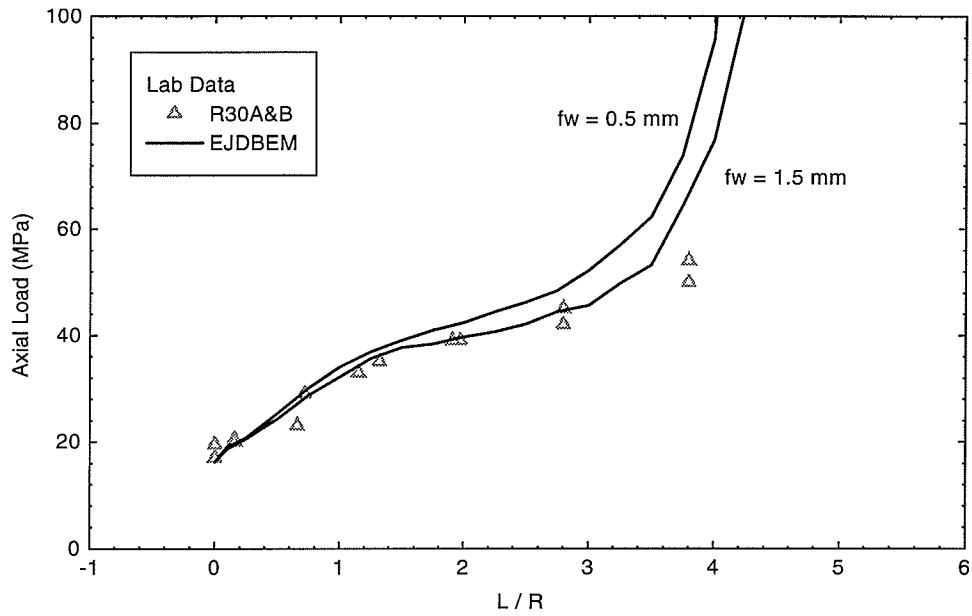
Figure 4.37: EJDBEM calibration results, $R = 30$ mm (elliptical fracture, finite boundaries with actual sample dimensions, one point averaging, $\Delta y = 2.5$ mm).
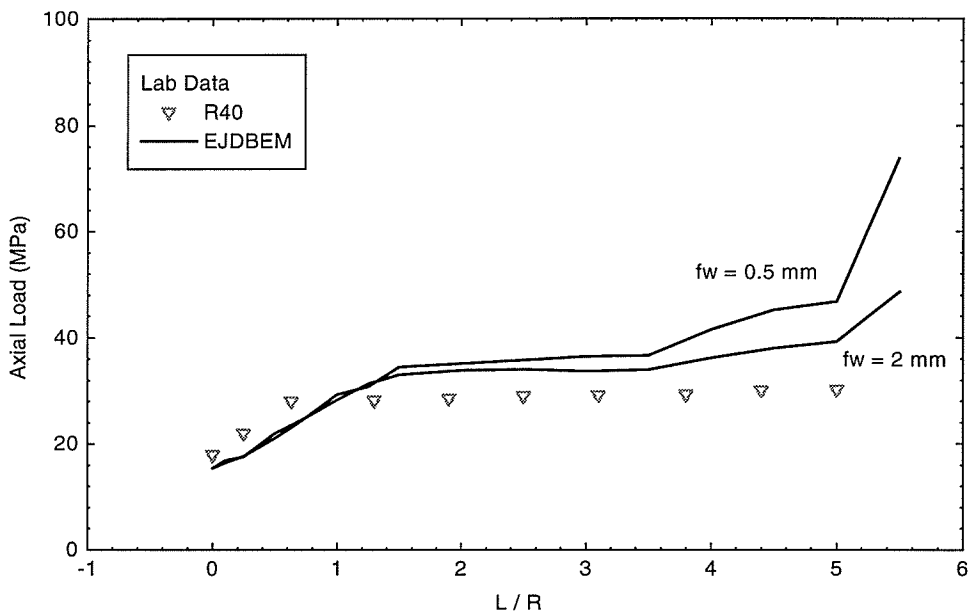


Figure 4.38: EJDBEM calibration results, $R = 40$ mm (elliptical fracture, finite boundaries with actual sample dimensions, one point averaging, $\Delta y = 2.5$ mm).
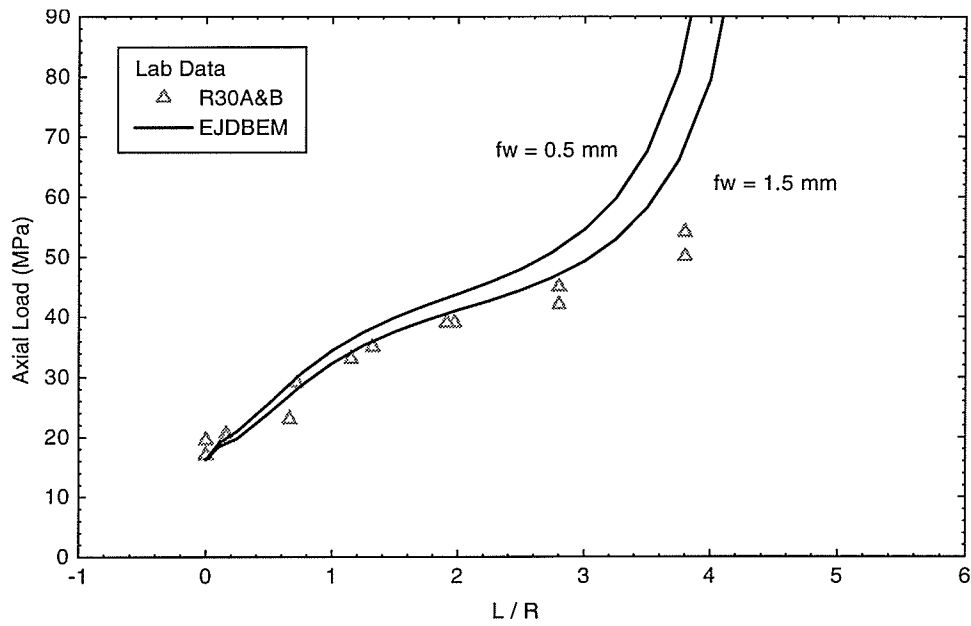
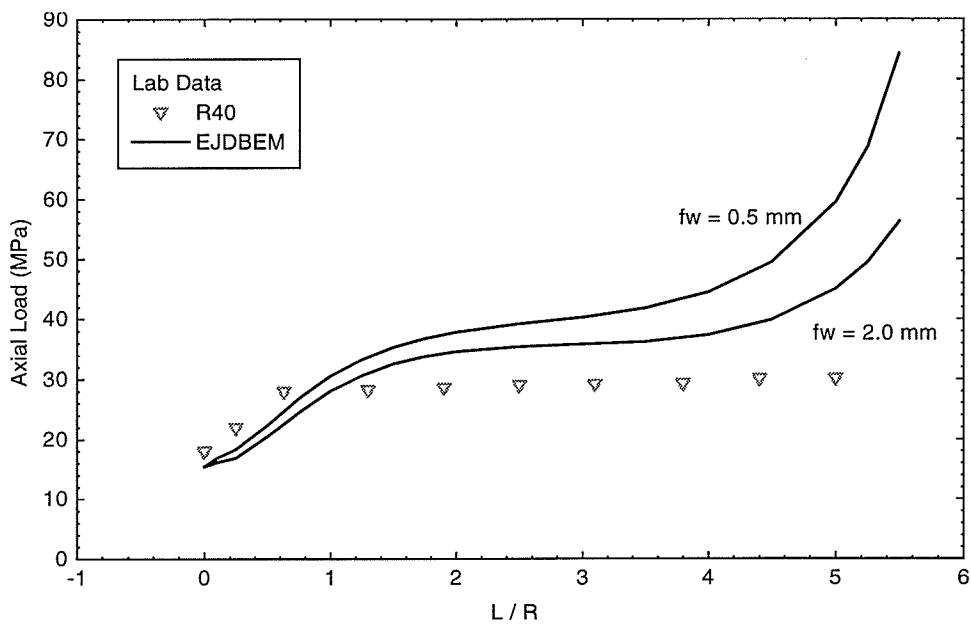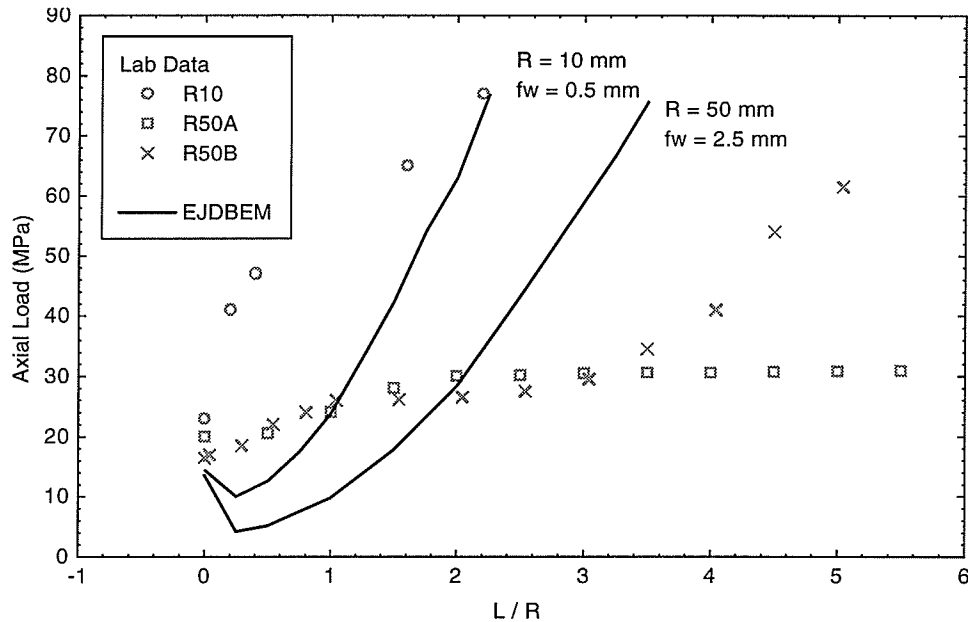Figure 4.39: EJDBEM calibration results (elliptical fracture, infinite boundaries, one point averaging, $\Delta y = 0.159$ mm).

Sih, Paris and Sih).

### 4.2.3 Tracking the State of Stress at the Tip of a Propagating Fracture

The state of stress at various points in the EJDBEM model were tracked to get a better understanding of how stresses are distributed throughout the model and which components contribute to the fracture process. This exercise is similar to what was done in section 4.1.3 except the boundary element solution is used here with a circular fracture tip and the one-point averaging scheme (instead of the finite element solution with the flat fracture tip and two-point averaging scheme). In this exercise the influence of tension on remote fracture initiation is investigated further.

Two models were investigated; one with finite boundaries and the other with infinite boundaries. Figure 4.40 tracks the tensile stresses as well as USR at the remote fracture nucleation point near an $R = 10$ mm hole while the propagating primary fracture is maintained in a critical state (USR $= 1$). In this case a remote fracture would initiate when the

primary crack reached a length of approximately $L/R = 1.6$ at a load of about 65 MPa. The crack tip compression has too much influence on fracture propagation in this case. In the laboratory, remote fractures for the $R = 10$ mm samples initiated between 86 and 108 MPa at $L/R \approx 2.5$. When the same model is run using a maximum tension fracture criterion a good match is obtained with the R10 primary fracture data set as well as with the remote initiation point (Figure 4.41).

Figures 4.42 and 4.43 are similar to the previous two figures except that infinite boundaries are used in the models. In both the USR and maximum tension cases a remote fracture initiates at reasonable values for applied load and primary fracture length. In Figure 4.42 (USR criterion) a remote fracture initiates at a primary fracture length of approximately $L/R = 2.25$ at a load of about 78 MPa. In Figure 4.43 (maximum tension criterion) a remote fracture initiates at a primary fracture length of approximately $L/R = 2.5$ at a load of about 100 MPa. The stiffening effect of the infinite boundary pushes the remote initiation point to a higher load than that produced with a model with finite boundaries. Also, it is interesting that the model using the USR criterion results in a remote fracture initiating earlier than the model using the maximum tension criterion.

In this exercise (Figures 4.40–4.43) all models used identical fracture parameters (fracture width $= 0.5$ mm, $\Delta y = 1.5$ mm). This resulted in different curve fits to the R10 data set, especially when finite boundaries were used (Figures 4.40 and 4.41). A smaller $\Delta y$ in Figure 4.41) would produce a propagation curve more closely resembling that in Figure 4.40. This would, in turn, drive the remote fracture initiation load down to a level closer to that observed in Figure 4.40.

This modeling exercise was done out of interest to see the extent compressive forces had on remote fracture formation. Several important factors were purposely overlooked to accommodate this simplified model. One important factor to consider is the location of the critical point in the remote fracture region. The critical point in the remote region does not remain fixed as the primary fracture grows; it moves in response to the changing geometry.
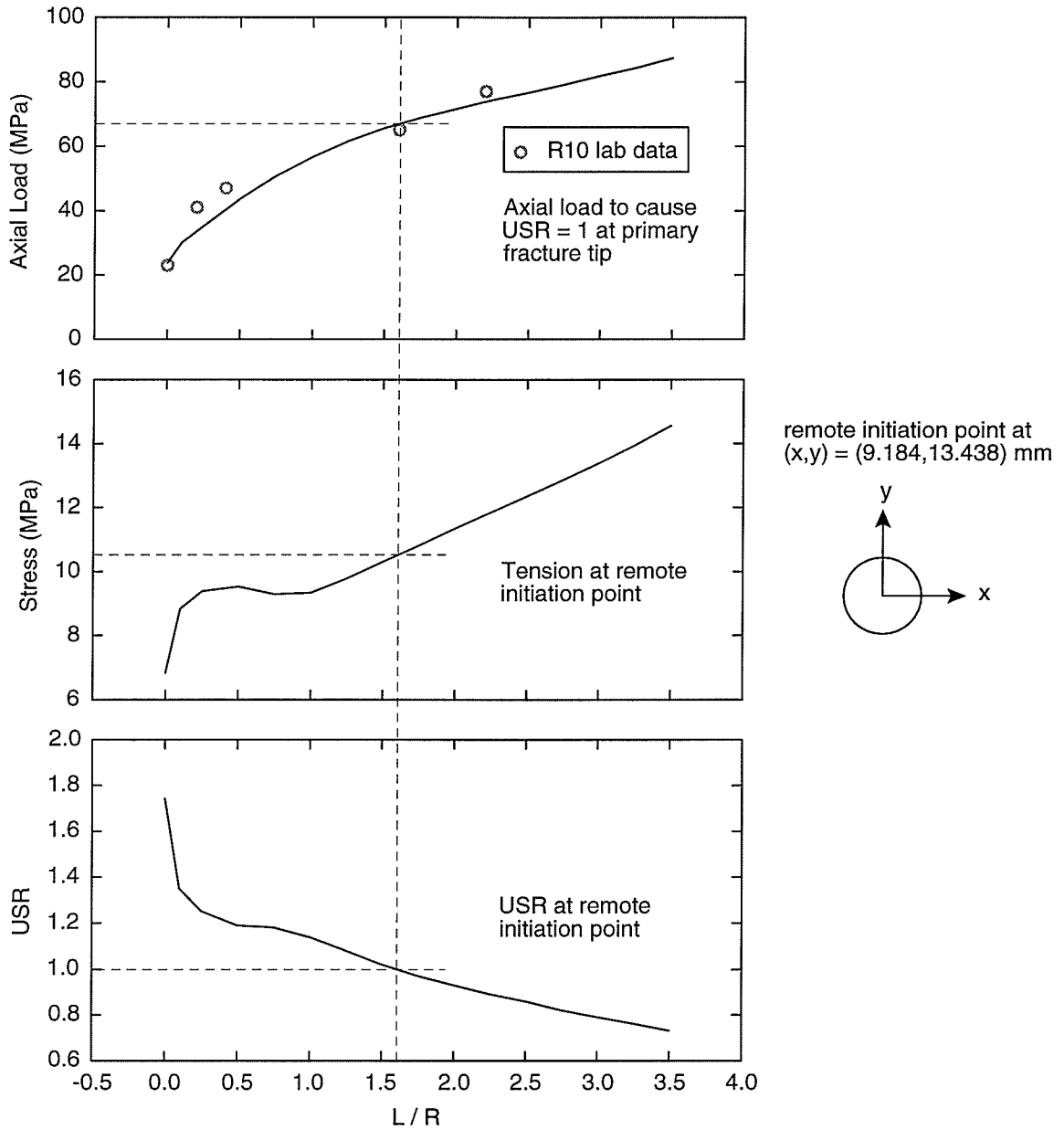
Figure 4.40: Modeled crack tip stresses from a propagating crack from an $R = 10$ mm cavity (EJDBEM model, USR fracture criterion, finite boundaries, $W = 10R$, $H = 30R$, circular-tip fracture, one-point averaging, fracture width $= 0.5$ mm, $\Delta y = 1.5$ mm).
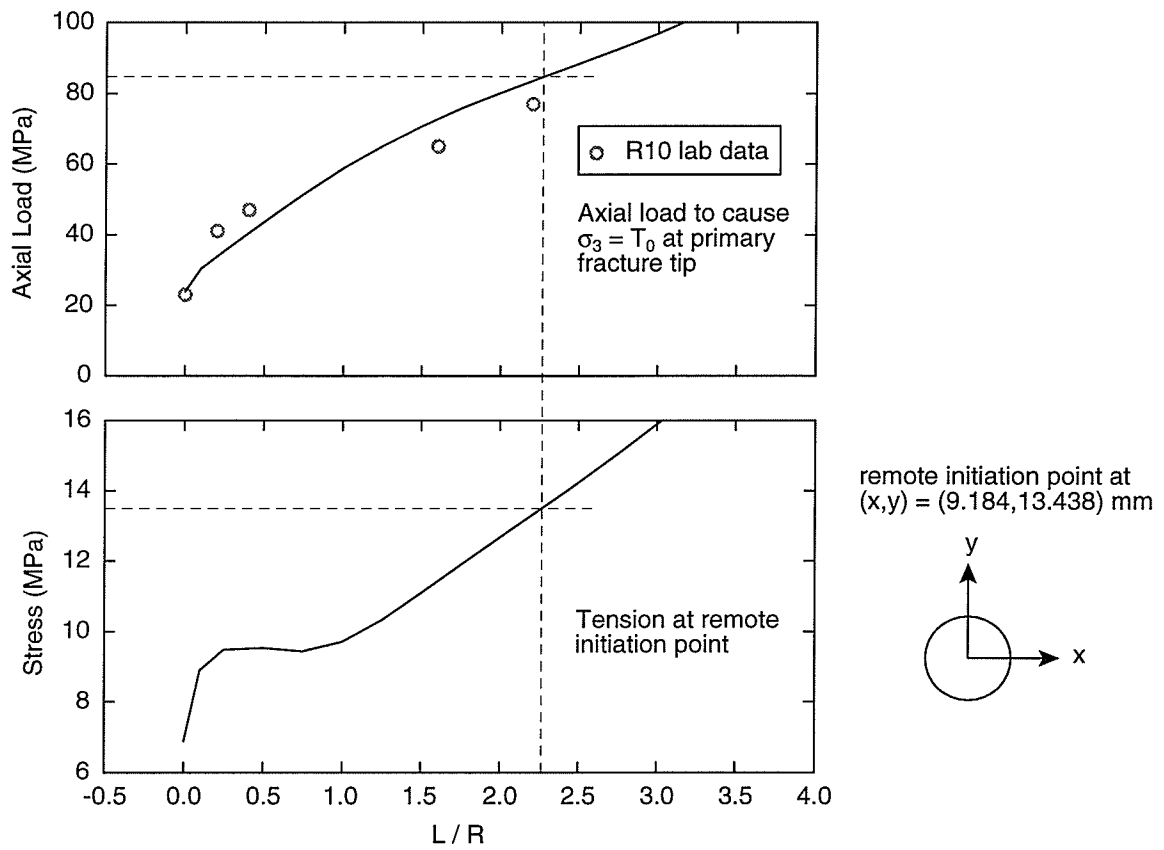
Figure 4.41: Modeled crack tip stresses from a propagating crack from an $R = 10$ mm cavity (EJDBEM model, maximum tension fracture criterion, finite boundaries, $W = 10R$, $H = 30R$, circular-tip fracture, one-point averaging, fracture width $= 0.5$ mm, $\Delta y = 1.5$ mm).
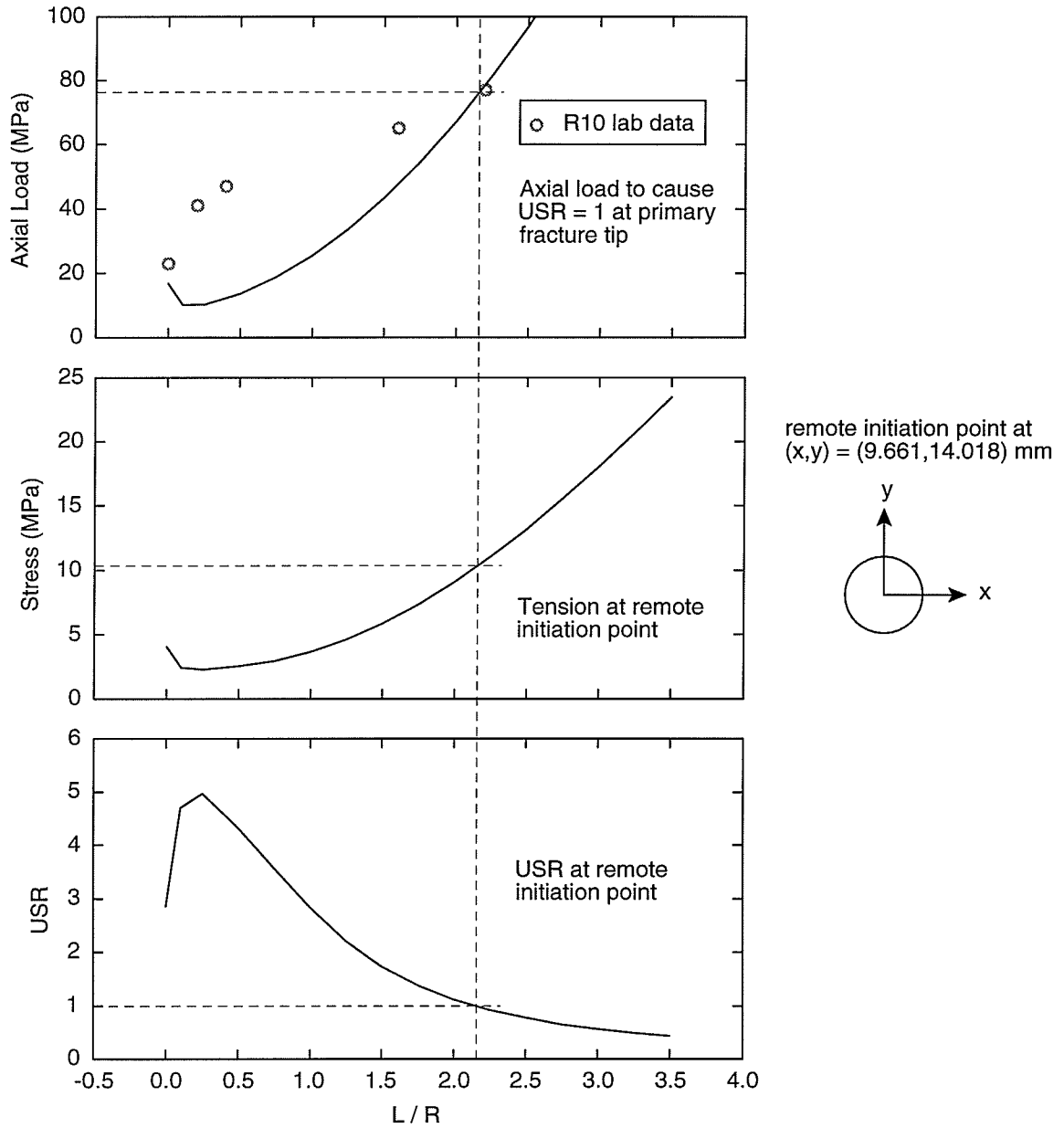
Figure 4.42: Modeled crack tip stresses from a propagating crack from an $R = 10$ mm cavity (EJDBEM model, USR fracture criterion, infinite boundaries, circular-tip fracture, one-point averaging, fracture width $= 0.5$ mm, $\Delta y = 1.5$ mm).
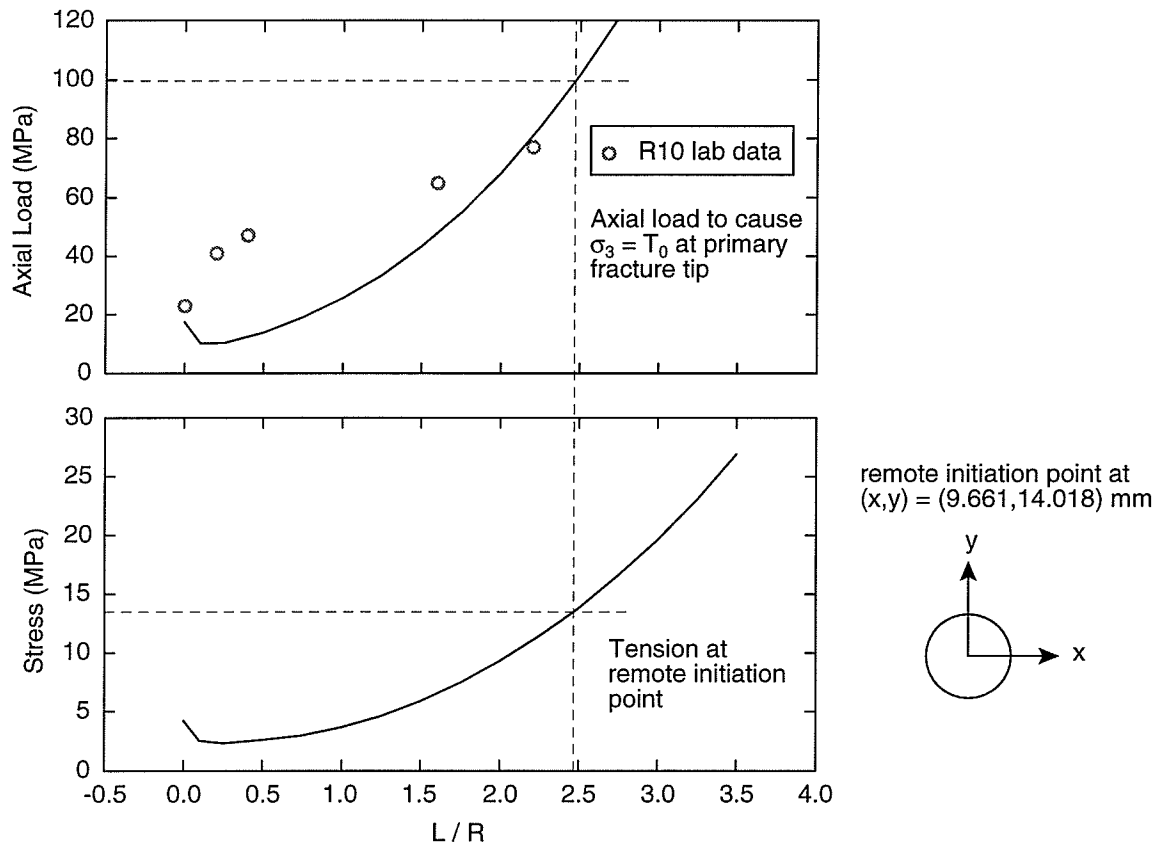
Figure 4.43: Modeled crack tip stresses from a propagating crack from an $R = 10$ mm cavity (EJDBEM model, maximum tension fracture criterion, infinite boundaries, circular-tip fracture, one-point averaging, fracture width $= 0.5$ mm, $\Delta y = 1.5$ mm).

Also, the critical initiation point will change location in response to the fracture criterion used (USR or maximum tension in this case). In the cases shown here a fixed remote fracture initiation point was chosen and assumed to be the same for the USR and maximum tension models. Boundary influences also contribute to remote fracture behavior. The finite boundary cases modeled in Figures 4.40 and 4.41 do not represent the physical sample accurately. Nor do the infinite boundaries of Figures 4.42 and 4.43. The results shown here illustrate that compressive forces produce a dramatic difference in remote fracture initiation when finite model boundaries are used. Ingraffea [43] cites having difficulty initiating remote (secondary) fractures in his model due to insufficient tensile forces. Perhaps compressive forces are the missing key.

## 4.3  Summary and Discussion of Numerical Modeling Results

Table 4.1 provides cross-references to figures of the numerical modeling results that produced good matches to the laboratory data. In summary, the $\sigma(\theta)_{\max}$ theory of classical linear elastic fracture mechanics represents the size dependent primary crack propagation phenomenon very well when actual specimen dimensions are used in the model. Good results are also obtained with boundary element solutions using either an elliptical or fixed-width crack in a model using actual specimen dimensions. Arguments can be made to scale fracture width in proportion to hole size or maintaining a constant fracture width throughout the modeling. When all boundary influences are removed (infinite boundaries) a good match to laboratory data is obtained with a fixed-width fracture model and scaling fracture width in proportion to hole size.

The hardening trend shown by some of the primary fracture propagation curves can be attributed to platen boundary influences or the formation of remote fractures. Compression testing of larger samples would allow primary fractures to propagate a greater distance before being influenced by platen boundaries. It is interesting to point out that in order

| Model | Fracture Type | Block Dimensions | Figure | Page |
|-------|---------------|------------------|--------|------|
| SIMEX | zero-width $\frac{1}{4}$ pt. singularity | actual | 3.77–3.80 | 105–107 |
| EJDBEM | fixed-width circular-tip | actual | 4.28–4.31 | 141–142 |
| EJDBEM | fixed-width circular-tip | infinite | 4.33 | 144 |
| EJDBEM | elliptical | actual | 4.35–4.38 | 146–147 |

Table 4.1: Cross references to figures of best numerical results.

to avoid boundary influences in numerical modeling it is a general rule of thumb to make the model boundary dimensions at least ten times the maximum structure dimension (both in the x and y dimensions). With this in mind a model with an $R = 50$ mm hole with a primary fracture length of $L/R = 5$ would require a block of height and width equal to 6 m to minimize boundary effects. This is obviously impractical to test in the laboratory.

The suite of laboratory samples used in this thesis were of variable relative size. A reason for this is that all the tested samples were not exclusively designed for this thesis. Some of the test results were obtained from testing done years prior to the commencement of this thesis. An ideal set of laboratory samples for fracture propagation testing would have identical relative dimensions (i.e., $H/R = C_1$, $W/R = C_2$, $D/R = C_3$, where $C_n$ is a constant value) resulting in similar boundary influences for all tests. On the same note, to obtain a better assessment of the lateral boundary influences a suite of tests could be performed on blocks with varying lateral dimension and identical height and hole size. Tests on blocks with variable height and constant width and hole size would shed some light on platen boundary influences. Nonetheless, it is very encouraging to see that the size-dependent fracture propagation data that was gathered for this thesis can be, for the

most part, explained with either classical linear elastic fracture mechanics or stress-based finite-width fracture models.

Bažant [4] actually suggests a method which can account for the influence of the nonuniformity of relative block dimensions. However, this method relies on comparing similar structures within the blocks (i.e., blocks with only primary fractures cannot be compared with blocks with both primary and remote fractures) as is the case with his fracture law presented in Chapter 3. Bažant's size effect law did produce an excellent fit to the lab data until the point where remote fractures initiated (Figure 3.39, page 68) therefore further curve fitting was not attempted. This good fit is also an indication that the nonuniformity of the relative block sizes may not have had a substantial influence on the primary fracture propagation results.

## 4.4   Stress Averaging and Modeling of Step-Out Fractures

In a different series of similar experiments performed on granite samples obtained from AECL's Underground Research Laboratory (not included here), the affect of confining pressure was tested on fracture propagation on biaxially loaded samples. An interesting result of these experiments is that under sufficient confining pressure an $R = 50$ mm sample will produce remote fractures prior to producing primary fractures. In the lab testing done for this thesis, only the smallest hole ($R = 2.5$ mm) produced remote fractures without any indication of primaries forming under uniaxial loading conditions (see Figure 2.4, page 11). In the remaining samples, primary fractures always initiated before the remote fractures. The $R = 2.5$ mm sample had a block width of $43.2R$. The $R = 50$ mm samples had block widths of $10R$. It could very well be that the large width of the $R = 2.5$ mm sample contributed to the suppression of primary formation through a confining pressure affect.

The stress averaging model can also offer an explanation for the aforementioned phenomenon without the need for varying the lateral boundary dimension. When a block with

a circular void is loaded in uniaxial compression (Figure 4.44) a high tensile stress concentration develops at the apex of the hole as well as forming two lobes of high tension at either side of the apex. It is these tensile stresses that play the dominant role in fracture initiation and propagation. If stress averaging is assumed to occur over a circular area, an appropriately sized averaging circle can be found that will take advantage of the high stress concentration in one of the lobes and produce a critical condition at the remote initiation point, indicated by the cross in the center of the averaging circle in Figure 4.44, before a critical condition exists at the primary crack initiation point at the apex of the opening. When the averaging circle is placed at the apex of the circular void a large portion of it will contain a region of low stresses. This produces a less critical condition at the apex of the hole than at the remote fracture initiation point. Therefore as hole size decreases the relative size of the averaging circle increases which in turn increases the tendency for remote fractures to form prior to the formation of primary fractures. It should be pointed out that once a certain size averaging circle is exceeded, remote fractures always initiate prior to primary fractures with the stress averaging model. This averaging mechanism is also a possible explanation for the absence of natural "wing-cracks" in rock specimens loaded in compression. If the $R = 2.5$ mm hole size is a small enough flaw to result in remote fracture formation (due to stress averaging) then smaller scale material flaws could not be expected to act as starters for primary fractures (such as wing cracks). Perhaps all small scale fractures we see initiating in rock specimens are remote fractures.

It was originally thought that the step-out condition that occurs with propagating fractures was a function of fracture length. Figure 4.45 shows results of part of this study. This figure shows averaged $\sigma_3$ stress contours at the tip of a propagating isolated elliptical fracture with the lightest colored contour indicating the most tensile region. As the elliptical fracture lengthened it was hypothesized that the tendency for remote fractures to form would increase. This argument followed directly from the observation of only remote fractures forming in the smallest hole tested ($R = 2.5$ mm). As was just discussed, a conjecture
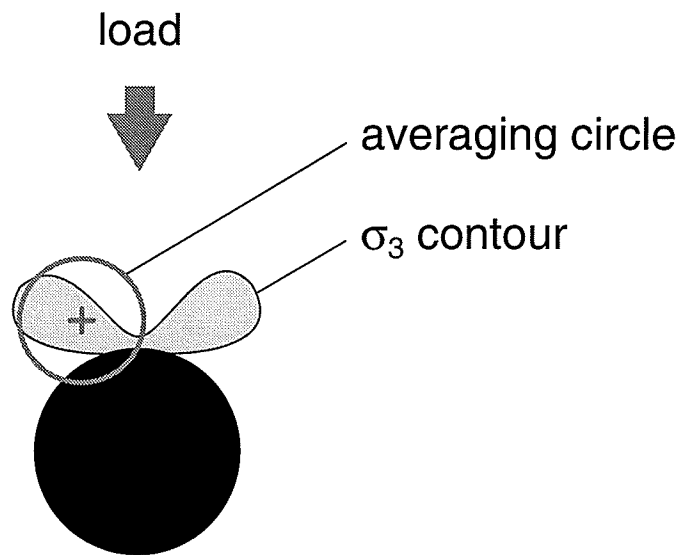
Figure 4.44: Formation of remote fractures without primary fractures.

that could be made is the smaller the hole the greater the tendency for remote fractures to form before primary fractures. Similarly, a thinner fracture would be expected to produce remote fractures more readily than a wider fracture (the elliptical fracture becomes progressively thinner near it's tip as it lengthens). It was found that with a sufficiently large averaging circle, step-outs could always be made to form at a fracture tip, with no propagation occurring at the actual fracture tip. With smaller averaging circles, the critical condition always occurred at the fracture tip proper with no step-outs occurring. It was always either consistent fracture tip failure or consistent step-out conditions at a fracture tip; not a combination of both phenomenon. However, it was found that the difference between the critical condition at the fracture tip and the step-out location was extremely small. This prompted the following additional study.

Dzik and Lajtai [26] have, in fact, demonstrated that the step-out condition is a function of material inhomogeneity as well as crack length. In a homogeneous material it was found that increasing the crack length increased the tendency for step-out conditions, but that it was not possible to actually initiate a step-out fracture by changing crack length alone. By
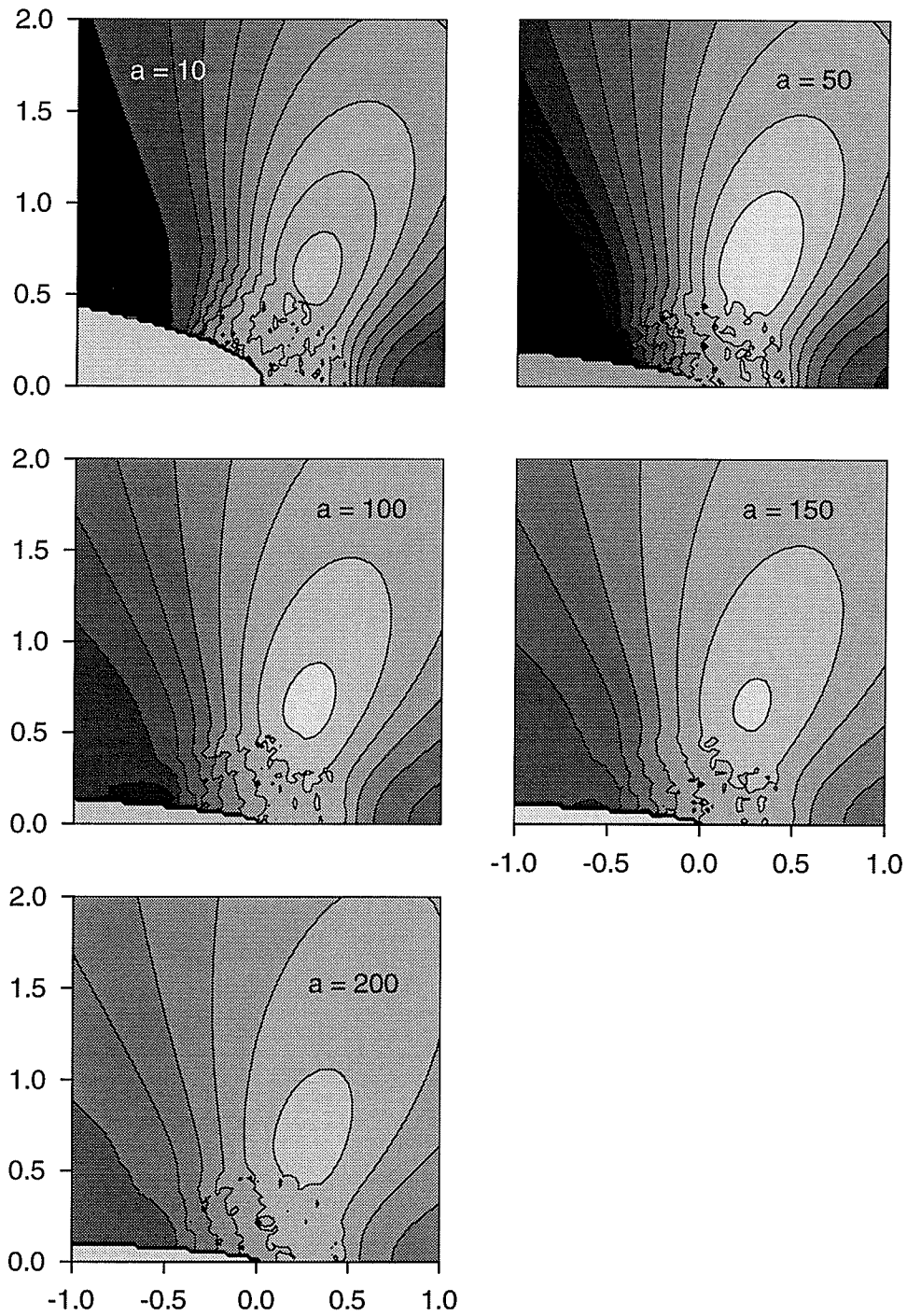
Figure 4.45: $\sigma_3$ contours near the tip of a propagating elliptical fracture. $a = 10$–$200$ mm, $b = 1$ mm, $d = 0.5$ mm, horizontal load $= 100$ MPa.
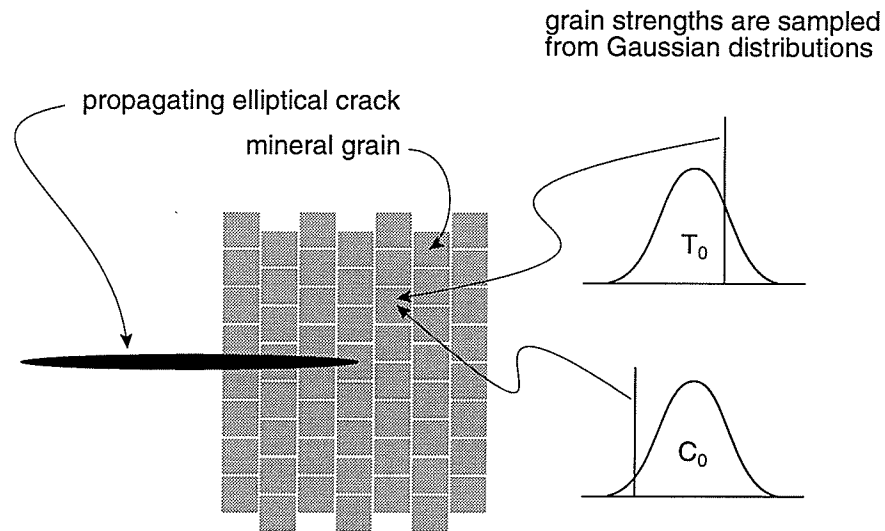
Figure 4.46: Randomly distributed material strengths.

adding material inhomogeneity into the model it was possible to generate step-out fractures. A probabilistic model was incorporated into EJDBEM for this purpose. In this model a fracture was propagated through a regular lattice of mineral grains (Figure 4.46). Each grain was randomly assigned a material strength. The material strength was assumed to be Gaussian distributed. It was found that small deviations in material strength were enough to create the occasional step-out condition observed in laboratory samples. Figure 4.47 shows two identically loaded elliptical fractures. The homogeneous material (left) would fail at the fracture tip while the heterogeneous material (right) would have a critical point in the step-out region under sufficient load.

With this type of a probabilistic model it is possible to generate a very long unstable crack sequence under certain conditions with an elliptical crack. As an isolated elliptical crack grows under an applied axial compressive load it becomes progressively more difficult to propagate. In a homogeneous material, a finite-width elliptical crack will reach an equilibrium length $(L)$ at a given load level $(P)$ (stable propagation). If the same initial crack is placed into a heterogeneous material and the material is loaded to a level $P$, the crack
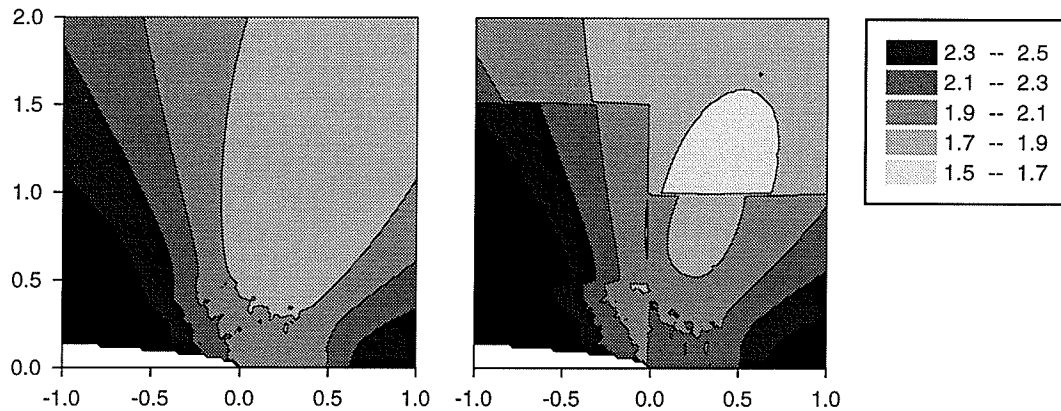
Figure 4.47: USR contours near elliptical fracture tip. Homogeneous material (left) and heterogeneous material (right). $a = 109$ mm, $b = 1$ mm, $d = 1$ mm, grain size $= 1$ mm, horizontal load $= 100$ MPa, standard deviation of $C_0$ and $T_0$ $= 10$ MPa and 1.5 MPa respectively.

may step-out before it reaches a length $L$. When a step-out occurs from the parent crack, the step-out crack will initially have a lower aspect ratio than the parent crack and will propagate in an unstable manner until it reaches the same dimensions as the stable crack (length $L$ at load $P$). If a second step-out occurs (from the first step-out) it will continue propagating until its aspect ratio reaches the equilibrium level. From this argument it can be seen that an axial crack array has the potential to propagate very rapidly through a heterogeneous material at a constant load. This may offer another explanation for the rapid propagation trends sometimes seen in laboratory testing. Figure 4.48 shows the results of a crude simulation of this phenomenon.

The step-out phenomenon is a key element in understanding *en echelon* crack formation which often leads to the shear band type of failure commonly observed in compression testing of cylindrical samples of rock (Figure 4.12, page 125) or concrete. This aspect of fracture propagation obviously warrants further study.

When stress averaging is done it is difficult to produce "clean" results very close to the fracture tip as can be seen in Figure 4.45. This problem is a direct result of the discontinuous stress field created by the fracture as well as by the stress averaging technique. A fracture
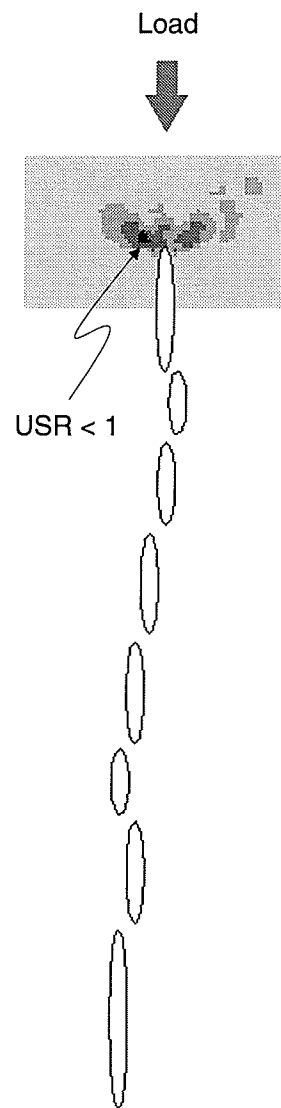
Figure 4.48: Propagating fractures through a heterogeneous material.

Do stresses from one side of an open fracture influence stresses on the other side?

Averaging circle increased in size to compensate for area lost to void space.
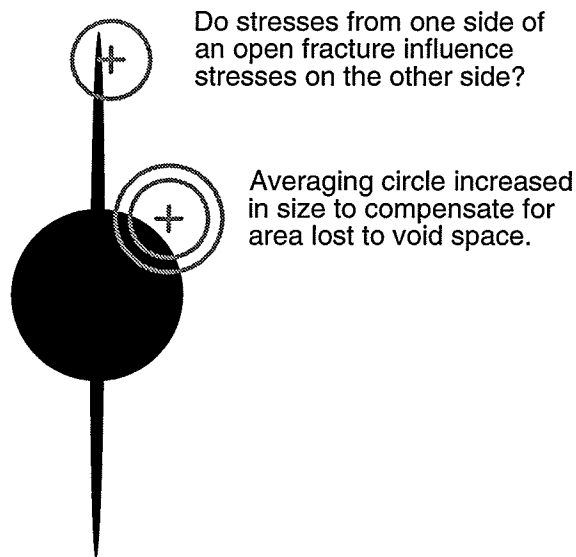
Figure 4.49: Problems with stress averaging.

creates a discontinuity in the material as well as in the stress field. This problem raises some additional questions. When averaging is done near a fracture boundary (or any boundary) a portion of the averaging circle can cross the boundary into a region where no material exists (Figure 4.49). When this occurs, several options exist on how to proceed. One option is to compensate for the lost averaging area by adding the lost averaging area to that portion the averaging circle in the region containing material. Another option is to only use the results where the averaging circle is completely inside the material. A similar type of problem exists at the fracture tip. If the fracture tip intersects the averaging circle, but does not completely split it into two portions (Figure 4.49), is it realistic to assume that stresses from each side of the fracture influence the average stress? These questions also warrant further attention.

# Chapter 5

# Summary, Conclusions, and Future Research

## 5.1 Summary

### 5.1.1 Laboratory Testing Results

Fracture propagation data was collected during the compressional loading of Cold Spring granite blocks. The specimens were of variable size and each had a circular hole drilled through the narrowest dimension. Hole radius ranged from 2.5 mm to 50 mm. Although the initiation and propagation histories of all fracture types (primary, remote, spalling) were tracked, this thesis focused on studying primary fractures. These fractures emanate from the tensile stress concentration of the circular void.

The primary fracture propagation data basically shows two contrasting trends controlled through a complex size-boundary effect (Figures 5.1 and 5.2). A stable mode was exhibited by the specimens with the small radius holes ($R = 10$ mm) while an almost unstable mode was demonstrated by the specimens with the large radius holes ($R = 40, 50$ mm). The intermediate sized samples, for the most part, showed primary fracture propagation behavior that was transitional between that exhibited by the two extreme hole sizes ($R = 10$ and 50 mm). This data set represents the most complete size effect data set available for polycrystalline materials! The significance of this point can not be overstated. In the open literature, it seems that most authors rely on one or two small scale laboratory tests with

which to calibrate their models. These small scale tests typically show the very stable propagation trends exhibited by the small radius samples ($R = 10$ mm) of this thesis. The size dependent crack initiation phenomenon was already successfully modeled by Carter [18] using a Lajtai's [56] stress averaging technique. The extension of these crack initiation studies to model the diverse crack propagation behavior exhibited by the laboratory data was the challenge of this thesis.

### 5.1.2 Analytical Fracture Models

Analytical models for primary crack propagation from a circular void loaded in compression were evaluated against the laboratory data. Two of the models (Sammis and Ashby [80] and Rummel [79]), which used infinite boundaries, show a concave upward (very stable) trend to the propagation load versus primary crack length curve (Figure 5.2). Although this stable trend was shown by the data sets obtained from the small radius specimens ($R = 10$ and 20 mm) an adequate fit could not be obtained from these models (Figure 3.21, page 47 and Figure 3.26, page 51). This is the result of different boundary conditions between the analytical (infinite boundary) and the physical (finite boundary) models.

Not all the analytical solutions predict the "concave-up" stable conditions. Two additional models (Rooke and Cartwright [78] and Kemeny and Cook [50]) based on simplifications of the actual geometry of the circular void-primary crack problem show an initial instability followed by a "concave-down" stable propagation trend for primary cracks (Figure 5.2). These models also did not produce adequate fits to the observed phenomenon (Figure 3.17, page 44 and Figure 3.32, page 55).

Two analytical models that produced much better results were those of Bažant [3, 5] and Carpinteri et al. [16] (Figure 3.39, page 68 and Figure 3.44, page 76). These models group the propagation data into geometrically similar sets (i.e., grouped by common $L/R$). This essentially treats each group of data as crack initiation events at the tip of a primary crack emanating from a circular void. A size effect model is then fit to each group of crack
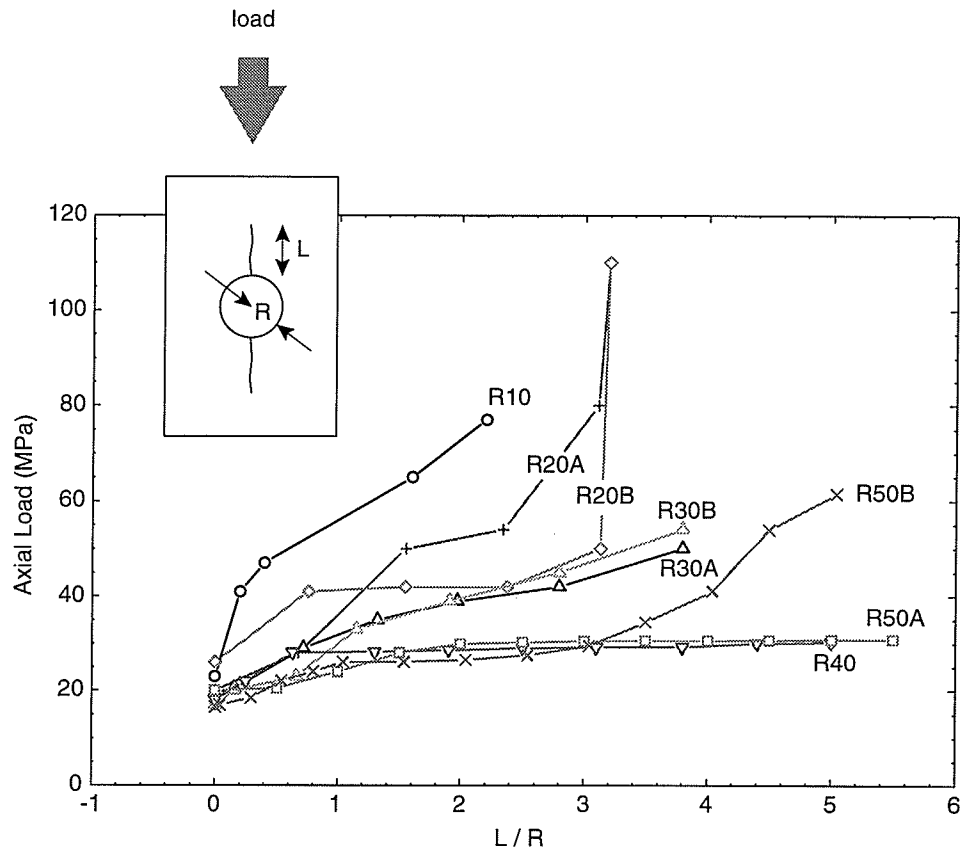
Figure 5.1: Crack propagation stress for primary fractures versus normalized crack length.
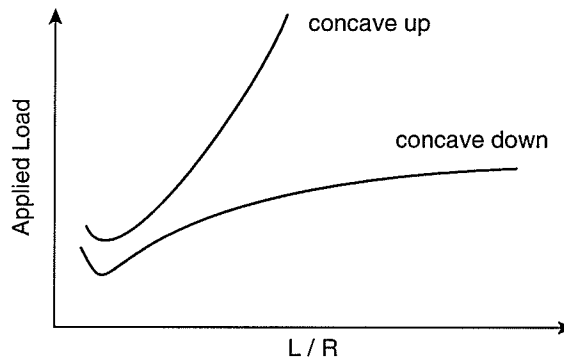


Figure 5.2: Fracture propagation trends predicted by numerical and analytical models.

initiation events. Bažant's models are based on energy balance considerations at the tip of a propagating crack band while Carpinteri's model is based on a multifractal scaling law. One reason why these models produced good results when compared to the previous analytical models is that Bažant's and Carpinteri's models compensate for the boundary influence in the laboratory data by specifying that the data must be grouped into geometrically similar objects. Although the laboratory specimens were not precisely geometrically similar, the minor differences in geometry did not appear to adversely affect the functioning of these models. A cumbersome problem with both of these models is a large number of parameters must be determined to get the models to match the entire data set. Also, the models are not conducive to extrapolating the propagation trends. For this reason an attempt was made to find a functional relation between the model parameters and normalized crack length. A functional relation between Bažant's model parameters and crack length could not be found, however, surprisingly good results for Carpinteri's model parameters were obtained (Figure 3.45, page 77 and Figure 3.46, page 78).

As was previously stated grouping the laboratory data into geometrically similar sets essentially treats fracture propagation as a series of crack initiation events. In the literature survey it was found that Griffith's model and an exponential model produced good results when fit to the primary crack initiation data. Because of these findings it was decided to try to fit Griffith's model and an exponential model to the "grouped" fracture propagation data. Griffith's model, when applied to the grouped data, produced very good results (Figure 3.48, page 81). Griffith's equation is very simple, containing only a single parameter. A strong functional relation was obtained between this Griffith parameter and crack length (Figure 3.49, page 82) resulting in the formulation of a new predictive tool for size dependent crack propagation problems. A similar exercise was tried with the exponential model and a linear relation between the function parameter and crack length was found (Figure 3.53, page 86) resulting in yet another simple predictive tool for size dependent crack propagation problems. This new exponential model was also able to represent the diversity of the

laboratory results quite well (Figure 3.54, page 87).

## 5.1.3 Numerical Fracture Mechanics Based Models

Numerical fracture mechanics based models were able to represent the primary fracture propagation phenomenon quite precisely when actual specimen boundary dimensions were used in the modeling in combination with the $\sigma(\theta)_{\max}$ theory of mixed-mode fracture-mechanics to represent size-effect (Figures 3.77–3.80, pages 105–107). Modeling was done with two fracture mechanics based programs that were built specifically to model fracture propagation (FRANC2D [87] and SIMEX [1]). Both are finite element models and in both models fracture tips were modeled using quarter-point singularity elements. With these models it was also demonstrated that the specimen boundary dimensions substantially contributed to the propagation trends exhibited by the primary fractures.

## 5.1.4 Finite Width Fracture Models with Stress Averaging

Despite the promising results obtained with Bažant's and Carpinteri's analytical models the models are restricted in functionality in the sense that fracture propagation directions could not be predicted. This is because energy balance is solved for without any regard for the spatial distribution of fractures.

Good results were also obtained with the numerical fracture mechanics models (FRANC2D and SIMEX). However, a fracture model was still required that could potentially explain all the fracturing phenomenon observed under compressive loads. Numerical fracture mechanics models are still largely based on the zero-width simplification for fractures. This restriction prohibits the modeling of an isolated fracture that is oriented parallel to the compressive load. In laboratory testing it can be readily seen that fractures that are coaxial with the loading direction are able to propagate. A solution to this problem is to open up the zero-width fracture to some finite width, making it sensitive to axial compressive loads. FRANC2D has this feature, but SIMEX does not. Fracture mechanics based models

also suffer from the inability to correctly predict crack initiation stresses and locations in a modeled material. Crack initiation is a size dependent phenomenon. Size effect in fracture mechanics is modeled only at fracture tips. In locations where there are no fractures a size dependent crack initiation criterion is not available to the classical fracture mechanics modeler (a starter crack is usually assumed). A solution to the problems encountered with the classical fracture mechanics models is to use a finite-width fracture in combination with Lajtai's [56] stress averaging technique to compensate for size effect. Lajtai's stress averaging can be done anywhere in the material domain regardless of whether or not a fracture exists at that location. This is an essential feature for modeling multiple fractures in a material.

The success of the numerical fracture mechanics models in representing the primary fracture propagation data can be attributed partially to the fact that primary fractures propagate under predominantly tensile stresses induced by the circular opening. Regions where tensile forces are reduced (remote regions) or even cease to exist (compressive stress concentration) would undoubtedly cause difficulties for classical fracture mechanics. Using a fracture criterion based on both in plane principal stresses ($\sigma_1$,$\sigma_3$) offers a solution to this problem. Lajtai's [61] USR fracture criterion does just this by taking into account the contribution of the minimum principal stress, $\sigma_3$, as well as the maximum principal stress, $\sigma_1$, acting on a material point.

A model containing all the features (finite-width fracture, size effect anywhere in the material domain, fracture criterion based on both $\sigma_1$ and $\sigma_3$) required to correctly model fractures under compressive loads was not available. For these reasons finite element program InSight$^{2D}$ and boundary element program EJDBEM were developed. Both programs model fractures as discrete finite-width openings which make the fractures sensitive to compressive stresses acting parallel to the fracture axis. The models account for the size effect observed in physical model testing by replacing stresses occurring at a specific point in the material with stresses that are averaged over a finite area. The models incorporate Lajtai's

USR fracture criterion which accounts for influences from both in plane principal stresses. A fixed-width fracture model as well as an elliptical fracture model were evaluated.

The finite-width fracture model produced results similar to those found with the fracture mechanics based finite element codes (FRANC2D and SIMEX) (Figures 4.28–4.31, pages 141–142 and Figures 4.35–4.38, pages 146–147). Once again it was found that the best results were obtained when the actual specimen boundary dimensions were used in the modeling. Arguments can be made for maintaining a constant fracture width or scaling fracture width in proportion to hole size. The elliptical and fixed-width fractures can both be calibrated to the laboratory data and behave almost identically when finite specimen boundaries are used in the modeling. When infinite boundaries are considered, the elliptical and fixed-width fractures behave differently. The elliptical fracture becomes extremely difficult to propagate. This model could not be calibrated to the laboratory data even when fracture width was scaled in proportion to hole size. On the other hand the fixed-width fracture could be calibrated to the laboratory data, when infinite boundaries were considered, but only by scaling fracture width in proportion to the hole size (Figure 4.33, page 144).

When an isolated finite-width fracture is loaded axially in compression the elliptical fracture and fixed-width fracture behave quite differently. The elliptical fracture becomes increasingly difficult to propagate as it lengthens due to the tapering of the fracture and the corresponding decrease in radius of curvature at the tip. The fixed-width fracture, on the other hand, eventually reaches a length after which the load required to sustain fracture propagation remains constant. As a result it is much easier to propagate than the elliptical fracture. This is probably the reason why the fixed-width fracture model could be calibrated to the laboratory data when infinite boundaries were considered.

## Step-Out Fractures and *En Echelon* Crack Arrays

Under certain conditions, a fracture propagating under the influence of an external compressive load will stop propagating and a secondary fracture will initiate adjacent to the

original and now stalled crack tip. This is sometimes called a "step-out" fracture (Figure 4.11, page 124). The step-out phenomenon is important because it is this progressive process that leads to *en echelon* crack formation which can ultimately lead to a macroscopic shear type failure often observed in laboratory compression tests (Figure 4.12, page 125).

Although it is beyond the scope of this thesis topic it was shown that the finite-width fracture model with stress averaging and USR fracture criterion could produce step-outs (Figure 4.48, page 162). This model relies on propagating finite-width fractures through heterogeneous media (an option incorporated into EJDBEM).

## 5.2 Conclusions

This investigation into fracture propagation under compressive loads has demonstrated that existing fracture mechanics models are adequate for modeling fractures under compressive loading conditions, but only in specific cases. In the data set used in this thesis the primary fractures where driven by predominantly tensile forces which is a problem conducive to classical fracture mechanics. A fracture model capable of correctly representing the size dependent initiation and propagation histories of any compressive stress induced fracture in a brittle material was not available. This thesis presents such a model. This finite-width, size dependent, compression sensitive fracture model was calibrated to primary fracture propagation data obtained from laboratory testing. This modeling also demonstrated the significant boundary influences that came into effect during the laboratory testing. This "unified" fracture model also shows promise in modeling macroscopic failure processes such as shear band formation in compression testing and spalling type events in underground excavations (Figure 2.5, page 12).

There are numerous practical implications of this thesis. Laboratory measurements and *in situ* measurements of material strength are known to be governed by the formation and propagation of fractures. Nevertheless, engineers still rely on empirical models to predict macroscopic failure. These approximations are adequate in low stress environments, but

in high stress regimes rock can become "damaged" through the formation of a pervasive system of micro-fractures. This damage and its mechanisms are not yet fully understood or quantifiable. Understanding fracture behavior is therefore paramount to solving this problem. On a different scale a numerical model capable of correctly modeling fractures as they actually occur underground would obviously benefit the ground control engineer. From the high level waste management perspective a predictive tool such as this would prove to be invaluable in estimating the risk factors involved in burying waste deep in plutonic rock masses.

Even though this thesis has provided considerable insight into the fracture process there are always unanswered questions. Several areas slated for future work are listed below.

1. Boundary influences. Investigate influence of specimen width on fracture propagation further. Is increasing specimen width similar to applying confining pressure? Is the absence of primary fractures in the smallest hole ($R = 2.5$ mm) the result of a boundary effect (large specimen width) or is it a size effect? Because of the economy of the small hole size a series of uniaxial compression tests could be done relatively inexpensively on a set of blocks of varying width and constant height. Strain gauges would not even be required. If primary fractures formed in narrow samples then a boundary influence would be indicated.

2. Confining pressure influence. Some cracks may close. This requires the introduction of friction and the solution of a nonlinear problem.

3. Step-out modeling. Step-outs are observed under compressive as well as tensile conditions. This important phenomenon is a key component in representing *en echelon* crack formation which often leads to the ultimate collapse of structures.

4. Calibrate models to initiation and propagation of all three fracture types (primary,

remote, spalling).  Primary and remote fractures are feasible to model, but the fractures in the compressive stress concentration occur in swarms and may be difficult to model with discrete fractures.

# Bibliography

[1] M. L. Ayari. SIMEX user's manual. internal report, Department of Mechanical Engineering, University of Manitoba, Winnipeg, Manitoba, Canada, 1993.

[2] R. S. Barsoum. Triangular quarter-point elements as elastic and perfectly plastic crack tip elements. *Int. J. Numer. Methods Eng.*, 11:85–98, 1977.

[3] Z. P. Bažant. Size effect in blunt fracture: concrete, rock, metal. *J. Eng. Mech.*, 110(4):518–535, 1984.

[4] Z. P. Bažant and M. T. Kazemi. Size effect in fracture of ceramics and its use to determine fracture energy and effective process zone length. *J. Am. Ceram. Soc.*, 73(7):1841–1853, 1990.

[5] Z. P. Bažant, M. T. Kazemi, T. Hasegawa, and J. Mazars. Size effects in Brazilian split-cylinder tests: measurements and fracture analysis. *ACI Mater. J.*, 88:325–332, 1991.

[6] Z. T. Bieniawski. Mechanism of brittle fracture of rock. Parts I, II, and III. *Int. J. Rock Mech. Min. Sci.*, 4(4):395–430, 1967.

[7] Z. T. Bieniawski, H. G. Denkhaus, and U. W. Vogler. Failure of fractured rock. *Int. J. Rock Mech. Min. Sci.*, 6:323–341, 1969.

[8] E. Bombolakis. Photoelastic investigation of brittle crack growth within a field of uniaxial compression. *Tectonophysics*, 1(4):343–351, 1964.

[9] E. Bombolakis. Photoelastic study of the initial stages of brittle fracture in compression. *Tectonophysics*, 6(6):461–473, 1968.

[10] O. L. Bowie. Analysis of an infinite plate containing radial cracks originating at the boundary of an internal circular hole. *Journal of Mathematics and Physics*, 35:60–71, 1956.

[11] W. F. Brace and E. G. Bombolakis. A note on brittle crack growth in compression. *J. Geophys. Res.*, 68:3709–3713, 1963.

[12] W. F. Brace and J .D. Byerlee. Recent experimental studies of brittle fracture of rocks. In C. Fairhurst, editor, *Proc. 8th U.S. Symp. on Rock Mechanics, Minneapolis*, pages 58–81. American Institute of Mining Engineers, 1966.

[13] W. F. Brace, B. Paulding, and C. Scholz. Dilatancy in the fracture of crystalline rocks. *J. Geophys. Res.*, 71:3939–3953, 1966.

[14] J. W. Bray. Some applications of elastic theory. In E. T. Brown, editor, *Analytical and Computational Methods in Engineering Rock Mechanics*, pages 32–94. Allen and Unwin, London, 1987.

[15] A. Brown, N. M. Soonawala, R. A. Everitt, and D. C. Kamineni. Geology and geophysics of the Underground Research Laboratory Site, Lac du Bonnet Batholith, Manitoba. *Can. J. Earth Sci.*, 26:404–425, 1989.

[16] A. Carpinteri, B. Chiaia, and G. Ferro. Size effects on nominal tensile strength of concrete structures: multifractality of material ligaments and dimensional transition from order to disorder. *Materials and Structures*, 28:311–317, 1995.

[17] B. J. Carter. *Remote fracturing around underground openings*. MSc thesis, Civil Engineering Department, University of Manitoba, Winnipeg, Manitoba, Canada, 1988.

[18] B. J. Carter. *Physical and numerical modelling of fracture in rock: With special emphasis on the potash mines of Saskatachewan*. PhD thesis, Civil Engineering Department, University of Manitoba, Winnipeg, Manitoba, Canada, 1992.

[19] B. J. Carter, E. J. S. Duncan, and E. Z. Lajtai. Fitting strength criteria to intact rock. *Geotech. Geol. Eng.*, 9:73–81, 1991.

[20] B. J. Carter, E. Z. Lajtai, and Y. Yuan. Tensile fracture from circular cavities loaded in compression. *Int. J. Fract.*, 57:221–236, 1992.

[21] B. Cotterell. Brittle fracture in compression. *Int. J. Fract. Mech.*, 8(2):195–208, 1972.

[22] B. Cotterell and J. R. Rice. Slightly curved or kinked cracks. *Int. J. Fract. Mech.*, 16(2):155–169, 1980.

[23] S. L. Crouch and A. M. Starfield. *Boundary Element Methods in Solid Mechanics*. George Allen & Unwin Ltd., London, 1983.

[24] F. D. E. Cuisiat. Fracture mechanics analysis of the mechanisms leading to borehole spalling. In H. J. Siriwardane, editor, *Proc. 8th Int. Conf. of the Association for Computer Methods and Advances in Geomechanics (IACMAG94), Morgantown, West Virginia*, volume II, pages 1573–1578. A. A. Balkema, Rotterdam, 1994.

[25] Y. Du and A. Aydin. Interaction of multiple cracks and formation of echelon crack arrays. *Int. J. Numer. Anal. Methods Geomech.*, 15:205–218, 1991.

[26] E. J. Dzik and E. Z. Lajtai. Modeling the axial tensile fractures of the compressive stress field. *Rock Mech. Rock Eng.*, submitted 1995.

[27] F. Erdogan and G. C. Sih. On the crack extension in plates under plane loading and transverse shear. *J. Basic Engr. ASME*, 85:519–527, 1963.

[28] R. A. Everitt, A. Brown, C. C. Davison, M. Gascoyne, and C. D. Martin. Regional and local setting of the Underground Research Laboratory. In R. S. Sinha, editor, *Proc. Int. Symp. on Unique Underground Structures, Denver*, volume 2, pages 64:1–23. CSM Press, Denver, 1990.

[29] M. P. Fischer, D. Elsworth, R. B. Alley, and T. Engelder. Finite element analysis of the modified ring test for determining Mode I fracture toughness. *Int. J. Rock Mech. Min. Sci. Geomech. Abstr.*, 33(1):1–15, 1996.

[30] N. C. Gay. Fracture growth around openings in thick-walled cylinders of rock subjected to hydrostatic compression. *Int. J. Rock Mech. Min. Sci. Geomech. Abstr.*, 10:209–233, 1973.

[31] N. C. Gay. Fracture growth around openings in large blocks of rock subjected to uniaxial and biaxial compression. *Int. J. Rock Mech. Min. Sci. Geomech. Abstr.*, 13:231–243, 1976.

[32] L. P. Gonano. *Stress gradient and size effect phenomenon in brittle materials*. PhD thesis, James Cook University, Northern Queensland, Australia, 1974.

[33] A. A. Griffith. The phenomenon of rupture and flow in solids. *Phil. Trans. R. Soc. London*, 221A:163–198, 1921.

[34] A. A. Griffith. Theory of rupture. In *First International Congress on Applied Mechanics, Delft*, pages 55–63, 1924.

[35] T. Hao. Theory of formation of a main crack in a cracked brittle-elastic body under compression. *Int. J. Fract.*, 42(2):R43–R46, 1990.

[36] E. Hoek. Experimental study of rock-stress problems in deep-level mining. In S. E. Rossi, editor, *Proc. of the First Int. Congress on Experimental Mechanics, New York*, pages 177–194, 1963.

[37] E. Hoek. Rock fracture around mining excavations. In *Proc. of the Fourth Int. Conf. Strata Control and Rock. Mech., New York*, pages 334–348, 1964.

[38] E. Hoek and Z. T. Bieniawski. Brittle fracture propagation in rock under compression. *J. Fract. Mech.*, 1(3):137–155, 1965.

[39] E. Hoek and E. T. Brown. *Underground Excavations in Rock*. The Institution of Mining and Metallurgy, London, 1982.

[40] H. Horii and S. Nemat-Nasser. Compression-induced microcrack growth in brittle solids: axial splitting and shear failure. *J. Geophys. Res.*, 90:3105–3125, 1985.

[41] H. Horii and S. Nemat-Nasser. Brittle failure in compression: splitting, faulting, and brittle ductile transition. *Phil. Trans. R. Soc. London, Math Phys. Sci.*, 319:337–374, 1986.

[42] C.E. Inglis. Stresses in a plate due to the presence of cracks and sharp corners. *Trans. R. Instn. Nav. Archit.*, 60:219–230, 1913.

[43] A. R. Ingraffea. The strength ratio effect in the fracture of rock structures. In *Proc. 20th U.S. Symp. on Rock Mech., Austin, Texas*, pages 153–162, 1979.

[44] A. R. Ingraffea and F. E. Heuze. Finite element models for rock fracture mechanics. *Int. J. Numer. Anal. Methods Geomech.*, 4:25–43, 1980.

[45] A. R. Ingraffea and R. A. Schmidt. Experimental verification of a fracture mechanics model for tensile strength prediction of Indiana limestone. In *Proc. 19th U.S. Symp. on Rock Mech., Stateline, Nevada*, pages 247–253, 1978.

[46] G. Irwin. Fracture dynamics. *Fracturing of Metals, American Society of Metals, Cleveland, Ohio*, pages 147–166, 1948.

[47] J. C. Jaeger and N. G. W. Cook. *Fundamentals of rock mechanics*. Chapman and Hall, London, third edition, 1979.

[48] I. W. Johnston. Strength of intact geomechanical materials. *J. Geotech. Engng. Div. ASCE*, 111(6):730–749, 1985.

[49] J. M. Kemeny and N. G. W. Cook. Crack models for the failure of rocks in compression. In C. S. Desai, E. Krempl, P. D. Kiousis, and T. Kundu, editors, *Proc. 2nd Int. Conference Constitutive Laws for Engineering Materials, Theory and Applications*, volume 1, pages 879–887, Tucson, Arizona, 1987. Elsevier Science Publishing Co.

[50] J. M. Kemeny and N. G. W. Cook. Micromechanics of deformation in rocks. In S. P. Shaw, editor, *Toughening Mechanics in Quasi-Brittle Materials*, volume 2, pages 155–188. Klewer Academic, The Netherlands, 1991.

[51] J. K. Kim and S. H. Eo. Size effect in concrete specimens with dissimilar initial cracks. *Mag. Concr. Res.*, 42:233–238, 1990.

[52] J. K. Kim, S. H. Eo, and H. K. Park. Size effect in concrete structures without initial crack. In *Fracture Mechanics: Application to concrete*, volume SP-118, pages 179–196. American Concrete Institute, Detroit, 1989.

[53] G. Kirsch. Die theorie der elastizitat und die bedürfnisse der festigkeitslehre. *Viet. Ver. Deut. Ing.*, 42:797–807, 1898.

[54] R. L. Kranz. Microcracks in rocks: A review. *Tectonophysics*, 100:449–480, 1983.

[55] E. Z. Lajtai. A theoretical and experimental evaluation of the Griffith theory of brittle fracture. *Tectonophysics*, 11:129–156, 1971.

[56] E. Z. Lajtai. Effect of tensile stress gradient on brittle fracture initiation. *Int. J. Rock Mech. Min. Sci.*, 9:569–578, 1972.

[57] E. Z. Lajtai. Brittle fracture in compression. *Int. J. Fract.*, 10(4):525–536, 1974.

[58] E. Z. Lajtai. Creep and crack growth in Lac du Bonnet granite due to compressive stress. In L. A. Simpson, editor, *Proc. of the Fifth Canadian Fracture Conference, Winnipeg, MB*, pages 229–238. Pergamon Press, Oxford, 1981.

[59] E. Z. Lajtai. The deformation, fracture and strength of Lac du Bonnet Granite. internal report, Department of Geological Engineering, University of Manitoba, Winnipeg, Manitoba, Canada, 1988.

[60] E. Z. Lajtai. Time-dependent behaviour of the rock mass. *Geotech. Geol. Eng.*, 9:109–124, 1991.

[61] E. Z. Lajtai, B. J. Carter, and E. J. S. Duncan. Mapping the state of fracture around cavities. *Eng. Geol.*, 31:277–289, 1991.

[62] E. Z. Lajtai and E. J. Dzik. Searching for the damage threshold in intact rock. In M. Aubertin, F. Hassani, and H. Mitri, editors, *Proc. Second North American Rock Mechanics Symposium (NARMS96), Montreal, 1996*, volume 1, pages 701–708. A. A. Balkema, Rotterdam, 1996.

[63] E. Z. Lajtai and V. N. Lajtai. The collapse of cavities. *Int. J. Rock Mech. Min. Sci. Geomech. Abstr.*, 12:81–86, 1975.

[64] E. Z. Lajtai and R. H. Schmidtke. Delayed failure in rock loaded in uniaxial compression. *Rock Mech. Rock Eng.*, 19:11–25, 1986.

[65] E. Z. Lajtai, R. H. Schmidtke, and L. P. Bielus. The effect of water on the time-dependent deformation and fracture of a granite. *Int. J. Rock Mech. Min. Sci. Geomech. Abstr.*, 24(4):247–255, 1987.

[66] N. Lundborg. The strength-size relation of granite. *Int. J. Rock Mech. Min. Sci.*, 4:269–272, 1967.

[67] E. Madenci. Slightly open, penny-shaped crack in an infinite solid under biaxial compression. *Theor. Appl. Fract. Mech.*, 16(3):215–222, 1991.

[68] C. D. Martin. Excavation response in a highly stressed rock mass. In *Proc. OCED NEA Workshop on Excavation Response in Geological Repositories for Radioactive Waste*, pages 331–340, Winnipeg, Canada, 1989. OECD, Paris.

[69] C. D. Martin. *The Strength of Massive Lac du Bonnet Granite Around Underground Openings*. PhD thesis, Department of Civil and Geological Engineering, University of Manitoba, Winnipeg, Manitoba, Canada, 1993.

[70] F. A. McClintock and J. B. Walsh. Friction on Griffith cracks in rocks under pressure. In *Proc. 4th U.S. Nat. Congr. Appl. Mech.*, volume 2, pages 1015–1021. Am. Soc. Mech. Eng., New York, 1962.

[71] V. Nesetova and E. Z. Lajtai. Fracture from compressive stress concentrations around elastic flaws. *Int. J. Rock Mech. Min. Sci. Geomech. Abstr.*, 10:265–284, 1973.

[72] E. Orowan. Fundamentals of brittle behavior in metals. In *Fatigue and Fracture of Metals (MIT Symposium, June, 1950)*. John Wiley & Sons, New York, 1952.

[73] K. Palaniswamy. *Crack propagation under general, in-plane loading*. PhD thesis, California Institute of Technology, Pasadena, USA, 1972.

[74] P. C. Paris and G. C. Sih. Stress analysis of cracks. In *ASTM STP 381*, pages 30–81. American Society of Testing and Materials, Philadelphia, 1965.

[75] S. Peng and A. M. Johnson. Crack growth and faulting in cylindrical specimens of Chelmsford granite. *Int. J. Rock Mech. Min. Sci.*, 9:37–86, 1972.

[76] R. S. Read and C. D. Martin. Technical summary of AECL's Mine-by Experiment Phase 1: Excavation response. AECL Report AECL-11311, Atomic Energy of Canada Limited, 1996.

[77] O. M. Reyes. *Experimental Study and Analytical Modelling of Compressive Fracture in Brittle Materials*. PhD thesis, Department of Civil Engineering, Massachusetts Institute of Technology, USA, 1991.

[78] D. P. Rooke and D. J. Cartwright. *Compendium of stress intensity factors*. The Hillingdon Press, Middlesex, 1976.

[79] F. Rummel. Fracture mechanics approach to hydraulic fracturing stress measurements. In B. K. Atkinson, editor, *Fracture mechanics of rock*, pages 217–240. Academic Press, London, 1987.

[80] C. G. Sammis and M. F. Ashby. The failure of brittle porous solids under compressive stress states. *Acta. Metall.*, 34(3):511–526, 1986.

[81] R. A. Schmidt and T. J. Lutz. $k_{Ic}$ and $j_{Ic}$ of Westerly Granite - Effects of thickness and in-plane dimensions. In S. W. Frieman, editor, *Fracture Mechanics Applied to Brittle Materials, ASTM STP 678*, pages 166–182. American Society for Testing and Materials, 1979.

[82] G. C. Sih. *Handbook of Stress Intensity Factors for Researchers and Engineers*. Lehigh University, Bethlehem, PA, 1973.

[83] G. C. Sih. *Methods of analysis and solutions of crack problems*, volume 1. Noordhoff International Publishing, Leyden, 1973.

[84] G. C. Sih. Strain-energy-density factor applied to mixed mode crack problems. *Int. J. Fract.*, 10(3):305–321, 1974.

[85] P. Tapponnier and W. F. Brace. Development of stress-induced microcracks in Westerly granite. *Int. J. Rock Mech. Min. Sci. Geomech. Abstr.*, 13:103–112, 1976.

[86] W. R. Wawersik and C. Fairhurst. A study of brittle rock fracture in laboratory compression experiments. *Int. J. Rock Mech. Min. Sci.*, 7:561–575, 1970.

[87] P. A. Wawrzynek and A. R. Ingraffea. FRANC2D a two-dimensional crack propagation simulator, version 2.7 user's guide. internal report, Department of Structural Engineering, Cornell University, Ithaca, New York, USA, 1993.

[88] W. Weibull. A statistical theory of the strength of materials. *IngvetenskAkad. Handl.*, 151:5–45, 1939.

[89] H. M. Westergaard. Bearing pressures and cracks. *J. Appl. Mech.*, 6:49–53, 1939.

[90] B. N. Whittaker, R. N. Singh, and Sun G. *Rock Fracture Mechanics: Principles, Design and Applications*. Number 71 in Developments in Geotechnical Engineering. Elsevier, London, first edition, 1992.

[91] B. J. S. Wilkins, A. R. Reich, and W. R. Wallace. Slow microcracking in plutonic rocks. AECL Technical Record TR-264, Atomic Energy of Canada Limited, 1984.

[92] Y. G. Yuan, E. Z. Lajtai, and M. L. Ayari. Fracture nucleation from a compression-parallel finite-width elliptical flaw. *Int. J. Rock Mech. Min. Sci. Geomech. Abstr.*, 30(7):873–876, 1993.